



**HAL**  
open science

# Atomistic Simulations of Ultrafast Laser-induced Devitrification of Metallic Glasses

Djafar Iabbaden

► **To cite this version:**

Djafar Iabbaden. Atomistic Simulations of Ultrafast Laser-induced Devitrification of Metallic Glasses. Mechanical engineering [physics.class-ph]. Université Jean Monnet - Saint-Etienne, 2023. English. NNT : 2023STET0005 . tel-04540670

**HAL Id: tel-04540670**

**<https://theses.hal.science/tel-04540670>**

Submitted on 10 Apr 2024

**HAL** is a multi-disciplinary open access archive for the deposit and dissemination of scientific research documents, whether they are published or not. The documents may come from teaching and research institutions in France or abroad, or from public or private research centers.

L'archive ouverte pluridisciplinaire **HAL**, est destinée au dépôt et à la diffusion de documents scientifiques de niveau recherche, publiés ou non, émanant des établissements d'enseignement et de recherche français ou étrangers, des laboratoires publics ou privés.



N°d'ordre NNT : 2023STET005

# THÈSE de DOCTORAT DE L'UNIVERSITÉ JEAN MONNET SAINT-ÉTIENNE

Membre de la COMUE de LYON

École Doctorale 488

Sciences Ingénierie Santé SIS

Sciences des matériaux et génie mécanique

Soutenue publiquement le 27/01/2023, par :  
**Djafar IABBADEN**

---

## Atomistic Simulations of Ultrafast Laser-induced Devitrification of Metallic Glasses

---

Devant le jury composé de :

Leonid Zhigilei, Professeur, Université de Virginie, Rapporteur

Anne Tanguy, Professeur, LAMCOS/INSA, Rapporteur

Jean-François Pierson, Professeur, Institut Jean Lamour/Université de Lorraine  
Nancy, Président

Jonathan Amodeo, Chercheur CNRS, Aix Marseille Univ/Université de Toulon,  
Examineur

Claudio Fusco, Maître de conférences, MATEIS/INSA Lyon, Invité

Dmitry Ivanov, Chercheur, Université de Kassel, Invité

Florence Garrelie, Professeur, Laboratoire Hubert Curien/UJM, Co-directrice de  
thèse

Jean-Philippe Colombier, Professeur, Laboratoire Hubert Curien/UJM, Directeur  
de thèse

# Dedication

To my mum and dad,  
who instilled in me that three things are important in life:  
love, dream and education.  
I dedicate you this work

“A method is more important than a discovery, since the right method will lead to new and even more important discoveries.”

— Lev Landau

# Acknowledgements

Five years ago, I left my beloved homeland Kabylia to embark on a thrilling adventure in France. I am proud to say that my goal to become a Doctor of Theoretical Physics is finally achieved. The experience has been nothing short of exhilarating, with each day presenting new challenges and opportunities for learning. I've had the pleasure of working with individuals from diverse backgrounds, that has enriched my experience immeasurably. Looking back, I feel that I am not just a product of the circumstances, but a result of the hard choices I've made throughout my life, starting with my decision to pursue physics. Despite the challenges and intense workload, I never lost faith and motivation. I held firm to the belief that things would work out, and they did.

I would like to extend my sincere gratitude to my dear supervisor, Professor Jean-Philippe COLOMBIER, for accepting me into his research group and for guiding me through all my Ph.D. journeys. Since the moment I arrived in the laboratory, he made me feel comfortable and was always available to provide guidance and support. I am thankful for his wise suggestions, valuable advice, and the time he dedicated to help. He went above and beyond to ensure that I had all the resources I needed to complete smoothly my thesis, including access to computing facilities and laboratory equipment. He also encouraged me to participate in conferences, summer schools, and workshops, which allowed me to meet and collaborate with peers in my field. I was struck by his genuine interest in my work and the pleasure he took in discussions and collaboration. I appreciated the freedom he gave me to conduct my investigations, and his trust in my abilities as a young researcher. He had a positive impact on my career, and I will always be grateful for the chance he gave me to work beside a scientist of his calibre. He will always be remembered as a mentor that took me under his wing, thank you for everything.

I would like to express my deep appreciation to Professor Florence GARRELIE for her contributions to this work. I am grateful for her expertise, critical eye, and insightful suggestions, which helped shape my work and bring it to fruition.

During our numerous meetings, she provided rigorous analysis and insightful interpretations of the results, her dynamic, and clear guidance was invaluable.

I would like to extend my gratitude to a remarkable person, Dr. Jonathan AMODEO. Over the past three years, he has been an exceptional instructor to me in the field of molecular dynamics. I can not stress enough how much I have learned from him during my Ph.D. Starting from the basics to advanced techniques, he has guided me every step to become a true expert in performing atomistic modeling. I am grateful for his patient and meticulous teaching, which allowed me to analyze results, utilize different simulation tools, interpret the findings, and effectively communicate my work through writing articles. I consider myself lucky to cross such a knowledgeable and dedicated mentor. Our discussions were always enlightening, and his vast experience provided me with invaluable insights, helping me overcome challenges and put my ideas into practice. I owe my skills and knowledge in molecular dynamics to Dr. AMODEO and I am forever grateful for his guidance. Thank you for being a crucial part of my research work.

I address particular thanks to Dr. Claudio FUSCO, for passing me his molecular dynamics knowledge during my Ph.D. research meetings. I want to thank him for his patient explanation, constructive suggestions, rigorous attitude toward the obtained results, and for providing a really valuable comment and criticism.

I express my gratitude to Dr. Dmitry IVANOV for being a part of my jury member. Also, for his willingness to take me on as his student was a valuable opportunity that I will always cherish. I want to thank him for the time he spent teaching me his simulation code line by line, sharing his expertise, and imparting his knowledge on molecular dynamics modeling of laser-matter interaction. The experience I gained under his guidance has been instrumental in expanding my skillset and opening new doors for my career. I will always be indebted for the skills he has imparted to me, and for the opportunity to learn from one of the best in the field.

I am deeply thankful to Professor Jean-François PIERSON for accepting the role of president for my Ph.D defense jury. His presence and valuable scientific insights during the defense made a tremendous impact on the future possible outcome of the concurrent work.

I extend my heartfelt gratitude to the referee of my jury namely Professor Leonid ZHIGILEI and Professor Anne TANGUY for their time, effort, and dedication in serving as my evaluators. I am especially grateful for the insightful critiques and suggestions that you provided, which helped the improvement my work quality.

I would like to address a warm thank to Thomas GAUTRAIS our laboratory engineer for his exceptional help. He was always giving me a valuable suggestions for the optimal use of the local computing facilities at various stages of this Ph.D work.

I would like to thank GENCI-TGCC, CINES (project gen7041), and P2HPD computing center facility of Lyon University for providing me access to high-performance computing.

My deepest respect goes to my daily colleague Dr. Arshak TSATURYAN for his motivation, the time we spent together, and the fruitful discussions we had. These past years would not have been the same without his presence.

I deeply want to thank my daily colleagues: Lucas, Mathilde, Priya, Yannick, Ilemona, Daniel, Anthony, Yoan, Marion, Gerges, and Cédric for sharing with me the office, friendship, memories, and countless other things.

My sincerest thanks are due to my dearest Mom, Dad, brothers, and sisters for their unconditional love, motivation, and encouragement throughout all my studies. I owe you everything.

Finally, I want to express my gratitude to all my friends for the encouragement and the support they provided when I needed them over the last few years.

# Contents

<b>Dedication</b>	<b>ii</b>
<b>Acknowledgments</b>	<b>v</b>
<b>List of Figures</b>	<b>ix</b>
<b>List of Tables</b>	<b>xx</b>
<b>Nomenclature</b>	<b>xxvi</b>
<b>Abstract</b>	<b>xxviii</b>
<b>Résumé</b>	<b>xxx</b>
<b>Thesis scope and objectives</b>	<b>4</b>
<b>1 Overview of metallic glasses and ultrafast lasers processes</b>	<b>5</b>
1.1 Introduction . . . . .	5
1.2 Ultrafast lasers processes . . . . .	6
1.2.1 Applications of ultrafast lasers . . . . .	6
1.2.2 Ultrafast laser processing conditions . . . . .	8
1.2.3 Ultrafast laser modeling and induced mechanisms . . . . .	9
1.2.4 Atomistic modeling of ultrashort laser interaction with materials . . . . .	11
1.3 Metallic glasses . . . . .	13
1.3.1 Glass transition temperature . . . . .	14
1.3.2 Structure of metallic glasses . . . . .	16
1.3.3 Metallic Glass forming ability . . . . .	16
1.3.4 Metallic Glass formability . . . . .	17
1.4 CuZr binary alloy phase diagram . . . . .	18
1.5 Imperfections in solids . . . . .	20
1.6 Classical theory of crystallization . . . . .	22

1.7	Ultrafast laser inducing devitrification of Metallic glasses . . . . .	24
1.8	Summary conclusion . . . . .	29
<b>2</b>	<b>Theory and analysis</b>	<b>30</b>
2.1	Introduction . . . . .	30
2.2	A brief overview of molecular statics . . . . .	31
2.3	Integration of Newton's equation . . . . .	33
2.4	LAMMPS code . . . . .	35
2.5	Global organization of the input script . . . . .	35
2.5.1	Interatomic potential . . . . .	35
2.5.2	Potential cutoff . . . . .	38
2.5.3	Neighbor lists construction . . . . .	38
2.5.4	Timestep . . . . .	39
2.5.5	Boundary conditions . . . . .	39
2.5.6	Thermodynamic ensembles . . . . .	39
2.5.7	Build of the initial structures . . . . .	40
2.6	Two temperature model . . . . .	40
2.7	TTM-MD implemented in LAMMPS . . . . .	43
2.8	Post-processing of LAMMPS output data with OVITO . . . . .	48
2.8.1	Radial distribution function . . . . .	48
2.8.2	Common Neighbor Analysis . . . . .	49
2.8.3	Polyhedral Template Matching . . . . .	50
2.8.4	Construct surface mesh . . . . .	50
2.8.5	Wigner-Seitz defect analysis . . . . .	51
2.8.6	Entropy . . . . .	52
2.9	Summary conclusion . . . . .	53
<b>3</b>	<b>Phase transition in crystalline and amorphous CuZr alloys</b>	<b>54</b>
3.1	Introduction . . . . .	54
3.2	CuZr metallic glasses samples elaboration . . . . .	56
3.2.1	Determination of the theoretical melting temperatures . . . . .	56
3.2.2	Melting temperature of the B <sub>2</sub> -Cu <sub>50</sub> Zr <sub>50</sub> and C11 <sub>b</sub> -Cu <sub>33.3</sub> Zr <sub>66.7</sub> structures . . . . .	57
3.2.3	CuZr metallic glasses initial structure . . . . .	61
3.2.4	Rapid solidification and theoretical glass transition temperatures . . . . .	63
3.2.5	Surface impact on the amorphous structures . . . . .	67
3.3	Laser-matter interaction setup . . . . .	69
3.3.1	Determination of electronic meshing . . . . .	70

3.3.2	Computational details . . . . .	72
3.4	Irradiation of B <sub>2</sub> -Cu <sub>50</sub> Zr <sub>50</sub> crystalline structure: formation of twins	73
3.5	Irradiation of C11 <sub>b</sub> -Cu <sub>33.3</sub> Zr <sub>66.7</sub> crystalline structure: formation of defects . . . . .	77
3.6	Ultrafast laser interaction with Metallic-Glasses: ablation threshold mechanism . . . . .	80
3.7	Summary conclusion . . . . .	83
<b>4</b>	<b>Modeling of cavitation formation in amorphous CuZr alloy</b>	<b>85</b>
4.1	Introduction . . . . .	85
4.2	Outline of the objectives . . . . .	86
4.3	Simulation setup and computational details . . . . .	87
4.4	Modeling the ultrafast laser irradiation of $\alpha$ -Cu <sub>35</sub> Zr <sub>65</sub> . . . . .	90
4.4.1	Nanovoids formation . . . . .	90
4.4.2	Thermodynamics of the voids formation in $\alpha$ -Cu <sub>35</sub> Zr <sub>65</sub> . . . . .	91
4.4.3	Front expansion average velocity . . . . .	95
4.4.4	Quantification of voids . . . . .	96
4.5	Experimental versus modeling results . . . . .	97
4.6	Summary conclusion . . . . .	99
<b>5</b>	<b>Atomistic simulation of CuZr Metallic glass devitrification</b>	<b>100</b>
5.1	Introduction . . . . .	100
5.2	Ultrafast laser driving devitrification strategy . . . . .	101
5.3	Devitrification by including defects . . . . .	102
5.4	CuZr initial specimen configurations . . . . .	103
5.4.1	Spontaneous crystallization . . . . .	105
5.4.2	Melting and glass transition temperatures . . . . .	106
5.4.3	Laser-matter computational details . . . . .	108
5.5	CuZr alloy nanocomposite creation via ultrafast laser . . . . .	109
5.5.1	Local structure during the ultrafast laser devitrification . . . . .	110
5.5.2	Confirmation of crystalline state by virtual XRD analysis . . . . .	113
5.6	Devitrification mechanism in $\alpha$ -Cu <sub>21.9</sub> Zr <sub>78.1</sub> . . . . .	116
5.6.1	Critical temperature of the crystals growth . . . . .	121
5.6.2	Spatial cartography of temperature and pressure during devitrification . . . . .	122
5.6.3	Entropy computation during the devitrification . . . . .	123
5.6.4	Amorphous CuZr-alloy devitrification free energy computation . . . . .	125
5.7	Application to phononic thermal conductivity . . . . .	126

5.8 Summary conclusion . . . . .	128
<b>Conclusion</b>	<b>131</b>
<b>Vita</b>	<b>133</b>
<b>APPENDICES</b>	<b>134</b>
<b>A Build LAMMPS with make in MPI</b>	<b>134</b>
<b>B LAMMPS script to determine the melting temperatures</b>	<b>136</b>
<b>C LAMMPS script to prepare amorphous sample</b>	<b>140</b>
<b>D Simulation of laser-matter interactions using LAMMPS</b>	<b>143</b>
<b>E ABINIT script to compute the internal energy</b>	<b>153</b>
<b>F Input parameter file of ttm/mod</b>	<b>155</b>
<b>G Gaussian script to compute Gibbs free energy</b>	<b>157</b>
<b>H Fortran90 code to produce the initial ttm/md electron temperature</b>	<b>159</b>
<b>I LAMMPS input script to compute the XRD pattern</b>	<b>161</b>
<b>J Entropy calculation using LAMMPS</b>	<b>163</b>
<b>K LAMMPS script for calculating the total RDF</b>	<b>165</b>
<b>L LAMMPS script for computing equilibrium phononic thermal conductivity</b>	<b>168</b>
<b>M Electronic properties of CuZr systems</b>	<b>171</b>
<b>N Calculation of NRBC dumping factors</b>	<b>177</b>

# List of Figures

1.1	The timescale of the physical phenomena associated with the interaction of a femtosecond laser pulse with transparent materials.	8
1.2	Overview of the regimes of laser interactions with metals: (a) melting, (b) microstructure, (c) spallation and (d) phase explosion.	11
1.3	Local twinned zones in Ni target. The FCC atoms are colored in blue, green atoms corresponds to HCP crystals and red atoms belong to the liquid phase. . . . .	12
1.4	Atomic configurations generated by the solidification process. The atoms surrounding individual vacancies, divacancies, and larger vacancy clusters are colored by blue, green, and red, respectively.	12
1.5	A typical surface structuration with dislocations and vacancy presence below the frozen protrusion is exposed. Atoms are colored by their potential energy. . . . .	13
1.6	Schematic representation of the volume evolution with respect to temperature during the elaboration of MG. Different temperatures are shown : $T_g$ , $T_m$ and the supercooling region where $T_g < T < T_m$ .	15
1.7	Schematic representation of a) hypothetical glassy alloy compound and b) crystalline form of the same compound. . . . .	16
1.8	The equilibrium Cu-Zr phase diagram showing three intermetallic phases relevant to the current study are indicated. The shading of the composition axis indicates the approximate range over which the Cu-Zr system exhibits a strong glass-forming tendency. . . . .	19
1.9	Diagram summarizing the classification of defects based on dimensionality and types in crystalline solids. . . . .	20
1.10	Representation of possible crystal defect types in solids a) 0-D and b) 2-D kind. . . . .	21
1.11	Schematic showing the effect of temperature on nucleation and crystal growth rates. . . . .	23

1.12	Illustrations of different pathways for crystal nucleation and growth. (a) Classical one-step pathway. (b) A parallel process of aggregate formation and crystal nucleation. (c) A multi-step process with a precursor (MIP) for nucleation. . . . .	27
2.1	Typical methods in computational materials science in terms of size and time. . . . .	30
2.2	Two dimension representation of potential $r_{cut}$ and $r_{list}$ radius under periodic boundary conditions. . . . .	38
2.3	A typical evaluation of the radial distribution function RDF functions of the different possible phases of crystalline, amorphous, and liquid. . . . .	49
2.4	(a) The output data triangulated the surface mesh of a nanoparticle. (b) Final surface after the smoothing process. . . . .	51
2.5	A typical workflow of Wigner-Seitz defect analysis to identify point defects (vacancies and interstitials) in the structures. . . . .	51
3.1	<i>in silico</i> potential energy per atom versus temperature in B <sub>2</sub> -Cu <sub>50</sub> Zr <sub>50</sub> crystal alloys to determine the melting temperature $T_m$ during the heating and cooling process. . . . .	58
3.2	<i>in silico</i> potential energy per atom versus temperature in C11 <sub>b</sub> -Cu <sub>33.3</sub> Zr <sub>66.7</sub> crystal alloys to determine the melting temperature $T_m$ during the heating and cooling process. . . . .	58
3.3	<i>in silico</i> CuZr crystal alloys and their equivalent liquid counterparts were obtained after submitting the initial crystalline simulation boxes to the protocol mentioned in Figure 3.6. (a,c) and (b,d) are the crystalline and liquid states of the B <sub>2</sub> -Cu <sub>50</sub> Zr <sub>50</sub> and C11 <sub>b</sub> -Cu <sub>33.3</sub> Zr <sub>66.7</sub> structures respectively. Atom colors refer to the local crystalline structure as computed using the PTM algorithm without chemical differentiation of the atoms. . . . .	59
3.4	The partial RDFs display the triplet distributions involving Cu–Cu, Cu–Zr, and Zr–Zr pair atoms of B <sub>2</sub> -Cu <sub>50</sub> Zr <sub>50</sub> liquid structure at 2000 K. . . . .	60
3.5	The partial RDFs display the triplet distributions involving Cu–Cu, Cu–Zr, and Zr–Zr pair atoms of C11 <sub>b</sub> -Cu <sub>33.3</sub> Zr <sub>66.7</sub> liquid structure at 2000 K. . . . .	61
3.6	Amorphization path that is used to build metallic glasses initial samples $\alpha$ -Cu <sub>50</sub> Zr <sub>50</sub> and $\alpha$ -Cu <sub>33.3</sub> Zr <sub>66.7</sub> . The fabrication protocol is set by mimicking the experimental procedure. . . . .	62

3.7	OVITO snapshots of amorphous and the corresponding crystal seeds in CuZr alloys systems where (a,c), (b,d) show the crystalline B <sub>2</sub> -Cu <sub>50</sub> Zr <sub>50</sub> , C11 <sub>b</sub> -Cu <sub>33.3</sub> Zr <sub>66.7</sub> and amorphous counterpart α-Cu <sub>50</sub> Zr <sub>50</sub> , α-Cu <sub>33.3</sub> Zr <sub>66.7</sub> respectively. Atom colors refer to the local crystalline structure as computed using the PTM algorithm without chemical differentiation of the atoms. . . . .	63
3.8	<i>in silico</i> normalized volume (with respect to the initial optimized volume V <sub>0</sub> ) versus temperature in α-Cu <sub>50</sub> Zr <sub>50</sub> to determine the glass transition temperature T <sub>g</sub> during the cooling process. . . . .	64
3.9	<i>in silico</i> normalized volume (with respect to the initial optimized volume V <sub>0</sub> ) versus temperature in α-Cu <sub>33.3</sub> Zr <sub>66.7</sub> to determine glass transition temperature T <sub>g</sub> during the cooling process. . . . .	64
3.10	The partial RDFs of α-Cu <sub>50</sub> Zr <sub>50</sub> amorphous structure. . . . .	66
3.11	The partial RDFs of α-Cu <sub>33.3</sub> Zr <sub>66.7</sub> amorphous structure. . . . .	66
3.12	The amorphous structure a) α-Cu <sub>50</sub> Zr <sub>50</sub> with the presence of the surface. b) The partial RDFs of α-Cu <sub>50</sub> Zr <sub>50</sub> amorphous structure with the presence of the free surface. . . . .	68
3.13	The amorphous structure a) α-Cu <sub>33.3</sub> Zr <sub>66.7</sub> with the presence of the surface. b) The partial RDFs of α-Cu <sub>33.3</sub> Zr <sub>66.7</sub> amorphous structure with the presence of the free surface. . . . .	68
3.14	Simulation setup geometry used to model ultrafast laser pulse interaction in CuZr alloys using TTM-MD simulations. Atoms are located inside the rectangular box and the overlying red grid represents the electronic cell domain for the finite difference (FD) solution of Equation (2.43). There is no energy transfer with the vacant space beyond the top surface. Additionally, the rear region of the sample represents the NRBC region. . . . .	70
3.15	Temporal evolution of both electronic T <sub>e</sub> and lattice T <sub>a</sub> temperatures at the same point of the space (four grids larger below the initial defined surface) based on various grids 100, 300, 500, 702, and 1000. The system B <sub>2</sub> -Cu <sub>50</sub> Zr <sub>50</sub> is used as a benchmark to determine the appropriate meshing . A laser with a pulse duration of τ = 100 fs and an absorbed fluence of F <sub>abs</sub> = 48 mJ/cm <sup>2</sup> was used. . . . .	71

3.16	Snapshots of the atomic configurations evolution in a) at several times: 0 ps, 20 ps, 60 ps, 80 ps, 100 ps, 120 ps, 160 ps, and 200 ps in B <sub>2</sub> -Cu <sub>50</sub> Zr <sub>50</sub> target during ultrafast laser irradiation of $\tau = 100$ fs pulse duration and $F_{\text{abs}} = 160$ mJ/cm <sup>2</sup> absorbed fluence. The atoms are colored according to their local atomic structure of the binary alloy by using the PTM. The double dashed arrow in the upper part of the target shows the liquefied surface. b) Deformation gradient in the transformed zone following the $x$ -direction at different times. c) Zoom on the dashed region where the PTM algorithm is applied to each sub-lattice monoatomic lattice showing twinned martensite transformation. d) Enlarged view of the chemical species of the new twinned-B19 phase emergence after the irradiation. . . . .	74
3.17	Atomic disposition within B <sub>2</sub> -Cu <sub>50</sub> Zr <sub>50</sub> crystalline structure. a) A twinned B19 structure formation and. b) A hypothetical B19 AuCd alloy structure. . . . .	75
3.18	Zoom in a portion of a B <sub>2</sub> -Cu <sub>50</sub> Zr <sub>50</sub> twinned crystalline structure (all atoms are colored in blue). a) Shows the twinning planes and the coherent boundaries. b) A hypothetical twinning transformation in alloys for comparison purposes. . . . .	75
3.19	Spatiotemporal evolution of thermodynamic quantities in the B <sub>2</sub> -Cu <sub>50</sub> Zr <sub>50</sub> transformed region located in the subsurface (zoom region) area target: a) pressure, and b) lattice temperature. The initial surface position is given by $x_{\text{surface}} = 556.68$ nm following the $x$ -direction. . . . .	76
3.20	Snapshots of atomic configurations evolution in a) at several times: 0 ps, 20 ps, 60 ps, 80 ps, 100 ps, 120 ps, 160 ps, and 200 ps in the C11 <sub>b</sub> -Cu <sub>33.3</sub> Zr <sub>66.7</sub> sample target during ultrafast laser irradiation of $\tau = 100$ fs pulse duration and $F_{\text{abs}} = 160$ mJ/cm <sup>2</sup> of absorbed fluence, the double dashed arrow in the upper part of target shows the liquefied surface. The atoms are colored according to their local atomic structure using PTM algorithm. b) Enlarged view of interstitial and substitutional defects formation in subsurface within C11 <sub>b</sub> -Cu <sub>33.3</sub> Zr <sub>66.7</sub> target after the irradiation at different times. c) Temporal defects ratio evolution in Cu <sub>33.3</sub> Zr <sub>66.7</sub> (C11 <sub>b</sub> ) target sorted according to the displacement vector $\delta y > 1$ Å. Atoms satisfying this condition are expected to be in defective positions. This is achieved using displacement vectors analysis. . . . .	77

3.21	Spatiotemporal evolution of thermodynamic quantities in the sub-surface transformed region (zoom region): a) pressure, and b) lattice temperature evolution in C11 <sub>b</sub> -Cu <sub>33.3</sub> Zr <sub>66.7</sub> sample target. The initial surface position is given by $x_{\text{surface}} = 547.30$ nm following the $x$ axis direction. . . . .	79
3.22	Snapshots of the structural evolution in the amorphous structures: a) $\alpha$ -Cu <sub>50</sub> Zr <sub>50</sub> , and b) $\alpha$ -Cu <sub>33.3</sub> Zr <sub>66.7</sub> using TTM-MD method at various time steps: 0 ps, 100 ps, 300 ps, 400 ps, 700 ps, and 1 ns. The atoms are colored according to their local atomic structure using the PTM algorithm, and two atomic contrasts are shown. The zone delimited by a double dashed arrow in the upper part of the targets corresponds to the liquid phase and the inner part is the amorphous phase. The irradiation conditions are $\tau = 100$ fs pulse duration and $F_{\text{abs}} = 160$ mJ/cm <sup>2</sup> of absorbed fluence. . . . .	80
3.23	Spatiotemporal evolution of thermodynamic quantities in the surface region: a) pressure, and b) lattice temperature evolution in $\alpha$ -Cu <sub>50</sub> Zr <sub>50</sub> sample target. The initial surface position is given by $x_{\text{surface}} = 0$ nm following the $x$ axis direction. . . . .	81
3.24	Spatiotemporal evolution of thermodynamic quantities in the surface region: a) pressure, and b) lattice temperature evolution in $\alpha$ -Cu <sub>33.3</sub> Zr <sub>66.7</sub> sample target. The initial surface position is given by $x_{\text{surface}} = 0$ nm following the $x$ axis direction. . . . .	82
4.1	STEM (Scanning Transmission Electron Microscopy) pictures in BF (Bright Field), HAADF (High Angle Annular Dark Field) STEM mode of a nanowell zone irradiated with 50 bursts, a HR-STEM image on a location surrounded in blue with the 2D-FT as inset reveals a crystalline structure under an fluence of 60 mJ/cm <sup>2</sup> with 50 pulses. . . . .	88
4.2	Simulation setup geometry used to model nanowell insertion and void formation by ultrafast laser pulse interaction with amorphous $\alpha$ -Cu <sub>35</sub> Zr <sub>65</sub> using TTM-MD simulations. . . . .	89
4.3	Outer surfaces mesh showing the evolution of nanocavities within amorphous $\alpha$ -Cu <sub>35</sub> Zr <sub>65</sub> at several key times $t = 35, 40, 45, 55, 70, 85, 110, 130,$ and $165$ ps. The target was subjected to an ultrafast laser conditions of $\tau = 60$ fs and $F_{\text{abs}} = 60$ mJ/cm <sup>2</sup> . The construct surface mesh algorithm was applied using a probing radius of $r_{\text{probe}} = 3.22$ Å as implemented in OVITO. . . . .	90

4.4	Temporal evolution of the average pressure and the total number of voids $N_{Voids}$ during the time of the void formation process within $\alpha$ -Cu <sub>35</sub> Zr <sub>65</sub> target. We notice that the maximum negative value of pressure (blue line) coincides with the maximum value of the formed voids (red line). . . . .	91
4.5	The temperature spatial maps around the void forming zone at the key times of $t = 35, 45, 110,$ and $165$ ps within the amorphous $\alpha$ -Cu <sub>35</sub> Zr <sub>65</sub> . The ultrafast laser conditions of $\tau = 60$ fs and $F_{abs} = 60$ mJ/cm <sup>2</sup> were used. . . . .	92
4.6	The pressure spatial maps around the void forming zone at key times of $t = 35, 45, 110,$ and $165$ ps within the amorphous $\alpha$ -Cu <sub>35</sub> Zr <sub>65</sub> . The ultrafast laser conditions of $\tau = 60$ fs and $F_{abs} = 60$ mJ/cm <sup>2</sup> were used. . . . .	94
4.7	The time dependence of the average velocity of the subsurface region elongation along the $x$ -axis during the cavitation process within amorphous $\alpha$ -Cu <sub>35</sub> Zr <sub>65</sub> . The ultrafast laser conditions of $\tau = 60$ fs and $F_{abs} = 60$ mJ/cm <sup>2</sup> were used. . . . .	95
4.8	The temporal evolution of the total number of voids $N_{Voids}$ (blue line) and the total volume of voids (red line) is shown. The process of void formation is characterized by four stages: void nucleation, growth/coalescence, contraction, and stable void trapping. . . . .	96
4.9	a–d) High-Angle Annular Dark-Field (HAADF) STEM images of a FIB lamella obtained from a non-irradiated area displaying the initial columnar morphology of the thin film, d) the lack of visible order is characteristic of an amorphous structure; e) SEM picture of the FIB lamella extracted zone from the non-irradiated sample. f–i) HAADF STEM images of a FIB lamella obtained from a textured area irradiated under the fluence of 60 mJ/cm <sup>2</sup> with 50 pulses, exhibiting nanowells on the sub-surface of the thin film. h) shows an open nanowell. i) shows columns of atoms characteristic of a crystalline structure surrounding this nanowell. j) SEM picture of the FIB lamella extracted zone from the irradiated sample.	97
4.10	EDS image mapping of the STEM zone under an fluence of 60 mJ/cm <sup>2</sup> with 50 pulses. . . . .	98
5.1	Representation of metallic glass devitrification investigation strategy flowchart. . . . .	101

5.2	Defects designed to trigger devitrification in $\alpha$ -Cu <sub>50</sub> Zr <sub>50</sub> structure, a-e) Represent a BCC-like crystalline sphere inclusion within amorphous structure with proportion of 46.1 and 2.3 % respectively. b-c) Show a crystalline BCC-like-amorphous interface with a BCC-like proportion of 20.5 and 82.3 % respectively. d) Represent void inclusion within the amorphous structure. . . . .	102
5.3	Representation of different Cu <sub>1-x</sub> Zr <sub>x</sub> metallic glasses samples produced after amorphization cycle. The compositions are: (a) Cu <sub>19.4</sub> Zr <sub>80.6</sub> , (b) Cu <sub>19.9</sub> Zr <sub>80.1</sub> , (c) Cu <sub>21.9</sub> Zr <sub>78.1</sub> , (d) Cu <sub>23.5</sub> Zr <sub>76.5</sub> , (e) Cu <sub>24.9</sub> Zr <sub>75.1</sub> , and (f) Cu <sub>26</sub> Zr <sub>74</sub> . The local atom's structure is colored according to the common neighbor analysis algorithm (CNA). . . . .	104
5.4	The total RDFs of the various CuZr MGs after the amorphization process. The complete amorphization of the sample is characterized by the double splitting of the second peak. . . . .	105
5.5	The total RDFs of $\alpha$ -Cu <sub>21.9</sub> Zr <sub>78.1</sub> at different times $t = 0$ ns and $t = 100$ ns. The plots demonstrate that the double splitting of the second peak is preserved confirming the amorphous character of the structure. . . . .	106
5.6	<i>in silico</i> computation of the normalized volume versus temperature in BCC-like-Cu <sub>21.9</sub> Zr <sub>78.1</sub> alloy to determine the melting temperature $T_-$ during the heating stage. . . . .	107
5.7	<i>in silico</i> computation of the normalized volume versus temperature in $\alpha$ -Cu <sub>21.9</sub> Zr <sub>78.1</sub> amorphous alloy to determine the glass transition temperature $T_g$ during the cooling stage. . . . .	108
5.8	Nucleation of BCC-like nuclei ( $\sim 15$ atomic plans) within the amorphous $\alpha$ -Cu <sub>21.9</sub> Zr <sub>78.1</sub> at $t \sim 8$ ns after the laser-energy deposition. . . . .	110
5.9	$\alpha$ -Cu <sub>21.9</sub> Zr <sub>78.1</sub> atomic configurations after ultrafast laser irradiation as a function of time. Emphasize of the devitrified region. a) global view of the devitrified region located at $35 \leq x \leq 63$ nm, b) magnification of a devitrified subdomain at $t = 16$ ns. The atoms are colored according to their local atomic structure computed using the PTM algorithm. Atoms colored in grey rely to hidden amorphous and liquid domains. . . . .	111
5.10	Mean position of the crystallization front propagation toward the surface versus time at $t = 8-16$ ns during the devitrification process in the $\alpha$ -Cu <sub>21.9</sub> Zr <sub>78.1</sub> MG sample. In blue, we can notice the formed crystalline BCC-like atoms at $t = 9, 11, 13$ and $16$ ns. . . . .	112

5.11	RDFs evolution in the $\alpha$ -Cu <sub>21.9</sub> Zr <sub>78.1</sub> sample at different times during the devitrification process. The double splitting of the secondary peak typical of the amorphous state disappears proving the emergence of a crystalline structure. . . . .	113
5.12	Evolution of the virtual XRD patterns in $\alpha$ -Cu <sub>21.9</sub> Zr <sub>78.1</sub> within the range of $20 \leq 2\theta \leq 120$ at times: 0 (amorphous) and 16 ns (crystalline) during the devitrification process via ultrafast laser irradiation. . . . .	114
5.13	Virtual XRD patterns of $\alpha$ -Cu <sub>21.9</sub> Zr <sub>78.1</sub> compared to the experimental patterns of the crystalline structures CuZr <sub>2</sub> and CuZr <sub>3</sub> . . .	115
5.14	Spatial evolution of the local pressure profile in $\alpha$ -Cu <sub>21.9</sub> Zr <sub>78.1</sub> at $t = 0-200$ ps. The laser processing conditions are $\tau = 100$ fs, $F_{\text{abs}} = 34$ mJ/cm <sup>2</sup> for the pulse duration and absorbed fluence respectively. A devitrified zone (in salmon), a non-devitrified zone (in aqua) are chosen to compare the impact of pressure on polyhedra, and NRBC region (in gray). . . . .	116
5.15	Time evolution of the polyhedra at $t = 0-16$ ns within the $\alpha$ -Cu <sub>21.9</sub> Zr <sub>78.1</sub> MG in the devitrified region located at $35 \leq x \leq 63$ nm and in a non-devitrified domain located at $65 \leq x \leq 93$ nm, a) $\langle 0, 1, 10, 4 \rangle$ , b) $\langle 0, 2, 8, 5 \rangle$ . A zoom in the time range of 0-0.2 ns is provided. . . . .	117
5.16	Spatial evolution profile of the local lattice temperature in $\alpha$ -Cu <sub>21.9</sub> Zr <sub>78.1</sub> at several key times 0.005, 0.5, 1, 5, 8, 10, 14, and 16 ns of the devitrification process. A devitrified zone (in salmon) and a non-devitrified zone (in aqua) are chosen to investigate the impact of temperature on the devitrification process. . . . .	119
5.17	Spatiotemporal evolution of thermodynamic quantities within the $\alpha$ -Cu <sub>21.9</sub> Zr <sub>78.1</sub> devitrified region: a) pressure (contour delimits the local region under contraction), and b) lattice temperature (contour delimits different temperature regimes below and above the melting temperature). . . . .	120
5.18	Spatial evolution of a) pressure, b) temperature saturated at $T_g$ , c) the spatial atomic transformed region within $\alpha$ -Cu <sub>21.9</sub> Zr <sub>78.1</sub> analyzed at $t = 16$ ns after ultrafast laser energy deposition, and d) crystallization front velocity during the devitrification. An irradiation of $\tau = 100$ fs pulse duration and $F_{\text{abs}} = 34$ mJ/cm <sup>2</sup> absorbed fluence are used. . . . .	122

5.19	Space and time evolution of the entropy variation $\Delta S = S(t = t_n) - S(t = 0)$ with respect to the initial amorphous phase (at $t = 0$ ns) during the devitrification. The ordered-crystalline region is colored in dark blue whereas the amorphous region is emphasized by light green environments. . . . .	124
5.20	Gibbs free energy calculation using the PM7 semiempirical method, a) Normalized free-energy landscape obtained for multiple configurations ( $\Delta G = G(t = t_n) - G(t = 0)$ ) of 184 atoms at $t = 0-16$ ns. b) Different atomic configurations captured during the devitrification process used to compute the Gibbs free energy at $t = 0, 1, 5, 10, 14,$ and $16$ ns. The copper and zirconium atoms are colored in red and blue respectively. . . . .	125
5.21	Phononic thermal conductivity of $\alpha$ -Zr <sub>78.1</sub> Cu <sub>21.9</sub> in the amorphous phase and in the nanocomposite at various temperatures. Note the factor 36 between the two phases at $T = 300$ K. . . . .	127
5.22	Preliminary result of the $\alpha$ -Cu <sub>50</sub> Ti <sub>50</sub> total devitrification during resolidification process via ultrafast irradiation of $\tau = 100$ fs pulse duration and $F_{\text{abs}} = 30$ mJ/cm <sup>2</sup> absorbed fluence at key times: 0 (amorphous), 1, 2, 3, and 4 ns (crystalline). . . . .	131
A.1	Numerical workflow diagram representing the steps applied in MD simulation realized using LAMMPS. . . . .	135
M.1	Crystalline initial structures from the CIF file used in first principle computation visualized by XCrySDen. Left: B <sub>2</sub> -Cu <sub>50</sub> Zr <sub>50</sub> , and C11 <sub>b</sub> -Cu <sub>33.3</sub> Zr <sub>66.7</sub> . The gray, brown atoms correspond to Zr and Cu respectively. . . . .	172
M.2	DFT calculation of the electronic specific heat as a function of electronic temperature for the two crystalline phases of CuZr alloy. . . . .	173
N.1	Spatial-temporal pressure color maps profile in amorphous B <sub>2</sub> -Cu <sub>50</sub> Zr <sub>50</sub> sample at instants $t = 0-150$ ps for several $\gamma_{\text{damp}}$ . In a) $\gamma_{\text{damp}} = 2.5 \cdot 10^{-1}$ eV ps $\text{\AA}^{-2}$ , b) $\gamma_{\text{damp}} = 2.5 \cdot 10^{-2}$ eV ps $\text{\AA}^{-2}$ , c) $\gamma_{\text{damp}} = 2.5 \cdot 10^{-3}$ eV ps $\text{\AA}^{-2}$ , and d) $\gamma_{\text{damp}} = 2.5 \cdot 10^{-4}$ eV ps $\text{\AA}^{-2}$ . An ultrafast laser pulse of $\tau = 100$ fs pulse duration and $F_{\text{abs}} = 160$ mJ/cm <sup>2</sup> absorbed fluence is used in these simulations. . . . .	179

- N.2 Spatial-temporal pressure color maps profile in amorphous  $\text{Cu}_{50}\text{Zr}_{50}$  sample at instants  $t = 0-150$  ps for several  $\gamma_{damp}$ . In a)  $\gamma_{damp} = 2.5 \cdot 10^{-1}$  eV ps  $\text{\AA}^{-2}$ , b)  $\gamma_{damp} = 2.5 \cdot 10^{-2}$  eV ps  $\text{\AA}^{-2}$ , c)  $\gamma_{damp} = 2.5 \cdot 10^{-3}$  eV ps  $\text{\AA}^{-2}$ , and d)  $\gamma_{damp} = 2.5 \cdot 10^{-4}$  eV ps  $\text{\AA}^{-2}$ . An ultrafast laser pulse of  $\tau = 100$  fs pulse duration and  $F_{abs} = 160$  mJ/cm<sup>2</sup> absorbed fluence is used in these simulations. . . . . 180
- N.3 Spatial-temporal pressure color maps profile in amorphous  $\alpha\text{-Cu}_{50}\text{Zr}_{50}$  sample at instants  $t = 0-150$  ps for several  $\gamma_{damp}$ . In a)  $\gamma_{damp} = 2.5 \cdot 10^{-1}$  eV ps  $\text{\AA}^{-2}$ , b)  $\gamma_{damp} = 2.5 \cdot 10^{-2}$  eV ps  $\text{\AA}^{-2}$ , c)  $\gamma_{damp} = 2.5 \cdot 10^{-3}$  eV ps  $\text{\AA}^{-2}$ , and d)  $\gamma_{damp} = 2.5 \cdot 10^{-4}$  eV ps  $\text{\AA}^{-2}$ . An ultrafast laser pulse of  $\tau = 100$  fs pulse duration and  $F_{abs} = 160$  mJ/cm<sup>2</sup> absorbed fluence is used in these simulations. . . . . 181
- N.4 Spatial-temporal pressure color maps profile in amorphous  $\alpha\text{-Cu}_{33.3}\text{Zr}_{66.7}$  sample at instants  $t = 0-150$  ps for several  $\gamma_{damp}$ . In a)  $\gamma_{damp} = 2.5 \cdot 10^{-1}$  eV ps  $\text{\AA}^{-2}$ , b)  $\gamma_{damp} = 2.5 \cdot 10^{-2}$  eV ps  $\text{\AA}^{-2}$ , c)  $\gamma_{damp} = 2.5 \cdot 10^{-3}$  eV ps  $\text{\AA}^{-2}$ , and d)  $\gamma_{damp} = 2.5 \cdot 10^{-4}$  eV ps  $\text{\AA}^{-2}$ . An ultrafast laser pulse of  $\tau = 100$  fs pulse duration and  $F_{abs} = 160$  mJ/cm<sup>2</sup> absorbed fluence is used in these simulations. . . . . 182

# List of Tables

2.1	Various computational methods and their scaling with the maximum number of atoms. . . . .	35
2.2	The different statistical ensembles implemented, used in MD simulation and the main physical property computed by LAMMPS. . . . .	40
2.3	Summary of all physical input properties units used to model an ultrafast laser irradiation of materials interaction. . . . .	47
3.1	The computed theoretical MD temperature compared to the experimental values of $B_2$ -Cu <sub>50</sub> Zr <sub>50</sub> structures. . . . .	65
3.2	The computed theoretical MD temperature compared to the experimental values of C11 <sub>b</sub> -Cu <sub>33.3</sub> Zr <sub>66.7</sub> structures. . . . .	65
3.3	Summary of all the average nearest neighbor distances in $\alpha$ -Cu <sub>50</sub> Zr <sub>50</sub> compared to different simulation and experimental methods. . . . .	67
3.4	Summary of all the average nearest neighbor distances in $\alpha$ -Cu <sub>33.3</sub> Zr <sub>66.7</sub> compared to different simulation and experimental methods. . . . .	67
3.5	Physical properties of crystalline and amorphous CuZr binary systems, namely specific heat constant $\gamma$ and electron–phonon factor $g_p$ , electronic thermal conductivity $\kappa_e$ , and electronic thermal diffusion $D_e$ at 300 K. . . . .	72
M.1	TTM-MD electronic specific heat fitting coefficients values obtained using DFT for crystalline CuZr binary systems. . . . .	173

# Nomenclature

## List of Abbreviations

$\mu$ VE Grand canonical ensemble

$E_i$  Internal energy

eV Electron volt

$n_{stability}$  Stability criterion

nm nanometers

BCC Body centered cubic

BMGs Bulk metallic glasses

CGM Conjugate gradient method

CIF Crystallographic information file

CNA Common neighbor analysis

CNT Classical nucleation theory

CPU Central processing unit

CSP Centrosymmetry parameter

DD Discrete dislocation dynamics simulations

DFT Density functional theory

DOS Density of states

EAM Embedded atom method

EDS Energy dispersive spectroscopy

EXAFS Extended X-Ray Absorption Fine Structure

FCC Face centered cubic  
FDTD Finite difference time domain  
FEM Finite difference method  
fs femtosecond  
GFA Glass forming ability  
GGA Generalized gradient approximation  
GPa Gigapascal  
HAZ Heat affected zone  
HCP Hexagonal close packed  
HD Hydrodynamic model  
ICO Icosahedral structure  
LAMMPS Large scale Atomic Molecular Massively Parallel Simulator  
laser Light amplification by the stimulated emission of radiation  
LIPSS Laser-induced periodic surface structures  
maser Microwave amplification by stimulated emission of radiation  
MC Monte carlo  
MD Molecular Dynamics  
MEAM Modified embedded atom method  
MG Metallic glass  
MPI Message passing interface  
MS Molecular statics  
NPT Isothermal isobaric ensemble  
ns nanosecond  
NVE Micro canonical ensemble  
NVT Canonical ensemble

P-T Pressure and temperature profiles  
PBC Periodic boundary condition  
PE Potential energy  
PRDF Partial radial distribution function  
ps picosecond  
PTM Polyhedral template matching  
RDF Radial distribution function  
ReaxFF Reactive force field interatomic potential  
STZ Shear transformation zone  
TD-DFT Time-dependent density functional theory  
TTM Two temperature model  
WSDA Wigner-Seitz defect analysis  
XRD X-ray diffraction

### **Greek Symbols**

$\alpha^2 F(\omega)$  Eliashberg function  
 $\gamma_p$  Coupling constant due to electron–phonon  
 $\gamma_s$  Coupling constant due to electron–stopping  
 $\gamma_{damp}$  Dumping factor  
 $\kappa_a$  Atomic thermal conductivity  
 $\kappa_e$  Electronic thermal conductivity  
 $\lambda$  Electron mean free path  
 $\mu$  Chemical potential  
 $\mu\text{m}$  Micrometer  
 $\nu$  Vibrational frequency  
 $\omega$  Phonon frequency

$\rho_e$	Density of electrons
$\sigma$	Electrical conductivity
$\sigma_{C-G}$	Crystal-Glass interface free energy
$\sigma_{xx}$	Per atom constraint tensor following x direction
$\sigma_{yy}$	Per atom constraint tensor following y direction
$\sigma_{zz}$	Per atom constraint tensor following z direction
$\tau_e$	relaxation time
$\theta$	X-ray diffraction scanning angle
$\xi$	Crystal growth
$\zeta$	Nucleation rate

### Latin Symbols

$\tilde{F}(t)$	Stochastic force
$\tilde{n}$	Complex optical index
$a$	Lattice parameter
$C_e$	Electronic specific heat
$D_e$	Electronic thermal diffusion
$dt$	Integration timestep
$E_F$	Fermi energy
$F$	Laser fluence
$f$	Fermi-Dirac distribution function
$F_i$	Force acting on particle i
$G$	Gibbs free energy
$g(r)$	Radial distribution function
$g_p$	Electron-phonon coupling
$J$	Total heat flux

$J_x$	Heat flux following x axis
$J_y$	Heat flux following y axis
$J_z$	Heat flux following z axis
$K$	Kelvin
$l_p$	Laser penetration depth
$L_x$	Length of the simulation box in x direction
$L_y$	Length of the simulation box in y direction
$L_z$	Length of the simulation box in z direction
$L_{NRBC}$	Length of the simulation dumping zone
$m_e$	Mass of electron
$m_i$	Mass of atom i
$M_{Cu}$	Atomic weight of copper
$M_{Zr}$	Atomic weight of zirconium
$N$	Total number of atoms
$n$	Ions density
$N_{Voids}$	Number of voids
$P$	Pressure
$P_e$	Electronic pressure
$r_i$	Position of atom i
$r_{cut}$	Potential cutoff distance
$r_{list}$	Neighbor list distance
$r_{probe}$	Probing radius
$r_{skin}$	skin depth distance
$S$	Entropy
$T$	Temperature

$t$	Time
$T_a$	Ionic temperature
$T_c$	Critical temperature
$T_e$	Electronic temperature
$T_g$	Glass transition temperature
$T_m$	Melting temperature
$T_x$	Crystallization transition temperature
$V$	Volume
$v$	Velocity
$V_0$	Volume at minimal potential energy
$v_f$	Fermi velocity
a	Acceleration
atm	Atmospheres pressure units
g	Grams
m	Meter
Q	Cooling rate
Q'	Heating rate
s	Second
W	Watts

### **Physics Constants**

$e$	Charge of electron
$k_B$	Boltzmann constant
$L_0$	Lorenz number
$\bar{h}$	Reduced Planck constant

### **Other Symbols**

Å	Angstrom
mol	Moles

# Abstract

Ultrafast laser processing is a modern method to architecture material at the nanoscale. A phase transformation can be triggered locally at nanometer scale. In this dissertation, we tackled different problems to understand the complex mechanisms of the ultrafast laser-inducing transformations within the CuZr alloys. A qualitative approach is used in which Molecular Dynamics and Two Temperature Models are combined. In this scope, a reliable Embedded Atom Method potential that is capable of describing both the ordered and disordered phases is employed. The present investigations focus on the structural evolution in crystalline CuZr alloys ( $B_2$ -Cu<sub>50</sub>Zr<sub>50</sub> and C11<sub>b</sub>- $\alpha$ -Cu<sub>33.3</sub>Zr<sub>66.7</sub>) and their amorphous counterparts ( $\alpha$ -Cu<sub>50</sub>Zr<sub>50</sub>,  $\alpha$ -Cu<sub>33.3</sub>Zr<sub>66.7</sub>). Depending on the laser delivered fluence and pulse duration, the main phenomenon encountered are twins formation, point defects generation, cavitation via solid-liquid phase transition through the ablation process, and devitrification. Additionally, the analysis clearly shows that many factors can affect the final specimen (e.g., initial phase structure, chemical stoichiometry, etc.). Actually, the first set of simulations showed that ultrafast laser interaction with the  $B_2$ -Cu<sub>50</sub>Zr<sub>50</sub> ordered structure led to the formation of a nano-twinned martensitic phase B19'. However, in the case of the C11<sub>b</sub>-Cu<sub>33.3</sub>Zr<sub>66.7</sub> point defects (vacancy, interstitial and substitutional) were detected. It was found that tensile stress is responsible for these transformations. Other theoretical investigations are in agreement with experimental work was performed to predict the cavitation formation on the amorphous  $\alpha$ -Cu<sub>33.3</sub>Zr<sub>66.7</sub> sample. The last result deals with the devitrification of the amorphous structure via an ultrafast laser. Concretely, several amorphous samples have been generated by a fast quenching of the liquids at  $10^{12}$  K.s<sup>-1</sup>. The composition played a crucial role in the construction and devitrification of metallic glasses. The  $\alpha$ -Cu<sub>21.9</sub>Zr<sub>78.1</sub> was selected as a candidate for investigation. We have identified that devitrification occurs roughly at  $\sim 9$  ns after the laser energy deposition. During the thermal relaxation process, we report a relative propagation of the crystallization front. This devitrification is partial, located on the subsurface, and favored by a combination of two elementary processes, breaking the icosahedral network and the deep supercooling condition. Indeed, the free energy

landscape confirms that the final amorphous-liquid-crystalline transition is characterized by an energy minimum.

**Keywords:** molecular dynamics, LAMMPS, TTM-MD, ultrafast laser, bulk metallic glass, amorphous structure, devitrification, twinning, defects, CuZr alloys, nanovoids, nanotwin, vacancy, cavitation, phase transformation, crystallization, nanocomposite.

# Résumé

Le traitement laser ultrarapide est une méthode moderne pour produire les matériaux nano-architecturés par une transformation de phase qui peut être déclenchée localement à l'échelle du nanomètre. Dans cette thèse, nous avons abordé différents problèmes pour comprendre les mécanismes complexes induits par un laser ultrarapide au sein des alliages CuZr. Une approche qualitative est utilisée dans laquelle la dynamique moléculaire et le modèle à deux températures sont combinés. Dans ce cadre, un potentiel de type EAM, capable de décrire à la fois les phases ordonnées et désordonnées est utilisé. Les recherches actuelles portent sur l'évolution structurale des alliages cristallins CuZr ( $B_2$ -Cu<sub>50</sub>Zr<sub>50</sub> et C11<sub>b</sub>- $\alpha$ -Cu<sub>33.3</sub>Zr<sub>66.7</sub>) et leurs homologues amorphes ( $\alpha$ -Cu<sub>50</sub>Zr<sub>50</sub>,  $\alpha$ -Cu<sub>33.3</sub>Zr<sub>66.7</sub>). En fonction de la fluence délivrée par le laser et de la durée de l'impulsion, le phénomène prédominant rencontré est la formation de maillage, la génération de défauts, la cavitation via le changement de phase solide-liquide à travers le processus d'ablation et la dévitrification. De plus, l'analyse montre clairement que de nombreux facteurs peuvent affecter l'échantillon final (par exemple, la structure de la phase initiale, la stoechiométrie chimique). En fait, la première campagne de simulations a montré que l'interaction laser ultra-rapide avec la structure ordonnée  $B_2$ -Cu<sub>50</sub>Zr<sub>50</sub> conduisait à la formation d'une phase martensitique nano-maillée B19'. Cependant, dans le cas du C11<sub>b</sub>-Cu<sub>33.3</sub>Zr<sub>66.7</sub>, des défauts ponctuels (vacances, interstitielles et substitutionnels) ont été détectés. Il a été constaté que la contrainte de traction est responsable de ces transformations. Une autre étude théorique en accord avec les travaux expérimentaux a été réalisée pour prédire la formation de cavités dans l'échantillon amorphe  $\alpha$ -Cu<sub>33.3</sub>Zr<sub>66.7</sub>. Le dernier résultat porte sur la dévitrification de la structure amorphe via un laser ultrarapide. Concrètement, plusieurs échantillons amorphes ont été générés par une trempe rapide des liquides à  $10^{12}$  K.s<sup>-1</sup>. La composition a joué un rôle crucial dans la construction et la dévitrification des verres métalliques. Le  $\alpha$ -Cu<sub>21.9</sub>Zr<sub>78.1</sub> a été sélectionné comme candidat pour mener les investigations. Nous avons identifié que la dévitrification se produit approximativement à  $\sim 9$  ns après le dépôt d'énergie laser. Au cours du processus de relaxation thermique, nous rapportons aussi une propagation relative du front de cristallisation. Cette

dévitrication est partielle, localisée en subsurface, et favorisée par la combinaison de deux processus élémentaires, la rupture du réseau icosaédrique et la condition de surfusion profonde. En effet, le paysage de l'énergie libre confirme que la transition finale amorphe-liquide-cristallin est caractérisée par une énergie minimale.

**Mots clés** : dynamique moléculaire, LAMMPS, TTM-MD, laser ultrarapide, verre métallique massif, structure amorphe, dévitrification, macles, défauts, alliages de CuZr, nanocavités, nanotwin, lacune, cavitation, transformation de phase, cristallisation, nanocomposite .

# Thesis scope and objectives

A heightened set of technological challenges has put enormous pressure on physicists to look for materials with excellent mechanical, chemical, and physical properties. These enhancements touch several aspects of the material, including strength and stiffness ideal for a harsh environment. Basically, it all came together in two ways: either through the synthesis of completely novel materials with distinct structures and performance, or by improving the existing ones through alloying, defects, or microstructural modifications. In fact, different processes are employed to do so. We can mention thermal treatment (quenching, annealing, and melting), electrodeposition of alloys, application of high pressures, or thermomechanical processing methods just to name a few. The most significant aim to develop interesting applications at different levels (nanometer, micrometer, and gross level) include superconductors [1], quasicrystals [2, 3], nanocrystalline materials [4, 5, 6, 7, 8], and metallic glasses [9, 10, 11]. Nanoarchitected materials are clearly attractive because of the specific properties that they inherit compared to their parent material. The realization of such material demands the triggering of a process far from equilibrium [12]. Among these we may mention the rapid solidification processing [13, 14, 15], mechanical alloying [16, 17, 18, 18], plasma processing [19], vapor deposition [20], irradiation, and spray deposition [21]. Such materials also are referred to as driven materials in [22]. The energization may happen as a solid-solid transformation or involve a change of state from solid to liquid, solid to gas, and crystal to amorphous. Amorphous structures are described as metastable phases. The properties of materials can be significantly changed by altering the crystalline structure through polymorphic changes or microstructural modification by introducing defects such as dislocations, impurities, vacancies, and grain boundaries. Furthermore, many other suggestions as a method to embed a nanovitreous (nanoglasses) structure in a crystalline material [8] or proceed to trap nanocrystals inside a glassy material matrix.

Due to their unique properties, new nanoarchitected materials have attracted attention. To this end, a strategy of using ultrafast laser as a manu-

facturing method emerged for developing future Bulk Metallic Glasses (BMGs) and their crystalline counterparts. In this way, it is possible to form materials in complex shapes and structures, but with improved properties due to the presence of dislocations, voids, or point defects. Therefore, since the glassy structure is random in nature, the presence of a local crystalline structure within the amorphous structure could contribute to improving properties. At this scale, MD appears to be a suitable subject for investigation. The main objective of this thesis is to investigate phase transitions in crystalline and amorphous compounds. In order to establish the thermodynamic response of these materials. An exhaustive review of the phase transition phenomena triggered by a femtosecond laser is presented to illustrate the originality of this work. To realize all these purposes, the Cu-Zr system has been selected as the most promising material family of interest candidate since it is used for numerous high-tech applications. These investigations rely on the fundamental understanding of these potentially enhanced properties. Thus, this Ph.D. dissertation is organized as follows:

- In chapter 1, we examine several aspects of metallic glasses, including their development, potential applications by trapping crystals within bulk metallic glasses, their distinctive properties, and to a lesser extent their disadvantages that are unfavorable to large-scale applications. In this context, a great deal of effort was put forth to overcome the different drawbacks related to their properties. However, to our knowledge few studies have explored the potential of subjecting amorphous structures to ultrafast laser irradiation. Details were provided to carefully design the chemical composition of the relevant amorphous alloys, phase stabilization parameters, and possible functionalization by ultrafast laser irradiation treatment. In this advanced process, surface properties can be altered depending on irradiation conditions, the subsurface state can be modulated, the wetting properties can be improved, or thin layers can be selectively nanocrystallized to form amorphous-crystalline nanocomposites. Design of metallic glass composites is the latest trend in metallic glass, showing breakthrough performance in terms of transportation properties.
- In chapter 2, to gain insights into these fascinating phenomena related to the laser-matter interaction, molecular dynamics simulation seems appropriate since it allows tracking the movement of atoms and faithfully reproducing their behavior after laser irradiation of the material. Additionally, this approach is able to provide a quantitative description of the temperature and pressure that are correlated to the thermal and mechanical process. In this

chapter a succinct and sufficient explanation of molecular dynamics is provided. Basically, this was achieved by explaining that molecular dynamics is based on integrating Newton's equations using Verlet algorithms. In order to accurately reproduce a laser event, the two-temperature model which describes the time evolution of the lattice and electron temperatures by two coupled non-linear differential equations is unified with the previous atomistic scheme. An overview on LAMMPS software was provided, including the script organization and all the mandatory ingredients to safely manage the investigations such as the choice of the interatomic potential, building the initial structure using specific tools, boundary conditions of the simulation box, the integration time step, the available thermodynamic ensemble, the initial laser properties, units, and the material electronics properties. We have to point out that performing atomistic simulation itself is not enough, thus, we exposed in the second part of this chapter the post-processing tools used throughout this dissertation especially OVITO software. The last goal is to identify the phase change, quantify the defects, characterize the amorphous structures, and visualize the cavitation. All algorithms permitting to achieve these operations were identified and discussed.

- In chapter 3, we expose different steps besides laser-matter interaction considerations. The first step is identifying the suitable interatomic potential for constructing CuZr metallic glasses from their crystalline counterparts and selecting the compositions that will be the most stable. Then, perform structural analysis to check whether the obtained structures are in the amorphous state. The second stage was to develop a simulation setup for laser-matter modeling, design a non-reflective boundary condition, and compute (ab initio) or collect (experimental data), depending on the electronic properties appropriate for each Cu-Zr alloy system. Accordingly, the results show that ultrafast pulse interactions with crystalline Cu-Zr systems in two distinct structures  $B_2$  and  $C11_b$  lead to structural changes (martensitic transition) and defect generation as a result of stress effects. Nevertheless, the simulation campaign conducted on the glassy counterpart indicates that no phase transitions occurred in the MG.
- In chapter 4, we present theoretical studies using atomistic methods in order to support and understand the results of the various experimental measurements. We were able to predict the nanovoids (cavitation) ascribed to the local effects of ultra-short laser irradiation and understand the thermodynamic process by exposing the pressure and temperature profiles. In such a case, ultrafast laser fluence and pulse duration are key factors for designing

the processing conditions. It should be emphasized that for this simulation another simulation scheme has been developed for the insertion of nanowells.

- In chapter 5, we expose various factors (composition, fluence, pulse duration, simulation time, etc.) that lead to a successful and original way to trigger an MG-crystal phase transition with an ultrafast laser. It deals with a local structural transformation from glassy to a crystalline structure by utilizing femtosecond laser local energy focus effects. This creates a permanent devitrification in CuZr glass that persists within the amorphous material. Qualitative characterization of the structural transformation has been performed. As a first step, determine the crystallographic group and the size of the formed crystal, then correlate these thermodynamic conditions (mainly pressure and temperature) to learn how devitrification crystals are formed. Furthermore, since the energetic aspect is an important key giving an extra grid of comprehension to this phenomenon, a series of free energy computations were successfully conducted. The last focus presents and discusses the results obtained by elaborating and invoking the classical crystallization theory model applied to this specific CuZr MG system devitrification. In the last section of this chapter, a concrete application is presented where the thermal conductivity of the devitrified amorphous system is much higher than its original amorphous structure.

# Chapter 1

## Overview of metallic glasses and ultrafast lasers processes

### 1.1 Introduction

Besides the normal crystalline structure, some alloys have the ability to be in a glassy state [23]. The development of this new category of metastable materials as an intermediate phase between liquid and solid is known as amorphous structures. They have been subjected to intense activity in the material science field with a thousand research papers published to understand their fundamental properties for industrial purposes. The first bulk metallic glass was elaborated by P. Duwez in 1960 at the California Institute of Technology [24]. His experience consisted of a rapid quenching (in a range of  $10^{4-6}$  K.s<sup>-1</sup>) of a molten Au<sub>80</sub>Si<sub>20</sub> binary alloy. The resulting specimen showed no crystalline fingerprint in the x-ray diffraction pattern [25]. Traditionally, in metallurgy three main techniques exist to reach this high solidification rate. The first is the droplet method, where the molten system is divided into small droplets and allowed to solidify by contact with a cold stream of air. The second is known as the Jet method. Here the flowing molten stream solidifies in contact with a chill surface. The third method involves laser surface treatments. The solidification is achieved through rapid heat extraction from the unmelted block. The next challenge that physicists accomplished in the early 80's was the production of a thin Metallic Glass (MG) sample with a slower quenching rate. A bunch of Metallic Glasses (MGs) developed having such characteristics as La<sub>55</sub>Al<sub>25</sub>Ni<sub>20</sub> [26], ZrTiAl [27], LaNiAl [28], ZrNiAlCu [29], ZrTiCuNiBe [30], and PdCuNiP alloy [31]. MGs can be classified as metal-metal and metal-metalloid glasses. In the metal-metal type MGs, only the metal atoms are involved such as Cu<sub>50</sub>Zr<sub>50</sub>, Ni<sub>50</sub>Ti<sub>50</sub> or Fe<sub>90</sub>Zr<sub>10</sub>. Whereas the metal-metalloid type contains roughly no more than 20 % of metalloid atoms such as Pd<sub>77</sub>Cu<sub>6</sub>Si<sub>17</sub>, Fe<sub>40</sub>Ni<sub>40</sub>P<sub>14</sub>B<sub>6</sub>, or Fe<sub>40</sub>Ni<sub>40</sub>B<sub>20</sub>. Incredibly, these

new kinds of components have a hardness twice larger than their crystalline counterparts, as well as high corrosion resistance. They are also a perfect candidate as reinforcing materials in composites, hydraulic binders cement, and mortars. Magnetically, they exhibit exceptional properties because their hysteresis cycles have a low coercive field and high permeability. They also have applications in the construction of power transformers [32]. However, they have the disadvantage of becoming brittle at low temperatures combined with the difficulty of obtaining them in bulk form [33].

## 1.2 Ultrafast lasers processes

### 1.2.1 Applications of ultrafast lasers

Since the invention of masers by Charles Townes in 1960's [34], a big step has been taken for the development of the laser. The first theoretical brick was laid in 1966 when DeMaria *et al* demonstrated that a revolutionary light source known as a femtosecond laser could exist [35]. Actually, intense research has been carried out to solve the problem of producing an ultrafast laser. The key date of 1991 saw the work of Spence *et al* when introduced the first commercial sapphire-based femtosecond laser [36]. Compared to the conventional laser, the main advantage of the femtosecond laser is the low heat affected zone which means an efficient energy delivery [37, 38]. It may seem a trivial detail, but the scientific community has been able to take advantage of this property for the completion of various applications, especially for the micromachining fabrication of the surfaces and bulk within metals-glasses [39, 40, 38, 41] or the elaboration of a nanoarchitected glassy materials [42, 43, 44, 45, 46, 47]. In the following, various typical applications are discussed and mentioned. The nuclear industry took advantage of ultrafast lasers by putting in the application an innovative method known as inertial confinement by laser [48]. It consists of fusing two light atomic nucleus into a heavier atomic nucleus using high laser energy to trigger a nuclear fusion reaction. The services of this type of laser have been employed and applied along fundamental physics, precisely for both plasma and particle physics. The proof is a new method of accelerating particles by laser for the production of electron beams [49]. The emergence and development of the ultrafast laser made an interdependence and connections between biology and imaging where fluorescence microscopy imaging technique allows an image of living tissue to a precision of millimeters [50]. The ultrafast laser is also useful for the spectroscopic study of atmospheric. The idea is to send high-power femtosecond laser pulses that propagate in the atmosphere as dynamically self-guided filaments

that emit in a continuum from the ultraviolet to the infrared. This white light exhibits a directional behavior with enhanced backward scattering. This can be used to explore the detection identification of aerosols or even laser-induced condensation and lightning control [51]. The field of telecommunication focuses its attention to generate electromagnetic pulses in the terahertz range by photoconductive effect. When these photoconductive antennas are illuminated with femtosecond pulses an electrical pulse is produced which has broad frequency spectra [52]. Femtosecond lasers have been commonly used for the clean and precise cutting of materials. Contrary to conventional laser machining where the part to be cut is heated which limits the precision due to quick cooling. A femtosecond laser vaporizes the material. Thus, the cut is more precise without the formation of voids or debris [53]. As mentioned previously, the ultrashort pulse duration is in order of a picosecond which corresponds to the time scale of the processes involved in chemical reactions. Therefore, no camera or detector is fast enough to observe them directly. However, femtosecond lasers make it possible to observe them indirectly by dividing the pulse into a probe and pump delayed with respect to the other [54]. The development of femtosecond lasers was also beneficial for life science, especially for a modern safe novel surgical treatment. Due to its high precision, it becomes in last decades a favorite tool in ophthalmology mainly by inducing two processes to perform tissue alteration as a consequence of the absorption process and tissue cutting into the cornea or cataracts [55, 56, 57, 58, 59, 60, 61]. Furthermore, the femtosecond lasers also evolved and expanded to reach the automotive industry manufacturing to improve fuel economy in cars. Contrary to a process such as mechanical ruling of the surface texturing, marking by femtosecond-lasers is shown to efficiently diffuse the associated oil film and significantly improve oil retention due to reduction of friction [62]. Typically, femtosecond lasers had been recognized in the manufacturing industry as ideal for processing such as marking, drilling, and cutting. This surgical delivery of energy reduces the heat-affected zone (HAZ) since the material is evaporated before any resolidification process is started. These enabling characteristics can be applied to a broad range of materials by triggering phase transformation, including metals, polymers, semiconductors, dielectrics, and glasses. If we focus on femtosecond laser interaction with glassy alloys for instance. Thus, plenty of applications emerged, the most spectacular is the controlled alteration of the refractive index with an ultrashort pulse which finds utility in the fiber optics for the elaboration of optical waveguide [63, 64, 65, 66, 67, 68]. Other applications to synthesized photonic crystals inside the photo-resist material [69], micro-fluid channels elaboration [70, 71].

### 1.2.2 Ultrafast laser processing conditions

Femtosecond or ultrafast lasers are lasers emitting light pulses with durations between a few (typically 50 fs) to hundreds (typically 1 ps) of femtoseconds. Concretely, the production of these short pulses is realized with the passive mode-locking technique. In addition, these sub-picosecond light pulses can be generated with different types of lasers either industrial or scientific. The most commonly used ultrashort lasers are solid-state bulk lasers which emit ultrashort pulses with durations between 30 fs to 30 ps. There are also diode-pumped lasers mainly based on neodymium-doped or ytterbium-doped laser gain media. The researchers working on ultrafast laser-matter interactions widely employ titanium-sapphire laser systems because they can deliver pulse durations below 5 fs with substantial average powers of several watts. A reliable ultrafast fiber laser device is widely used. They imply pulse durations between 50 and 500 fs and average power of milliwatts. Another type of ultrafast laser is the Dye laser which produces pulse durations of the order of 10 fs. They are commonly used for emission at different wavelengths, particularly in the visible spectrum. A broad kind of phenomena and contrasted response occur depending on the irradiated material (metallic, semiconductor, or dielectric) as shown in Figure 1.1.

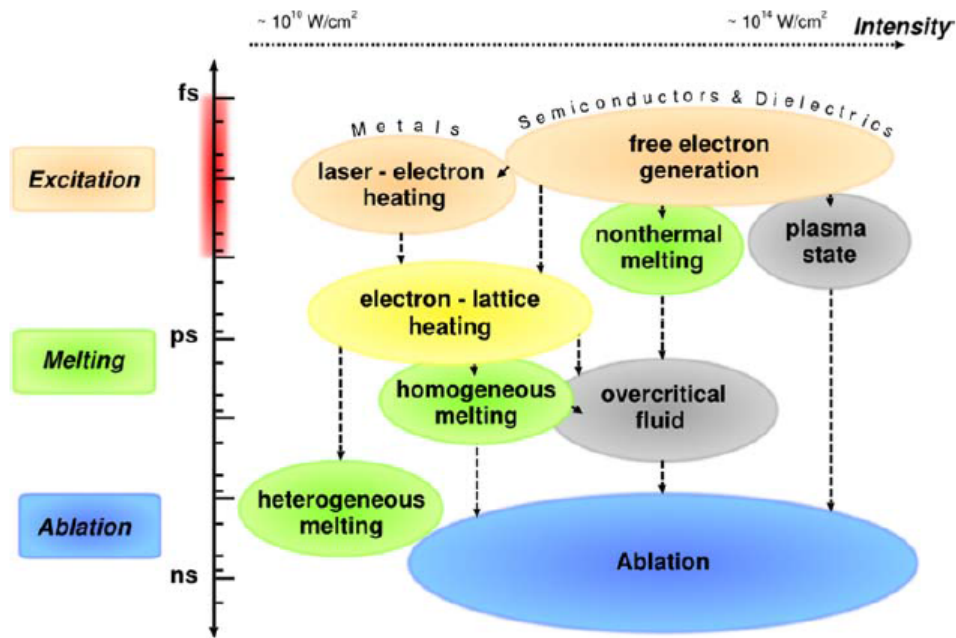


Figure 1.1: The timescale of the physical phenomena associated with the interaction of a femtosecond laser pulse with transparent materials. Adopted from [72].

A sophisticated new-generation semiconductor femtosecond type is used due to the advantage of delivering short pulse durations combined with high pulse repetition rates. It is clear that the major advantage of ultrafast lasers comes

from the fact that the pulse width is shorter than the electron-phonon relaxation time. This unique characteristic permits a narrowed and intense local energy peak deposition. Consequently, this localized feature makes it possible to tune, control and advance the structural properties of materials, allowing them to be used in nanotechnology applications.

Apart from the pulse duration usually specified as the full width at half maximum (fixed in most cases to 5 – 200 fs) which is the brand mark of ultrafast lasers, different center of the wavelengths are possible for a femtosecond laser. Mostly, the lower limit of the optical bandwidth corresponds to the inverse of pulse duration. Once the lower limit is reached the bandwidth-limited pulse appears, e.g. In some cases of 100 fs pulses around 1  $\mu\text{m}$  wavelength this limit is around 10 nm. Additional aspects include the parameter called pulse quality mainly associated with the laser temporal and spectral pulse shape handling. Moreover, in such a system, the pulse repetition rate is an additional relevant criterion. Generally, it is tenable from 10-100 of a megahertz. A burst mode can be flexibly adjusted, which is essentially excellent for applications such as laser material processing or micromachining. Here, the laser delivers energy carried by the pulse that reaches the material. Therefore, depending on the pulse energy (or fluence) equivalent to the average output power divided by the pulse repetition rate. Then, various surfaces or bulk modifications take place in the target. A last operating parameter can be added to the previous list. It is the polarization that has the ability to transform into other states during the light-matter process.

### 1.2.3 Ultrafast laser modeling and induced mechanisms

This section is a brief focus of both ultrafast lasers induced mechanisms and the suited simulation method to model them mainly in metallic targets. In the mechanisms triggered by ultrafast laser irradiation with a metallic sample, the energy deposited is first absorbed by the free electron present in the system. A process of a collision involving electrons leads to a rapid thermalization on a time scale of fs. On the contrary, ions cannot directly absorb light because they are too heavy to follow the oscillation of the electromagnetic wave. Still, ions are heated up due to their collision with electrons but regarding the mass difference only a small amount of energy is transmitted during the electron-ion interaction and the thermodynamic equilibrium is reached after times of few ps as reported in the work of Hüttner *et al* [73]. Based on this electron-ion exchange, we can argue that the energy transferred from electrons to the lattice depends on this coupling constant. Furthermore, the relaxation time to reach equilibrium de-

creases when the electron-phonon coupling constant increases as mentioned in the work of Elsayed-Ali *et al* [74]. The main specificity of femtosecond laser is a short pulse width combined a high energy per unit volume on a timescale faster than the electron-phonon coupling which implies a very small HAZ as discussed in the work of Buividas *et al* [75]. In literature, the ablation mechanisms were extensively studied in numerous investigations [76, 77, 78, 79, 80]. Actually, four distinct ablation mechanisms are suggested: spallation due to failure of the material following the creation of defects majorly nucleation of small nanovoids that grow under the action of the tensile stresses [81], phase explosion where the material is decomposition once it approaches the thermodynamic critical point temperature of a metastable homogeneous liquid turns into a mixture of liquid droplets [82], the fragmentation which is a disintegration of homogeneous materials into clusters under the action of a large strain rate [83], and finally the vaporization rather seen as desorption caused by exceeding cohesive energy, a collective ejection of monomers. In order to study closely the different mechanisms involved during this laser-matter interaction, numerical modeling appears to be the most effective way to explore the system evolution.

The first theoretical attempt to formalize the energy exchange between electrons and ions known as TTM model was done first by Kaganov and then Anisimov *et al* respectively [84, 85]. Two coupled differential equations are solved using a Finite Element Method (FEM) grid. This approach is implemented in the COMSOL software and works pretty well. This is described in the work of Kumar *et al* on titanium alloy where the temporal evolution of the electronic and ionic temperatures are obtained [86]. However, this multiphysics approach does not give the atomic and local structural arrangement. Therefore, a hybrid TTM-MD simulation seems to be appropriate to covert a such drawback, especially for a phase transformation investigation. A concrete implementation in order to combine the advantage of the TTM and MD model was performed by Ivanov *et al* on Au and Ni targets [87]. Another way to visualize the problem of ultrafast laser-matter interaction is to use a hydrodynamic model (HD) based on a fluid approach [88, 89], particularly to capture phenomena such as material ejection, evaporation, and plasma formation. An interesting investigation was performed by Colombier *et al* [90] to understand the mechanical behavior during the ablation of Cu and Al targets. Furthermore, these methods are also combined with experimental work to investigate the complex process as an arrangement of periodic nanovoids in Ni reported in the work of Sedao *et al* [91]. A research group used even a Monte Carlo (MC) to investigate the femtosec-

ond laser-induced plasma (two-phase laser plumes) expansion was developed by Volkov *et al* [92]. Since the laser is an electromagnetic wave, Finite Difference Time Domain (FDTD) method is applied to define the electric field profile by solving Maxwell equations as demonstrated in works of Rudenko *et al* [93] and Moreno *et al* [94]. To a lesser extent, Time-Dependent Density-Functional Theory (TD-DFT) computation is used to mimic the laser effect. This method is extremely efficient to investigate for instance structural effects related to electronic pressure, band gap, or laser-deposited energy [95, 96, 97, 98, 99].

#### 1.2.4 Atomistic modeling of ultrashort laser interaction with materials

The ultrafast lasers induce complex response mechanisms within the material sample, depending on the laser condition especially fluence different mechanisms can take place as shown in Figure 1.2.

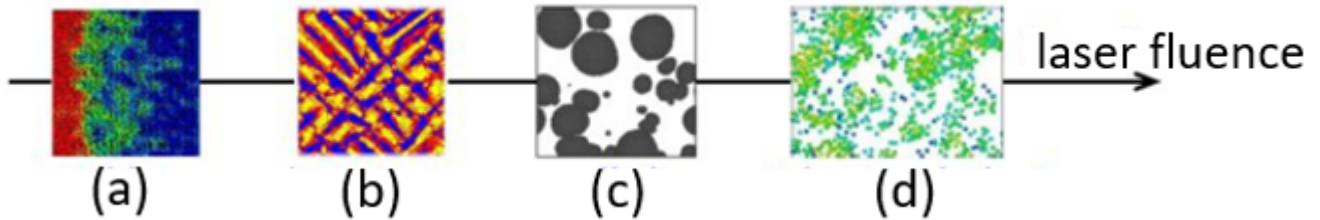


Figure 1.2: Overview of the regimes of laser interactions with metals: (a) melting, (b) microstructure, (c) spallation and (d) phase explosion. Adopted from [100].

A realistic modeling is clearly suited to orient experimental work and understand the process induced after the energy dose deposition. In this context, the state-of-the-art methods for the theoretical simulation pointed out the MD simulation seems to be the best complete investigation tool that changed the paradigm of understanding experimental physical processes occurring at the nanometer scale allowing direct experimental benchmarking. Moreover, it is pertinent to highlight that the quality or accuracy of the results depends on the model used, and the force field employed to perform a laser-matter simulation which has to match with the experiment data. The theoretical treatment of metals and semiconductors targets by a femtosecond laser reveals that two main observable modifications in terms of microstructuration may occur, either the generation of crystal defects (point, line, planar and bulk) [101, 102, 103], or a solid-liquid-solid (also solid-solid) phase transformation involving melting and solidification processes [87, 104, 105, 106, 107]. Actually, other fundamental mechanisms can be explored using these approaches such as cavitation, void formation, ablation,

vaporization, and crater formation [108, 109, 76, 110, 111]. In the work of Sedao *et al* [112] an MD simulation was performed to investigate structural changes in the surface of a Ni metallic target that has been triggered by a femtosecond laser. The observations reveal the formation of twinned structures inside the parent material as shown in Figure 1.3.

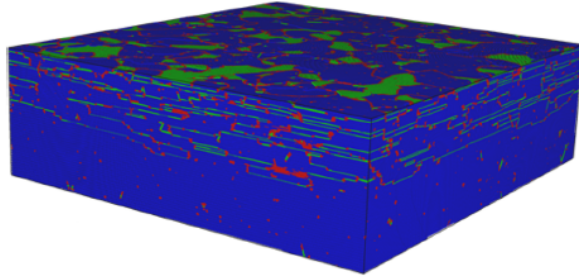


Figure 1.3: Local twinned zones in Ni target. The FCC atoms are colored in blue, green atoms corresponds to HCP crystals and red atoms belong to the liquid phase. Adopted from [112].

Here, the investigators directly implicate the phenomenon of resolidification as being at the origin of the twinning process. A similar twinning microstructuration (frozen nanospike) was reported by Wu *et al* in Ag [113]. A femtosecond laser interaction MD studies done by He *et al* [114] with Ni-based alloys ( $\text{Ni}_{50}\text{Fe}_{50}$ ,  $\text{Ni}_{80}\text{Fe}_{20}$  and  $\text{Ni}_{80}\text{Cr}_{20}$ ) show that a high emission of point defects and dislocations are correlated to thermoelastic stress and to solidification. The results are in Figure 1.4.

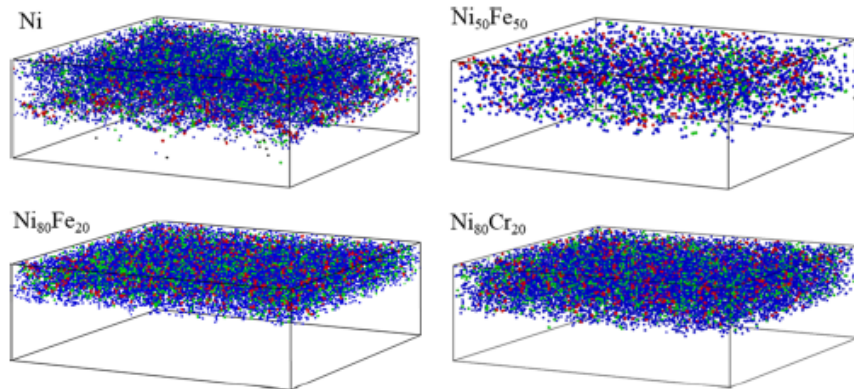


Figure 1.4: Atomic configurations generated by the solidification process. The atoms surrounding individual vacancies, divacancies, and larger vacancy clusters are colored by blue, green, and red, respectively. Adopted from [114].

There is a largely common crossed effect in several materials which MD can remarkably reproduce: the laser-induced periodic surface structures (LIPSS). The description of this pattern in the work of shugaev *et al* on Cr target [115] provides evidence of the role of surface melting and solidification with high densities

of dislocations and vacancies generated. The argument put forward is that redistribution due to ablation modulation causes the elongation of the liquid wall. The results are shown in Figure 1.5.

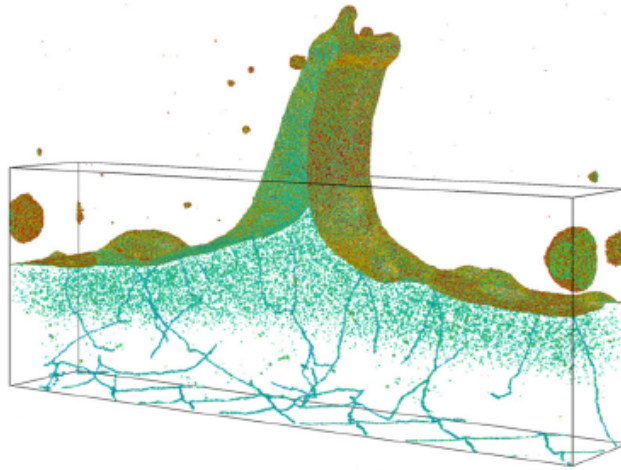


Figure 1.5: A typical surface structuration with dislocations and vacancy presence below the frozen protrusion is exposed. Atoms are colored by their potential energy. Adopted from [115].

### 1.3 Metallic glasses

The development of a broad class of Bulk Metallic Glasses (BMGs) alloys as a subclass of MG with extraordinary properties finds applications in many industries and even in different aspects of daily life, going from the field of functional materials, biomedical, and catalysis to microdevices. Unlike most crystalline systems, the BMGs are high strength making them ideal for aerospace industries and aircraft fasteners where the materials are subjected to a severe environment in terms of pressure and temperature [116, 117, 118]. The most plausible example is the Genesis spacecraft project launched by NASA to collect solar wind where a major part of this equipment is developed based on a new formula of BMGs. The melted surface due to the high temperature of these BMGs is ideal to capture the ions that are released in equal layers by combining them with sophisticated acid etching techniques [119]. Another game-changing property is the anti-corrosion capability of BMGs which finds applications in naval industry construction [120, 121]. These BMGs materials are also much in demand in chemical fabrication, especially for the elaboration of high-quality electrodes (for instance PdCuSiP BMG) [119]. The electronics industry is diligent in inventing novel coil chokes based on Fe-BMGs [119]. Moreover, a wide range of MG has the interesting ability of radiation damage resistance which makes them coveted by the nuclear industry for good nuclear reactor magnets use [122]. It is revealed that generally, the MG has high elasticity properties compared to the crystalline

counterparts [123, 124], this ability has been exploited by the manufacturers of sporting goods to commercialize in the market baseball bat and tennis racket frames [125, 119]. Digital and especially smartphone companies presented several kinds of high-quality cameras based on BMG [126]. The modern development of the shot-peening application for efficient energy transfer involving BMGs molded in a spherical shape is widely used [119]. The luxury brands also attached interest to BMGs for two reasons, their coating properties preserve the jewelry resistance over time, and the second reason is to stun the surface against the scratch that the traditional metals can not provide [119].

Another area of commercial interest is the field of health and biomedical where the research community has been able to take advantage of MG. Actually, a large part of MG families is biocompatible meaning that all problems related to allergies are avoided. Such BMGs are adequate for the design of medical components like prosthetic implants like pacemaker casings, knee-replacement devices, and surgical instruments. Indeed, ophthalmic cataract surgery instruments such as scalpel blades based on vitreloy are cheaper than those based on diamond, sharper, easily manufacturable, and longer lasting than steel [119, 125]. Defense technologies applications always require the development of military miniaturization materials that are stronger (high strength-to-weight ratio compared to titanium or stainless steel) ideal for antitank armor, lighter (for bulletproof design), and without sacrificing reliability at high temperatures and under constraints seems to be found in the reinforced heterogeneous ceramic-BMG composite that exhibits exactly these conditions [126, 125].

### 1.3.1 Glass transition temperature

MG construction is just a specific combination of two or more transition metals (Cu, Ni, Zr, Fe, Co, etc) in a given composition fraction. There are several methods to produce metallic glasses:

- Rapid quenching or cooling: This is the most commonly used method to produce metallic glasses. The process involves melting the metal and then quickly cooling it down to room temperature, typically in a few milliseconds, to prevent the metal from crystallizing [127].
- Mechanical alloying: This method involves the mechanical milling of elemental powders in a ball mill, which leads to the formation of a solid solution of the elements. This solid solution is then rapidly quenched to produce a metallic glass [18].

- Vapor deposition: In this method, the metal is evaporated in a vacuum and then deposited on a substrate, such as a rotating wheel or a liquid nitrogen-cooled copper block, which quickly cools the metal and forms a metallic glass [128].
- Melt spinning: This method involves the rapid solidification of a molten metal as it is ejected from a nozzle onto a rotating copper wheel. The high cooling rate of this process results in the formation of a metallic glass [129].
- Electrodeposition: In this method, metallic glasses are produced by electroplating, which involves the deposition of a metal onto a substrate using an electric current [130].

This quick cooling has the essential role in preventing the nucleation and growth of the crystalline phase. Technically, the liquid that is cooled below its glass transition temperature  $T_g$  experiences something similar to a second-order transition phase, but it is not exactly a transition phase in the thermodynamic sense. This glassy structure is a metastable structure [131] characterized by the increase of viscosity (order  $10^{12-13}$  Pa.s) accompanied by a slow of atoms movement such that they will not have the chance to rearrange themselves [132]. The quality of the MG is tightly related to the cooling rate  $Q$  given by the ratio  $Q = \frac{\Delta T}{\Delta t}$  as shown in Figure 1.6.

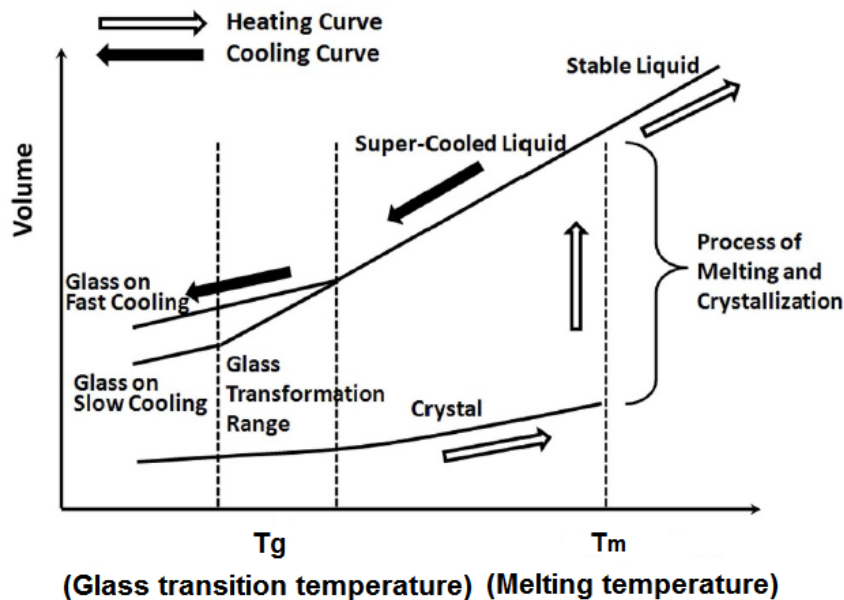


Figure 1.6: Schematic representation of the volume evolution with respect to temperature during the elaboration of MG. Different temperatures are shown :  $T_g$ ,  $T_m$  and the supercooling region where  $T_g < T < T_m$  [133].

### 1.3.2 Structure of metallic glasses

Crystalline alloys possess a long-range organization (belonging to the 14 Bravais lattice systems with 230 space groups), where atoms are arranged in a regular lattice repeating identically in three directions. Just by knowing the position of basis (i.e., a group of atoms) and the translation vectors, one can predict all the positions of the other atoms. The previous description is purely mathematical utopian. In reality, different kind of imperfections (vacancies, interstitials, impurities, substitutional, stacking fault, dislocations, or grain boundaries) that alternates the positions of the ideal atoms can be found inside the crystalline matrix. Unlike the crystals, the amorphous state atoms show a random arrangement where the periodicity is absent at a long-range order. However, it is worthy to mention that a short-range order exists in the case of amorphous structures. In literature, the word amorphous and glassy are commonly used as terminology to design a random atomic arrangement. According to the listed attributes, the structural difference between a MG and crystal is clearly established as shown in Figure 1.7.

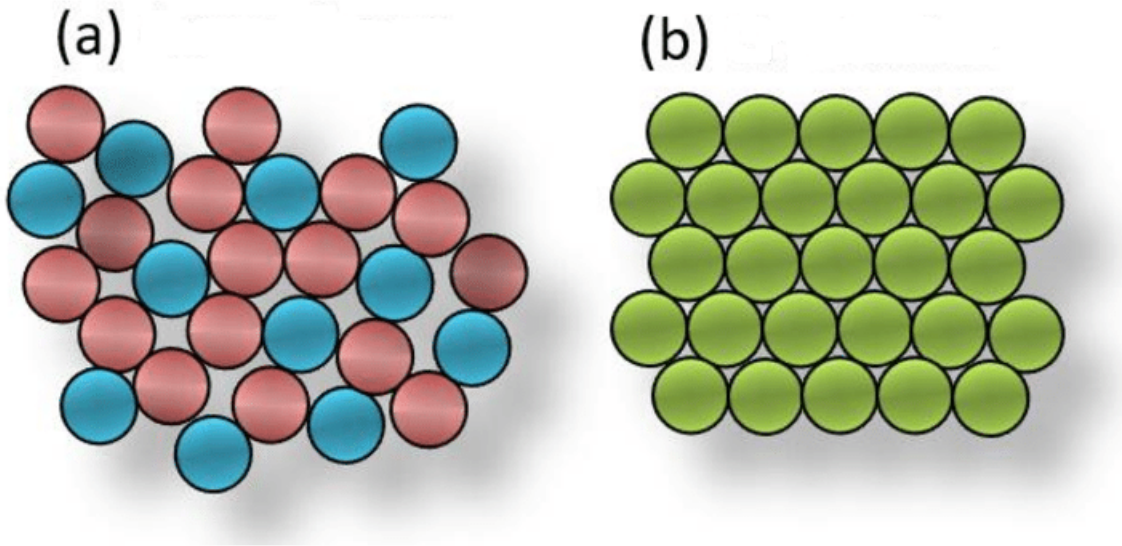


Figure 1.7: Schematic representation of a) hypothetical glassy alloy compound and b) crystalline form of the same compound. Adopted from [134].

### 1.3.3 Metallic Glass forming ability

The cooling rate has to be wisely chosen to design the MG since there is an infinity of choices. A critical value has to be clearly identified. It should satisfy two criteria: the cooling has to be rapid enough to freeze the liquid that turns to MG and at the same time avoid the emergence or formation of the crystalline phase. Consequently, the liquid forms the MG when the cooling rate is greater

than a critical value known as the concept glass forming ability (GFA). The rigorous definition of this key property is defined as the ease of vitrification for a material. According to thermodynamic kinetics, for a higher GFA, the critical cooling rate will be lower. Several conditions impact the value of this critical cooling rate. It depends mainly on the crystallization temperature  $T_x$ , the composition (chemical environment), and the structure (mono-atomic, binary, etc) of the material. As an illustration, several orders of magnitude may exist for the critical cooling rate. For instance  $Zr_{65}Be_{35}$  has a rate of  $10^7$  K.s<sup>-1</sup> [135] whereas the  $Zr_{41.2}Ti_{13.8}Cu_{12.5}Ni_{10}Be_{22.5}$  has a value of 1.4 K.s<sup>-1</sup> [136].

### 1.3.4 Metallic Glass formability

Several studies established that metallic species had a high probability of forming MG. A list of common conditions must be fulfilled for a MG to form at low cooling rates.

#### Confusion principle

The confusion principle calls for metal combinations that can form MG. The enthalpy of the mixture which is related to the stability of the system has to be negative [137]. This principle states that the ability to form a MG increases with the number of components involved [138]. Hence, the situation where the number of components in the system is greater than two allows an easier way to construct BMG [139, 137].

#### Atomic size difference criterion

In the case of an initial structure represented by atoms of kind 1, if we add atoms of kind 2 with a significant size difference, crystal phase distortion takes place, as referred by Innoue's rule [137]. This perturbation produces a large strain in the lattice causing subsequently an increase in the energy of the crystal state. In [140] Egami *et al* established a correlation between the constituent atomic sizes in binary alloys for instance and their structure. The study [141] confirms that when a liquid alloy is quenched, three distinct regimes may exist according to the atomic radius ratio  $R_1, R_2$  of atoms 1 and 2 respectively.

- The crystallisation occurs if :

$$0.95 \leq \frac{R_1}{R_2} \leq 1 \quad (1.1)$$

- The amorphous phase forms if :

$$0.6 \leq \frac{R_1}{R_2} \leq 0.95 \quad (1.2)$$

- The alloy splits into two pure crystalline phases (segregation) if :

$$\frac{R_1}{R_2} \leq 0.6 \quad (1.3)$$

### Species concentration criterion

The composition of the initial structure plays a primordial role to determine the physical properties of the formed MG. From a thermodynamic point of view, the stability of this MG is related to the change of free energy impacted by mixing two different elements 1 and 2. The Equation 1.4 expresses the relation between the composition and the stability as follows:

$$\Delta G_{mix} = \alpha X_1 X_2 + RT(X_1 \ln X_1 + X_2 \ln X_2) \quad (1.4)$$

Where  $G_{mix}$ ,  $X_1$ ,  $X_2$ , and  $\alpha$  represent the free energy of the mixture, atomic concentrations of atoms (1 and 2), and a constant proportional to the molar heat of the mixture. The  $R$  is the gas constant and  $T$  is the absolute temperature.

## 1.4 CuZr binary alloy phase diagram

In this work, the order-disorder evolution of CuZr systems in both crystalline and amorphous structures during laser-matter interaction is investigated. To find the appropriate composition to reach a specific application, it is, therefore, necessary to explore the interdependency between chemical composition and crystallographic structure. In this context, the phase diagram appears to be a useful tool for BMG development as shown in Figure 1.8.

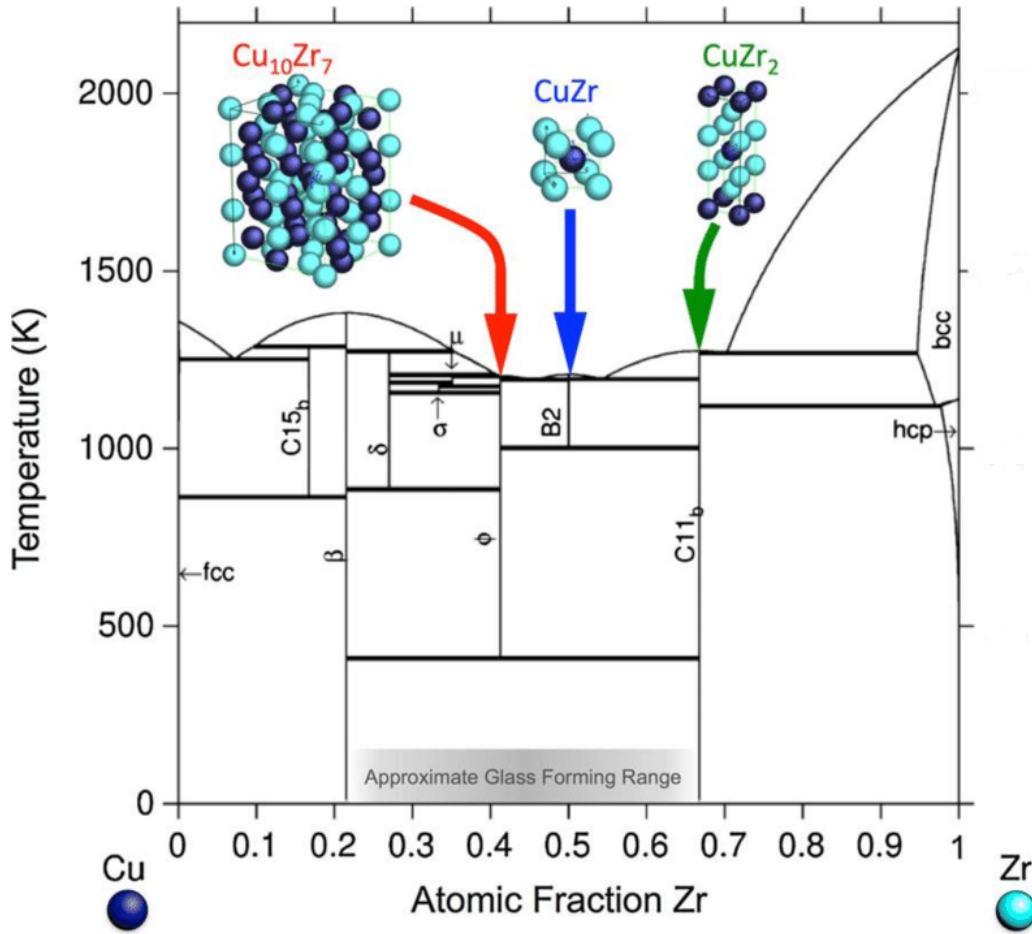


Figure 1.8: The equilibrium Cu-Zr phase diagram showing three intermetallic phases relevant to the current study are indicated [142]. The shading of the composition axis indicates the approximate range over which the Cu-Zr system exhibits a strong glass-forming tendency. Adopted from [143].

The above diagram provides information about crystalline phases stability of CuZr alloy, and according to this diagram, it is clear that CuZr is interesting because of their good GFA in a wide range of composition going from  $\sim 20$  to  $80$  Zr-% [144, 145]. It is revealed at the extremity of the diagram individual phases exist, obviously that only Cu in FCC phase and Zr in HCP (or BCC-phase) subsist. Concerning the Zr, special attention should be paid to it due to its high reactivity with oxygen, especially at high temperatures (discussed in chapter 4). According to the phase diagram, at a concentration of  $40$  Zr-% and in the temperature range of  $1000 \text{ K} < T < 1500 \text{ K}$  the phases  $\text{Cu}_{10}\text{Zr}_7$  appears. On the other hand at  $50$  Zr-% the CuZr binary alloys is in B2 structure for temperatures in the range of  $\sim 1000 \text{ K} < T < 1200 \text{ K}$ . For the system known as  $\text{CuZr}_2$ , charge with  $\sim 67$  Zr-% the structure is  $\text{C11}_b$  in the temperature range of  $1200 \text{ K} < T < 1400 \text{ K}$ . All of these correlations are used to understand the key thermodynamic criteria for quantifying amorphization and crystallization

kinetics. Moreover, the influence of  $B_2$  short-range ordering role in the disordered phase in the supercooled domain during the devitrification process is outlined in chapter 5.

## 1.5 Imperfections in solids

An alloy is a combination of two or more elements where at least one is a metal. The particular case in which we have only two elements is known as a binary alloy. The result of alloying is a metallic substance with properties different from those of its components. Moreover, the formed alloy is never perfect defects always are present. As a result, controlling the proportion and type of these defects is a major challenge that yield to a profound impact on the behavior of the materials properties. In fact, using the term defect is sort of a misnomer since these characteristics are intentionally used to manipulate the behavior of materials. Generally, imperfections in crystalline solids are classified according to their dimension as follows: point defects (0-D defects), line defects (1-D defects), surface defects (2-D defects), and volume defects (3-D defects) as summarized in Figure 1.9.

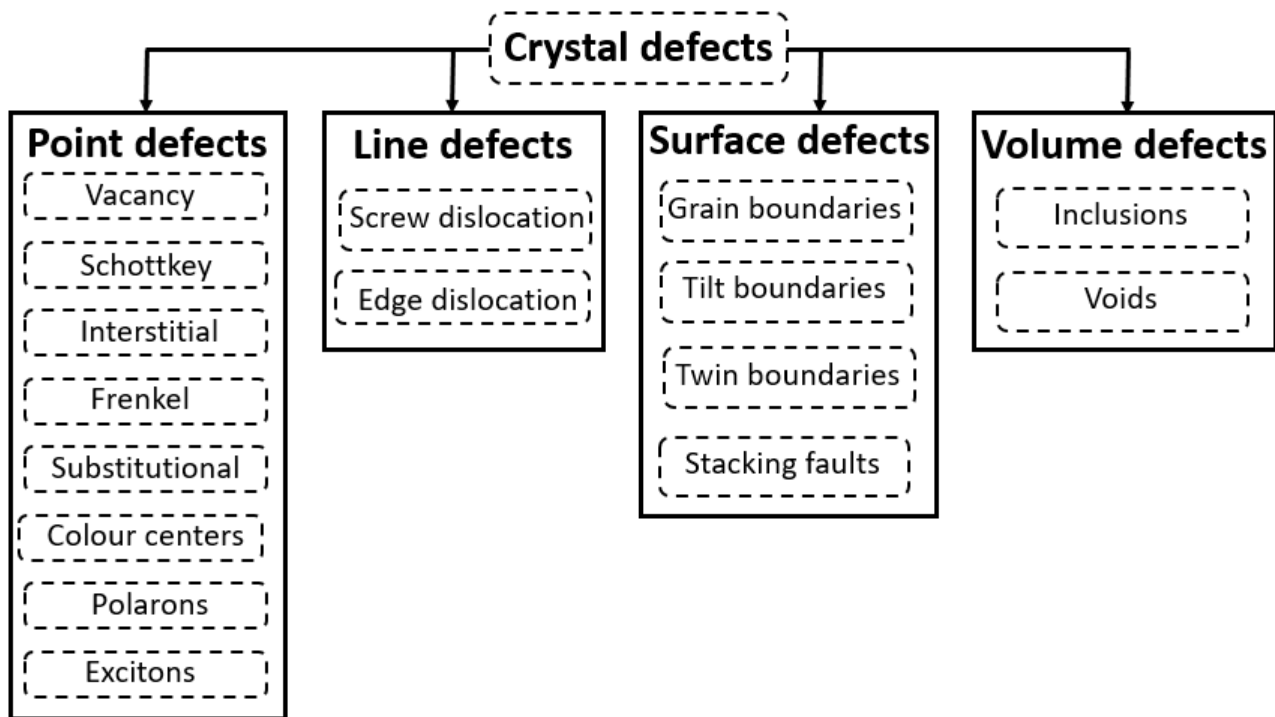


Figure 1.9: Diagram summarizing the classification of defects based on dimensionality and types in crystalline solids.

A number of properties of materials are controlled by defects. For example, electrical and thermal conductivity in metals are greatly reduced by point

defects, electronic conductivity in semiconductors is affected by substitution defects, diffusion by vacancies, ionic conductivity by vacancies, and Hardness by dislocations concentration in crystalline materials. As a way to give a more understanding of the coming chapters, especially the third one, we will dissect and discuss point defects and surface defects in greater detail.

Point defects occur when an atom is missing or is in an irregular place in the lattice structure. It includes self-vacancies, interstitial, and substitutional. In general, substitutional impurity atoms are usually close in size (within approximately 15%) to the bulk atom as presented in Figure 1.10.

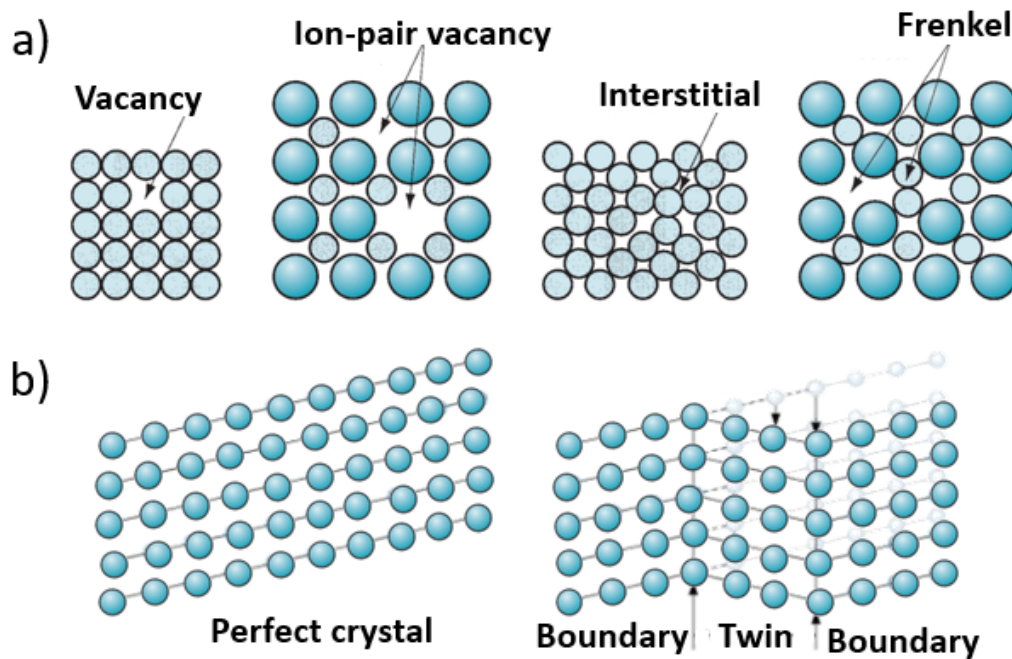


Figure 1.10: Representation of possible crystal defect types in solids a) 0-D and b) 2-D kind.

There are several types of point defects that can occur in a crystalline material. These include:

- Vacancies are the most common type of point defect, and they occur when an atom or ion is missing from its lattice site in the crystal. Vacancies can be created by thermal fluctuations or radiation damage.
- Interstitial occurs when an extra atom or ion occupies an interstitial site in the crystal lattice. This can occur due to thermal energy or radiation damage.
- Substitutional takes place when an atom or ion in the crystal is replaced by a different atom or ion. This can occur due to impurities or doping.

- Schottky arises when an equal number of cations and anions are missing from the crystal lattice of an ionic compound. This results in a vacancy defect, as there are now fewer ions in the lattice than there should be. Because the missing ions are balanced, there is no net charge in the lattice. This type of defect is commonly observed in compounds with high coordination numbers, such as NaCl and KCl. It can occur due to thermal vibrations that cause ions to leave their lattice sites, or due to the presence of impurities that prevent ions from occupying their correct positions.
- Frenkel defect consists on an ion or atom in a crystal lattice is displaced from its normal lattice site and moves into an interstitial site (a vacant site between atoms in the lattice). This creates a vacancy (an empty site) where the ion or atom was originally located, and an interstitial defect where it moved to. Frenkel defects typically occur in ionic crystals where the cation is much larger than the anion, causing the cation to be easily displaced from its lattice site.

Surface defects include twin boundaries, which are created mainly by a transition from a higher symmetry structure to a lower symmetry one, where a number of variants can coexist, or by rapid loading and deformation. The shear force that causes atomic displacements is such that the atoms on one side of a plane (twin boundary) mirror the atoms on the other side. In addition, it takes place along defined planes and directions depending on the initial crystallography of the system.

## 1.6 Classical theory of crystallization

The simplest definition of nucleation or germination is the emergence of small nucleus of a new phase inside or at the limits of a homogeneous parent phase due to a substantial change in temperature, and pressure. A theory based on this phenomenon is commonly employed to give a qualitative study of the phase transition kinetics. In reality, nucleation occurs hand in hand with another process known as crystal growth. As discussed, when we consider the specific problem of a glass-to-crystal transformation, from a strict thermodynamic point of view devitrification consists of two kinetic processes, nucleation, and crystallization. This phenomenon is mainly dominated by nucleation which dictates the time needed to see the first nucleus as shown in Figure 1.11.

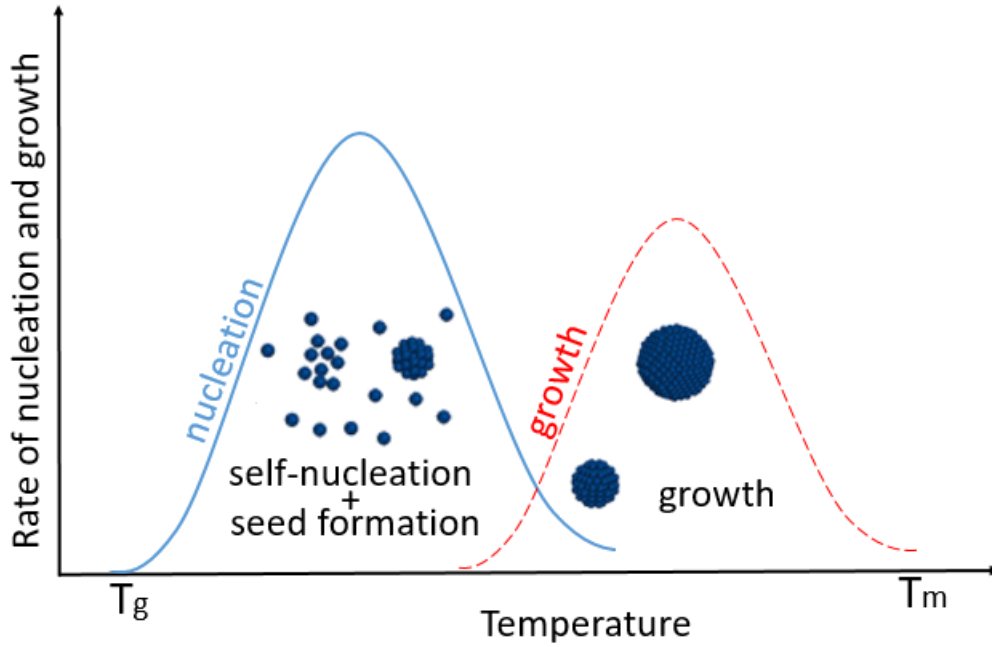


Figure 1.11: Schematic showing the effect of temperature on nucleation and crystal growth rates. Adopted from [146].

In addition, it is imperative to point out that a nucleus has to reach a critical size in order to avoid dissolution in the glassy matrix. Thus, a critical size is necessary for this upcoming phase to survive in the glassy hosting matrix as expressed in Equation 1.5. The formation of a seed of radius  $r$  from the preexisting phase requires the crossing of the free energy barrier. It is composed mathematically of surface and volume contributions with the assumption that atoms have a spherical shape as described in [147] and given by:

$$\Delta G(T) = -\frac{4\pi r^3}{3}\Delta G_V(T) + 4\pi r^2\sigma \quad (1.5)$$

Where  $\Delta G_V$  represents the free energy difference per volume between the glassy and the crystalline states,  $\sigma$  is the crystal-glass interfacial free energy and  $r$  is the radius of the crystal nucleus.

The Equation 1.5 displays a maximum corresponding to the critical nucleus radius size  $r^*$  given by:

$$\left(\frac{d\Delta G(T)}{dr}\right)_{r=r^*} = -4\pi r^{*2}\Delta G_V(T) + 8\pi r^*\sigma = 0 \quad (1.6)$$

Therefore, the Gibbs free energy that the system has to overcome to form this critical nucleus is given by Equation 1.7 as:

$$\Delta G^*(T) = \frac{16\pi}{3} \frac{\sigma^3}{\Delta G_V^2(T)} \quad (1.7)$$

Furthermore, it is pertinent to mention that the amorphous structure is metastable. Despite this, systems tend to be in their crystalline stable phase. To do so, we have to give atoms the ability to rearrange their local structure. Thus, the ideal temperature range to maximize growth is in  $T_g < T < T_m$ . Two major forms of nucleation process may exist, either homogeneous meaning that nucleation occurs in the bulk, whereas heterogeneous nucleation occurs at the surface of the system [148]. The nucleation rate  $\zeta$  is predicted using Arrhenius equation [149] as:

$$\zeta = \Omega\zeta_0 \exp\left(-\frac{\Delta G^*(T)}{k_B T}\right) \quad (1.8)$$

Where  $k_B$ ,  $\Omega$ ,  $T$ ,  $\Delta G^*$ , denote the Boltzmann constant, volume in the transformed zone, temperature, and Gibbs free energy barrier to pass from the metastable to crystalline phase respectively.

Likewise, the crystal growth rate  $\xi$  is given by:

$$\xi = a_0\nu \exp\left(-\frac{\Delta E}{k_B T}\right) \left[1 - \exp\left(-\frac{\Delta G}{k_B T}\right)\right] \quad (1.9)$$

Where  $a_0$  is the lattice constant,  $\nu$  is the vibrational frequency,  $\Delta E$  the kinetic barriers, and  $\Delta G$  thermodynamic barrier to crystal growth. In addition, according to Equations 1.8 and 1.9 both nucleation and crystal growth rate are temperature dependent.

## 1.7 Ultrafast laser inducing devitrification of Metallic glasses

Ultrafast laser process inducing phase transformation and structural modification within ordered nanocrystalline alloys or metastable disordered systems as MGs received extensive research. This interest attention for decays is due to their properties suitable for various applications, such as magnetic fabrication [150], electrocatalysis for energy storage [151], coating superior properties [152], standing ductility [153], catalytic [154], and exhibit interesting high reflection in visible light making them useful for optical applications [155]. Despite all these tremendous efforts dedicated designing a material with exceptional enhanced properties for both nanotechnology and industrial applications, it is still far to satisfy all fabrication challenges. To overcome these difficulties, an original idea sprouts, which is the combination of amorphous and crystalline structures in a new single alloy. This hybrid material may inherit interesting properties from either the amorphous or nanocrystalline or even exhibit an extraordinary new improved property. The investigation of the devitrification of amorphous material reveals

a promising potential to achieve a such purpose due to the anisotropic characteristics induced by the presence of nanocrystals inside the amorphous material. So far, in literature, the only theoretical way proposed to achieve devitrification is the MD by an annealing approach. It consists of keeping the amorphous sample enough time in its supercooled state to crystallize. To induce amorphous-crystalline phase change is known in the literature as devitrification.

This phenomenon is a challenging exercise to achieve. The simplest way to crystallize a MG is the annealing process by maintaining the system enough time in a supercooling state till the first crystalline seed appears. To control the final crystalline phase state, the velocity of seed emergence, its location, or even the size of this new crystalline phase is not fully clear and still an open question. As a first insight, understanding this order-disorder transformation depends on the glass-forming ability which gives the tendency of a material to form an amorphous structure. As a general rule, the microstructuration of mono-atomic amorphous structures designed by liquid quenching is easier to activate due to the strong ability to be in an ordered phase. This behavior is confirmed in both amorphous [156, 157] and liquid Al [158, 159, 160] and in amorphous Ti [157]. MD study shows also that devitrification via the supercooling procedure of amorphous Cu [161] is possible. Another process known as devitrification under stress is experienced [162]. The theoretical vitrification-devitrification transformation cycle study of Fe MG led by annealing process [163] showed a competition between two types of cluster configurations icosahedral-like and crystal-like. They support that a critical cooling rate exists below which FCC-like configurations become dominant leading to crystallization otherwise the icosahedral-like configuration takes advantage of the glass phases. Such behavior was also observed in many other metals like in the computational study of Zr [164]. Analogous devitrification behavior of amorphous Ni with different methods using both simulations and experimental evidence is reported in various depositions [165, 166]. The study [167] reveals the existence of shear deformation to induce transformation. Propagating exothermic waves associated with crystallization front in amorphous Ni is investigated in [168]. This study confirms that atoms rearrangement in a stable crystalline phase corresponds to minimal energy. The enhancement of crystal forming ability was reported in [169] by the mean of structural difference between liquid and crystal toward the interface tension which suppresses the amorphous structure and promotes crystal formation. Unfortunately, because of their low glass-forming ability, experimental vitrification of the monoatomic MG is challenging and quite not commonly studied [170] but a novel experimental method

called rapid solidification was successfully used to achieve amorphization of pure metallic element [171].

A broad family of glasses are a good candidate for devitrification, the most interesting among them is known as shape memory MG-alloy encompassed in the binary alloys category. The NiTi amorphous structure is considered as a good school case example that displays an important performance for devitrification facility behavior [172]. Plenty of studies have shown that glass-crystal phase change takes place in a wide range of binary alloys, we can mention NiZr [173, 174, 175], CuTi [176, 177], PdSi [178], FeNi [179, 180], SiAl [181, 182], SiAu [183], NiAu [184], and NiAl [185]. The study [186] dealing with PbF<sub>2</sub> isothermal devitrification brings new elements that may affect the features of the crystallization history. First, is the heating rate, and the second is the defects inclusion impact. The erbium Er<sup>3+</sup> presence in PbF<sub>2</sub> glassy matrix favors the glass-crystal transition. Moreover, it decreases devitrification temperature by modifying the Pb atoms mobility [187]. In addition, the study [188] established that the devitrification process in an amorphous CuNi system may also be triggered by high pressure. They speculate that it is correlated to structural stability through the reduction of the incubation time of crystallization. An interesting investigation comparing the behavior of ZrPd and CuZr MGs alloys has been made to understand devitrification from a structural point of view [189]. It was established that by employing Voronoi indexes analysis, the amorphous-quasicrystal transformation of ZrPd and not of CuZr finds its origin in the abundance of icosahedral-like clusters which are close to the ordered phase resulting in a low-energy barrier for a transformation. The results on NiNb MG [190, 191] reveals that crystallization occurs above  $T_g$ .

Furthermore, study [192] highlights that devitrification is obtained and boosted in NiNb amorphous alloy through a hybrid treatment via combining a shear mechanical effect with high pressure. Recent works on ZrCo MG [193] bring another ingredient to the devitrification process understanding in total agreement with experimental results. It demonstrated the important role of the atomic concentration species impact. Thereby the liquid-glass transformation for instance occurs for Co concentrations range of 30–90 %. A deep theoretical atomistic clarification by the mean of radial distribution function (RDF) is employed in order to identify and track the devitrification of TiAl MG alloy [194] confirmed with experimental evidence [195]. Recently, a simulation method bearing on CuZr devitrification called seeding has been reported in [196]. The approach is to insert

a perfect B2 structure inside the glassy structure in order to activate the crystallization process. This method is terribly efficient with glasses having a good forming ability where the nucleation is considered as a rare event. Considerable interest in multicomponent MGs mixtures crystallization has been reported in the literature because of their several potential high technological applications. We can mention ternary alloys as CuZrPd [197], AlNiCo [198], CuZrAl [199, 200], and AlNiLa [201]. A couple of studies have been made to surround the formation of the crystals in quaternary MG from a pure experimental view. Successes have been observed on samples such ZrCoAlFe [202], LaAlNiCu [203], ZrTiNiCuBe [204, 205], and ZrTiCuNiAl [206]. Among the major studies of quinary amorphous structures crystallization, they support that the devitrification is due to two parameters the atomic element size and the stoichiometry of the mixtures, a hypothetical diagram summarizing the devitrification steps is provided in Figure 1.12.

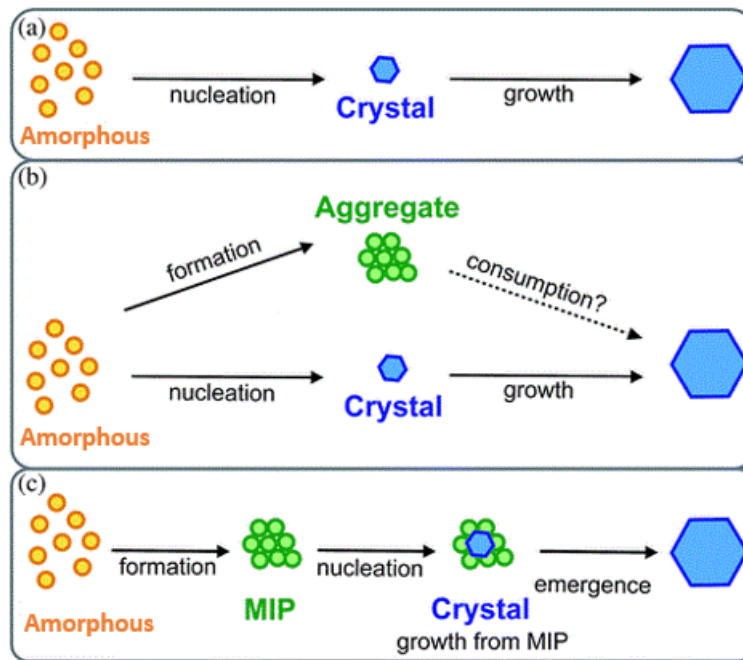


Figure 1.12: Illustrations of different pathways for crystal nucleation and growth. (a) Classical one-step pathway. (b) A parallel process of aggregate formation and crystal nucleation. (c) A multi-step process with a precursor (MIP) for nucleation. Adopted from [207].

It was confirmed experimentally that devitrification can be achieved by an X-ray beam in CuZr. This confirms that this phenomenon is sensitive also to the irradiation type [142]. In this paper, we focus on Zr-based alloy devitrification particularly CuZr MG via an ultrafast laser pulse. A recent attempt to study ultrafast laser interaction with amorphous CuZr materials targets using atomistic computation is mentioned in [208]. Unfortunately, no amorphous-crystalline

phase transition is discussed or mentioned. The response for the absence of any phase transition in this amorphous alloy was partially elucidated in the work of [209] where they claim that the devitrification of such a system is a rare event due to the very slow rate of nucleation. To circumvent this problem different novel methods were developed. [210]. One of the methods is to artificially sandwich the supercooled CuZr MG between pure Zr and Cu layers, which allows nanocrystals to form. Few other experimental works were performed to achieve the amorphous-crystal transformation cycle by an ultrafast laser shot [42, 211, 43, 42, 44, 212, 213, 45, 214, 215, 46]. However, the mechanism and influence of thermodynamic conditions leading to these transformations remain unclear.

The novelty of this work is to guide and trigger a local devitrification with an ultrafast laser pulse using atomistic methods. To understand the mechanism involved during the devitrification, we have selected CuZr MG as a candidate. The preliminary observations demonstrate that samples are easier to devitrify. Thus, the presence of Zr favors this phase transformation. The determination of ultrafast laser irradiation conditions suitable to activate and then control the amorphous-crystal transformation is fundamental. In reality, the key to understand this phase transition requires finding laser conditions that permit the successful prediction of a stable crystalline structure (cross-energy barrier) and then determining the thermodynamic quantities (temperature and pressure) to have a global view of the transformed region. In addition, a complementary explanation can be obtained using Classical Nucleation Theory (CNT). There are several studies concerning the glass formation, kinetics, and phase transformation mechanisms during devitrification in Cu-Zr binary systems [216, 217, 218, 219, 220].

These studies revealed several details concerning crystallization transformations involving the phases, the kinetics of the crystallization of individual phases under isothermal and constant-heating conditions, and structural dynamics associated with devitrification in Cu-Zr binary systems. In this dissertation, we focus on Zr-based alloy devitrification, particularly CuZr MG via an ultrafast laser. The first attempt to study ultrafast laser interaction with amorphous CuZr materials targets using atomistic computation was [208]. The devitrification of a such system is a rare event due to the slow rate of nucleation [209].

## 1.8 Summary conclusion

Despite maturity of the laser technology as a material processor, exploring the possibility of reorganizing amorphous structures, especially MGs, can open up many possibilities. This can open up new opportunities for the development of extraordinary materials. In order to exploit these materials for industrial technology, a relevant fundamental investigation is required to gain a deeper insight into the response of the material. The goal of the study is to elucidate the causes of these atomic rearrangements, which are largely caused by nonequilibrium mechanisms. To understand laser-matter interactions in amorphous alloys, a theoretical study involving atomistic pictures is imperative. An overview of the used model will be presented, as well as its advantages and limitations. Furthermore, how the concurrent model can be enhanced and obtain accurate results.

# Chapter 2

## Theory and analysis

### 2.1 Introduction

A variety of numerical techniques have been developed at different time and length in order to conduct a different kind of investigations. These methods include ab initio techniques (DFT), Molecular Statics and Dynamics (MS and MD), Monte Carlo (MC) methods, phase-field kinetic methods, Dislocation Dynamics (DD), as well as the traditional FEM Finite Element Method (FEM) as shown in Figure 2.1.

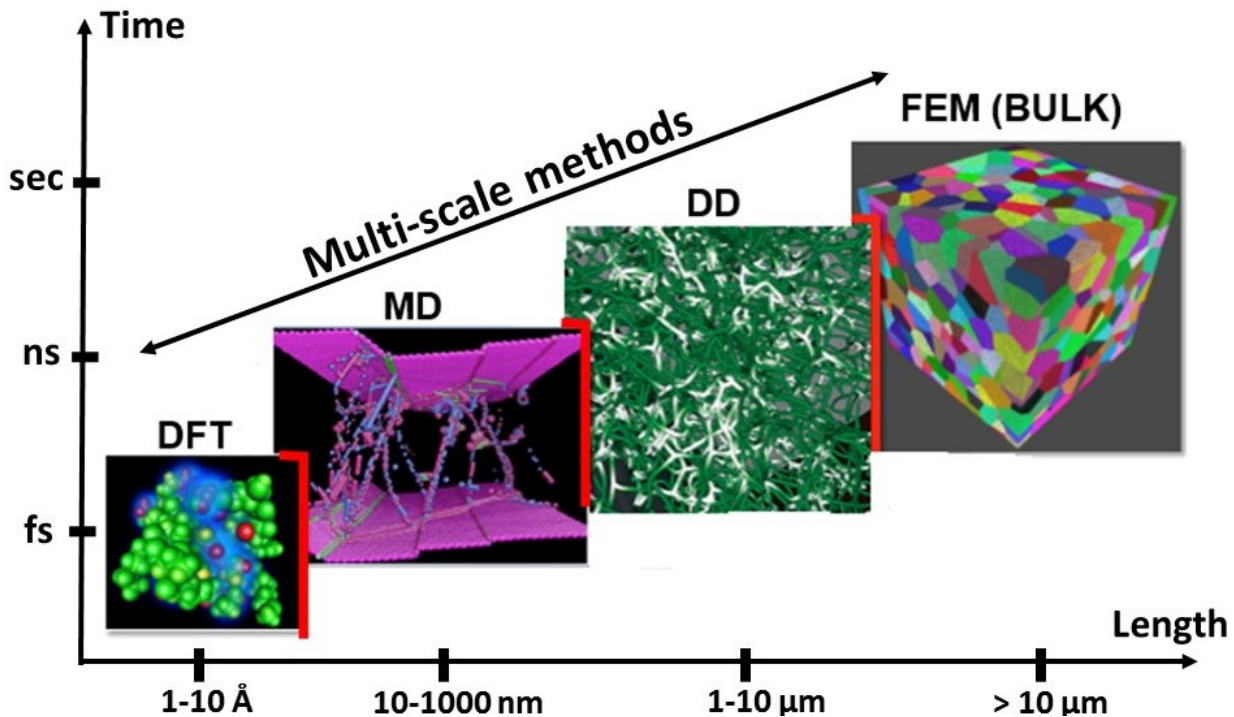


Figure 2.1: Typical methods in computational materials science in terms of size and time. Adopted from [221].

The multiscale perspective means that each technique is most effective in handling problems within a specific length scale, from the nano to micro level (ab

initio, MS, and MD), then to the micro to meso level (DD and phase-field), and finally to the meso to macro level (FEM). The outcome of each scale is fed into the next, with the ultimate goal of determining macroscopic behavior starting from quantum mechanics.

Ab initio methods solve the Schrödinger equation directly, but are limited to small clusters of atoms due to the computational demands. MS and MD use established interatomic potentials to calculate the equilibrium positions of atoms at zero temperature or the trajectories of atoms by integrating Newton's second law. MC methods calculate integrals through random number generation and are particularly useful for computing thermodynamic functions. DD calculates group dislocation behavior by treating dislocations as elastic curves that interact with one another through simplified laws. Phase-field methods, based on kinetic laws such as the Langevin equation, predict phase evolution and consider fluctuations. Finally, FEM solves continuum problems governed by known constitutive laws by dividing the domain into finite elements, which allows for effective problem solving through the inversion of algebraic matrices by high-speed computers.

In the 50's, Alder and Wainwright introduced the MD method to examine the interactions of rigid spheres [222]. This method takes advantage of the deterministic nature of classical mechanics and argues that, given knowledge of the initial velocities and positions of a system, it is possible to capture the temporal evolution of the system by integrating Newton's equations of motion. MD is a powerful theoretical investigation method that uses basic numerical concepts and is particularly useful for treating systems with numerous particles where analytical analysis is not possible. The application of MD has benefited many fields, including solid-state physics (such as cracks, nanoindentation, glass elaboration, laser-matter interaction, and ion bombardment), biochemistry (such as polymers, proteins, and DNA), and chemistry (such as molecular interaction behavior and rare events). A variety of codes, including LAMMPS [223], AMBER [224] and NAMD [225] are available to researchers for use in MD simulations.

## 2.2 A brief overview of molecular statics

MS simulations are commonly used in materials science, chemistry, and biophysics to study the structure and stability of molecules, materials, and biological systems. The method provides valuable information about the energetic of molecular systems, including the bonds between atoms, the distribution of charge, and the stability of different configurations. Additionally, it can be used

to optimize the structure of molecules and materials to improve their properties and performance.

MS is a computational method used to study the behavior of systems at zero temperature. The method calculates the equilibrium positions of the atoms based on the interatomic potentials, which describe the interactions between the atoms. The first step is to define the system, including the number of atoms, their types and positions, and the interatomic potentials to be used. Next, the forces between the atoms are calculated using the interatomic potentials. The equilibrium positions of the atoms are then determined by minimizing the potential energy of the system. In MS, the system is assumed to be at a constant temperature and pressure, and all motions are considered to be frozen. The method provides a snapshot of the system at a single point in time and does not account for any time-dependent processes, such as chemical reactions or thermal or mechanical processes [226].

The Conjugate Gradients (CG) method is a numerical optimization technique used in MS to solve systems of linear equations. It is a type of iterative algorithm, which means that it iteratively improves an approximate solution to the problem until a satisfactory solution is found. The method operates by constructing a sequence of search directions that are conjugate to each other, meaning that they are orthogonal to all previous search directions. This allows the method to converge faster than other iterative methods, such as gradient descent, which only use the gradient of the objective function [227].

The CG method starts with an initial approximation to the solution and then iteratively improves the solution by computing a search direction that is conjugate to the previous search direction. The search direction is then used to update the approximation to the solution. The process is repeated until the solution converges to a satisfactory level of accuracy or a maximum number of iterations is reached. The CG method has several advantages over other optimization techniques, including that it is fast, well-conditioned, and easily implementable. The mathematical algorithm for the CG method can be described as follows:

- Initialize: choose an initial approximation to the solution,  $x_0$ , and set the residual,  $r_0 = b - Ax_0$ , where  $b$  is the right-hand side of the system of linear equations and  $A$  is the coefficient matrix.
- Choose a search direction: compute the search direction,  $p_0$ , by setting  $p_0 = r_0$ .

- Update the solution: define a scalar step size  $\alpha$  by computing the inner product of the residual and the search direction,  $\alpha = (\mathbf{r}_0, \mathbf{p}_0) / (\mathbf{p}_0, \mathbf{A}\mathbf{p}_0)$ . Update the approximation to the solution by  $\mathbf{x}_1 = \mathbf{x}_0 + \alpha\mathbf{p}_0$ .
- Update the residual: compute the new residual,  $\mathbf{r}_1 = \mathbf{b} - \mathbf{A}\mathbf{x}_1$ , and update the search direction,  $\mathbf{p}_1$ , by computing the conjugate gradient formula,  $\beta = (\mathbf{r}_1, \mathbf{r}_1) / (\mathbf{r}_0, \mathbf{r}_0)$  and  $\mathbf{p}_1 = \mathbf{r}_1 + \beta\mathbf{p}_0$ .
- Repeat steps of updating the solution and residual until the residual is below a desired tolerance or a maximum number of iterations is reached.

## 2.3 Integration of Newton's equation

In MD atoms are considered as point particles that interact with each other by the mean of an interatomic potential  $\mathbf{U}(\mathbf{r}_i)$ . Therefore, if the potential is not adequate to describe the property, we target, no reliable connection with the real world is possible. The equation of motion solved is given below:

$$\mathbf{F}(\mathbf{r}_i) = m_i\ddot{\mathbf{r}}_i \quad (2.1)$$

Where  $\mathbf{F}(\mathbf{r}_i)$ ,  $m_i$ ,  $\ddot{\mathbf{r}}_i$  are force, mass and acceleration of the atom  $i$ . The force applied on the atom  $i$  is obtained from the derivative of the potential energy  $U(\mathbf{r}_i)$  with respect to the  $\mathbf{r}_i$ :

$$-\frac{\partial U(\mathbf{r}_i)}{\partial \mathbf{r}_i} = m_i \frac{\partial^2 \mathbf{r}_i}{\partial t^2} \quad (2.2)$$

As mentioned above Equations of motion are deterministic. If we know the initial coordinates and velocities, it is possible to recover the trajectory of the system. The numerical solution of Equation 2.2 for a set of  $N$  atoms, can be achieved using Verlet integrators [228]. The algorithm is formulated in a simple mathematical manner and allows the combination of multiple relevant ingredients. This includes compliance with conservation laws of energy and moment, accuracy, and stability during integration, and it is the least expensive with respect to computing costs. The mathematical implementation of Verlet algorithm is based on Taylor expansion at times  $(t + \Delta t)$  (forward) and  $(t - \Delta t)$  (backward) in the vicinity of the positions as given by Equations 2.3 and 2.4 as follows:

$$\mathbf{r}_i(t + \Delta t) = \mathbf{r}_i(t) + \frac{\Delta t}{1!}\dot{\mathbf{r}}_i(t) + \frac{\Delta t^2}{2!}\ddot{\mathbf{r}}_i(t) + \frac{\Delta t^3}{3!}\dddot{\mathbf{r}}_i(t) + O(\Delta t^4) \quad (2.3)$$

$$\mathbf{r}_i(t - \Delta t) = \mathbf{r}_i(t) - \frac{\Delta t}{1!}\dot{\mathbf{r}}_i(t) + \frac{\Delta t^2}{2!}\ddot{\mathbf{r}}_i(t) - \frac{\Delta t^3}{3!}\dddot{\mathbf{r}}_i(t) + O(\Delta t^4) \quad (2.4)$$

The sum of Equations 2.3 and 2.4 gives:

$$\mathbf{r}_i(t + \Delta t) + \mathbf{r}_i(t - \Delta t) = 2\mathbf{r}_i(t) + \Delta t^2 \ddot{\mathbf{r}}_i(t) + O(\Delta t^4) \quad (2.5)$$

In Equation 2.5 we inject 2.1

$$\mathbf{r}_i(t + \Delta t) = 2\mathbf{r}_i(t) + \mathbf{F}_i \frac{\Delta t^2}{m_i} - \mathbf{r}_i(t - \Delta t) \quad (2.6)$$

By the same procedure, we subtract Equations 2.3 from 2.4 and let's neglecting Taylor's third order term, we can predict the updated position as:

$$\mathbf{r}_i(t + \Delta t) - \mathbf{r}_i(t - \Delta t) = 2\Delta t \dot{\mathbf{r}}_i(t) + O(\Delta t^3) \quad (2.7)$$

Finally, we end with the Verlet velocity given by the following equation:

$$\mathbf{v}_i(t) = \dot{\mathbf{r}}_i(t) = \frac{\mathbf{r}_i(t + \Delta t) - \mathbf{r}_i(t - \Delta t)}{2\Delta t} \quad (2.8)$$

Where the  $\Delta t$  is the discretization timestep often chosen to be 1 fs in MD simulations.

In reality, Verlet velocity algorithm is widely used many MD codes. Concretely, it is achieved in four steps to compute the updated positions, velocity, and accelerations from the previous time steps by:

$$\mathbf{r}_i(t + \Delta t) = \mathbf{r}_i(t) + \mathbf{v}_i(t)\Delta t + \frac{1}{2} \frac{\mathbf{F}_i(t)}{m_i} \Delta t^2 \quad (2.9)$$

The half velocities are defined by:

$$\mathbf{v}_i(t + \frac{\Delta t}{2}) = \mathbf{v}_i(t) + \frac{1}{2} \frac{\mathbf{F}_i(t)}{m_i} \Delta t \quad (2.10)$$

So, with the updated position we can define the forces:

$$\mathbf{F}_i(t) \rightarrow \mathbf{F}_i(t + \Delta t) \quad (2.11)$$

Finally, the velocities are:

$$\mathbf{v}_i(t + \Delta t) = \mathbf{v}_i(t + \frac{\Delta t}{2}) + \frac{1}{2} \frac{\mathbf{F}_i(t + \Delta t)}{m_i} \Delta t \quad (2.12)$$

These four steps complete the computation of all the quantities ( $\mathbf{r}_i$ ,  $\mathbf{v}_i$  and  $\mathbf{F}_i$ ) at  $t + \Delta t$ . Then, Equation 2.9 starts again. The half step can be banished by combining together Equations 2.10 and 2.12 giving:

$$\mathbf{v}_i(t + \Delta t) = \mathbf{v}_i(t + \frac{\Delta t}{2}) + \frac{1}{2} \left[ \frac{\mathbf{F}_i(t) + \mathbf{F}_i(t + \Delta t)}{m_i} \right] \Delta t \quad (2.13)$$

## 2.4 LAMMPS code

During this research work, a classical molecular dynamics code called LAMMPS [229] developed by Sandia national laboratory was used. LAMMPS is an acronym that stands for Large-scale Atomic Molecular Massively Parallel Simulator. This software is open source written in C++ language and runs in parallel through a message-passing interface (MPI). It is also adapted to supercomputers with multiple processors making the simulation significantly faster. Technically, LAMMPS is governed by Newton’s equations of motion, supports various potentials, and provides a bunch of options and flavors to perform several kinds of computations. It provides around 70 packages, 210 fixes, and 140 compute commands to calculate various physical quantities (global or local) such as pressure, temperature, and free energy. Supplemental information about setting up LAMMPS is provided in the appendix A.

## 2.5 Global organization of the input script

Any LAMMPS script follows the standard procedure (flow chart) of initialization, equilibration, integration, and finally data production for post-processing. The time consumed to complete these steps is in general linearly (some algorithms gives a  $N \log(N)$  or  $N^2$ ) dependent with respect to the total number of atoms in the simulation box as reviewed in the table 2.1.

Table 2.1: Various computational methods and their scaling with the maximum number of atoms.

Methods	Time scaling	Maximum number of atoms
MD	$O(N)$	$\sim 10^{11}$
Hartree–Fock	$O(N^4)$	$\sim 100$
DFT	$O(N^3)$	$\sim 500$

### 2.5.1 Interatomic potential

A necessary ingredient to perform MD simulation using LAMMPS is the availability of the appropriate fitted empirical potential according to experimental or ab initio data (like the lattice parameter, cohesive energy, bulk modulus, and vacancy formation energy), which means there is no versatile potential. The potential represents the manner that atoms belonging to the ionic pattern feel each other. The interaction has to balance between the simple physics laws of repulsion (at short range), and attraction (at long range) behavior, and eventually faithfully recover the minimum potential corresponding to the equilibrium

state. Since the potential is produced by fitting specific properties for a specific application. For instance, a selected potential describing well mechanical properties does not mean that it will reproduce transport properties. Thus, it's always recommended to check the transferability of the potential you are dealing with because globally the potentials are fitted according to static properties (at  $T = 0$  K) or at finite temperature ( $\propto T$ ). A notable advance has been made to generate a reliable potential for different applications and materials (metals, semiconductors, dielectrics, ceramics, and even for DNA or biophysics). Many potential files are accessible and free to download. A wide potential variety is published in the NIST interatomic repository website [230].

There is a large variety of potentials. Here, we report briefly the most widely used for metallic applications.

- Lennard–Jones potential

This form is among the simplest forms of the pair potentials family. The reason is that it considers only two neutral atoms or molecules interactions and neglects all the other possible combinations. The most known in this range of potential is LennardJones potential [231] defined as:

$$U_{LJ}(r) = 4\epsilon \left[ \left(\frac{\sigma}{r}\right)^{12} - \left(\frac{\sigma}{r}\right)^6 \right] \quad (2.14)$$

Where  $\epsilon$  is the potential well depth,  $\sigma$  is the interatomic distance at which the core-core potential vanishes, and  $r$  is the distance between the two interacting objects (particles, molecules, etc).

- Embedded atom model

The EAM formalism was introduced by Daw *et al* [232] to describe metallic alloys. This approach resembles the mean-field approximation that treats the behavior of electronic effects in ab initio methods. The idea is that the energy of a solid can be written as a unique function of electronic distribution. Indeed, the energy is computed by a contribution of two terms, the embedding part which represents the interaction of every atom of the system with the local electron density of the entire system, and the second part finds its origins in the electrostatic interactions between different atoms [233, 234, 235]. More details can be found in [236], nevertheless, the mathematical expression of the EAM potential is given as:

$$U_{EAM} = \sum_{j<i} U_{ij}(r_{ij}) + \sum_i F_i(\rho_i) \quad (2.15)$$

Where the  $U_{ij}(r_{ij})$  is the pair potential interaction between the atoms  $i$  and  $j$ ,  $F_i(\rho_i)$  is the embedding energy function, and  $r_{ij}$  is the distance between the atoms in the sites  $i$  and  $j$ .

The  $\rho_i$  represents the electron density felt by the atom in the site  $i$  due to the presence of the other atoms in the system. The mathematical expression is just a linear superposition of the valence electrons from the other atoms given as:

$$\rho_i = \frac{1}{2} \sum_{j(\neq i)} \rho_j(r_{ij}) \quad (2.16)$$

Equation 2.15 shows that the EAM potential does not account for angular forces. To overcome this directional bonding drawback another generalization of the EAM type of potential called modified embedded atom model (MEAM) was developed by Baskes *et al* [237, 238].

- Tersoff potential

In general diamond structures such as Si and SiC are characterized by their bond angle and order. Thus, based on this reality Tersoff [239, 240] identified this geometrical atomic configuration impact and has developed a representative potential in the following form:

$$U_{Tersoff} = \frac{1}{2} \sum_{i \neq j} U_R(r_{ij}) + \frac{1}{2} \sum_{i \neq j} B_{ij} U_A(r_{ij}) \quad (2.17)$$

Where  $U_R$  and  $U_A$  represent repulsive and attractive potentials, the  $B_{ij}$  is the bonding between atoms  $i$  and  $j$ .

- Reactive force field

Reactive force field (ReaxFF) potential were first developed by van Duin *et al* [241]. The main originality of this formalism is the dynamic contribution of chemical bonding (bond forming–breaking) to the potential energy, despite the fact that this kind of potential is roughly 10–100 times slower than the previously cited potentials. Technically, to determine the fitting parameters for this ReaxFF potential, ab initio computation must be used. In the concrete case of LAMMPS code different versions of ReaxFF potential are implemented [242, 243, 244].

## 2.5.2 Potential cutoff

The maximum distance applied in a simulation is defined as the cutoff distance  $r_{cut}$ . The choice of the appropriate cutoff distance is very significant. The reason is that if this parameter is wisely defined the computation time cost can be decreased. The main reason for this is due to the characteristic of potential tails becoming negligible at long distances. As a general rule  $r_{cut}$  has to be half the primary box size, otherwise, an atom in the concurrent box will interact with its image which is physically meaningless. In other words, an atom should not feel the presence of the other atoms the beyond the  $r_{cut}$  distance. A typical value can be given for the previously cited potentials, for instance  $r_{cut}$  (LJ) =  $3.2 \sigma$ ,  $r_{cut}$  (EAM) =  $5 \text{ \AA}$ , and  $r_{cut}$  (Tersoff) =  $3 \text{ \AA}$ .

## 2.5.3 Neighbor lists construction

One way to manage the exponential increase of unnecessary calculations in pairwise force calculations is to set a  $r_{cut}$  radius and define a neighbor list.

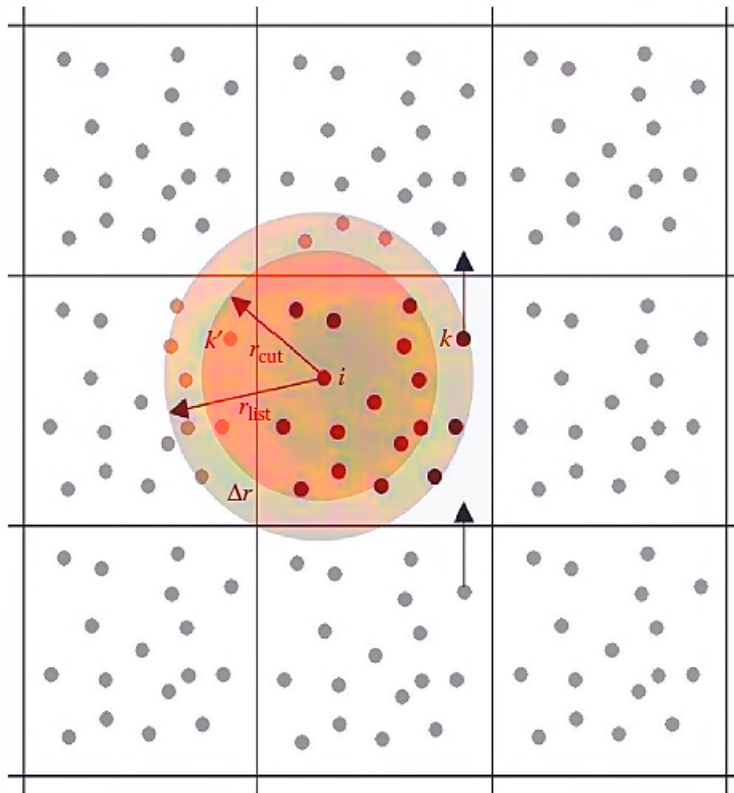


Figure 2.2: Two dimension representation of potential  $r_{cut}$  and  $r_{list}$  radius under periodic boundary conditions. Adopted from [221].

In this technique, a 3D sphere of radius  $r_{list}$  ( $r_{list} \sim 1.1 r_{cut}$ ) is drawn around each atom as shown in Figure 2.2. A list of neighbors is established within the

circle. Once a particle leaves the  $r_{cut}$  radius and the skin depth ( $r_{skin} = r_{list} - r_{cut}$ ), an update of the neighbor list is triggered to compute the particle's total force.

#### 2.5.4 Timestep

The discretization time  $\Delta t$  mentioned in Equation 2.3 is known in most of the MD simulations as timestep. The suitable value is the femtosecond (fs) range which is the scale of the atomic bond vibration. To complete the simulation in a reasonable amount of time, a compromise is recommended regarding the time step. On the one hand, it has to be small enough such that the computation performed would be accurate. On the other hand, not too large to prevent overgoing fluctuation signs of instability.

#### 2.5.5 Boundary conditions

Boundary conditions define the manner in which the neighborhood is organized on the edge of the simulation box following each direction. The simplest image of boundary condition is whether a particle is going to disappear or instantly reappear from the other side when it crosses the simulation box. There are mainly four styles of boundary conditions in LAMMPS:  $p$  stands for periodic which means that the atoms within a simulation box are allowed to cross the box boundary and reenter from the other side. On the contrary, in the case of non-periodic conditions, if a particle crosses the box borders, it disappears. Three types are available in this case:  $s$  (free surface) the surface position is set to encompass the atoms in that dimension, no matter how far they move. Fixed abbreviated by  $f$  where this rigid condition act as a wall and does not move with time but if an atom moves outside the face it will be deleted, and  $m$  is similar to  $s$ , however, it allows small displacements of atoms in response to forces exerted on the cell.

#### 2.5.6 Thermodynamic ensembles

A thermodynamic ensemble provides an elegant way to derive the basic properties of a realistic thermodynamic system. Depending on constraints applied to a given system, different degrees of freedom may be considered. In contrast, a completely isolated system is best described by the microcanonical ensemble; on the other hand, a completely opened system to the outside world is well described by the grand canonical ensemble, and the isothermal-isobaric ensemble can be used to describe an amorphous system as we shall see in the following chapters. There

is no specific rule for choosing an ensemble. The only thing we need to consider is that the ensemble needs to represent the physical reality we want to describe.

Table 2.2: The different statistical ensembles implemented, used in MD simulation and the main physical property computed by LAMMPS.

Abbreviation	Statistical ensemble	Thermodynamic description
NVT	canonical	equilibrium volume and temperature
NPT	isothermal-isobaric	equilibrium pressure and temperature
NVE	microcanonical	equilibrium volume and total energy
$\mu$ VT	grand canonical	equilibrium volume and temperature

In order to update the atom’s positions, velocities, and forces, the Equation of motion must be time integrated with the appropriate statistical ensembles. There are different possibilities implemented in LAMMPS as summarized in the table 2.2.

### 2.5.7 Build of the initial structures

To start an MD simulation, the initial atomic configuration has to be provided. Plenty of ways exist to achieve this, depending on the complexity of the system. Thus, if the initial structure is a simple common crystallographic structure such as BCC, FCC, HCP, or diamond a possibility to do it with LAMMPS exists. However, if the structure is more complex (Insert specific defects, dislocation, voids, change the crystallographic orientation, build nanotube, etc.) LAMMPS permits the reading of external structures customized with specific software like ATOMSK [245] or simply find the Crystallographic Information File (CIF) available in several websites [246, 247, 248] and use after converting it to LAMMPS structure input format. Moreover, we have to pay attention that an additional step has to be performed before any concrete MD simulation. The aim of Molecular Statics (MS) computation is to drive the atoms to their minimal potential energy. The most used method for such computation in LAMMPS is the conjugate Gradient Method (CGM) [249].

## 2.6 Two temperature model

The major convenient mathematical model widely used in the computational physics community to manage laser-matter interaction at an atomistic scale is the Two Temperature Model (TTM) introduced by Anisimov *et al* [85]. In reality, the theoretical formulation of this model is based on coupling the diffusion equations for electrons and the lattice with the electron-phonon coupling term.

Once the energy dose is deposited by the ultrafast laser, two distinct mechanisms linked to ions and electrons are activated (at least for metals and a large part of semiconductors).

The electron–electron scattering process [250] due to the absorbance of photons by the electrons with a typical time of  $\sim 1$  ps. The second process is the electron–phonon scattering [251, 252] resulting to balance the energy difference between the hot electron and cold ions with a typical time of roughly  $\sim 10$  ps. Thus, the model combines these two phenomena and translates them into two coupled differential equations:

$$\begin{cases} C_e(T_e)\frac{\partial T_e}{\partial t} = \nabla(\kappa_e(T_e, T_a)\nabla T_e) - G(T_e)(T_e - T_a) + Q_{laser}(\vec{r}, t) \\ C_a(T_a)\frac{\partial T_a}{\partial t} = \nabla(\kappa_a(T_a)\nabla T_a) + G(T_e)(T_e - T_a) \end{cases} \quad (2.18)$$

Where  $C_e(T_e)$ ,  $C_a(T_a)$  are the heat capacity and  $\kappa_e$ ,  $\kappa_a$  are the thermal conductivity of the electrons and the lattice respectively. The  $G(T_e)$  is the electron-phonon coupling factor.  $T_e$ ,  $T_a$ ,  $Q_{laser}$  represent electronic, ionic temperatures and is the external source term corresponding to the energy brought by the laser source.

The challenge to proceed to the next step which is the modeling with LAMMPS is the prior knowledge of the electronic properties of the concerned material invoked above ( $C_e(T_e)$ ,  $\kappa_e(T_e)$  and  $G(T_e)$ ). Thus, either we collect experimental data or use first principles calculation in the framework of the Density Functional Theory (DFT). The ABINIT package is suitable to handle such computations [253]. The electronic heat capacity is computed as follows:

$$C_e(T_e) = \int_{-\infty}^{\infty} g(\epsilon) \frac{\partial f(\epsilon, \mu, T_e)}{\partial T_e} d\epsilon \quad (2.19)$$

Where  $g(\epsilon)$  is the electron density of states at the energy level  $\epsilon$ ,  $\mu$  the chemical potential at  $T_e$  and  $f(\epsilon, \mu, T_e) = [\exp((\epsilon - \mu)/(k_B T_e)) + 1]^{-1}$  is the Fermi distribution function.

The free electron model is justified to describe noble metals in a non-equilibrium state. The mathematical derivation is described in [254]. The heat capacity of the electrons is approximated with Sommerfeld expansion:

$$C_e(T_e) = \gamma T_e \quad (2.20)$$

Where  $\gamma = \frac{\pi^2 N_e k_B}{2T_f}$  if  $T_e \ll T_f = \frac{E_f}{k_B}$ ,  $N_e$ ,  $T_f$ ,  $k_B$ ,  $E_f$  are the density of electrons, the Fermi temperature, the Fermi energy and the Boltzmann constant respectively.

Many physical and chemical processes are due to the emission of hot electrons caused by the laser excitation of metals. In the same scope, thermal expansion has two main origins: the thermal pressure and the inharmonicity of the ion-ion interaction, especially at high temperatures. The stress  $\sigma_e$  created by the electrons can be computed according to the following equation:

$$\sigma_e = -\gamma_e \int_{T_0}^{T_e} C_e(T) dT \quad (2.21)$$

Where  $\gamma_e$  is the Grüneisen constants,  $T_0$  is the ambient temperature,  $T_e$  is the electronic temperature and  $C_e$  is the electronic heat capacity.

The number of electron is computed as:

$$N_e = \int_{-\infty}^{\infty} f(\epsilon, \mu, T_e) g(\epsilon) d\epsilon \quad (2.22)$$

The electron-phonon coupling factor is calculated as:

$$G(T_e) = -\frac{\pi \hbar k_B \lambda \langle \omega^2 \rangle}{g(\epsilon_F)} \int_{-\infty}^{\infty} g^2(\epsilon) \frac{\partial f(\epsilon, \mu, T_e)}{\partial \epsilon} d\epsilon \quad (2.23)$$

Where  $\langle \omega^2 \rangle$  is McMillan's second moment of the phonon spectrum and  $\lambda$  is the electron-phonon mass enhancement parameter. We have to note that the electron-phonon coupling factor  $G$  is assumed as a constant value as first-order approximation.

Performing laser-matter simulations requires knowledge of thermal conductivity. This quantity dictates the behavior of the thermal diffusion (spread or confinement of energy) through the material. This quantity is divided into two contributions: lattice thermal and electronic. It is electronic temperature dependent, thus an ab initio approach is appropriate for determining this property. To do so, the Kubo-Greenwood formalism implemented in the framework of DFT allows the determination of the Onsager coefficients which permit the numerical determination of the thermal conductivity [255]. Generally, for MD simulation studies purposes the thermal conductivity is obtained by Wiedmann-Franz Law [254, 256]. This semiclassical approximation treatment states that the ratio of

electrical conductivity  $\sigma$  and thermal conductivity  $\kappa_e$  is proportional to the electronic temperature as shown in Equation 2.24.

$$\frac{\kappa_e}{\sigma} = L_0 T_e \quad (2.24)$$

Where  $L_0$  is a constant value known as the Lorenz number defined by:

$$L_0 = \left( \frac{k_B}{e} \right)^2 \frac{\pi^2}{3} \quad (2.25)$$

Here  $k_B$  is the Boltzmann constant and  $e$  is the electronic charge.

Some other phenomenological formula proposed by Inogamov *et al* [257] are also widely used in TTM-MD model to fulfill the low and high temperature asymptotic behavior of  $\kappa_e(T_e)$ . The low temperature part ( $T_e \ll T_f$ ) is covered by the Drude theory as given by Equation 2.26.

$$\kappa_e(T_e) = \frac{1}{3} v_F^2 C_e(T_e) \tau_e \quad (2.26)$$

Where  $v_F^2$  is Fermi velocity,  $C_e(T_e)$  electronic specific heat, and  $\tau_e$  the relaxation time. At  $T_e \ll T_f$  the specific heat is given by Equation 2.20, thus the relaxation time is given as:

$$\frac{1}{\tau_e} = A_1 T_e^2 + A_2 T_a \quad (2.27)$$

Here  $A_1$  and  $A_2$  are fitting parameters, thus it is obvious that the accuracy of Equation 2.27 depends on the right determination of parameter  $A_1$  and  $A_2$ . Finally, the  $\kappa_e(T_e)$  takes the form given in Equation 2.28.

$$\kappa_e(T_e) = \frac{1}{3} v_F^2 \frac{\gamma T_e}{A_1 T_e^2 + A_2 T_a} \quad (2.28)$$

## 2.7 TTM-MD implemented in LAMMPS

Despite that the TTM model described in Equation 2.18 considers electrons, it has some limitations including thermoelastic stress. The idea of combining atomistic ionic and continuum electron subsystems led to the construction of a hybrid model. Several earlier works have been done to implement this approach for atomistic investigations. We can mention Ivanov *et al* [87], Schäfer *et al* [258], Hakkinen *et al* [259], Finnis *et al* [260], yuan *et al* [261] and Ullah *et al* [262].

The idea behind this hybrid coupling is to replace the second equation (describing the evolution of the ion) in 2.18 by classical force field molecular dynamics combined with an inhomogeneous finite heat reservoir modeled as a continuum on a regular grid characterizing electrons. The algorithm implementing this fix was derived from a cascade simulation where a primary knock-on atom (PKA) was initialized with a high velocity to simulate a radiation effect [263]. The fundamental TTM-MD equations ruling the behavior of a system under the ultrafast pulse is performed using the USER-MISC package [264] as described in Duffy *et al* [265] and Pisev *et al* [266]. This LAMMPS package accounts for electronic effects and provides the implementation of the TTM-MD hybrid method expressed in Equation (2.29):

$$m_j \frac{\partial v_j}{\partial t} = -\nabla_j U(r_1, \dots, r_n) + F_j^{lang}(T_e - T_a) - \frac{\nabla P_e}{n_i} \quad (2.29)$$

Where  $m_j$  and  $v_j$  are respectively the mass and velocity of the  $j^{th}$  atom,  $-\nabla_j U(r_1, \dots, r_n)$  is the force produced by the empirical potential.  $P_e$  is the electronic pressure, and  $n_i$  is the ion's density.  $T_a$ ,  $T_e$  represent the ionic and electronic temperature respectively. The  $t$ ,  $r$  represent the considered time and position, and the  $F_j^{lang}$  is the random force due to the electron-phonon coupling defined as:

$$F_j^{lang}(t) = -\gamma_i m_i v_i + \tilde{F}(t) \quad (2.30)$$

$$\begin{cases} \gamma_i = \gamma_p + \gamma_s & \text{for } v_i > v_0 \\ \gamma_i = \gamma_p & \text{for } v_i \leq v_0 \end{cases} \quad (2.31)$$

$\gamma_p$ ,  $\gamma_s$  and  $v_0$  represent the electron-phonon contribution coefficients, electron-stopping and threshold velocity due to the electron-stopping interaction respectively.  $\tilde{F}(t)$  is a random stochastic force term that is determined by the local electronic temperature.

Furthermore, the mathematical expression of both  $\gamma_p$ ,  $\gamma_s$  is computed by simple manipulation and assumptions. If we assume that the energy loss of an atom  $i$  with velocity  $v_i$  at each timestep with value  $\Delta t$  due to a friction force  $F_i$  is  $\Delta U_i$  [267, 268], the expression describing  $\Delta U_i$ :

$$\Delta U_i = F_i v_i \Delta t = \gamma_i v_i^2 \Delta t \quad (2.32)$$

In a cell grid  $j$  with constant  $T_e$ , the total energy loss is :

$$\Delta U_{loss} = \Delta t \sum_{i \in j} \gamma_i v_i^2 = \Delta t \sum_{i \in j} \gamma_p v_i^2 + \Delta t \sum_{i' \in j} \gamma_s v_i'^2 \quad (2.33)$$

On the other hand, the energy gain of the electronic system at each timestep is given as:

$$\Delta U_{gain} = G_p T_a \Delta V \Delta t + G_s T_a' \Delta V \Delta t \quad (2.34)$$

The conservation of energy impose  $\Delta U_{gain} = \Delta U_{loss}$ , leading to the expression:

$$\begin{cases} \sum_{i \in j} \gamma_i v_i^2 = G_p T_a \Delta V \\ \sum_{i' \in j} \gamma_s v_i'^2 = G_s T_a' \Delta V \end{cases} \quad (2.35)$$

It becomes from the previous Equations 2.33, and 2.34:

$$\begin{cases} \frac{3}{2} k_B T_a = \frac{1}{N} \sum_{i \in j} m v_i^2 \\ \frac{3}{2} k_B T_a' = \frac{1}{N'} \sum_{i' \in j} m v_i'^2 \end{cases} \quad (2.36)$$

Finally:

$$G_p = \frac{3N k_B \gamma_p}{\Delta V m_i} \quad (2.37)$$

$$G_s = \frac{3N' k_B \gamma_s}{\Delta V m_i} \quad (2.38)$$

$N$  is the total number of atoms inside the electronic grid cell  $j$  with a volume  $\Delta V$ ,  $N'$  is the total number of atoms involved in the electronic stopping which satisfies the condition  $v_i > v_0$ ,  $k_B$  is the Boltzmann constant,  $V$  is the electronic grid volume, and  $m$  is the atomic mass of the species used.

Actually, we know from [265] that the electronic stopping power is proportional to the ion velocity as described in the following equation:

$$\frac{dE}{dx} = \nu E^{1/2} \quad (2.39)$$

$$m \frac{du}{dt} = \nu \left(\frac{m}{2}\right)^{1/2} u \quad (2.40)$$

$$\gamma_s = \nu \left(\frac{m}{2}\right)^{1/2} u \quad (2.41)$$

$\nu$  is a proportionality constant determined from the Lindhard and Scharff model [269], and  $m$  is the mass.

The  $\tilde{F}(t)$  is a random force giving the effect of noise verifying the fluctuation-dissipation theorem [270, 169].

$$\begin{cases} \langle \tilde{F}(t) \rangle = 0 \\ \langle \tilde{F}(t)(t') \cdot \tilde{F}(t) \rangle = 2k_B T_e m_i \gamma_p \delta(t' - t) \end{cases} \quad (2.42)$$

Where  $k_B$  is the Boltzmann constant,  $m_i$  is the atomic mass of the used species, and  $\delta(t' - t)$  is the step function.

The electronic subsystem is modeled by a one-dimensional heat diffusion equation following the  $x$  direction with an external heat source:

$$C_e(T_e) \frac{\partial T_e}{\partial t} = \nabla(\kappa_e(T_e) \nabla T_e) - G_p(T_e - T_a) + \frac{I(t)e^{-x/l_p}}{l_p} \quad (2.43)$$

Where  $\kappa_e(T_e)$  is the electronic thermal conductivity,  $C_e(T_e)$  the electronic specific heat,  $G_p$  electron-ion coefficient, and  $I(t) = I_0 e^{-x/l_p}$  is the external absorbed intensity following Beer-Lambert law [271]. The equivalent absorbed laser fluence is defined as  $F_{\text{abs}} = I \cdot \tau$  with  $\tau$  the pulse duration and  $l_p$  the penetration depth.

In this LAMMPS package, the electronic specific heat is fitted according to Equation 2.44 as:

$$C_e(X) = C_0 + (a_0 + a_1 X + a_2 X^2 + a_3 X^3 + a_4 X^4) e^{-(AX)^2} \quad (2.44)$$

Where  $C_0$ ,  $a_0$ ,  $a_1$ ,  $a_2$ ,  $a_3$ ,  $a_4$ ,  $A$  are the corresponding fitting parameters and  $X = T_e/1000$ .

An electron pressure contribution  $P_e(T_e) = BC_e(T_e)T_e$  is expected to induce a blast force in the computation according to Equation (2.29), with  $B$  a material-dependent constant. From the previous considerations, the electronic pressure gradient is calculated near the surface [266] as:

$$\nabla_x P_e(T_e) = \left[ \frac{C_e(T_e)T_e \lambda}{(x + \lambda)^2} + \frac{x}{x + \lambda} + \frac{C_e(T_e)_{x+\Delta x} - C_e(T_e)_x}{\Delta x} \right] \quad (2.45)$$

Where  $x$  is the coordinate measured from the instantaneous surface position, and  $\lambda$  is the effective electron mean free path.

A proper description of systems thermodynamics is provided by the  $\kappa_e(T_e)$ . In fact, to feed the simulation model, the LAMMPS package considers that there is a linear relation between conductivity and electronic-specific heat based on the physical observation that thermal conductivity does not decrease with electronic temperature (at least in the case of metals) following relation:

$$\kappa_e(T_e) = D_e C_e(T_e) \quad (2.46)$$

For the smooth and correct implementation of the concurrent model, an appropriate stability criterion  $n_{stability}$  which depends on the initial electronic properties used for the modeling was established and defined according to Equation 2.47.

$$n_{stability} \geq \frac{2 \Delta t \kappa_e}{v_{grid} C_e} \quad (2.47)$$

Where  $\Delta t$  is the MD timestep,  $v_{grid}$  the elementary volume of the electronic meshing,  $\kappa_e$  electronic conductivity, and  $C_e$  the minimal electron heat capacity.

This ttm/mod fix in MISC LAMMPS package is only compatible with metal units. For the smooth running of the previous computation, all the previous quantities need to be put in the units mentioned in the 2.3.

Table 2.3: Summary of all physical input properties units used to model an ultrafast laser irradiation of materials interaction.

Parameter	Physical meaning [unit]
$C_e$	electronic specific heat [ $eV/(e^- \text{\AA}^3 \text{K})$ ]
$D_e$	electronic thermal diffusion coefficient [ $\text{\AA}^2/\text{ps}$ ]
$\gamma_p$	friction due to the electron-ion [ $g/(mol \text{ ps})$ ]
$\tau$	pulse duration [ps]
$I_0$	absorbed laser pulse intensity [ $eV/(\text{\AA}^2 \text{ ps})$ ]
$l_p$	depth of skin layer [ $\text{\AA}$ ]

In the following studies, I utilized a DFT computed  $C_e(T_e)$  for crystalline structures  $B_2$  and  $C11_b$  to determine their electronic specific heat at varying electron temperatures. However, for the amorphous counterpart. I employed the Sommerfeld expansion to investigate its electronic specific heat. As for the

electron–phonon coupling factor,  $G(T_e)$ , a constant value obtained from experimental data was utilized. In determining the electronic thermal conductivity,  $\kappa_e(T_e)$ , I employed equation , where  $D_e$  is a constant value at 300 K. This equation allowed to accurately calculate the electronic thermal conductivity of the system at different electron temperatures, providing valuable insights into the system’s behavior.

## 2.8 Post-processing of LAMMPS output data with OVITO

After an MD simulation using LAMMPS, various data of each atom (position, velocity, energy, pressure, temperature, etc.) are stored. The energetic and thermodynamic quantities output obtained are accessed in several manners, including from a simple print into the file, time-binning averages, or dump files to construct movies of the system behavior which are visualized through various software such as OVITO [272], Para-View [273] and VMD [274].

OVITO stands for Open Visualization Tool [275]. It is a versatile scientific visualization tool developed by Stukowski at the University of Darmstadt that is frequently used to visualize numerical results and post-process classical molecular dynamics results. In addition to the coupling with Python which facilitates analyzing data, a bunch of structural analysis algorithms is implemented to investigate and identify the local structure (crystalline, amorphous, liquid) as discussed in the following sections.

### 2.8.1 Radial distribution function

The radial distribution function (RDF) measures the probability of finding a particle at a distance  $r$  with respect to a reference atom. The analysis of the  $g(r)$  function is the most common method to check whether the structure is in a crystalline, amorphous, or liquid phase as shown in Figure 2.3.

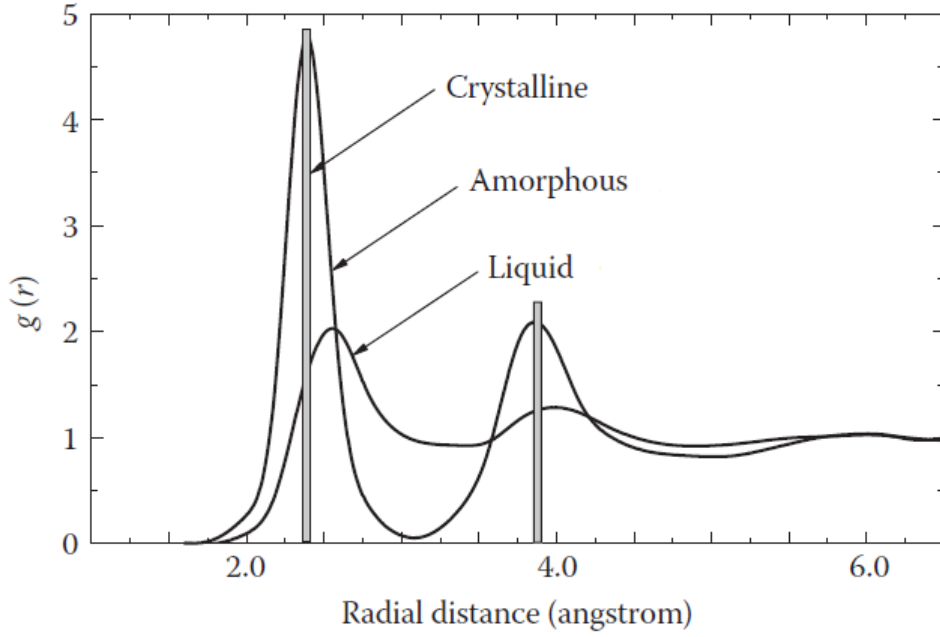


Figure 2.3: A typical evaluation of the radial distribution function RDF functions of the different possible phases of crystalline, amorphous, and liquid. Adopted from [221].

The general expression to compute the  $g(r)$  function is given by the following equation:

$$g(r) = \frac{V}{N^2} \left\langle \sum_{i=1}^n \frac{n(r)}{4\pi r^2 \Delta r} \right\rangle \quad (2.48)$$

$V$  is the volume,  $N$  is the number of atoms, and  $n(r)$  is the number of particles that can be found in the shell between  $r$  and  $r + \Delta r$ .

For systems with more than one kind of atom, another interesting flavor of RDF known as partial radial distribution function (PRDF) is computed. For a binary substance with two atoms labeled as  $\alpha$  and  $\beta$  Equation 2.48 is given as:

$$g_{\alpha\beta}(r) = \frac{V}{N_{\alpha}N_{\beta}} \left\langle \sum_{i=1}^{N_{\alpha}} \frac{n_{i\beta}(r)}{4\pi r^2 \Delta r} \right\rangle \quad (2.49)$$

$n_{i\beta}(r)$  represents the number of  $\beta$ -type particles located in a spherical shell of thickness  $\Delta r$  at the distance  $r$  from a  $\alpha$ -type particle. The  $N_{\alpha}$  and  $N_{\beta}$  are respectively the total number of  $\alpha$  and  $\beta$ -type particles in the system.

## 2.8.2 Common Neighbor Analysis

Common Neighbor Analysis algorithm (CNA) categorizes the crystal structures in the material according to the disposition of atoms and the topology of bonds

around a referent atom [276, 277]. For each atom, CNA locates the  $N$  nearest neighbors defined by a cutoff distance which depends on the perfect crystal structure. Three quantities are calculated: the number of neighbors with respect to the central atom and its nearest neighbors that they share in common  $n_{cn}$ , the total number of bonds connecting these common neighbors  $n_b$  and the number of bonds in the longest chain of bonds connecting these common neighbors  $n_{1cb}$ . These three numbers, which are recorded as a triplet  $(n_{cn}, n_b, n_{1cb})$  for all  $N$  nearest neighbors form the signature characterizing the local structure around the central atom. For instance, an FCC crystal for which  $N = 12$  have  $(n_{cn}, n_b, n_{1cb}) = (4, 2, 1)$  for all 12 nearest neighbors, while a BCC crystal for which  $N = 14$  should have  $(n_{cn}, n_b, n_{1cb}) = (6, 6, 6)$  for 8 nearest neighbors. This algorithm implementation in OVITO is described in detail [278]. Atoms are classified according to their atomic structures from 0 to 4, depending on the number of matching atoms. The numbers 0, 1, 2, 3, and 4 correspond respectively to the liquid or amorphous structures, face-centered cubic, hexagonal close-packed, body-centered cubic, and icosahedral.

### 2.8.3 Polyhedral Template Matching

The Polyhedral Template Matching (PTM) is another structural analysis algorithm particularly useful when a noticeable thermal effect is present in the analyzed simulation box [279]. Additionally, it provides additional information besides local structures, such as crystal orientation, elastic deformation gradient, and strain. Unlike the CNA analysis, the numbers are classified as follows: 0, 1, 2, 3, 4, 5, 6, 7, and 8. These correspond to liquids or amorphous structures, face-centered cubic, hexagonal close-packed, body-centered cubic, icosahedral, simple cubic, Cubic diamond, Hexagonal diamond, and graphene, respectively.

### 2.8.4 Construct surface mesh

OVITO offers the capability to construct surface and volume meshing by displaying a 3D shape manifold as shown in Figure 2.4. Concretely, this algorithm generates a geometric description of the inner and outer boundaries of an atomistic solid in terms of a triangulated surface mesh as described in [280]. This visualization is useful for quantifying the formation of voids within the materials, detecting surfaces and interfaces, as well as measuring porosity.

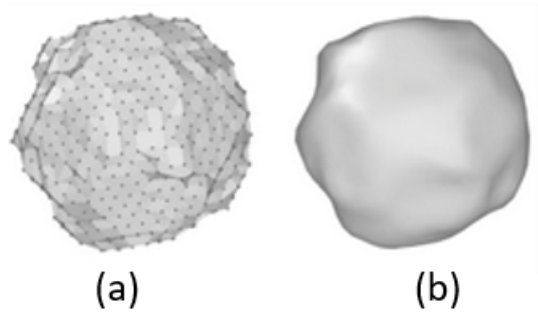


Figure 2.4: (a) The output data triangulated the surface mesh of a nanoparticle. (b) Final surface after the smoothing process. Adopted from [281].

The results of the triangulated output data are displayed in Figure 2.4(a). Our study employs a variation of a previous method called the alpha-shape method. In this method, a sphere of radius  $r_{probe}$  is selected as a probe and compared to a Delaunay sphere. Based on this comparison, the algorithm determines which regions are part of the enclosed empty space. The final surface mesh of a nanoparticle, after undergoing a smoothing process, is presented in Figure 2.4(b).

### 2.8.5 Wigner-Seitz defect analysis

The Wigner-Seitz defect analysis (WSDA) identifies point defects (vacancies and interstitials) in crystalline structures. Technically, this algorithm needs two configurations, the reference which is generally the perfect crystal where every site is occupied by one atom, and the final structure that you suspect that it hosts defects as shown in Figure 2.5.

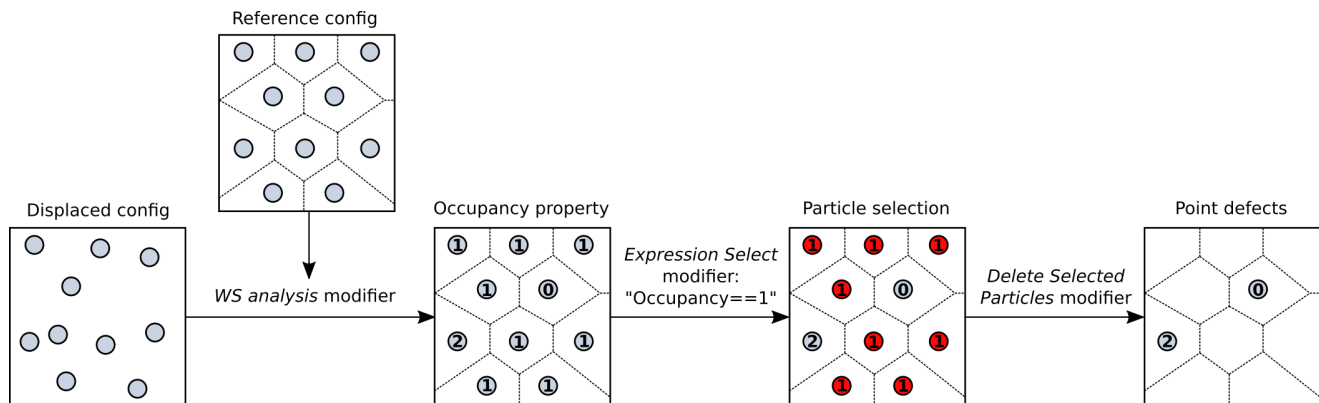


Figure 2.5: A typical workflow of Wigner-Seitz defect analysis to identify point defects (vacancies and interstitials) in the structures [282].

The algorithm considers the atoms of the reference as a site and those of the final one as normal atoms. Mathematically, an integer number is assigned to each site. This means that if no atoms of the final structure are detected in the

sites a zero is assigned meaning that a vacancy is present. On the other hand, if a site is occupied with more than one atom it is considered as interstitial and an integer of 2, 3, and so forth is attributed.

OVITO has the ability to differentiate between monoatomic and alloy structures by analyzing the elemental composition of the particles within a simulation. An alloy is a substance made up of two or more chemical elements, while a monoatomic system is made up of particles composed of a single chemical element. The algorithms that precede OVITO are primarily intended to detect crystallographic structures within monoatomic systems, such as FCC, BCC, HCP, and others.

OVITO has a useful feature that enables users to visualize the chemical composition of a system via a color-coding scheme. This feature allows for the easy identification of different elements within simulation data, as well as the ability to monitor their behavior over time. However, OVITO is limited in its ability to identify complex crystallographic structures such as B<sub>2</sub> or C11<sub>b</sub>. To overcome this limitation, the algorithms are applied to each sub-lattice system, which ultimately builds the full atomic alloy brick. The final crystallographic structure, such as C11<sub>b</sub>, is achieved by combining the FCC and BCC sub-systems in a particular way that ensures they are colored in the same manner to avoid any confusion.

### 2.8.6 Entropy

There is one interesting property that can be used to distinguish the fingerprints of ordered (crystalline) and disordered (amorphous) environments: entropy and is computed using the formula described in [283, 284]. For an atom,  $i$  is the entropy is computed as:

$$S_S^i = -2\pi\rho k_B \int_0^{r_m} [g(r)\ln(g(r)) - g(r) + 1]r^2 dr \quad (2.50)$$

Where  $r$  is a distance,  $g(r)$  is the radial distribution function of atom  $i$  and  $\rho$  is the density of the system.

The  $g(r)$  computed for each atom  $i$  can be noisy and therefore it is smoothed according to:

$$g_m^i(r) = \frac{1}{4\pi\rho r^2} \sum_i \frac{1}{\sqrt{2\pi\sigma^2}} \exp\left(-\frac{(r - r_{ij})^2}{2\sigma^2}\right) \quad (2.51)$$

The  $g(r)$  computed for each atom  $i$  can be noisy and therefore it is smoothed according to: with  $j$  goes through the neighbors of atom  $i$ , and  $\sigma$  is a parameter to control the smoothing.

## 2.9 Summary conclusion

There was a discussion of the MD paradigm and several simulation ingredients, especially the interatomic potential and its impact on simulation dynamics. It was revealed and discussed in detail the theoretical approaches used in this case, namely the TTM-MD model implemented in the LAMMPS package. Moreover the general organization of the LAMMPS program and the input required to perform MD computation was exposed. The importance of the simulation box, the integration time and the appropriate thermodynamic ensemble is stressed. We exposed the different tools used to build the initial crystal structures. The different electronic parameters relevant to laser-matter interaction were discussed and the validity of the approximations was demonstrated. In addition, since the data from the MD was visualized and analyzed, various features of OVITO software and the advantages of several involved algorithms were established.

# Chapter 3

## Phase transition in crystalline and amorphous CuZr alloys

### 3.1 Introduction

Upon ultrafast laser structuring process light is temporally confined allowing photoexcitation of band gap materials and quasi-isochoric heating of metallic or semi-metallic materials [285]. At the same time, beam focusing and polarization manipulation allows the energy concentration at the nano-scale [286]. Significant results evidenced that phase transformation can be triggered in material alloys, implying both glasses and crystalline materials [287, 288, 289, 290]. Subpicosecond laser irradiation shorter than electron–phonon relaxation time is able to cause structural distortion in solid lattices, inducing order–disorder changes in covalently bonded materials [291, 292], metal–insulator transitions [293, 294]. The typical martensitic transformation is the face–centered–cubic to body–centered–cubic transformation in steels [295]. Martensite structural changes occur in shape memory alloys, and in pure elements such as tantalum and titanium [296, 297], where a body–centred–cubic to hexagonal–close–packed transformation is observed [298]. Besides, femtosecond (fs) irradiation of titanium alloys that revealed the opportunity to tune the structural states of surface, through a laser-driven  $\alpha$  to  $\beta$  phase transformation related to the combined effect of ultrafast heating and cooling or strong shock waves [299]. Recent theoretical predictions highlighted that direct solid–solid transition can be transiently triggered in pure metals by ultrafast laser due to the strong coupling between electronic and ionic structures but remains to be experimentally confirmed for permanent crystalline states [300, 301]. Metallic glasses, usually formed by liquid quenching, have shown the capability for undergoing crystallization during molding on the micrometer ( $\mu\text{m}$ ) to nanometer (nm) scale owing to the low viscosity in the supercooled liquid state [302]. This behavior remains unexplored in

response to ultrashort laser irradiation.

In this work, we employed atomistic modeling to investigate the laser-induced architecturation of CuZr alloys based on the work [303]. This reveals how mechanical stress induced by the shock wave affects the structural features and the stability of certain compositions. The energy dynamics of the photoexcited solid are investigated by employing the Two Temperature Model (TTM) [304]. This approach is used to describe the thermal diffusion and the energy transfer from the excited electrons to the colder lattice under an electron–phonon exchange. In order to understand the response to this swift heating, it is necessary to couple the TTM to classical hydrodynamics or Molecular Dynamics (MD). TTM-MD has successfully been implemented to provide insights on phase transition [265, 263], defect formation [101, 112] or laser-ablation mechanisms [87]. Most of the reported works used MD approaches and explored the interaction of an ultrafast laser with pure metals as Al [110], Cr [107], Cu [305] and Au [306], semiconductors as Si [307] or even graphite [308]. A first attempt to understand the behavior of a CuZr under an ultrafast laser pulse was reported in [208] but no phase transitions were detected especially in the crystalline states.

The choice of a CuZr system is not fortuitous, because in its amorphous state this Metallic Glass (MG) plays a fundamental role in advanced material engineering, from biomedical applications for antimicrobial properties [309] to metallurgy and anticorrosion properties [310]. Recently, this kind of amorphous system was irradiated by ultrafast laser for surface nanostructuring applications [311, 312]. Single-shot ultrafast laser interaction with metallic alloys were investigated in nanostructuring conditions far from equilibrium conditions. Unusual phase transformation emerges in the subsurface region of the ultrafast-irradiated target. Phase transitions are expected to originate from atomic rearrangements either due to thermoelastic stresses [313, 314, 114] in response to the propagation of the pressure wave throughout the system or during the solidification process that proceeds under high undercooling conditions [102, 315, 112]. This chapter aims to settle the relative role of both processes by focusing on the CuZr binary alloys with different compositions in both crystal and their equivalent amorphous counterparts structures, in particular the  $\alpha$ -Cu<sub>50</sub>Zr<sub>50</sub> and  $\alpha$ -Cu<sub>33.3</sub>Zr<sub>66.7</sub>. The results demonstrated that phase stability upon laser pulse and microstructural transformations depend strongly on the initial crystallographic structure. The semiempirical potential used to model the vitrification of the Cu-Zr alloys confirms that the initial concentrations (50 % and 66.7 % of Zr) are stable and lead

to a reasonable agreement with the experimental and phase diagram observations [316]. In contrast, the thermodynamical response is substantially different for amorphous systems irradiated by similar laser conditions. A solid-liquid transition was observed in the amorphous samples. However, no solid-solid (meaning amorphous–crystalline) structural transformation was noticed for the evaluated stoichiometry as MG accommodates the distortion even in the lack of long-range translational order maintaining mechanical stability.

## 3.2 CuZr metallic glasses samples elaboration

### 3.2.1 Determination of the theoretical melting temperatures

The purpose of this section is to explain how to compute an extremely crucial property which is the melting point in order to investigate laser-matter interaction. This quantity is discussed because it is involved in the different process during the laser energy deposition and beyond during solidification. Herein, we present briefly the most used methods in the community to compute  $T_m$  mainly for metallic targets that can be extended to semiconductors and dielectrics. Generally, the determination of  $T_m$  is not straightforward but rather an accumulation of several MD simulations is needed. Indeed, from a pure thermodynamics point of view, the  $T_m$  corresponds to the temperature where a solid-liquid phase coexists as described in the method known as thermodynamics integration developed by Frenkel *et al* [317]. The Gibbs free energy of the solid and liquid phases in the system is defined as  $G_S = G_L$ , with  $G_i = U_i + PV - TS_i$ , where  $U_i$  is the internal energy,  $P$  represents pressure,  $V$  the volume,  $T$  the temperature, and  $S_i$  the entropy. This is expressed in Equation 3.1 as:

$$\frac{G_i}{T_m} = \frac{G_i}{T_m} - \int_{T_0}^{T_m} \frac{E(t) + PV(t)}{t^2} dt \quad (3.1)$$

Here,  $T_0$  refers to the temperature of the initial system,  $E(t)$  represents its internal energy,  $V$  represents the volume, and  $P$  is the pressure computed by MD for a range of temperatures.

Another widely used manner to define the  $T_m$  is known as the hysteresis method, which has two variants: one and two phases [318]. This approach consists of heating the system above the melting temperature and the abrupt change in the potential energy (or volume) is defined as  $T_+$ . In the same way, we subject the system to a cooling process below  $T_m$  and the slope change of the poten-

tial energy is labeled as  $T_-$ . Finally, the melting temperature is obtained by employing Equation 3.2 as:

$$T_m = T_+ + T_- - \sqrt{T_+ T_-} \quad (3.2)$$

This last method (which is used in chapter 5) is based on a single-phase approach in which the system is simply heated from its solid to a liquid state. The melting temperature corresponds to the abrupt change in the potential energy of the system as described in [319, 320].

### 3.2.2 Melting temperature of the $B_2\text{-Cu}_{50}\text{Zr}_{50}$ and $C11_b\text{-Cu}_{33.3}\text{Zr}_{66.7}$ structures

The melting temperature  $T_m$  was computed for  $B_2\text{-Cu}_{50}\text{Zr}_{50}$  (CsCl prototype) and  $C11_b\text{-Cu}_{33.3}\text{Zr}_{66.7}$  (MoSi<sub>2</sub> prototype) crystalline structures. To accomplish this purpose, we have used the Embedded Atom Model (EAM) interatomic potential developed for CuZr systems by Mendeleev *et al* [316].

A simulation box of 54000 and 55566 atoms were prepared for  $B_2\text{-Cu}_{50}\text{Zr}_{50}$  and  $C11_b\text{-Cu}_{33.3}\text{Zr}_{66.7}$  respectively. The simulation protocol started with an energy minimization process employing the conjugate gradient algorithm [321] with a force norm criterion of  $10^{-8}$  eV/Å. Then, we distributed the velocity (equivalent to 300 K in microcanonical ensemble NVE). Finally, we heated the system from 300 K to 2000 K during 1.7 ns with a constant heating rate using the NPT ensemble. Damping coefficients of 0.1 ps and 1.0 ps in the Nose-Hoover (thermostat-barostat) style were used respectively for temperature and pressure. The results are shown in Figures 3.1 and 3.2.

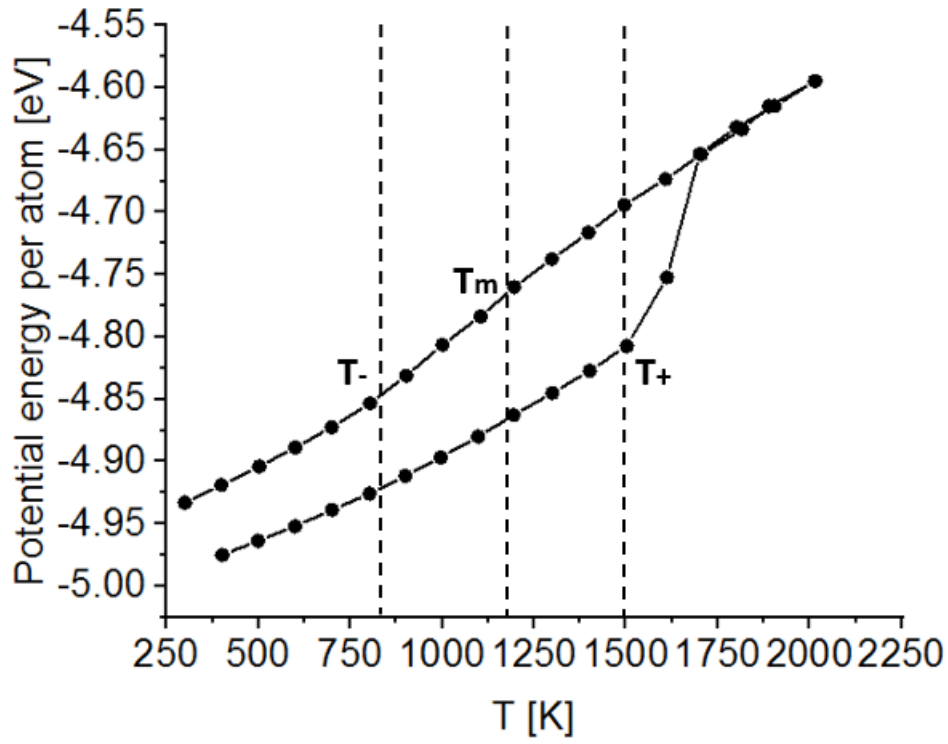


Figure 3.1: *in silico* potential energy per atom versus temperature in B<sub>2</sub>-Cu<sub>50</sub>Zr<sub>50</sub> crystal alloys to determine the melting temperature  $T_m$  during the heating and cooling process.

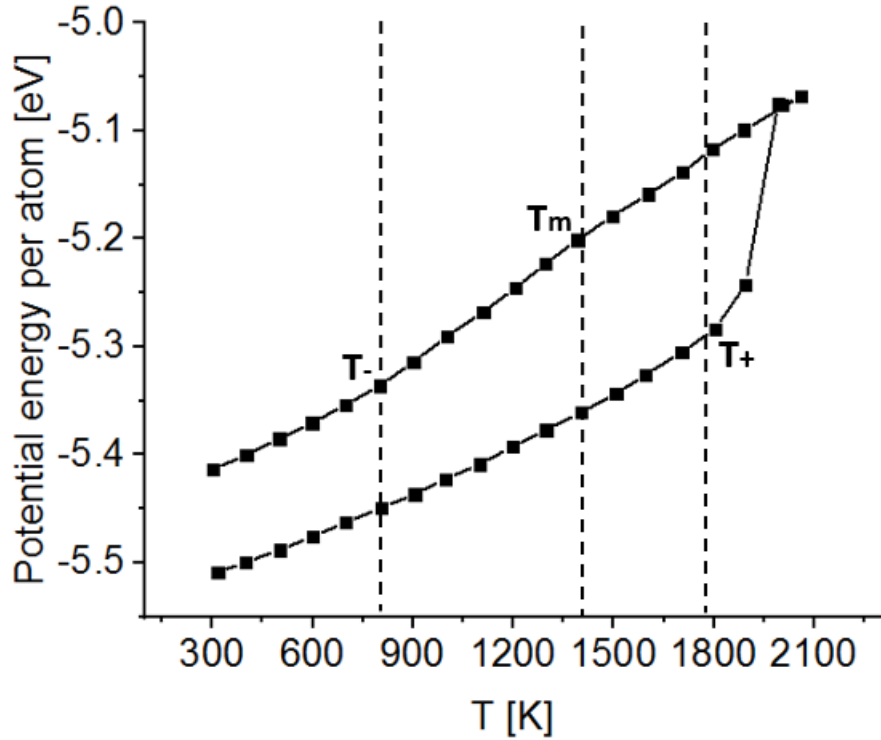


Figure 3.2: *in silico* potential energy per atom versus temperature in C<sub>11b</sub>-Cu<sub>33.3</sub>Zr<sub>66.7</sub> crystal alloys to determine the melting temperature  $T_m$  during the heating and cooling process.

Figures 3.1 and 3.2 exhibit the change of potential energy as a function of temperature in  $B_2$ -Cu<sub>50</sub>Zr<sub>50</sub> and C11<sub>b</sub>-Cu<sub>33.3</sub>Zr<sub>66.7</sub>. We notice that the potential energy increases linearly up to a certain temperature which represents  $T_+$  where an abrupt jump appears in the (PE-T) curves corresponding to the sign of a phase transition. Based on Figures 3.1 and 3.2, the value of  $T_m = 1207 (\pm 50\text{K})$ ,  $1401 (\pm 50\text{K})$  K for  $B_2$ -Cu<sub>50</sub>Zr<sub>50</sub> and C11<sub>b</sub>-Cu<sub>33.3</sub>Zr<sub>66.7</sub> respectively.

Exhaustive information about the experimental values of these crystalline structures melting points using different experimental approaches and techniques is provided by Turchanin *et al* [322]. It has been reported that for the  $B_2$ -Cu<sub>50</sub>Zr<sub>50</sub> the experimental values of  $T_m$  are 1206-1233 K, and for the C11<sub>b</sub>-Cu<sub>33.3</sub>Zr<sub>66.7</sub> a values of 1273-1338 K. We mention that the hysteresis method and the inter-atomic potential used to reproduce the liquid phase properly with values very close to those previously reported experimentally (see Tables 3.1 and 3.2). In order to provide additional proof that the final obtained structures are in liquid state, the PTM algorithm was used to probe the local structure [279] as shown in Figure 3.3.

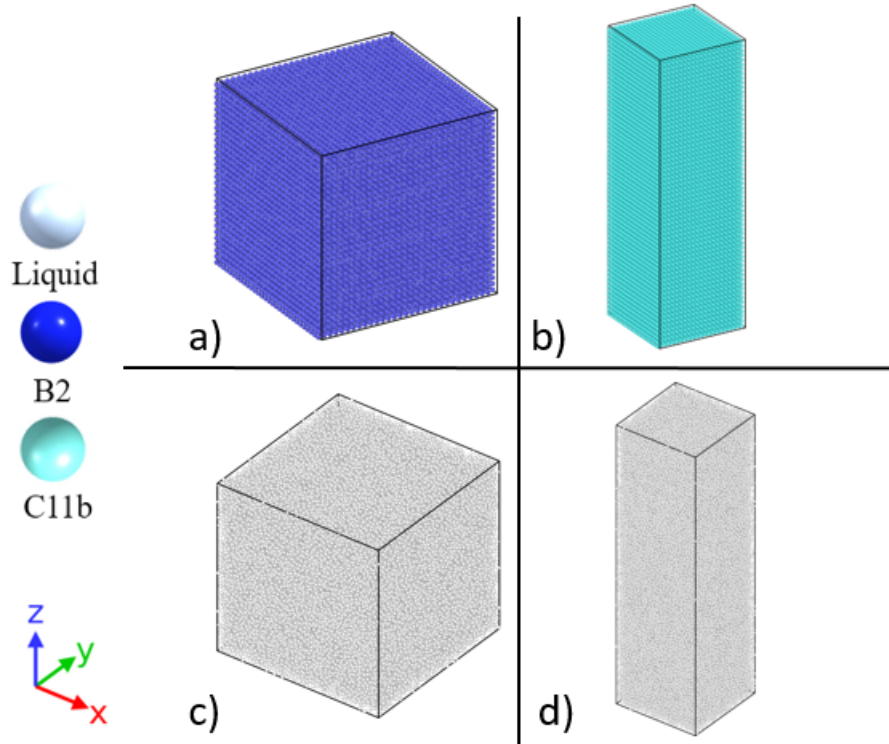


Figure 3.3: *in silico* CuZr crystal alloys and their equivalent liquid counterparts were obtained after submitting the initial crystalline simulation boxes to the protocol mentioned in Figure 3.6. (a,c) and (b,d) are the crystalline and liquid states of the  $B_2$ -Cu<sub>50</sub>Zr<sub>50</sub> and C11<sub>b</sub>-Cu<sub>33.3</sub>Zr<sub>66.7</sub> structures respectively. Atom colors refer to the local crystalline structure as computed using the PTM algorithm without chemical differentiation of the atoms.

The partial RDFs were computed to probe the spatial local structure environment organization. The results are shown in Figures 3.4 and 3.5.

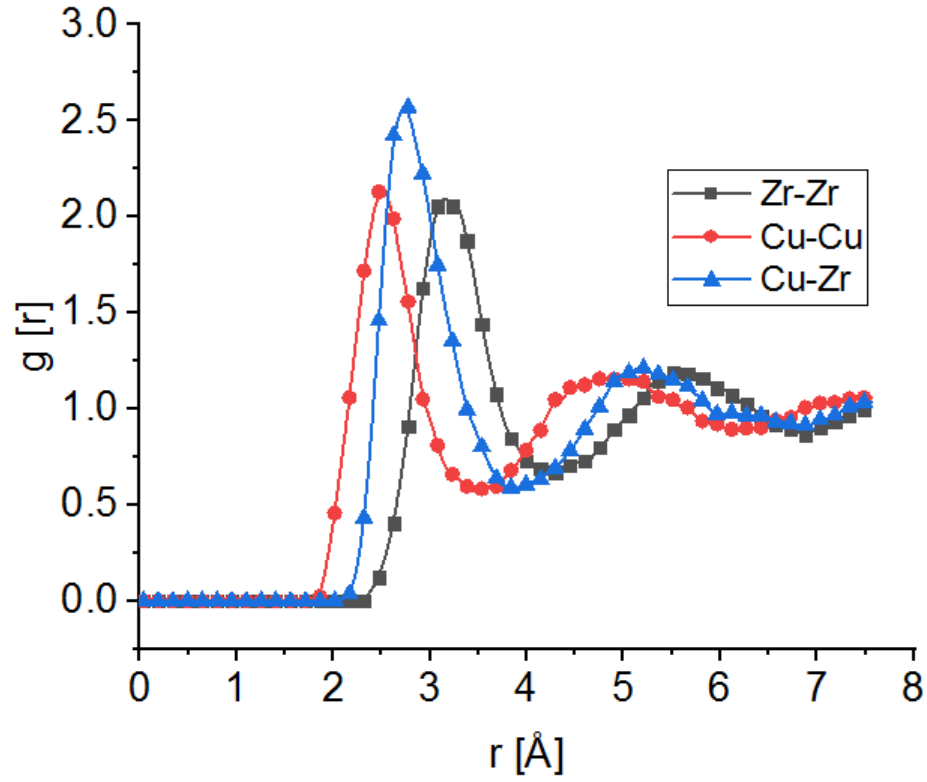


Figure 3.4: The partial RDFs display the triplet distributions involving Cu–Cu, Cu–Zr, and Zr–Zr pair atoms of  $B_2\text{-Cu}_{50}\text{Zr}_{50}$  liquid structure at 2000 K.

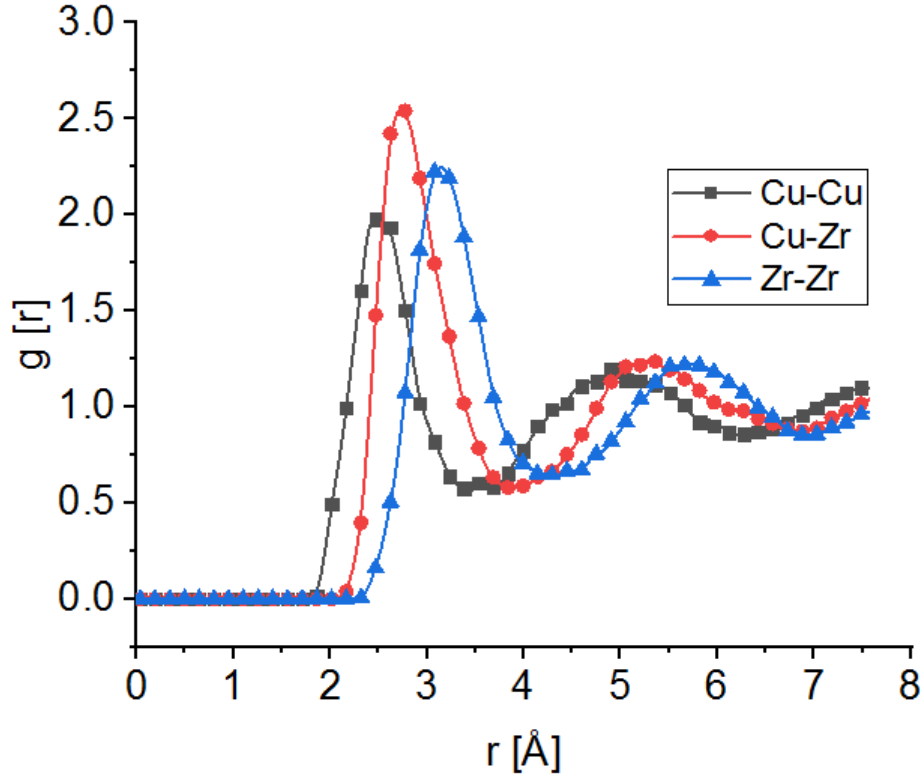


Figure 3.5: The partial RDFs display the triplet distributions involving Cu–Cu, Cu–Zr, and Zr–Zr pair atoms of  $C11_b\text{-Cu}_{33.3}\text{Zr}_{66.7}$  liquid structure at 2000 K.

Figures 3.4 and 3.5 display the triplet distributions involving Cu–Cu, Cu–Zr, and Zr–Zr PRDFs of the final liquid state at temperature 2000 K computed for both  $B_2\text{-Cu}_{50}\text{Zr}_{50}$  and  $C11_b\text{-Cu}_{33.3}\text{Zr}_{66.7}$  respectively.

In addition, we observe from the PRDF that unlike ordered structure where sharp peaks exist, here only two peaks are noticed. The first peak of each pair occurs at  $r(\text{Cu-Cu}) = 2.52 \text{ \AA}$ ,  $r(\text{Cu-Zr}) = 2.73 \text{ \AA}$ ,  $r(\text{Zr-Zr}) = 3.19 \text{ \AA}$ ,  $r(\text{Cu-Cu}) = 2.45 \text{ \AA}$ ,  $r(\text{Cu-Zr}) = 2.71 \text{ \AA}$ ,  $r(\text{Zr-Zr}) = 3.15 \text{ \AA}$  for  $B_2\text{-Cu}_{50}\text{Zr}_{50}$  and  $C11_b\text{-Cu}_{33.3}\text{Zr}_{66.7}$  respectively. We also observe the second peak broadening less pronounced and remarkably shorter than the first peak, which is consistent with the melted nature of the systems. The same figures establish that these second peaks are defined at  $r(\text{Cu-Cu}) = 4.83 \text{ \AA}$ ,  $r(\text{Cu-Zr}) = 5.21 \text{ \AA}$ ,  $r(\text{Zr-Zr}) = 3.19 \text{ \AA}$  and  $r(\text{Cu-Cu}) = 5.64 \text{ \AA}$ ,  $r(\text{Cu-Zr}) = 5.32 \text{ \AA}$ ,  $r(\text{Zr-Zr}) = 5.76 \text{ \AA}$  for  $B_2\text{-Cu}_{50}\text{Zr}_{50}$  and  $C11_b\text{-Cu}_{33.3}\text{Zr}_{66.7}$  respectively.

### 3.2.3 CuZr metallic glasses initial structure

After determining the melting temperatures for both compositions. The process of producing amorphous blocks can begin. The knowledge of these  $T_m$  is primordial, since to have high quality metallic glasses we have to liquefy the systems in

order to erase the crystalline memory of the initial seeds.

Two crystalline CuZr supercells are prepared using ATOMSK [245], the B<sub>2</sub>-Cu<sub>50</sub>Zr<sub>50</sub>, C11<sub>b</sub>-Cu<sub>33.3</sub>Zr<sub>66.7</sub> of dimension 9.69×3.55×3.55 nm<sup>3</sup> and 3.56×3.56×12.35 nm<sup>3</sup> respectively. The energy of the B2 and C11<sub>b</sub> is minimized and relaxed with the conjugate gradient algorithm [321]. The systems are then replicated along the three directions of space up to a size of about 1092 × 15 × 15 nm<sup>3</sup>. During the whole preparation process, Periodic Boundary Conditions (PBCs) are applied. To cancel residual pressure in the samples during the relaxation, a force norm criterion of 10<sup>-8</sup> eV/Å was employed. Then, the system is thermalized up to 300 K using the NPT ensemble (5 ps) and further equilibrated at constant PT conditions for another 5 ps.

To prepare both MGs samples namely α-Cu<sub>50</sub>Zr<sub>50</sub> and α-Cu<sub>33.3</sub>Zr<sub>66.7</sub>, the B<sub>2</sub> and C11<sub>b</sub> structures are first equilibrated at 300 K in the NVE ensemble for 100 ps and then heated up to 2000 K (above the theoretical melting point of  $T_m = 1207$  K, 1401 K (±50 K) for Cu<sub>50</sub>Zr<sub>50</sub>, and Cu<sub>33.3</sub>Zr<sub>66.7</sub> respectively) using NPT during 170 ps. Annealing is performed at 2000 K for 100 ps to erase the crystalline memory of the samples. This process is followed by a fast quench run from 2000 K to 300 K at a cooling rate of 10<sup>12</sup> K.s<sup>-1</sup>. The obtained glassy states are then equilibrated at the ambient temperature of 300 K for an extra 100 ps to remove internal stress within the final structure. The different stages of this computation are summarized in Figure 3.6.

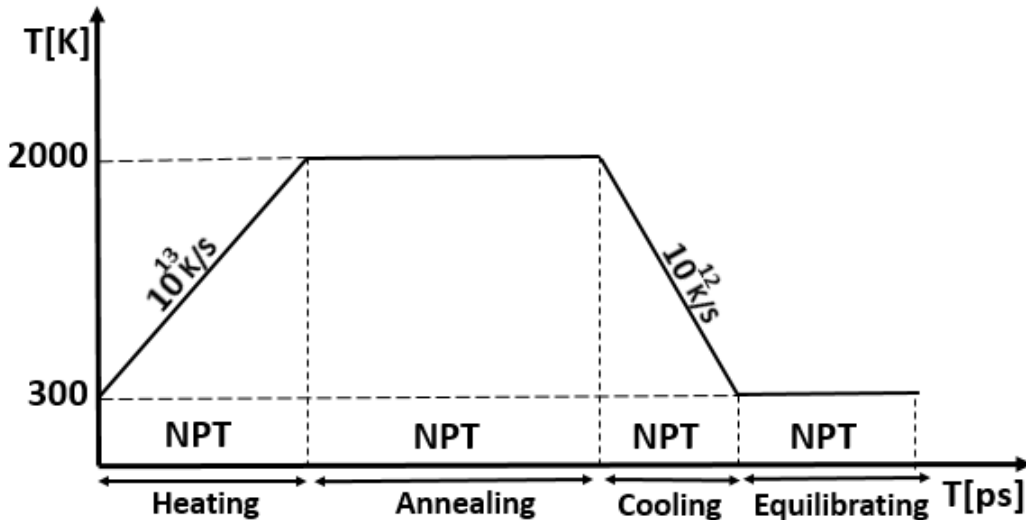


Figure 3.6: Amorphization path that is used to build metallic glasses initial samples α-Cu<sub>50</sub>Zr<sub>50</sub> and α-Cu<sub>33.3</sub>Zr<sub>66.7</sub>. The fabrication protocol is set by mimicking the experimental procedure.

The outcome of the crystalline alloys that are submitted to the protocol described in Figure 3.6, the final amorphous structure under this thermodynamical path is shown in Figure 3.7.

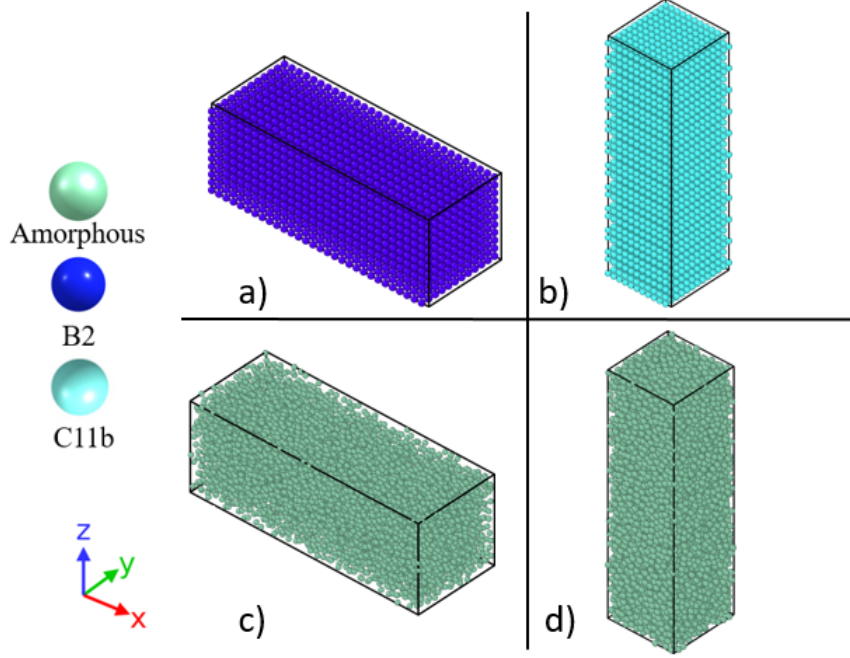


Figure 3.7: OVITO snapshots of amorphous and the corresponding crystal seeds in CuZr alloys systems where (a,c), (b,d) show the crystalline B<sub>2</sub>-Cu<sub>50</sub>Zr<sub>50</sub>, C11<sub>b</sub>-Cu<sub>33.3</sub>Zr<sub>66.7</sub> and amorphous counterpart  $\alpha$ -Cu<sub>50</sub>Zr<sub>50</sub>,  $\alpha$ -Cu<sub>33.3</sub>Zr<sub>66.7</sub> respectively. Atom colors refer to the local crystalline structure as computed using the PTM algorithm without chemical differentiation of the atoms.

The MGs are replicated along the 3 directions of space before the last 300 K equilibration run of 10 ps. The damping coefficients of 0.1 ps and 1.0 ps in the Nose-Hoover (thermostat-barostat) style are used respectively for temperature and pressure. The final MG samples size is about  $874 \times 7 \times 13 \text{ nm}^3$ . Finally, for both MGs and crystalline structures the half-part along  $x$  of the samples is suppressed (*i.e.*, the matter stands in the  $[L_x/2, L_x]$  with  $L_x$  the box length along  $x$ ) to introduce the empty space necessary to accommodate the laser-matter interaction and possible matter ablation.

### 3.2.4 Rapid solidification and theoretical glass transition temperatures

A relevant property associated with the description of glass material formation is known as glass transition temperature  $T_g$ . In order to access this property in both B<sub>2</sub>-Cu<sub>50</sub>Zr<sub>50</sub>, C11<sub>b</sub>-Cu<sub>33.3</sub>Zr<sub>66.7</sub> structures, a normalized volume versus the temperature during the cooling process is plotted as shown in Figures 3.8 and 3.9.

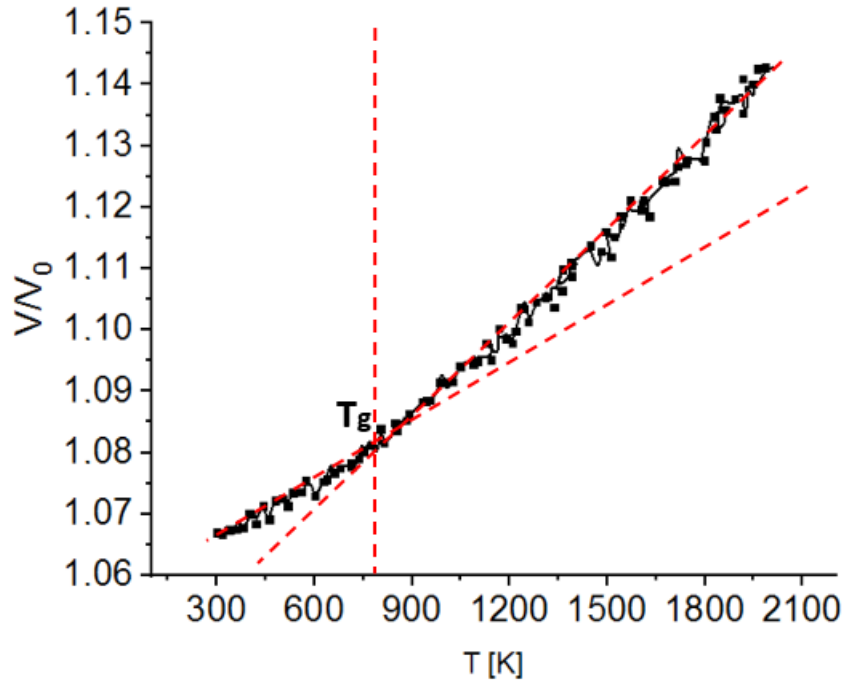


Figure 3.8: *in silico* normalized volume (with respect to the initial optimized volume  $V_0$ ) versus temperature in  $\alpha$ -Cu<sub>50</sub>Zr<sub>50</sub> to determine the glass transition temperature  $T_g$  during the cooling process.

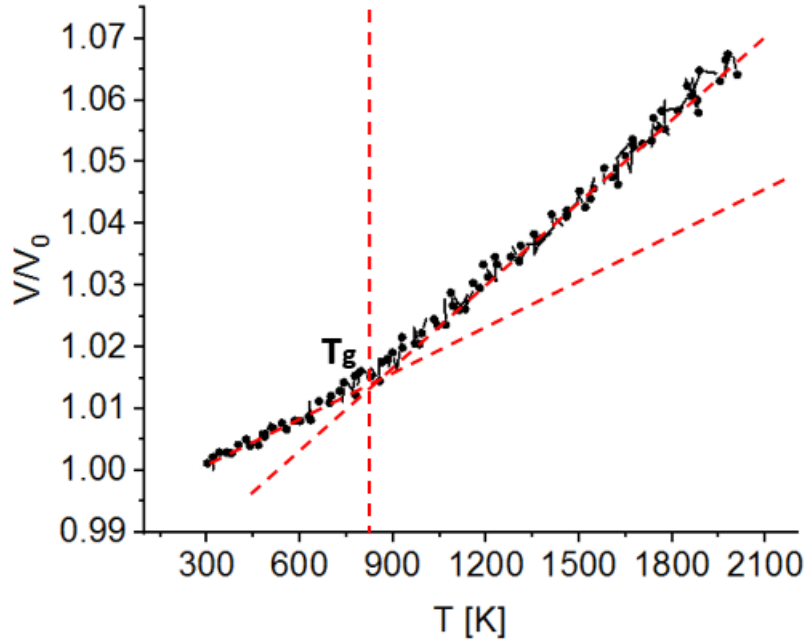


Figure 3.9: *in silico* normalized volume (with respect to the initial optimized volume  $V_0$ ) versus temperature in  $\alpha$ -Cu<sub>33.3</sub>Zr<sub>66.7</sub> to determine glass transition temperature  $T_g$  during the cooling process.

We can notice a change of the slope in the normalized volume plot characterized by two slopes separated by  $T_g$  where the glass transition occurs. We have

to mention that this value is slightly shifted when the cooling rate is modified. The reason is the steep volume dependence of the molecular response time for local atomic rearrangement. Therefore, according to the MD results shown in figures 3.8 and 3.9, the EAM potential employed in this work gave values of  $762 \pm 50$  K,  $788 \pm 50$  K for  $\alpha$ -Cu<sub>50</sub>Zr<sub>50</sub>,  $\alpha$ -Cu<sub>33.3</sub>Zr<sub>66.7</sub> respectively. The comparison between experimental and computational works yields to satisfactory results, as summarized in Tables 3.1 and 3.2.

Table 3.1: The computed theoretical MD temperature compared to the experimental values of B<sub>2</sub>-Cu<sub>50</sub>Zr<sub>50</sub> structures.

Reference	method	$T_g$ (K)	$T_m$ (K)
<b>This work</b>	<b>simulation</b>	<b>762</b>	<b>1207</b>
[323]	experimental	666	1148
[324]	experimental	998	1226
[325]	experimental	672	1178
[326]	experimental	670	1231
[325]	simulation	735	1205
[327]	simulation	770	no data
[322]	experimental	no data	1208

Table 3.2: The computed theoretical MD temperature compared to the experimental values of C11<sub>b</sub>-Cu<sub>33.3</sub>Zr<sub>66.7</sub> structures.

Reference	method	$T_g$ (K)	$T_m$ (K)
<b>This work</b>	<b>simulation</b>	<b>788</b>	<b>1401</b>
[323]	experimental	616	no data
[328]	experimental	620	1292
[322]	experimental	no data	1373

In order to check the amorphous footprint of the final structures at the atomic level, a complementary analysis involving the PRDFs was performed. The final results are as shown in figures 3.10 and 3.11.

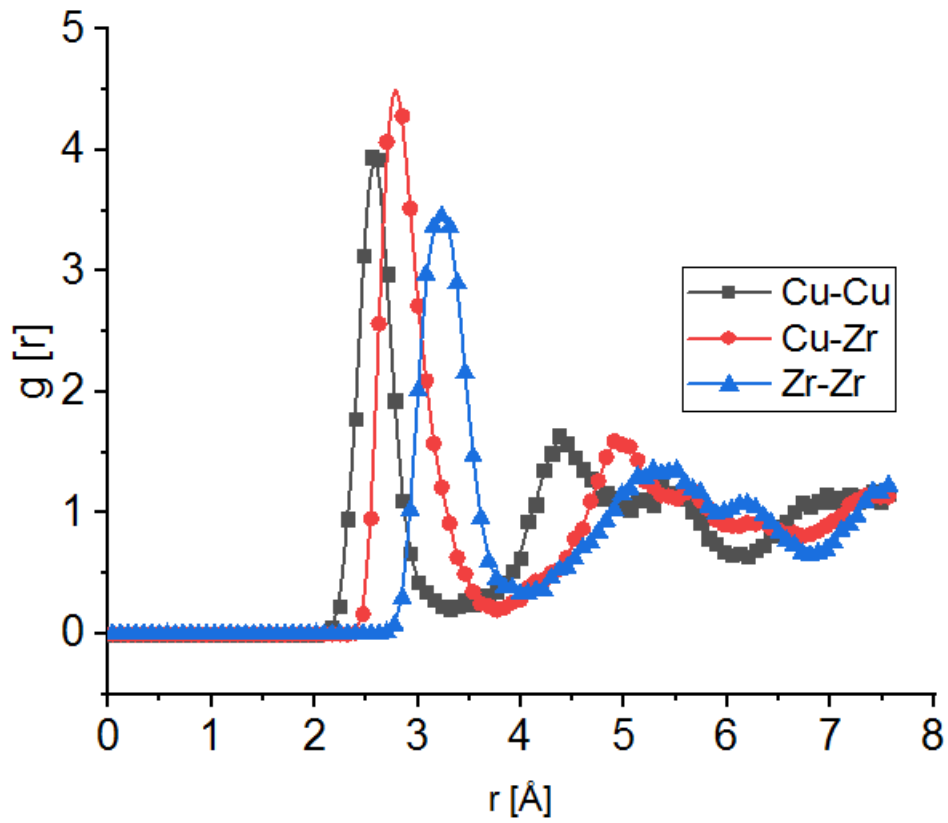


Figure 3.10: The partial RDFs of  $\alpha$ -Cu<sub>50</sub>Zr<sub>50</sub> amorphous structure.

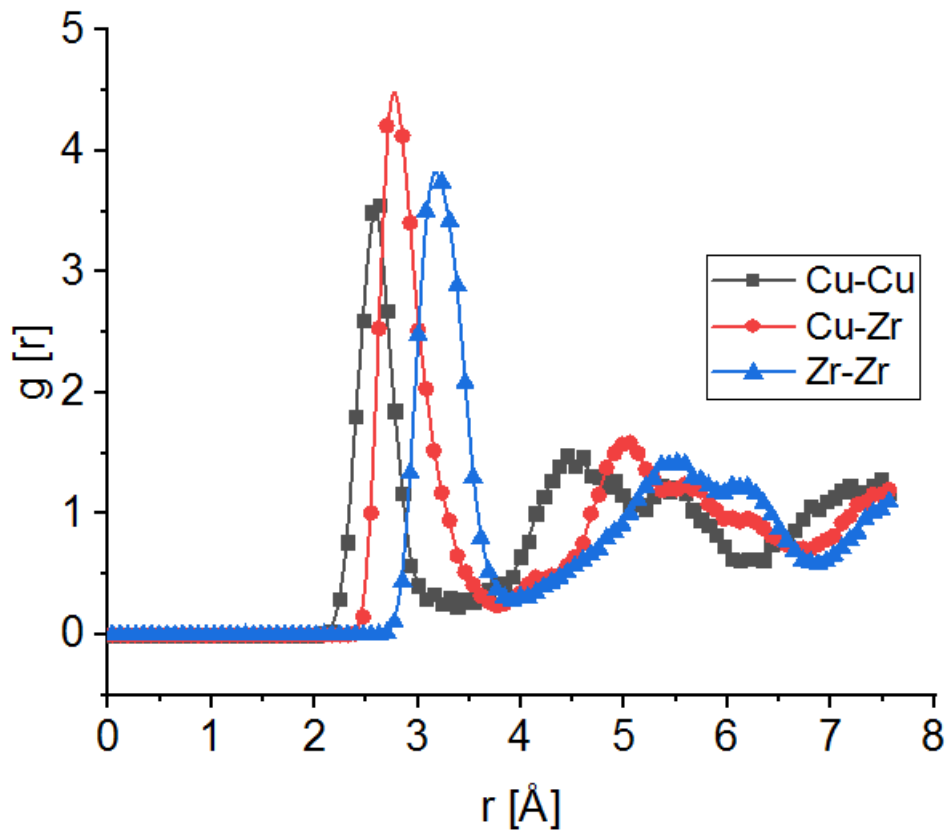


Figure 3.11: The partial RDFs of  $\alpha$ -Cu<sub>33.3</sub>Zr<sub>66.7</sub> amorphous structure.

A subtle double splitting of the second peak can be detected in the PRDFs patterns of both quenched liquid alloys, which demonstrate the amorphous nature of the samples. Comparison among PRDFs reveals a reasonable agreement of first and second peak positions with the MD results and those cited in the literature mainly experimental measurements. Thus, the MD calculation seems convincing for current work and all results are summarized in Tables 3.3 and 3.4.

Table 3.3: Summary of all the average nearest neighbor distances in  $\alpha$ -Cu<sub>50</sub>Zr<sub>50</sub> compared to different simulation and experimental methods.

Reference	Method	r(Cu-Cu)Å	r(Cu-Zr)Å	r(Zr-Zr)Å
<b>This work</b>	<b>simulation</b>	<b>2.52</b>	<b>2.73</b>	<b>3.19</b>
[329]	simulation	2.56	2.75	3.13
[330]	EXAFS	2.57	2.84	3.19
[331]	XRD	2.68	2.80	3.16
[332]	simulation	2.67	2.78	3.22
[208]	simulation	2.58	2.78	3.20
[333]	X-ray	2.53	2.77	3.18

Table 3.4: Summary of all the average nearest neighbor distances in  $\alpha$ -Cu<sub>33.3</sub>Zr<sub>66.7</sub> compared to different simulation and experimental methods.

Reference	Method	r(Cu-Cu)Å	r(Cu-Zr)Å	r(Zr-Zr)Å
<b>This work</b>	<b>simulation</b>	<b>2.45</b>	<b>2.71</b>	<b>3.15</b>
[323]	experimental	2.48	2.74	3.11
[333]	experimental	2.53	2.77	3.18
[208]	simulation	2.57	2.77	3.18

### 3.2.5 Surface impact on the amorphous structures

The previous amorphous structures were replicated for future laser-matter simulations and additional detail should be addressed concerning the surface effect on the amorphous structures. Therefore, we must carefully investigate whether the structural change may occur due to the surface effects. Concretely, we have increased the surface-bulk ratio. We have checked that the amorphous character of the systems is preserved as amorphous. For this purpose, we have computed the PRDFs, and the results are presented in Figures 3.12 and 3.13.

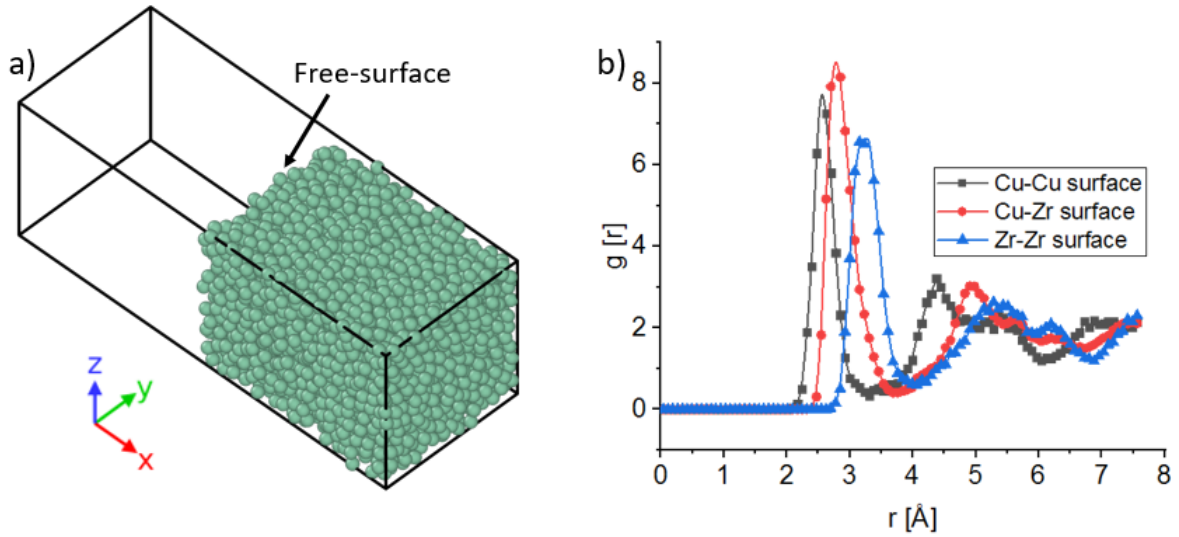


Figure 3.12: The amorphous structure a)  $\alpha$ -Cu<sub>50</sub>Zr<sub>50</sub> with the presence of the surface. b) The partial RDFs of  $\alpha$ -Cu<sub>50</sub>Zr<sub>50</sub> amorphous structure with the presence of the free surface.

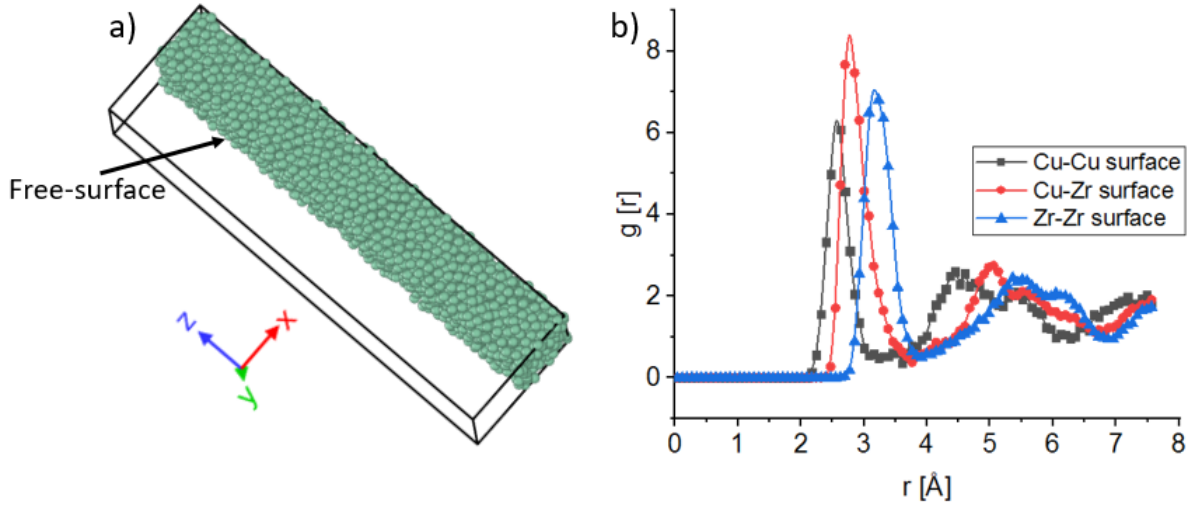


Figure 3.13: The amorphous structure a)  $\alpha$ -Cu<sub>33.3</sub>Zr<sub>66.7</sub> with the presence of the surface. b) The partial RDFs of  $\alpha$ -Cu<sub>33.3</sub>Zr<sub>66.7</sub> amorphous structure with the presence of the free surface.

The PRDFs of both structures 3.12(a) and 3.13(a) with surface presence show that the observed peaks values rise and they are more significant compared to perfect bulk as confirmed by Figures 3.12(b), 3.13(b) for  $\alpha$ -Cu<sub>50</sub>Zr<sub>50</sub> and  $\alpha$ -Cu<sub>33.3</sub>Zr<sub>66.7</sub> respectively. This is due to the inclusion of the empty volume that creates the surface. However, it is pertinent to mention that the shape of the PRDFs is not sensitive to the surface which means that the local structure is preserved as amorphous. The double splitting is preserved in both B<sub>2</sub>-Cu<sub>50</sub>Zr<sub>50</sub> and C11<sub>b</sub>-Cu<sub>33.3</sub>Zr<sub>66.7</sub>.

### 3.3 Laser-matter interaction setup

The heat diffusion Equation (2.43) is solved numerically on a  $702 \times 1 \times 1$  regular electronic cubic mesh as shown in Figure 3.14. The laser shot attenuation length is set according to the value shown in table 3.5. They are computed using the formula described in [208] as  $l_p = x l_p^{\text{Cu}} + (1 - x) l_p^{\text{Zr}}$ , where  $l_p^{\text{Cu}} = 12.2$  nm,  $l_p^{\text{Zr}} = 16.4$  nm are the penetration depth of Cu, Zr, and  $x$  is the percentage of Cu atoms present in each composition. A laser wavelength of 800 nm and a step function  $dx \approx 3$  nm for the  $T_e$  variation is used. No  $Pe$  is included in computation ( $B = 0$ ), this choice is justified by the fact that the hot electron blast force impact phenomenon occurring at the surface in a typical time of  $\sim 1$ -10 ps as discussed in the work of Gan *et al* [334].

In the concurrent investigation, the structuration occurs deep in the samples and the transformation starts around 80 ps. Therefore, this blast force has a negligible impact on the process except for increasing the computation time cost ( $\gamma_s$  and  $v_0$  are set to zero). We are modeling a laser-matter interaction which means that ions have a gain (not a loss) of energy proportional to the electron-phonon coupling factor as described in Equation 2.43. As mentioned in the work of Duffy *et al* [265],  $\gamma_s$  is included in cascade simulation to mimic the loss of energy of an atom due to electrons which is not suitable here. It is even counter intuitive, since the electrons are already hot they cannot dump the heat, instead they will communicate it to the cold ions. In addition, according to the original paper of Anisimov *et al* [304] no such term are included.

Herein, PBCs are set in  $y$  and  $z$  lateral directions, and free boundaries are imposed following the laser irradiation direction [100]. Ultrafast laser irradiation induces a strong temperature gradient normal to the surface which leads to the generation of a pressure wave (P-wave) propagating to the bulk of the target [335, 336]. A trial-and-error approach focused on the gradual extinction of the reflected P-wave is used. For this purpose, we define non reflecting boundary conditions (NRBC), made of a viscous damping region [337, 258, 108] with dimensions of  $L_{\text{NRBC}} = 100$  nm. A damping factor  $\gamma_{\text{damp}} = 2.5 \cdot 10^{-3}$  eV ps  $\text{\AA}^{-2}$  is used in this work in all simulations. The ultrafast process is modeled as a homogeneous dose energy deposition on the surface with a pulse duration of 100 fs. The TTM-MD stage pushes the system to an extreme nonequilibrium state which is held for 30 ps. The second stage of the simulation is a regular MD run in the NVE ensemble for (i) 170 ps for crystals and (ii) 970 ps for MGs.

We have to underline that the MG's were obtained by working in NPT ensemble (isothermal-isobaric) at 1 atm external pressure and with damping constants of 0.1 ps for the Nose-Hoover thermostat and 1.0 ps for the barostat respectively, the all post process visualization was performed by OVITO software [275]. An equivalent protocol was applied to the Cu-Zr amorphous ( $\alpha$ -Cu<sub>50</sub>Zr<sub>50</sub> and  $\alpha$ -Cu<sub>33.3</sub>Zr<sub>66.7</sub>) sample having the same stoichiometry.

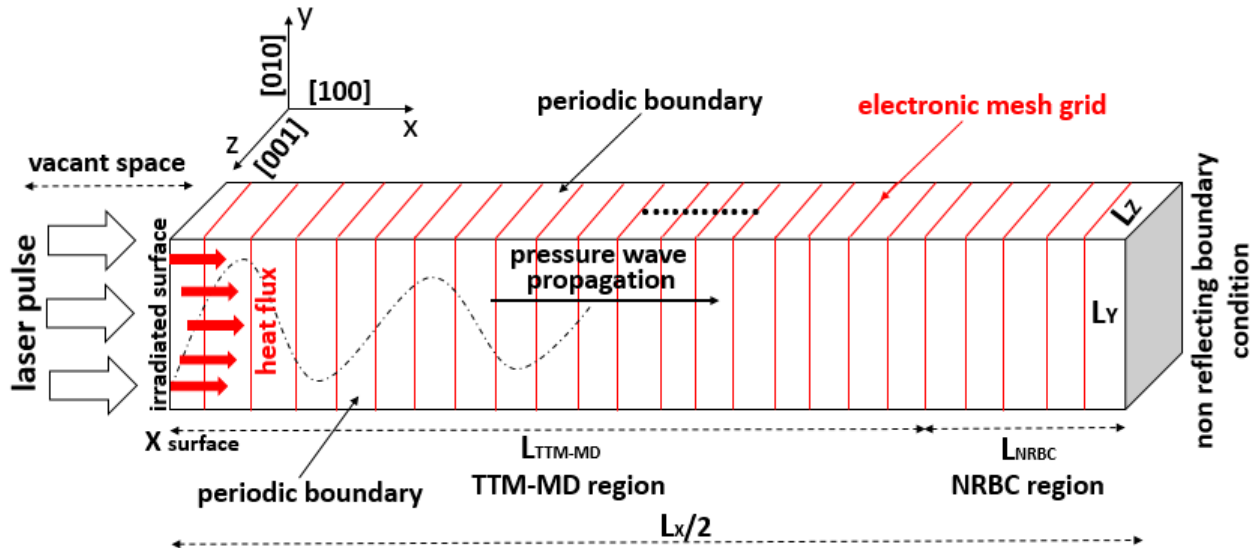


Figure 3.14: Simulation setup geometry used to model ultrafast laser pulse interaction in CuZr alloys using TTM-MD simulations. Atoms are located inside the rectangular box and the overlying red grid represents the electronic cell domain for the finite difference (FD) solution of Equation (2.43). There is no energy transfer with the vacant space beyond the top surface. Additionally, the rear region of the sample represents the NRBC region.

### 3.3.1 Determination of electronic meshing

As mentioned in the previous section, the heat equation is solved in a regular rectangular numerical mesh. To justify this choice in the present work ( $702 \times 1 \times 1$ ), a series of simulations were performed to determine a suitable mesh. We have to keep in mind that a substantial number of cells means more equations to solve. Therefore, the challenge is to keep the simulation accurate with a reasonable simulation time.

In order to proceed with heat propagation only along  $x$ -axis, a value of 1 is used for electronic meshing along  $y$  and  $z$  directions. In literature, it is redundant to see that a unit mesh volume of approximately  $8 \text{ nm}^3$  is advised. Instead, we investigated the appropriate value of  $N_x$  by preparing a B<sub>2</sub>-Cu<sub>50</sub>Zr<sub>50</sub> box with dimensions of  $1108.84 \times 16.15 \times 16.15 \text{ nm}^3$  following  $x$ ,  $y$ , and  $z$  respectively. The box is filled with atoms occupying the space  $> 554.84 \text{ nm}$ . In these test simulation

runs, the initial sample  $B_2-Cu_{50}Zr_{50}$  was minimized and relaxed. Moreover, a velocity distribution at 300 K in the NVE ensemble during 5 ps was performed. Then, the system was annealed at 300 K for an extra 10 ps using NPT ensemble. Finally, the laser was applied following the  $x$  direction by a TTM-MD process which was applied during 10 ps using different grids. The obtained results are shown in Figure 3.15.

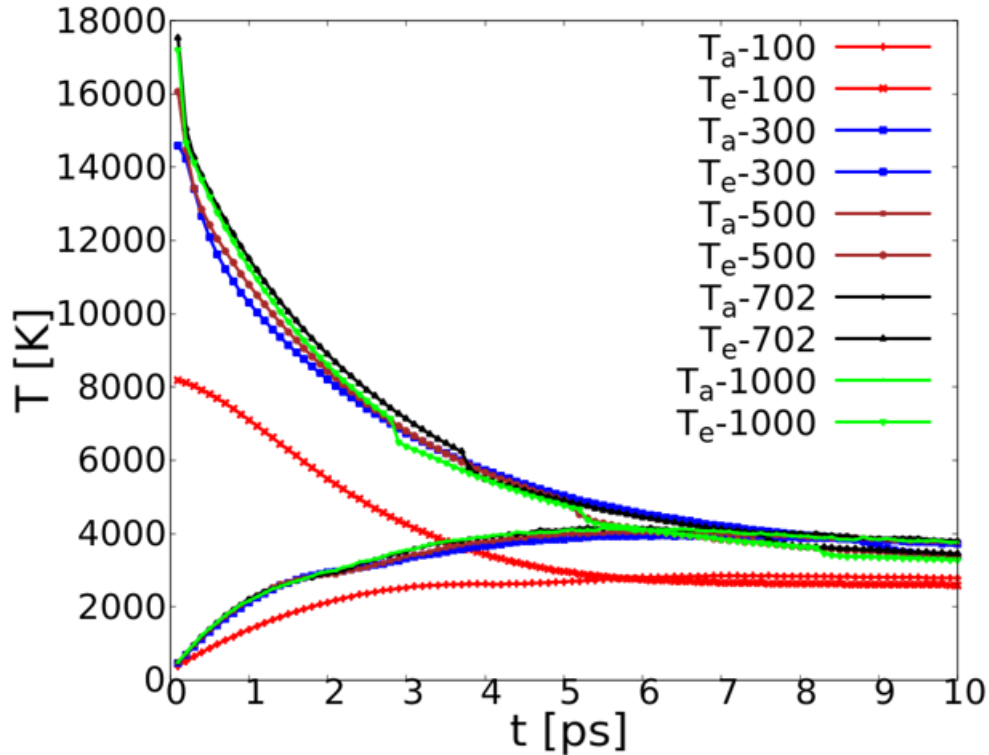


Figure 3.15: Temporal evolution of both electronic  $T_e$  and lattice  $T_a$  temperatures at the same point of the space (four grids larger below the initial defined surface) based on various grids 100, 300, 500, 702, and 1000. The system  $B_2-Cu_{50}Zr_{50}$  is used as a benchmark to determine the appropriate meshing. A laser with a pulse duration of  $\tau = 100$  fs and an absorbed fluence of  $F_{\text{abs}} = 48 \text{ mJ/cm}^2$  was used.

The temperature distribution is divided into two distinct time subdomains. From 0-5 ps the system is out of equilibrium where the  $T_e$  is very high and the lattice is cold. However, within the range 5-10 ps an equilibrium temperature is reached due to the coupling between the electronic-lattice subsystems. The current results reveal that a box of size 100 grids are not enough although the fact that after 5 ps the electronic and lattice temperatures coincide.

There is no significant effect on the temperature behavior for the grids 300 and 500. Nevertheless, the most effective configuration is obtained for 702. There is clearly a small change in  $T_e$  as well as  $T_a$  temperatures fluctuation compared to the 1000 curve. Therefore, for the rest of the simulations unless indicated, a

meshing of  $702 \times 1 \times 1$  is set for calculations. In addition, this grid adjustment is primarily used to reduce simulation time costs and ensure accurate simulations.

### 3.3.2 Computational details

The numerical simulations are carried out with the LAMMPS software [229] in which the CuZr systems are computed using the Embedded Atom Model (EAM) of Mendeleev *et al* [316]. A timestep of  $\Delta t = 1$  fs is utilized throughout the simulations in which the local atomic structures are investigated using the PTM [279] as implemented in the OVITO software [275]. The Table 3.5 summaries the TTM-MD input parameters properties and their justification for both crystals and their associate amorphous structures counterparts.

Table 3.5: Physical properties of crystalline and amorphous CuZr binary systems, namely specific heat constant  $\gamma$  and electron–phonon factor  $g_p$ , electronic thermal conductivity  $\kappa_e$ , and electronic thermal diffusion  $D_e$  at 300 K.

Property	B <sub>2</sub> -Cu <sub>50</sub> Zr <sub>50</sub>	C11 <sub>b</sub> -Cu <sub>33.3</sub> Zr <sub>66.7</sub>	$\alpha$ -Cu <sub>50</sub> Zr <sub>50</sub>	$\alpha$ -Cu <sub>33.3</sub> Zr <sub>66.7</sub>
$\rho_0$ [g cm <sup>-3</sup> ]	7.66	6.89	7.18	6.86
$g_p$ [ $10^{17}$ W m <sup>-3</sup> K <sup>-1</sup> ]	3.75 [208]	5.30 [208]	3.50 [208]	2.80 [208]
$\gamma$ [J m <sup>-3</sup> K <sup>-2</sup> ]	245.13 [208, 338]	194.20 [208, 338]	321.30 [208, 338]	384.70 [208, 338]
$\kappa_e$ [W m <sup>-1</sup> K <sup>-1</sup> ]	7.41 [339]	20.58 [339]	3.85 [340]	3.68 <sup>1</sup> [341]
$D_e$ [ $10^{-5}$ m <sup>2</sup> s <sup>-1</sup> ]	10.07	36.47	3.98	3.19
$l_p$ [nm]	14.30	14.80	14.30	14.80

To model laser-matter interaction the following typical command *fix TTM all ttm/mod 13423 ttm\_parameters 702 1 1 T\_init 100 T\_out.out* permit the energy deposition and mimicking a ultrafast laser event. Notably, TTM is a standard ID that we gave to the corresponding fix in order to invoke it for printing out the properties computed. Two of them can be accessed the `f_TTM[1]`, `f_TTM[2]` representing the electrons energy and the amount of energy transferred by the electrons to the ions via the electron-phonon coupling respectively. The number 13423 represents a random seed, and the 702 1 1 is the electronic mesh following  $x$ ,  $y$  and  $z$ . The `ttm_parameters` is an overarching cockpit file where we specify intrinsic properties relative to each material such as  $C_e(T_e)$ ,  $D_e(T_e)$  and  $g_p$ .

Moreover, its contains the ultrafast laser operating conditions, namely the absorbed fluence, pulse duration and the optical penetration depth. The `T_int` represents the initial electronic temperature at each node of the electronic grid. A FORTRAN 90 program has been developed to automatically generate these file

<sup>1</sup>Calculated using Wiedemann-Franz law  $\kappa_e = (\frac{L}{\rho_0})T_e$

adaptable according to our needs. The value 100 in the writing frequency steps of  $T_e$  and  $T_i$  blocks that are stored in T\_out file at every mesh node. Additional informations are provided in the appendices [H](#), [F](#), [D](#) and [M](#).

### 3.4 Irradiation of $B_2$ - $Cu_{50}Zr_{50}$ crystalline structure: formation of twins

Herein, we investigate the influence of a single ultrafast laser pulse on  $B_2$  and  $C11_b$  bulk crystalline CuZr as well as on two amorphous phases using atomistic simulations. The absorbed fluence of  $160 \text{ mJ/cm}^2$ , which is commonly used in this research to investigate phase transitions and defects formation, is obtained as a threshold for inducing these physical changes. This threshold value is often relevant to the damage threshold of the material in use, as any absorbed fluence above this value can cause significant damage due to laser-induced heating and associated stresses. In this study, different values of fluence were experimented with, including  $50 \text{ mJ/cm}^2$ ,  $80 \text{ mJ/cm}^2$ ,  $100 \text{ mJ/cm}^2$ ,  $120 \text{ mJ/cm}^2$ , and  $160 \text{ mJ/cm}^2$ . The latter value of  $160 \text{ mJ/cm}^2$  was determined as the maximum limit for laser processing to trigger permanent structural transformation and defects formation in the material.

Furthermore, the absorbed fluence of  $160 \text{ mJ/cm}^2$  is a convenient reference point for comparing the effects of the same laser parameters in different targets. By using a common reference point, results from different studies can be easily compared, and a common framework can be established for further research. Finally, the absorbed fluence of  $160 \text{ mJ/cm}^2$  is a relatively high value, making it suitable for many practical applications, including laser cutting and drilling to create precise features in various materials. Concretely, after the energy deposition on the surface, the sample thermalization is achieved by a strong electron–phonon coupling where both electrons and the ions reach the same equilibrium temperature. The final temperature gradient defines the position of the melting front below the surface as shown in [Figure 3.16](#).

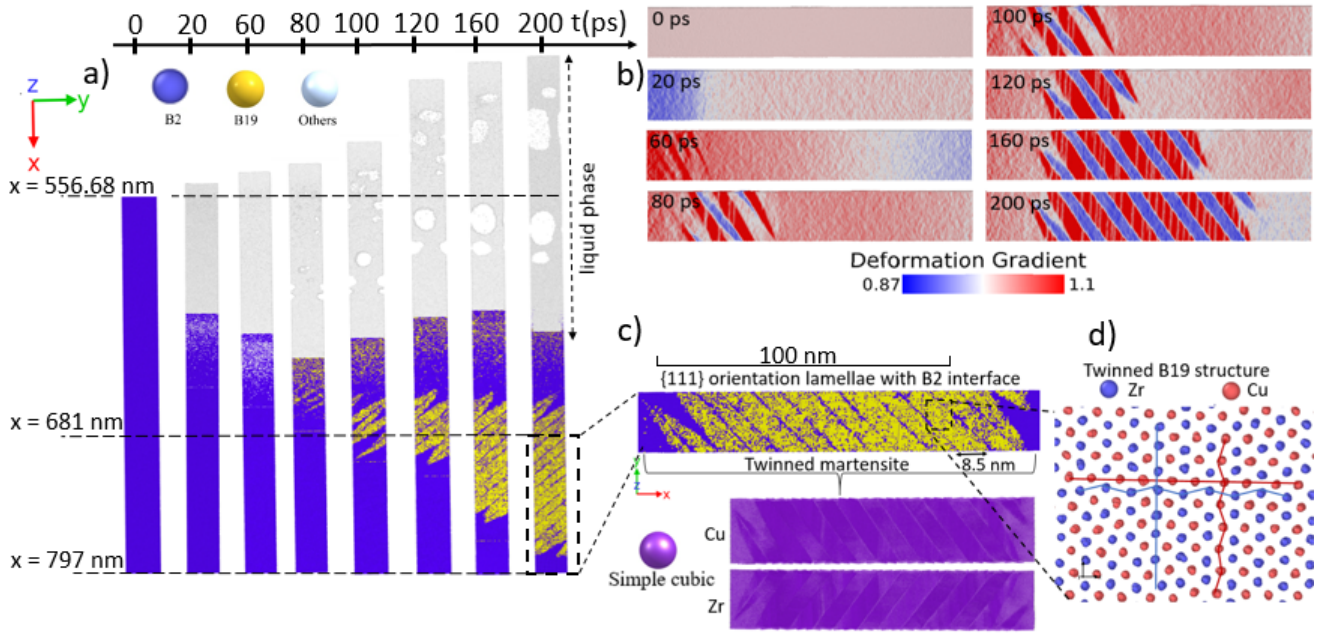


Figure 3.16: Snapshots of the atomic configurations evolution in a) at several times: 0 ps, 20 ps, 60 ps, 80 ps, 100 ps, 120 ps, 160 ps, and 200 ps in  $B_2$ - $Cu_{50}Zr_{50}$  target during ultrafast laser irradiation of  $\tau = 100$  fs pulse duration and  $F_{abs} = 160$  mJ/cm<sup>2</sup> absorbed fluence. The atoms are colored according to their local atomic structure of the binary alloy by using the PTM. The double dashed arrow in the upper part of the target shows the liquefied surface. b) Deformation gradient in the transformed zone following the  $x$ -direction at different times computed by the method described in . c) Zoom on the dashed region where the PTM algorithm is applied to each sub-lattice monoatomic lattice showing twinned martensite transformation. d) Enlarged view of the chemical species of the new twinned-B19 phase emergence after the irradiation.

Figure 3.16(a) shows the evolution of the  $B_2$  microstructure during the simulation. The local crystalline structure is investigated by applying the PTM method to the alloyed system without atomic species differentiation which leads to characterize the  $B_2$  perfect crystal structure and transformed domains environments (liquid, amorphous or new phase). Just after the laser pulse energy deposition, the upper part of the samples instantaneously melts as shown by a large number of atoms in defective configurations. At  $t = 80$  ps, several voids form below the CuZr surface at position  $x = 572$  nm and expand rapidly reaching their critical size at  $t = 200$  ps. In the meantime, a new crystalline phase nucleates and grows at position  $x \sim 700$  nm far deep in the sample starting from  $t = 60$  ps as shown in figures 3.16(c) and (d).

The transformed domain takes the shape of two nano-blades of  $\sim 8.5$  nm thickness each that propagates across the sample due to PBCs. The deformation gradient in the  $x$ -direction displayed in Figure 3.16(b) shows that the nano-blades follow a distribution with a spatial pseudo-periodicity separated by a thin

$B_2$  inter-layer. A closer look at the transformed structure allows the identification of two simple cubic sub-lattices attributed to Cu and Zr as in the original  $B_2$  phase. However, the atomic bonding changes from aligned to wavy or *zigzag* configurations along certain directions (see Figure 3.16(d)) typical of the  $B_{19}$  crystalline structure (*e.g.*, AuCd as shown in Figure 3.17(b)). This phase transition is similar to the martensitic transformation observed in  $B_2$  NiTi alloys [342, 343, 344]. The relative orientation between the two nano-blades allows to confirm the nucleation and propagation of two  $\{111\}$ -oriented  $B_{19}$  nanotwins.

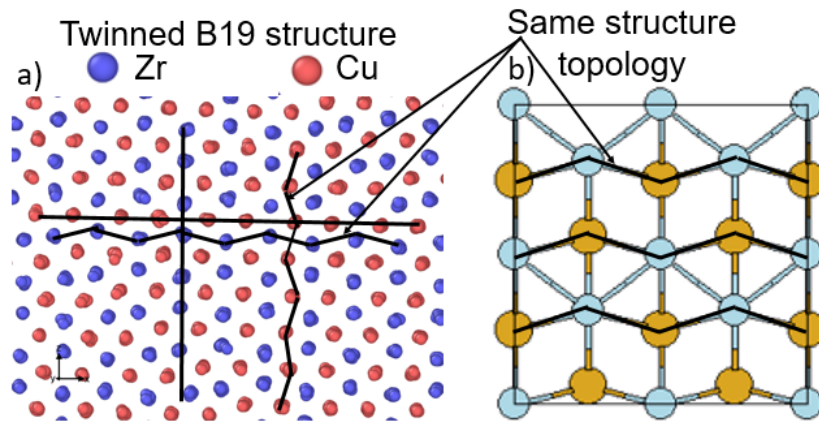


Figure 3.17: Atomic disposition within  $B_2$ - $Cu_{50}Zr_{50}$  crystalline structure. a) A twinned B19 structure formation and. b) A hypothetical B19 AuCd alloy structure. Adopted from [345].

Figure 3.18 shows an enlarged view of the twinned region within  $B_2$ - $Cu_{50}Zr_{50}$  crystalline alloy. We clearly notice the presence of a twinned region in the obtained final structure.

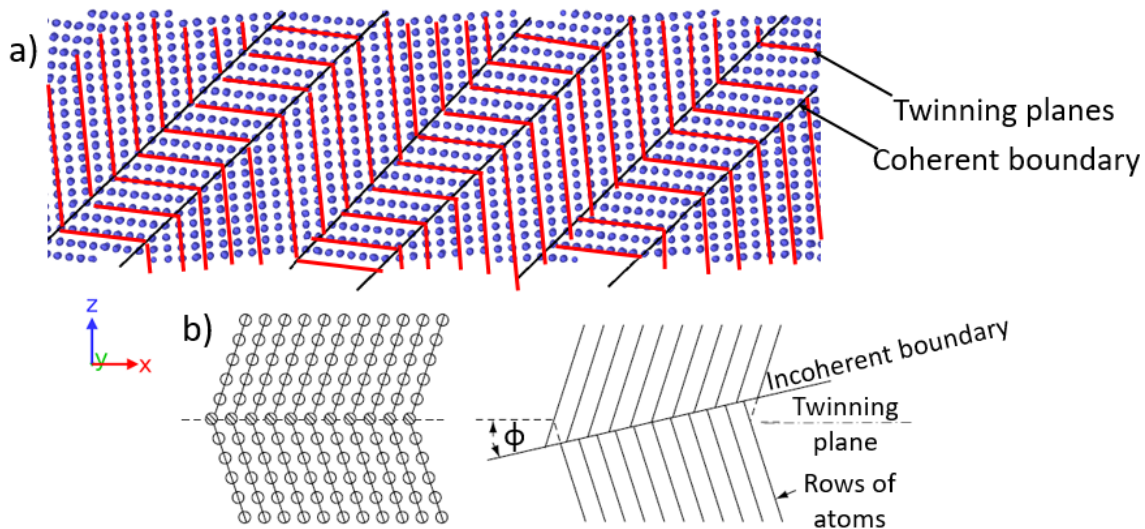


Figure 3.18: Zoom in a portion of a  $B_2$ - $Cu_{50}Zr_{50}$  twinned crystalline structure (all atoms are colored in blue). a) Shows the twinning planes and the coherent boundaries. b) A hypothetical twinning transformation in alloys for comparison purposes. Adopted from [147].

This process of cooperative displacement of atoms requires significant amounts of energy, which is provided by the laser pulse. Indeed, the laser pulse energy is responsible for local temperature gradients which induce the shock wave (P-wave) and then the aforementioned phase transformation. The pressure and temperature profile's time evolution in the transformed zone is shown in Figure 3.19.

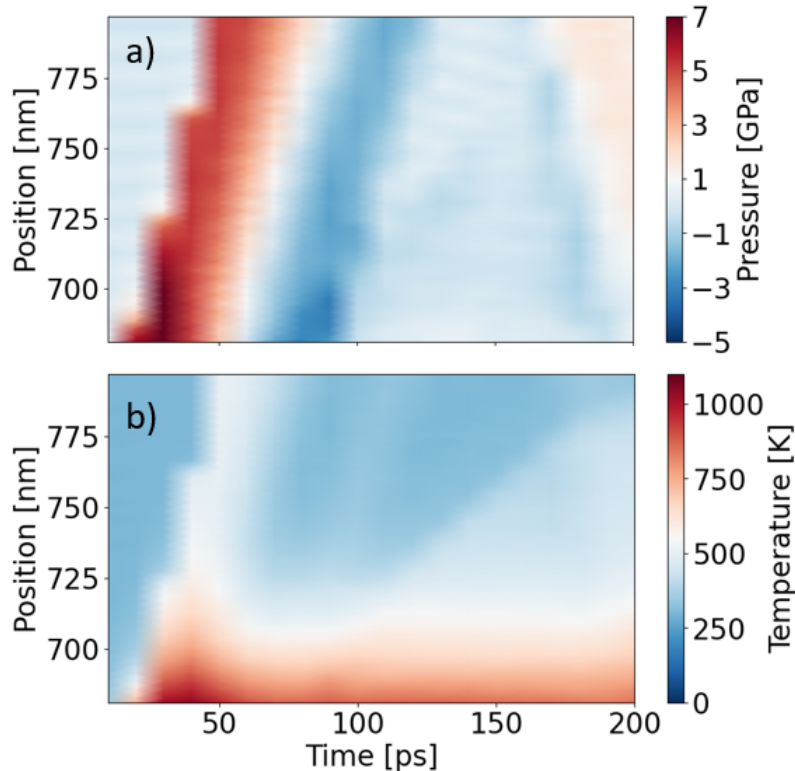


Figure 3.19: Spatiotemporal evolution of thermodynamic quantities in the  $B_2$ - $Cu_{50}Zr_{50}$  transformed region located in the subsurface (zoom region) area target: a) pressure, and b) lattice temperature. The initial surface position is given by  $x_{\text{surface}} = 556.68$  nm following the  $x$ -direction.

The pressure profile is characterized by loading (pressure wave) and unloading (rarefaction wave) P-waves. At early times ( $t = 0-60$  ps), the front of the loading P-wave reaches the emphasized region with a maximal value of  $\sim 7$  GPa but no transformation is noticed. The  $B_2$  to  $B_{19}$  phase transformation that starts at  $t = 80$  ps exactly coincides with the appearance of the rarefaction wave ( $\sim -5$  GPa extremum) as the loading wave progressively reflects the colder material. Hence, the phase transition is not due to the propagation of the pressure wave but more precisely to the unloading wave that has exceeded a critical level to activate the transformation [346]. Meanwhile, the temperature profile shows an increase up to  $\sim 1000$  K below the melting temperature  $T_m = 1207$  K. A mean  $T$  of  $\sim 600$  K is observed on the whole transformed zone, confirming that the solid-solid phase

transformation observed is driven by mechanical effects as observed in Figure 3.16(c).

### 3.5 Irradiation of $C11_b$ - $Cu_{33.3}Zr_{66.7}$ crystalline structure: formation of defects

Simulations were carried out to study the response of crystalline  $C11_b$ - $Cu_{33.3}Zr_{66.7}$  target under the effect of similar laser irradiation conditions. Figure 3.20 shows the results of the structural evolution analysis that is achieved using displacement vectors analysis [347].

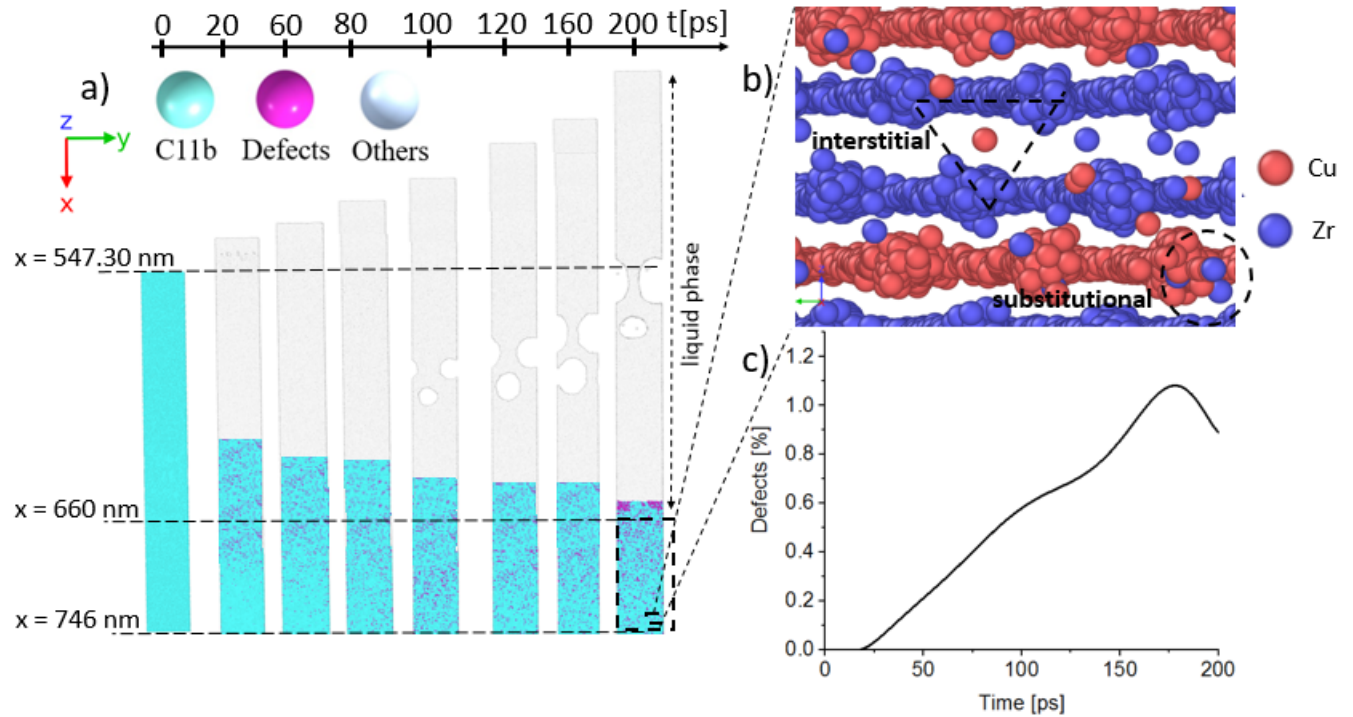


Figure 3.20: Snapshots of atomic configurations evolution in a) at several times: 0 ps, 20 ps, 60 ps, 80 ps, 100 ps, 120 ps, 160 ps, and 200 ps in the  $C11_b$ - $Cu_{33.3}Zr_{66.7}$  sample target during ultrafast laser irradiation of  $\tau = 100$  fs pulse duration and  $F_{abs} = 160$  mJ/cm<sup>2</sup> of absorbed fluence, the double dashed arrow in the upper part of target shows the liquefied surface. The atoms are colored according to their local atomic structure using PTM algorithm. b) Enlarged view of interstitial and substitutional defects formation in subsurface within  $C11_b$ - $Cu_{33.3}Zr_{66.7}$  target after the irradiation at different times. c) Temporal defects ratio evolution in  $Cu_{33.3}Zr_{66.7}$  ( $C11_b$ ) target sorted according to the displacement vector  $\delta y > 1$  Å. Atoms satisfying this condition are expected to be in defective positions.

Figure 3.20 shows the structural evolution of the  $C11_b$ - $Cu_{33.3}Zr_{66.7}$  sample. In particular, it provides an atomistic picture of the point defects generated in this case by the ultrafast laser pulse. First, in the  $t = 0$ -100 ps range, a liquid front is formed characterized by the coalescence of small nanovoids formation process

that grow to generates one large void below the surface in the  $t = 100-160$  ps range. However, the ablation regime only starts at  $t \sim 160$  ps causing a surface expansion of about 60 nm thickness which expands freely in the vacuum region. Figure 3.20(b) emphasizes a small area of subsurface material oriented along  $x = [100]$ . Using this projection, the classical C11<sub>b</sub> stacking along  $z = [001]$  shows some disturbances, and the original [100]-oriented Cu and Zr columns of atoms observed at 0 K can be schematized by pseudo-columnar domains separated by a thinner layer of atoms attributed to project elastoplastic deformation (that has not been confused with sub-lattice degradation or melting). In addition, point defects are identified up to  $x \sim 740$  nm.

Various kinds of point defects including interstitials as well as substitutionals Cu and Zr atoms are noticed. Atoms in the defective environment (point defects and highly sheared regions) are identified using a criterion on the atomic displacement along  $y$  and  $z$ ,  $\delta y$  and  $\delta z$  respectively (taking  $t = 0$  as a reference). The displacement criterion is chosen as about half the Cu-Zr or Zr-Zr bond length along  $y$ , ensuring to avoid counting atoms fluctuating around their equilibrium position.

We choose the  $y$  and  $z$  directions since they are less impacted by the P-wave-induced homogeneous matter displacement measured along the  $x$  direction. While the number of atoms with significant  $\delta z$  are only few (0.03 % of the atoms in the emphasized zone at  $t = 200$  ps), the number of atoms with  $\delta y > 1 \text{ \AA}$  continuously increases during the simulation (Figure 3.20(c)). The anisotropy observed between  $\delta y$  and  $\delta z$  corroborates the observed shear zones in the plane  $z = [001]$ .

Indeed, no defects are detected in the emphasized domain of the material from  $t = 0-25$  ps, however, the fraction of atoms in defective configuration grows up to a maximum 1.12 % at  $t = 175$  ps before decreasing to 0.93 % at the end of the simulation due to relaxation. For more clarity, we have computed this concentration by defining  $N_{total}$ ,  $N_{defects}$  number of total atoms and defects respectively. Therefore, the defect ratio was calculated as  $N_{defects}/N_{total}$ . The maximum percentage presented previously is acceptable to produce a stable structure. As mentioned previously, this quantitative estimation of the point defects concentration in the total volume of the system is consistent with literature previous results. To go further in understanding this phenomenon, we again look at the P-T profiles as shown in Figure 3.21.

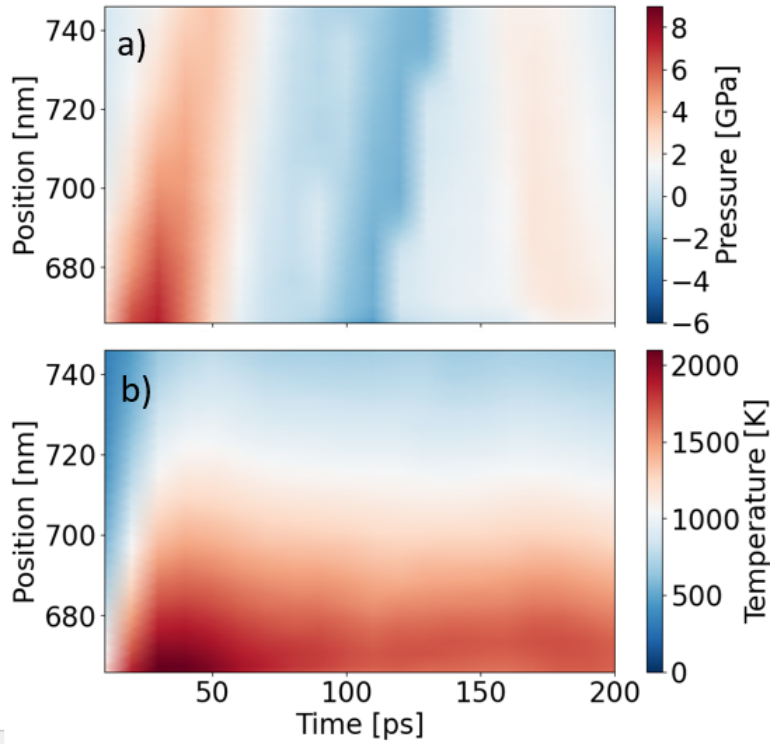


Figure 3.21: Spatiotemporal evolution of thermodynamic quantities in the subsurface transformed region (zoom region): a) pressure, and b) lattice temperature evolution in C11<sub>b</sub>-Cu<sub>33.3</sub>Zr<sub>66.7</sub> sample target. The initial surface position is given by  $x_{\text{surface}} = 547.30$  nm following the  $x$  axis direction.

The obtained value of  $\sim 1.12$  % is of the same order of magnitude as 0.25, 0.6 % vacancy concentration reported by He *et al* [348] for Cr and Ni respectively. This difference is mainly due to the following reasons. First, the material response (in this case Cr, Ni) to different laser irradiation conditions. Second, we discuss all types of defects, vacancies, interstitials, and substitutional defects while He *et al* they focus only on vacancy concentrations. Moreover, we can refer to other papers such as Karim *et al* [349] where they provides a concentration of vacancy equal to 0.6 % for Cr.

Figure 3.21(a) shows a strong P-wave is generated and reaches a maximum value of  $\sim 8$  GPa at  $t = 20$  ps. At  $t = 60$  ps the rarefaction P-wave propagates with a negative extremum front of  $\sim -6$  GPa appearing. The rarefaction wave and the defects population are highly correlated in terms of space and time. The lattice temperature shown in Figure 3.21(b) confirms that at the liquid-solid interface the temperature is  $\sim 2000$  K, higher than the melting point  $T_m = 1401$  K. We have to mention that below the solid-liquid interface the system is highly perturbed due to heat diffusion phenomenon but not melted. Here, we show that the electron-phonon coupling plays an extremely significant role in

the laser-matter interaction, and since the coupling factor is stronger for C11<sub>b</sub>-Cu<sub>33.3</sub>Zr<sub>66.7</sub> than for B<sub>2</sub>-Cu<sub>50</sub>Zr<sub>50</sub> (cf. Table 3.5) the temperature and P-wave maximum are higher in the case of C11<sub>b</sub>-Cu<sub>33.3</sub>Zr<sub>66.7</sub>.

### 3.6 Ultrafast laser interaction with Metallic-Glasses: ablation threshold mechanism

For comparison purposes with the crystal response, identical laser conditions are used. However, the amorphous samples total simulation time was extended up to 1 ns. As a result of the time extension, we expect that devitrification, or rather, an inverse amorphous-crystal transformation, could occur. This issue will be discussed and treated in detail in the chapter 5. Figure 3.22 shows the structural evolution of the amorphous samples.

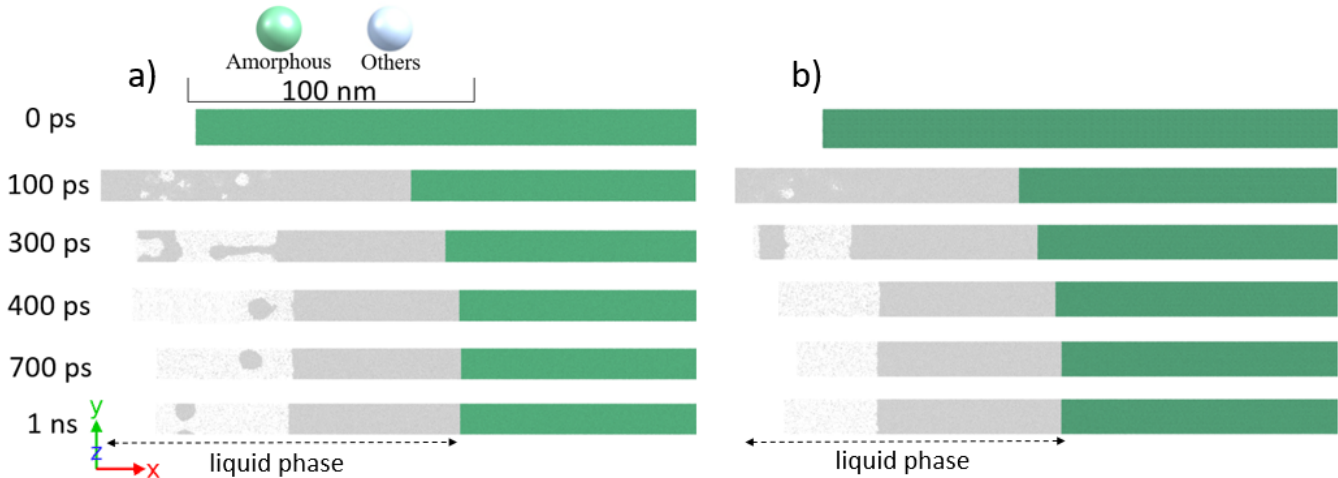


Figure 3.22: Snapshots of the structural evolution in the amorphous structures: a)  $\alpha$ -Cu<sub>50</sub>Zr<sub>50</sub>, and b)  $\alpha$ -Cu<sub>33.3</sub>Zr<sub>66.7</sub> using TTM-MD method at various time steps: 0 ps, 100 ps, 300 ps, 400 ps, 700 ps, and 1 ns. The atoms are colored according to their local atomic structure using the PTM algorithm, and two atomic contrasts are shown. The zone delimited by a double dashed arrow in the upper part of the targets corresponds to the liquid phase and the inner part is the amorphous phase. The irradiation conditions are  $\tau = 100$  fs pulse duration and  $F_{\text{abs}} = 160$  mJ/cm<sup>2</sup> of absorbed fluence.

Figure 3.22(a) shows the structural evolution of the  $\alpha$ -Cu<sub>50</sub>Zr<sub>50</sub> sample after the pulse energy deposition. As in the B<sub>2</sub>-Cu<sub>50</sub>Zr<sub>50</sub> case, results demonstrate surface liquefaction concomitant to the nucleation of voids preceding an ablation event. However, no phase transformation is observed. Regarding the CuZr phase diagram [145], local transformation into B<sub>2</sub> is possible and segregation could drive the formation of single crystalline inclusions (with FCC or HCP crystal structure).

Based on this reality, the nucleation of more complex phases is completely excluded. We conclude herein that laser-induced local phase transition within  $\alpha$ -Cu<sub>50</sub>Zr<sub>50</sub> can not be obtained using the same laser pulse conditions (pulse duration and fluence) as the one used to phase-transform B<sub>2</sub>-Cu<sub>50</sub>Zr<sub>50</sub> crystals assuming that this transition is possible at ps time scale. On the other hand, the amorphous  $\alpha$ -Cu<sub>33.3</sub>Zr<sub>66.7</sub> sample was also subjected to a 1 ns simulation with the same fluence and pulse duration, the result is as illustrated in Figure 3.22(b).

For both amorphous structures, a spallation process was triggered at  $t = 100$  ps through the growth of subsurface voids which induce at later times the ejection of a top liquid layer having a thickness of  $\sim 20$  nm without any sign of crystal nucleation. The pressure conditions leading to the ejection and disintegration of the upper part of the irradiated targets are illustrated in Figures 3.23, 3.24 corresponding to the responses of  $\alpha$ -Cu<sub>50</sub>Zr<sub>50</sub> and  $\alpha$ -Cu<sub>33.3</sub>Zr<sub>66.7</sub> respectively.

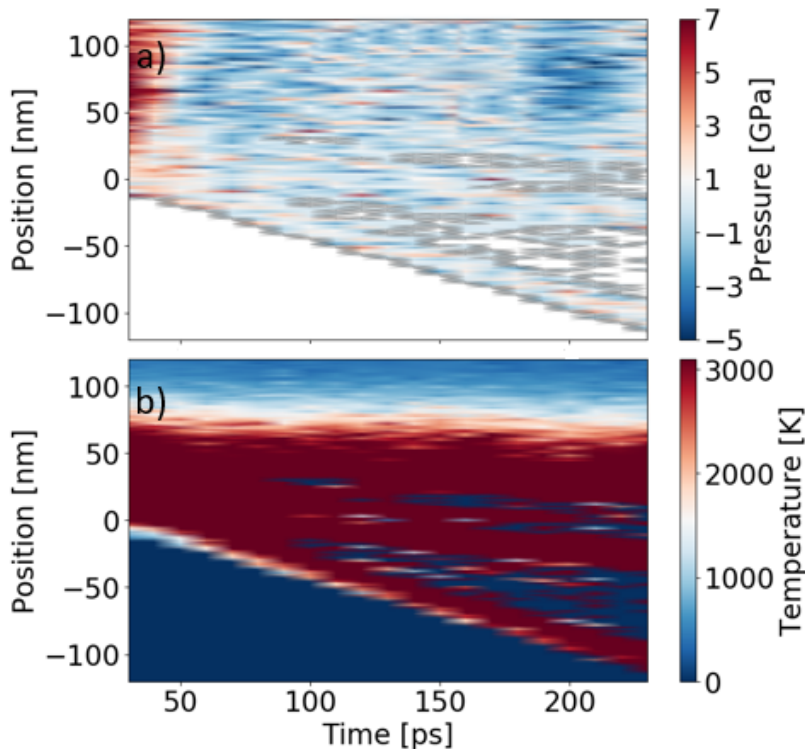


Figure 3.23: Spatiotemporal evolution of thermodynamic quantities in the surface region: a) pressure, and b) lattice temperature evolution in  $\alpha$ -Cu<sub>50</sub>Zr<sub>50</sub> sample target. The initial surface position is given by  $x_{\text{surface}} = 0$  nm following the  $x$  axis direction.

Figures 3.23(a), 3.24(a) show that at time range  $t = 0$ -40 ps the targets were subjected to an extreme compressive stress defined here with a maximum pressure value of  $\sim 7$  GPa. Moreover, at  $t = 70$  ps we can clearly detect the rarefaction

pressure wave with a maximum value of  $\sim -5$  GPa that penetrates deep into the material.

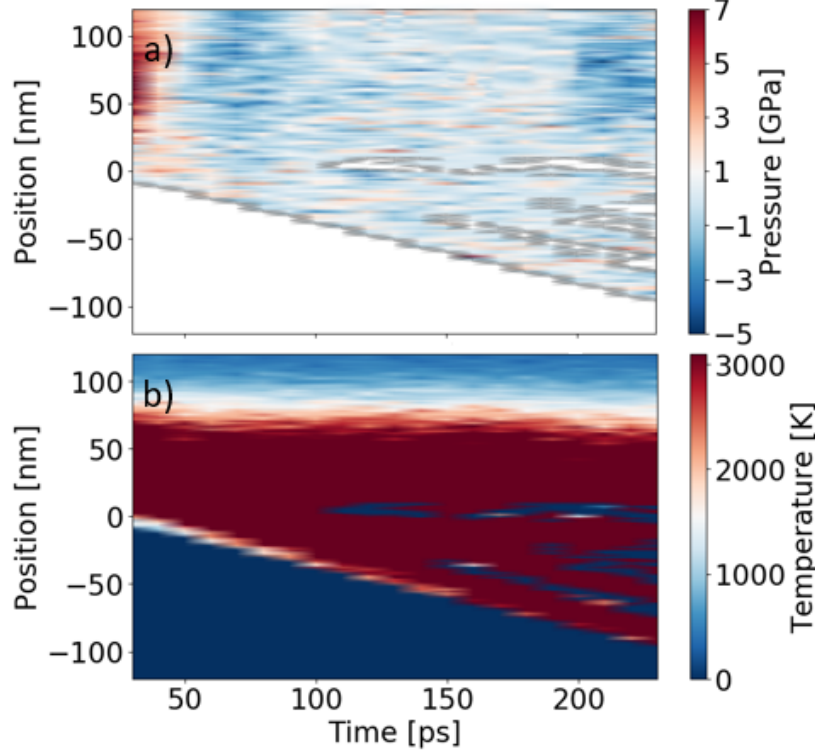


Figure 3.24: Spatiotemporal evolution of thermodynamic quantities in the surface region: a) pressure, and b) lattice temperature evolution in  $\alpha$ -Cu<sub>33.3</sub>Zr<sub>66.7</sub> sample target. The initial surface position is given by  $x_{\text{surface}} = 0$  nm following the  $x$  axis direction.

The origin of this tensile stress is due to the relaxation of the compressive pressure leading to a rapid expansion of the targets which generates tensile stress. During times of  $t = 100$  and  $230$  ps the region still experiences pressure depression. This tensile stress induces a process of cavitation by void formation which starts precisely at  $t = 100$  ps. The upper atomic layers were extracted over time, accompanied by atom debris ejections. In reality, the targets were characterized by the ejection of two thick layers that moved away gradually from the substrate. In addition, a disintegration into various liquid nanoparticles of different sizes is observed. These conditions of stress confinement occur under fast heating as shown by the temperature profile in Figures 3.23(b), 3.24(b) for the  $\alpha$ -Cu<sub>50</sub>Zr<sub>50</sub> and  $\alpha$ -Cu<sub>33.3</sub>Zr<sub>66.7</sub> targets respectively.

Meanwhile, we have in both amorphous targets as shown in Figures 3.23(b), 3.24 (b) a sharp increase of the temperature from 300 to a maximum value of 3000 K. During the temperature diffusion to the immediate subsurface zone, a value of  $\sim 1500$  K is recorded. At  $t = 230$  ps, the observation of the maps

corroborates that the ejected layers have a temperature of  $\sim 3000$  K. However, the ejected nanoparticles have temperatures oscillating within a values range of  $\sim 1000$ - $2500$  K. Based on these results, the individual droplets with temperatures  $\sim 1000$  K were expected to be in crystalline structure due to the rapid cooling, but the analysis shown in the previous Figure 3.22 that the amorphous character is dominant. It can be hypothesized that the absence of crystallization occurs (i) due to the tensile rarefaction wave magnitude sufficient to induce spallation in the molten part but not to reorganize atoms below the surface in an ordered manner, or (ii) due to the unfavorable stoichiometry.

### 3.7 Summary conclusion

Laser-induced structural transformations in Zr-based alloys for crystalline and glassy states are investigated here. The ultrafast thermomechanical response is compared between relevant stable crystalline structures  $B_2$ - $Cu_{50}Zr_{50}$ ,  $C11_b$ - $Cu_{33.3}Zr_{66.7}$  and the amorphous structures  $\alpha$ - $Cu_{50}Zr_{50}$ ,  $\alpha$ - $Cu_{33.3}Zr_{66.7}$ . The subsurface modification resulting from ultrafast laser irradiation is investigated by a hybrid simulation to capture the phenomenon occurring on a picosecond time scale. This combines a two-temperature model and molecular dynamics approaches to simulate laser-matter interaction at the mesoscale. In crystalline CuZr systems, the subsurface structural phase transition and defect formation processes attributed to ultrafast laser shots are predicted using TTM-MD atomistic calculations.

In summary, using the same laser conditions, two remarkable outcomes are reported here depending on the initial crystallographic structures. The original  $B_2$  crystalline sample phase-transform into twinned  $B_{19}$  while  $C11_b$  shows a huge deformation pattern including points defects and shear zones. Both transformations are driven by the rarefaction pressure wave. They are permanent as the materials reach metastable states in the calculations and are localized within the subsurface. Therefore, they can be captured experimentally. Concerning the  $B_2$  structure, the simulation corroborates that the phase transformation and the twinning process emerge in a quasi-ordered manner, exhibiting no spatial variability across the crystalline structure. In contrast, the response of the  $C11_b$  structure is different as the defects generation is noticed instead of a martensite phase transition. On the other hand, the response of the irradiated MGs counterparts shows a completely different structural response. Indeed, no crystallization is noticed under the same laser conditions. Besides the surface ablation in the MGs, we might have expected the laser shock to induce recrystallization by play-

ing a similar role as a nanoindenter [350, 351, 352].

Targeting innovative technological applications requires the control of local crystalline structures properties at the nanoscale that can be promoted by laser-matter interactions. Dislocations and twins that appear at the nanoscale as a strain relaxation mechanism can be frozen within a solid alloy. As predicted in the  $B_2$  structure, this leads to the emergence of advantageous mechanical properties [353]. Nano-sized twins are known to enhance hardness [354] and nano-twinned materials become more resilient to fracture and fatigue crack initiation during plastic deformation [355]. Nano-architecturing of the  $C11_b$  structure with defects (points defects, dislocations, stacking faults) could be exploited for battery applications [356], elaboration of high-performance thermoelectric materials [357] or improving the fracture toughness [358]. The originality of this work is that ultrafast laser irradiation could provide an effective method to tune a new generation of nano-architected CuZr alloys which might open new routes for future industrial applications. A promising route for manufacturing emergent metamaterials is the use of ultrafast laser pulses in complex alloy processing.

# Chapter 4

## Modeling of cavitation formation in amorphous CuZr alloy

### 4.1 Introduction

Many theoretical studies have been made to understand the impact nanovoid on the material properties in both crystalline and amorphous phases to check whether any enhancement occurs for a potential industrial application. As an illustration, the recent investigation of Hofer *et al* [359] on iron (Fe) provides strong evidence that voids presence few nanometers below the surface modifies the response of Fe to nanoindentation at ambient temperature. They showed that voids act as absorbers for dislocations and limit the extension of the plastic zone. Another study on gold (Au) performed by Tran *et al* [360] confirms that due to the presence of void in the system the deformation area is concentrated around it. This situation leads to a localized phase change. As a consequence, the material structure elsewhere is preserved. The voids nucleation was identified in the work of Bowman *et al* [361] on amorphous polyethylene as the dominating damage mechanism by driving chain dynamics throughout the distinct stages of the creep response. Furthermore, an interesting study on response of porous amorphous  $\alpha$ -Cu<sub>50</sub>Zr<sub>50</sub> under shock loading was performed by Wen *et al* [362]. It was shown that with the void collapse a plastic deformation is generated inducing shear transformation zone (STZ) nucleation within a limited region around the void. Moreover, Xin *et al* [363] presented an original work where they combined experimental and theoretical fabrication, the reaction of layered porous CaO/Co<sub>3</sub>O<sub>4</sub> offers an original way for controlling and tailoring the thermoelectric properties of materials. Intriguingly, it is found in the work of Neogi *et al* [364] that tailored nanovoid in FCC copper (Cu) crystal containing combinations that close and open cell pore greatly facilitates the energy absorption. Also, it was observed in the simulation presented by Zou *et al* [365] that the presence of

void inside the Nickel (Ni) provides a unique method to stabilize the diffusing oxygen atoms. Thus, efficient internal oxidation of Ni is initiated due to vacancy movement. In the same spirit, for the nanoengineered applications Liu *et al* [366] showed that adding void inside a superalloy composed of a realistic Ni<sub>3</sub>Al  $\gamma'$ -phase embedded in Ni  $\gamma$ -phase modify the dislocations within this material which conduct to decrease the ductility of the material.

A novel way that brings into play nanowells and nanocavities by a femtosecond laser process, especially inside transparent materials such as metallic glass or crystals is a promising manufacturing method for tuning new generations of material with outstanding properties. The cavitation mechanism triggered by an ultrafast laser is one of the most typical processes which is generally manifested by the production of voids that settle within the sub-surface region. This process was investigated by Shih *et al* [367] via irradiating a silver (Ag) target put inside the water to prevent spallation regime due to confinement. It was confirmed that the water presence stabilizes the voids formed and frozen in the molten part of the target during solidification. Extra pertinent information concerning the nanovoids formation mechanism in metals (Ni, Cr, Al, and Ag) was mentioned in the work of Shugaev *et al* [368]. In this spallation fluence working regime the theoretical computations finding corroborate that the apparition of voids coincides with a minimum value of the free energy barrier favored by the apparition of unloading wave. A primordial role is played by the surface morphology (nanoscale roughness on the surface) during the light-matter interaction is discussed in the work of Karim *et al* [369]. These results show an interfacial void within a thick Ag-silicate glass layer caused by the contraction of the interfacial region combined with tensile stresses produced by the unloading wave. A more challenging exercise of processing Ag nanoparticles by femtosecond laser technique capable to induce a permanent hollow was reported by Jiang *et al* [370]. The interpretation of results confirms that the morphological change mechanism is correlated to two process pressure relaxation and diffusion of the silver atoms.

## 4.2 Outline of the objectives

It is widely common to use the MD method as a theoretical tool in order to validate experimental results, especially when the mechanisms are ambiguous and not fully understood. This said, it is obvious that the MD setup and parameters must be as close as possible to the experimental ones. In this chapter, we present an original and exhaustive theoretical study of void formation that we benchmarked against experimental results. For such purpose, a computer *in silico* MD

approach appeared to be suitable in order to understand the experimental results presented by Prudent *et al* [371] of ultrafast laser inducing sub-surface nanowells within amorphous  $\alpha$ -Cu<sub>35</sub>Zr<sub>65</sub> is exposed. In this experimental investigation, ultrafast laser irradiation creates dense nanowell arrays. These nanowells have a flared shape, as observed through transmission electron microscopy, making them ideal for immobilizing chemical or biological substances. The size and density of the nanometric interstices in the film deposited by magnetron sputtering can be used to control the formation of cavitation-induced nanopores. In addition to topographic functionalization, laser irradiation also leads to structural changes at the nanoscale, as revealed by spectroscopic techniques such as energy-dispersive X-ray spectroscopy and electron energy loss spectroscopy. The results show that nanocrystals of monoclinic zirconia grow within the amorphous matrix, driven by a local oxidation process.

In contrast to experimental observation, both advantages of the model (to use single pulse instead multi-pulses nanowells are preserved) and limitations often encountered in MD (to predict complex mechanism as segregation and oxidation mechanisms) are explained and justified. Moreover, a quantitative characterization of the nucleation, growth, and coalescence of nanowells as well as their volume, and location during the response to laser irradiation was systematically described.

It was proven that experimentally, the roughness of the system has a huge impact on the formation and morphology of nanowells in the subsurface of the irradiated material [312]. Working with a very smooth surface state with low roughness is suitable for two reasons, favoring the creation of self-organized multi-scale structures under optimal conditions, and approaching simulation conditions where the surface is perfectly flat without any roughness. So, before laser irradiation, the MGs used had low root-mean-square roughness, roughly less than 2 nm, as measured with atomic force microscopy.

### 4.3 Simulation setup and computational details

A modified version of the previous laser-matter interaction setup presented in chapter 3 is used in the concurrent investigation. The main difference is the introduction of a cylindrical nanopore having a length of  $L_{TTM-MD}$  following  $x$ -direction and a diameter of 1 nm. The goal of tuning such an initial sample is to obtain a realistic sample identical to the experiment one in order to inves-

tigate the cavitation mechanism within amorphous  $\alpha\text{-Cu}_{35}\text{Zr}_{65}$  as shown in the experimental Figure 4.1.

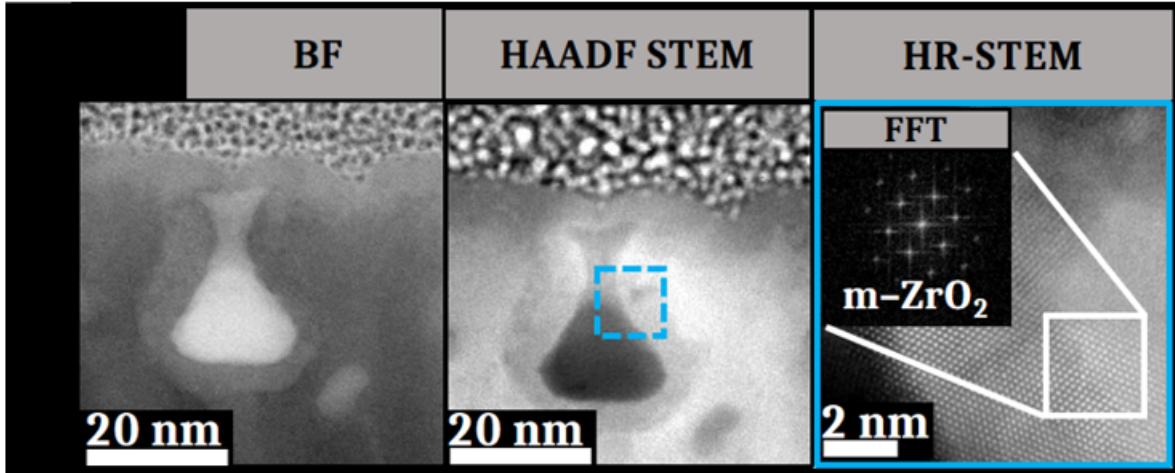


Figure 4.1: STEM (Scanning Transmission Electron Microscopy) pictures in BF (Bright Field), HAADF (High Angle Annular Dark Field) STEM mode of a nanowell zone irradiated with 50 bursts, a HR-STEM image on a location surrounded in blue with the 2D-FT as inset reveals a crystalline structure under an fluence of  $60 \text{ mJ/cm}^2$  with 50 pulses. Adopted from [371].

An initial  $\alpha\text{-Cu}_{35}\text{Zr}_{65}$  crystalline structure with 55566 atoms was subjected to the amorphization cycle 3.6 to prepare the initial amorphous  $\alpha\text{-Cu}_{35}\text{Zr}_{65}$ . The  $\alpha\text{-Cu}_{35}\text{Zr}_{65}$  supercell was replicated such that a simulation box of dimension  $813.83 \times 14.28 \times 12.40 \text{ nm}^3$  following  $x$ ,  $y$  and  $z$  respectively is obtained. To simulate laser-matter interaction, free boundary conditions were applied to the longitudinal laser  $x$ -direction, as well as periodic boundary conditions to the transverse directions  $y$  and  $z$ . The calculation box was divided into two distinct regions along  $x \sim 400 \text{ nm}$  for the vacuum and the MG thickness where the 100 nm rear side serves as non-reflecting boundary conditions as shown in Figure 4.2.

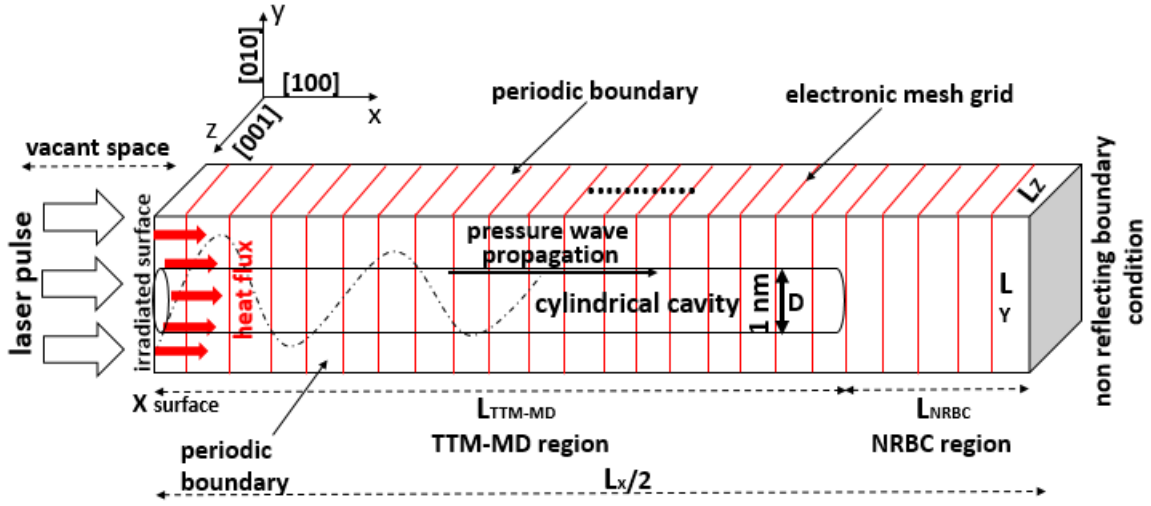


Figure 4.2: Simulation setup geometry used to model nanowell insertion and void formation by ultrafast laser pulse interaction with amorphous  $\alpha$ -Cu<sub>35</sub>Zr<sub>65</sub> using TTM-MD simulations.

To mimic a realistic morphology of the sample a cylindrical interstices between the columns along the  $x$ -direction of a 1 nm diameter was inserted. Before depositing the energy on the surface. The MG structure was relaxed under isothermal-isobaric ensemble (NPT) at 300 K and 1 bar pressure for 10 ps in Nose-Hoover (thermostat-barostat) style. Then the TTM-MD stage took place during 15 ps solved in an electronic grind of  $702 \times 1 \times 1$  with an MD integration timestep of  $\Delta t = 1$  fs. Finally, the system is evaluated by an MD simulation for an extra 150 ps duration using a micro-canonical ensemble.

To observe the formation of the void, the laser conditions were set in accordance with the experimental data. Preliminary ellipsometry measurements gave the complex optical index for cold material of  $\tilde{n} = n + ik = 2.6 + 3i$ . For the simulation, the skin depth  $l_p$  was fixed to  $\sim 15$  nm considering the expected transient change of  $\tilde{n}$  due to the induced electron-phonon nonequilibrium during the laser pulse energy deposition. As in the current experiment, an absorbed fluence of  $60 \text{ mJ/cm}^2$  and a pulse duration of 60 fs were used. The EAM potential employed was developed by Mendeleev *et al* [316], the thermodynamic quantities mapping (surface meshing) were obtained using the OVITO [275, 280] and the electronic properties employed were selected from table 3.5.

## 4.4 Modeling the ultrafast laser irradiation of $\alpha$ -Cu<sub>35</sub>Zr<sub>65</sub>

### 4.4.1 Nanovoids formation

Figure 4.3 illustrates nanocavitation in  $\alpha$ -Cu<sub>35</sub>Zr<sub>65</sub> MG. A series of snapshots in the time range of  $t = 0$ -165 ps indicate that cavitation growth and coalescence occur at around  $\sim 28$  nm deep under the initial melted surface.

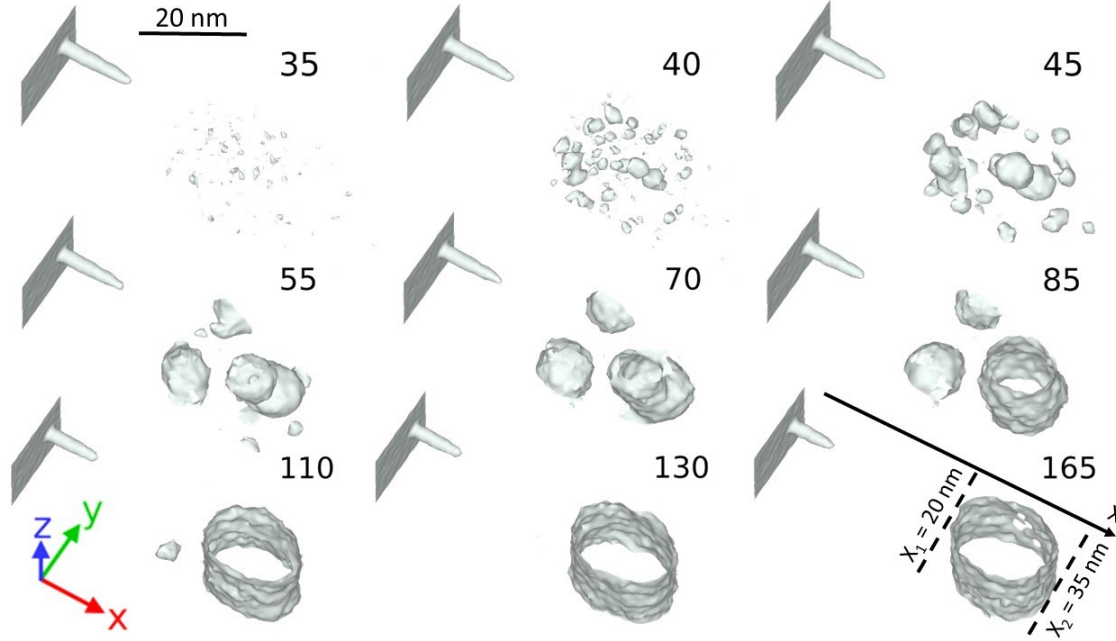


Figure 4.3: Outer surfaces mesh showing the evolution of nanocavities within amorphous  $\alpha$ -Cu<sub>35</sub>Zr<sub>65</sub> at several key times  $t = 35, 40, 45, 55, 70, 85, 110, 130,$  and  $165$  ps. The target was subjected to an ultrafast laser conditions of  $\tau = 60$  fs and  $F_{\text{abs}} = 60$  mJ/cm<sup>2</sup>. The construct surface mesh algorithm was applied using a probing radius of  $r_{\text{probe}} = 3.22$  Å as implemented in OVITO [275, 280].

The first pertinent observation we report is the progressive and partial collapse of the initial introduced cylindrical cavitation in the Heat Affected Zone (HAZ) at  $t = 35$  ps due to the expansion (elongation) of the target. Furthermore, we have identified four stages of void fraction evolution within  $\alpha$ -Cu<sub>35</sub>Zr<sub>65</sub>. Broadly, the first stage is the nucleation appearing in the time range of  $t = 25$ -35 ps. The second process is occurring at  $t = 35$ -45 ps where rapid growth is observed. In the third stage,  $t = 45$ -110 ps, these small voids merge and coalesce to form the larger ones. In the last stage where  $t = 110$ -165 ps the system exhibits a void expansion until reaching its final volume. All these stages are well known, described, and discussed in the literature, especially for monoatomic metallic targets [315, 110, 109, 372].

#### 4.4.2 Thermodynamics of the voids formation in $\alpha$ -Cu<sub>35</sub>Zr<sub>65</sub>

This section provides an in-depth look at how nanowells form. The first stage is to correlate quantitatively the number of formed voids with the temporal evolution of the pressure conditions on the surface. The result is shown in Figure 4.4.

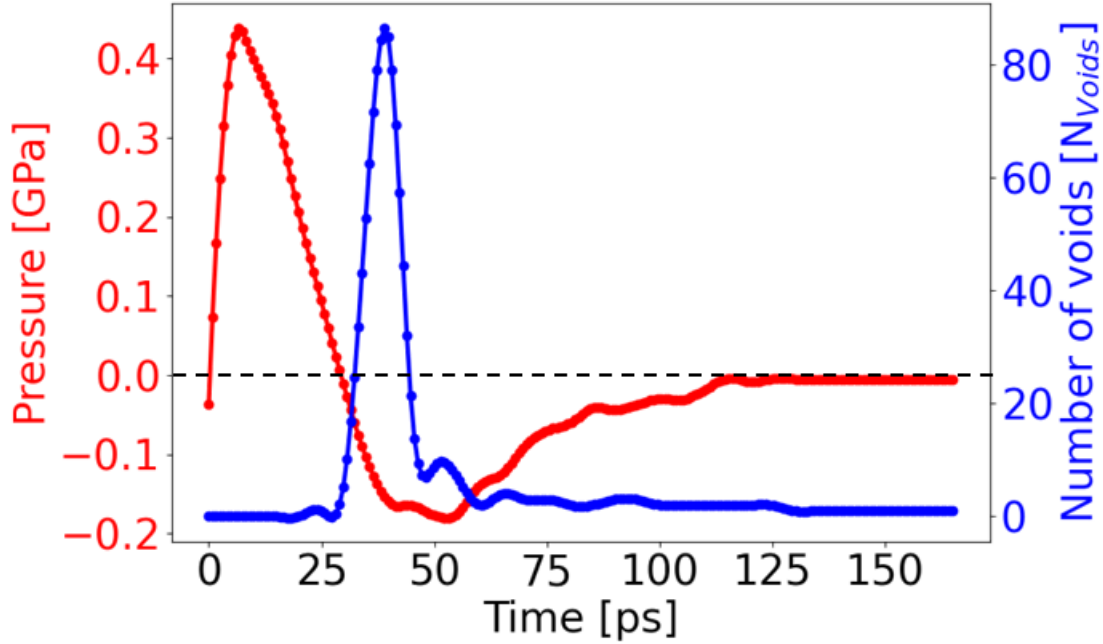


Figure 4.4: Temporal evolution of the average pressure and the total number of voids  $N_{Voids}$  during the time of the void formation process within  $\alpha$ -Cu<sub>35</sub>Zr<sub>65</sub> target. We notice that the maximum negative value of pressure (blue line) coincides with the maximum value of the formed voids (red line).

In Figure 4.4, the pressure is averaged over all the system regions, the goal is to identify a global trend rather than a local tendency for the formation of voids. We noted that for  $t = 0$ -25 ps the glass structure experiences loading stress with a maximum value of  $\sim 0.45$  GPa where the number of voids is 0. This observation corroborates that the formation of voids is not caused by compression pressure waves. In the time range of  $t = 25$ -35 ps, the nucleation process is triggered, where the decrease of pressure is noticed to reach a maximum value of  $\sim -0.2$  GPa marking the presence of an unloading pressure wave with tensile stress penetrating deep into the material. This unloading mechanism finds its origins in the relaxation of the free surface to evacuate the compressive stress as described in the paper [373]. Meanwhile, the number of voids with different volumes (See Figure 4.3) reaches its peak with 84 detected voids. Based on these observations, we claim that the tensile stress is sufficiently strong to favor void growth. During the time range of  $t = 45$ -110 ps, as well as the coalescence of voids, there is a clear drop in the number of voids from 84 to 6. This is accompanied by a progressive

reduction in tensile stress. When  $t = 110\text{-}165$  ps one permanent void appears on the surface with its critical size defined by a pressure tendency to 0 GPa.

In order to provide detailed information concerning the local thermodynamic (P-T) profiles during void formation, a spatial portion of 80 nm (depth for  $x$  in the range  $-15\text{-}65$  nm) and  $\sim 14$  nm thickness along  $x, y$  directions was selected near the cavitation zone. A data slice is performed following the  $z$  direction precisely at  $l_z/2$ , then from this middle plane, 2 neighboring atomic plans following each direction side ( $+z$  and  $-z$ ) were defined to average both temperature and pressure. The corresponding P-T results are shown in Figures 4.5 and 4.6.

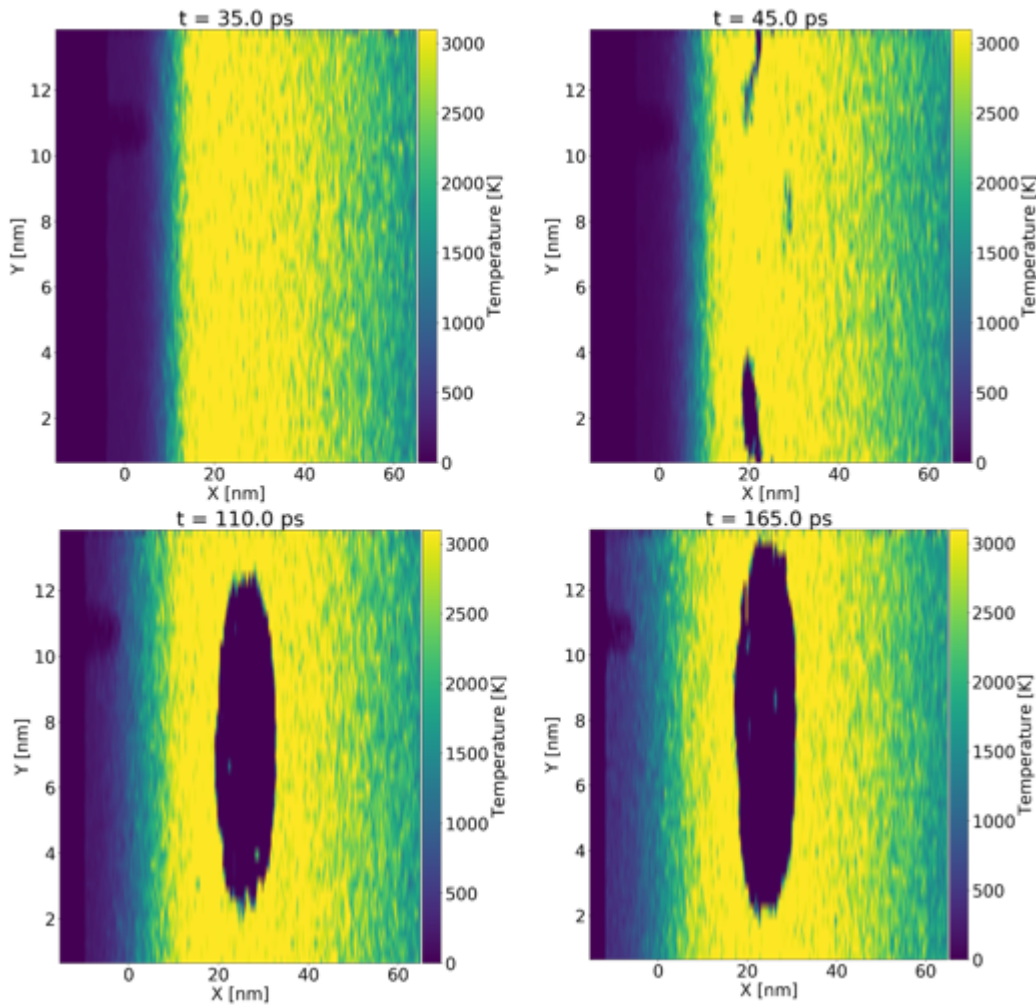


Figure 4.5: The temperature spatial maps around the void forming zone at the key times of  $t = 35, 45, 110,$  and  $165$  ps within the amorphous  $\alpha\text{-Cu}_{35}\text{Zr}_{65}$ . The ultrafast laser conditions of  $\tau = 60$  fs and  $F_{\text{abs}} = 60$  mJ/cm<sup>2</sup> were used.

Figure 4.5 illustrates the spatial temperature distribution around the cavitation zone when  $t = 35, 45, 110,$  and  $165$  ps correspond to nucleation, growth, coalescence, and expansion processes respectively. Indeed, we observed at  $t =$

35 ps that the surface front is not fitting with the 0 position meaning that an elongation following the  $x$ -axis occurred. The temperature in this region beyond the initial surface position is within a range of  $\sim 500$ - $1000$  K which indicates that quick solidification is ongoing. In addition, for  $x$  in the region  $\sim 15$ - $40$  nm the amorphous target is at  $T \sim 3000$  K much above the melting temperature indicating a solid-liquid phase transition.

Always at  $t = 45$  ps, maps reveal a relevant information, that several voids started to appear inside a liquid part of the system during homogeneous melting at a lattice temperature of  $T \sim 2800$  K. At  $t = 110$  ps this cavitation ( $\sim 28$  nm below the surface) causes a significant obstacle to heat propagation deep inside the sample. Due to the fact that the system is in a liquid phase in this region, it affects the electronic properties including the thermal conductivity around the cavitation region [315]. This substantial drop in thermal conductivity leads to the confinement of the laser energy in the subsurface. At a later time precisely  $t = 165$  ps, the temperature surrounding the void environment is  $T \sim 2500$  K. It is necessary to determine what prevents this void from collapsing. The answer is probably linked to the influence of pressure, as demonstrated in the cartography shown in Figure 4.6.

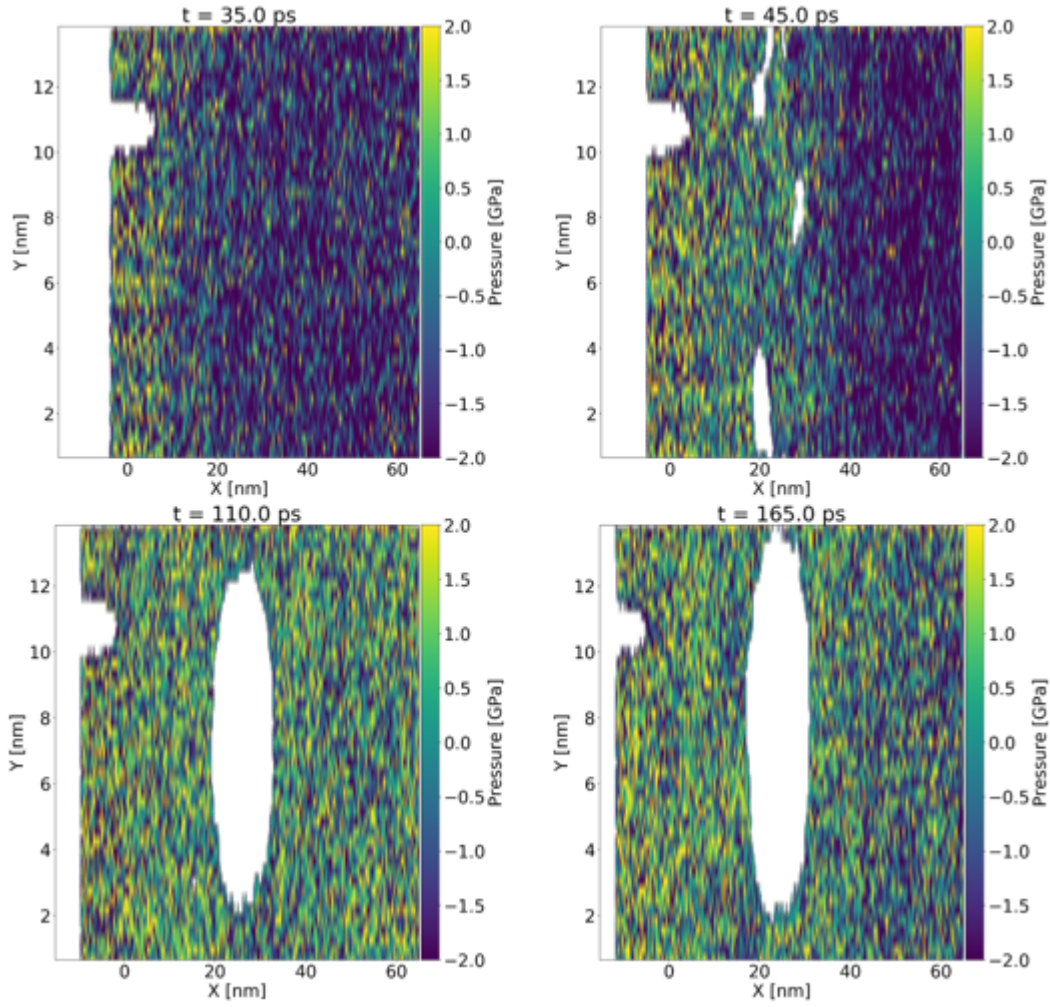


Figure 4.6: The pressure spatial maps around the void forming zone at key times of  $t = 35$ , 45, 110, and 165 ps within the amorphous  $\alpha$ -Cu<sub>35</sub>Zr<sub>65</sub>. The ultrafast laser conditions of  $\tau = 60$  fs and  $F_{\text{abs}} = 60$  mJ/cm<sup>2</sup> were used.

As mentioned in the previous chapter, fast laser heat deposition generates compressive pressure on the surface that travels through the material. Figure 4.6 shows that at  $t = 35$  ps, the x-y spatial map in the spatial region located  $x = -15$ -65 nm confirms that the system is under a tensile stress of  $\sim -2$  GPa due to the rarefaction pressure wave. Also, we noticed that at  $t = 45$  ps the first cavitation openings in the liquid are detected with a tensile pressure that is always  $\sim -2$  GPa. As a result, we assume that the rarefaction wave propagation comes up with a rapid expansion of the subsurface, leading to an elongation that permits cavitation. At  $t = 110$  ps, we clearly observe the presence of coalescence processes in the vicinity of the cavitation zone. This coalescence is accompanied by a relative drop in pressure from  $-2$  to  $\sim -0.5$  GPa. The accumulation of voids at  $t = 165$  ps under tensile stress allows the void to reach its maximum size as well as prevent its collapse.

### 4.4.3 Front expansion average velocity

The spatial-temporal evolution of the P-T indicates that the material experiences elongation due to the relaxation of laser-induced stresses. Indeed, the elongation of a thin liquid region was followed by significant nucleation of voids. This rapid expansion is characterized by an ejection velocity that stabilizes once a complete void is formed. The velocity of the surface front is shown in Figure 4.7.

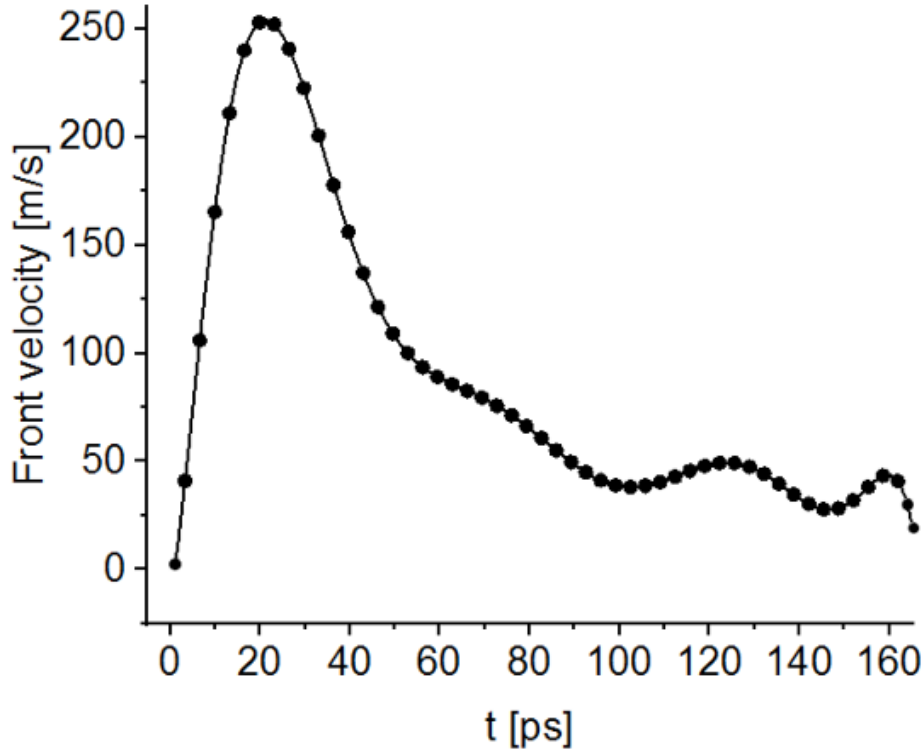


Figure 4.7: The time dependence of the average velocity of the subsurface region elongation along the  $x$ -axis during the cavitation process within amorphous  $\alpha$ -Cu<sub>35</sub>Zr<sub>65</sub>. The ultrafast laser conditions of  $\tau = 60$  fs and  $F_{\text{abs}} = 60$  mJ/cm<sup>2</sup> were used.

The expansion and cavitation processes are correlated. As the melted part reaches the vacuum region, it detaches from the main amorphous structure block. Thus, a region of about 60 nm thickness partially detaches and moves away. At this moderate absorbed fluence of 60 mJ/cm<sup>2</sup> no ablation occurs. The surface elongates in the direction  $-x$  in opposition to the direction of the femtosecond laser irradiation energy deposition.

During the time interval of  $t = 5$ -25 ps, the nucleation process began and small voids appeared. The sample front accelerated and reached a maximum velocity of  $\sim 250$  m/s in a total agreement with literature studies in this laser fluence regime [315, 110, 374]. As well, at times  $t = 25$ -110 ps this velocity decreases, which is logical as during coalescence the voids often have a tendency

to merge and no new voids appear. The velocity is almost constant at  $t = 110$ - $165$  ps, oscillating around 45 m/s, which is explained by the fact that the void has recovered its critical size.

#### 4.4.4 Quantification of voids

The previous studies provide a qualitative description of the evolution of voids after laser energy deposition. However, no insight into the exact volume of this formed void is delivered. Hence, the concurrent section complements the investigation by providing this missed information. A quantitative result of the total volume size evolution of voids formed within  $\alpha$ -Cu<sub>35</sub>Zr<sub>65</sub> amorphous target as functions of time is presented and discussed in Figure 4.8.

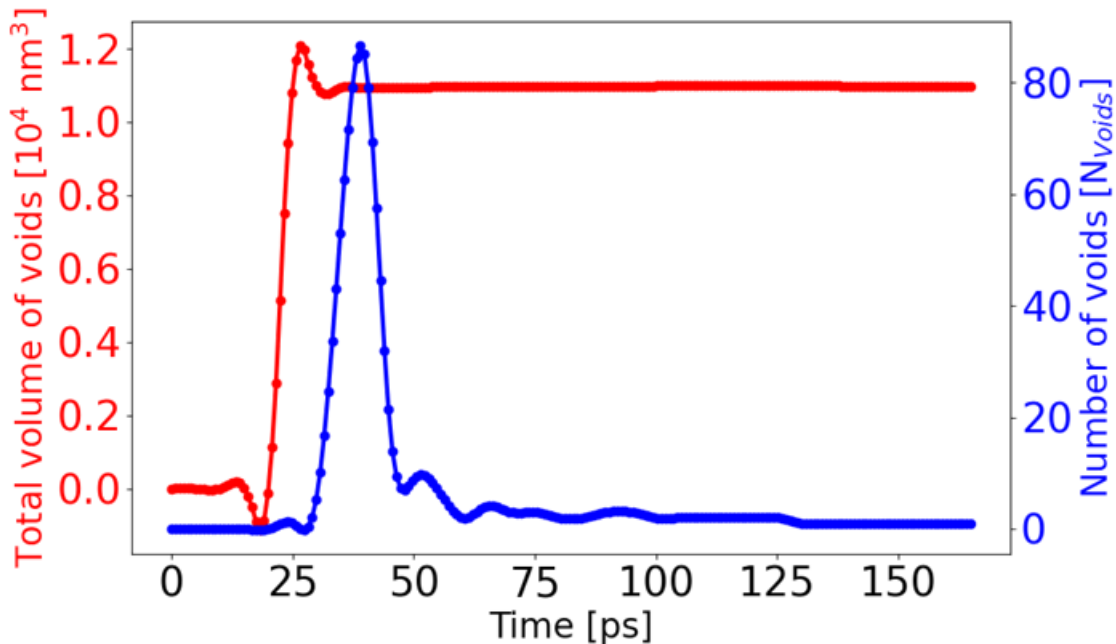


Figure 4.8: The temporal evolution of the total number of voids  $N_{Voids}$  (blue line) and the total volume of voids (red line) is shown. The process of void formation is characterized by four stages: void nucleation, growth/coalescence, contraction, and stable void trapping.

At  $t = 0$ - $25$  ps, no voids were detected and the value of the volume was 0. However, during the nucleation between 25 and 35 ps, the number of voids rises to  $\sim 85$  which lead to an abrupt increase in volume from 0 to  $\sim 1.2 \cdot 10^4 \text{ nm}^3$ . During the range of  $t = 35 - 110$  ps, the number of voids was drastically reduced due to coalescence process. A critical volume of  $\sim 1.15 \cdot 10^4 \text{ nm}^3$  was recorded with no notable drop of volume mainly due to a minimization of the surface energy of the voids. In the final stage when  $t = 110$ - $165$  ps, the volume expands to one big void with a critical value of  $\sim 1.13 \cdot 10^4 \text{ nm}^3$ , while the number of voids tends to remain constant.

## 4.5 Experimental versus modeling results

The mechanism behind the void formation was studied and observed experimentally with the same theoretical laser conditions as described in the work of Prudent *et al* [371], the results are shown in Figure 4.9.

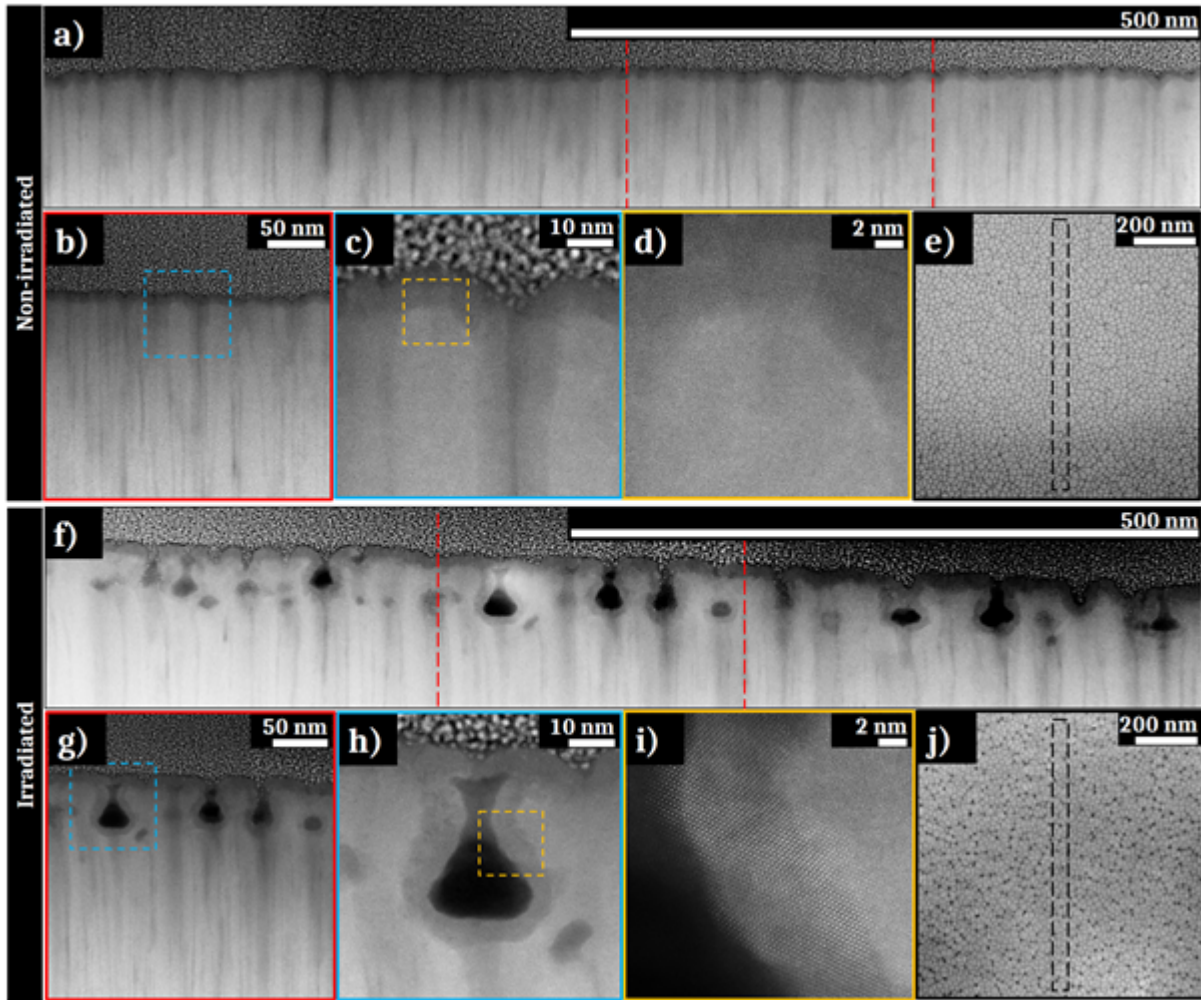


Figure 4.9: a–d) High-Angle Annular Dark-Field (HAADF) STEM images of a FIB lamella obtained from a non-irradiated area displaying the initial columnar morphology of the thin film, d) the lack of visible order is characteristic of an amorphous structure; e) SEM picture of the FIB lamella extracted zone from the non-irradiated sample. f–i) HAADF STEM images of a FIB lamella obtained from a textured area irradiated under the fluence of  $60 \text{ mJ/cm}^2$  with 50 pulses, exhibiting nanowells on the sub-surface of the thin film. h) shows an open nanowell. i) shows columns of atoms characteristic of a crystalline structure surrounding this nanowell. j) SEM picture of the FIB lamella extracted zone from the irradiated sample [371].

As a first insight, the data collected from experimental manipulations shown in Figures 4.9 a–d) show the lower part of the sample where a dark zone with different contrast on the subsurface is clearly noticeable. According to the interpretation, it is mainly due to the change of density within the amorphous

sample as confirmed in the enlarged view in Figure 4.9 d). The most interesting characterization is the obtained nanowells shown in Figure 4.9 j) where we clearly distinguish by comparing it to the sample before irradiation the voids and nanowells presence as shown in Figure 4.9 e-f). These nanowells are located  $\sim 50$  nm deep below the initial surface very close to the obtained theoretical value of  $\sim 40$  nm.

Moreover, compared to the simulation work only non-detached voids were recovered in a reasonable agreement with the experiment as illustrated in Figure 4.9 g-h). The chemistry near the voids was investigated to establish the chemical and structural features as shown in Figure 4.9 i). Surprisingly, a crystalline phase surrounding the voids was detected. It corresponds to monoclinic zirconia ( $m\text{-ZrO}_2$ ) produced by an oxidation process as illustrated in more details in Figure 4.10.

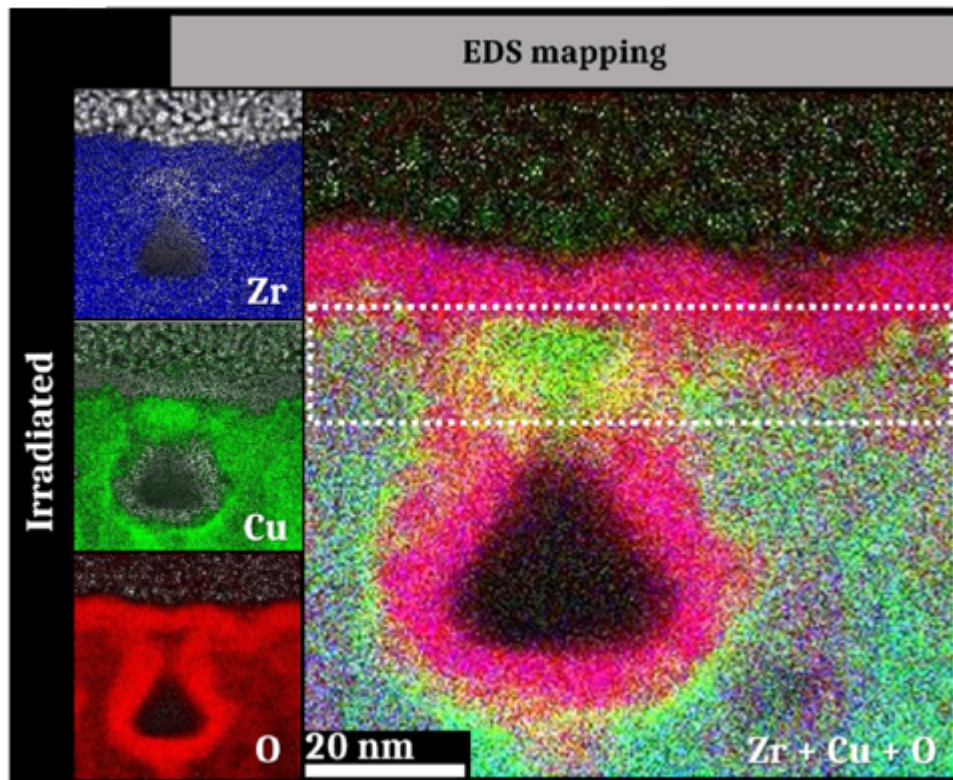


Figure 4.10: EDS image mapping of the STEM zone under an fluence of  $60 \text{ mJ/cm}^2$  with 50 pulses. Adopted from [371].

The result reported above exhibits the EDS mapping of the irradiated area showing particularly the distribution of each species element namely, Zr, Cu, and O. We notice on the top part of the void a large amount of Zr and O with a thickness of  $\sim 10$  nm. This region was characterized as completely oxide-

accompanied. Simultaneously, the Cu is segregated in the vicinity of the void.

This oxidation process was triggered by a femtosecond laser with a low rate (50 pulses) and under atmospheric pressure with oxygen present during the experiment. As a result, even though the MD single pulse model is realistic, unfortunately we were not able to capture this complex process involving oxygen by numerical modeling. This shows a limitation to modeling chemical reactions through bond formation and breaching. Therefore, this ability of short laser pulses to produce localized nanoscale oxide structures within the amorphous target may provide a more effective way of tuning surfaces for physical applications.

## 4.6 Summary conclusion

In summary, a combination of numerical and experimental study of structural modification within  $\alpha$ -Cu<sub>35</sub>Zr<sub>65</sub> sample irradiated by a femtosecond laser pulse was explored, discussed in order to understand the complex mechanisms responsible for this subsurface modifications. The MD simulation was useful to predict the experimental cavitation observation and give a complementary explanation attributed to fast melting and the relaxation dynamics of laser-induced tensile stress. The experimental work revealed an unusual phase transformation emergence at the subsurface by the presence of nanocrystalline layers of zirconia in the vicinity of these subsurface porous regions. These phase transitions are expected to originate from atomic rearrangements due to the abundance of oxygen throughout the oxidation process. Nevertheless, besides these mechanical effects the simulation failed to capture the chemical side of the process in this case oxidation. This limitation can be overcome in the future by developing a suitable adapted ZrO<sub>2</sub> ReaxFF interatomic potential. In addition, a free energy computation will give another answer of phase stability by demonstrating why a ZrO<sub>2</sub> crystalline phase is favored instead of copper oxides such Cu<sub>2</sub>O or CuO. These results are very useful for concrete technological application for possible enhancement of the catalytic activity of the surface, wettability, or trapping macro-molecules in these porous media for biological application.

# Chapter 5

## Atomistic simulation of CuZr Metallic glass devitrification

### 5.1 Introduction

Tremendous efforts were devoted to trigger, understand and control crystallization within amorphous materials, especially CuZr glassy alloys. So far, the major process found in the literature to devitrify CuZr metallic glasses is by an annealing procedure in the supercooling domain [375, 376]. As reported in the work of Zemp *et al* [377] and Ryltsev *et al* [378] that amorphous  $\text{Cu}_{64}\text{Zr}_{36}$  experiences the emergence of a primary crystal  $\text{Cu}_2\text{Zr}$  Laves phase that is composed of Cu-centered icosahedra and Zr-centered CN-16 Frank-Kasper polyhedra which is mainly due to structural relaxation. An interesting MD simulation was performed on bulk  $\text{Cu}_{64}\text{Zr}_{36}$  glass by Brink *et al* [379] where it was found that under mechanical constraints, a transition from glass-like to a glass-crystal (small crystallites) composite occurs as a result strain localization tendencies in the amorphous phase. An additional parameter that impacts devitrification was exposed by the work of Xie *et al* [380]. According to this investigation, the coating deposition process of CuZr amorphous structures on silicon revealed that during the deposition and growth of CuZr amorphous systems, devitrification occurs depending on the initial composition. Furthermore, new insight was provided in the work of Hu [196] *et al* to understand the devitrification process and its correlation to GFA in amorphous  $\text{Cu}_{50}\text{Zr}_{50}$  with a crystalline inclusion during annealing. It has been demonstrated that factors such as crystallization driving force, glass-crystal interface, and particle attachment rate play a critical role in affecting the GFA for the efficient design of future composites. Actually, the glass-crystal interface effect was explained in the work of Duan *et al* [210]. A supercooled  $\text{Cu}_{64}\text{Zr}_{36}$  liquid was sandwiched between two pure Cu and Zr thick layers, where the confinement caused devitrification via interfacial effects. Also,

they noted that when the separation distance of Cu-wall and Zr-wall is within 10 to 12 Å, a maximum liquid-crystal transition was observed. As far as we know, no theoretical work has used an ultrafast laser pulse to induce phase transitions within CuZr glasses metallic. To elucidate the mechanisms involved during nanodevitrification, an exhaustive hybrid MD analysis is presented herein.

## 5.2 Ultrafast laser driving devitrification strategy

Driving devitrification within Cu-Zr MG system with an ultrashort laser is a complex process that needs an adapted investigation method. Therefore, a theoretical modeling study that combines TTM with deterministic classical MD is proposed. The idea is to predict the correct laser conditions giving rise to devitrification namely, fluence and pulse duration. In addition to the P-T thermodynamic conditions, the initial chemical environment also affects the crystal's emergence and growth. In contrast, a different behavior was observed when we decreased the presence of Zr where no crystal growth was detected. The investigation strategy chronology is summarized in the flow chart shown in Figure 5.1.

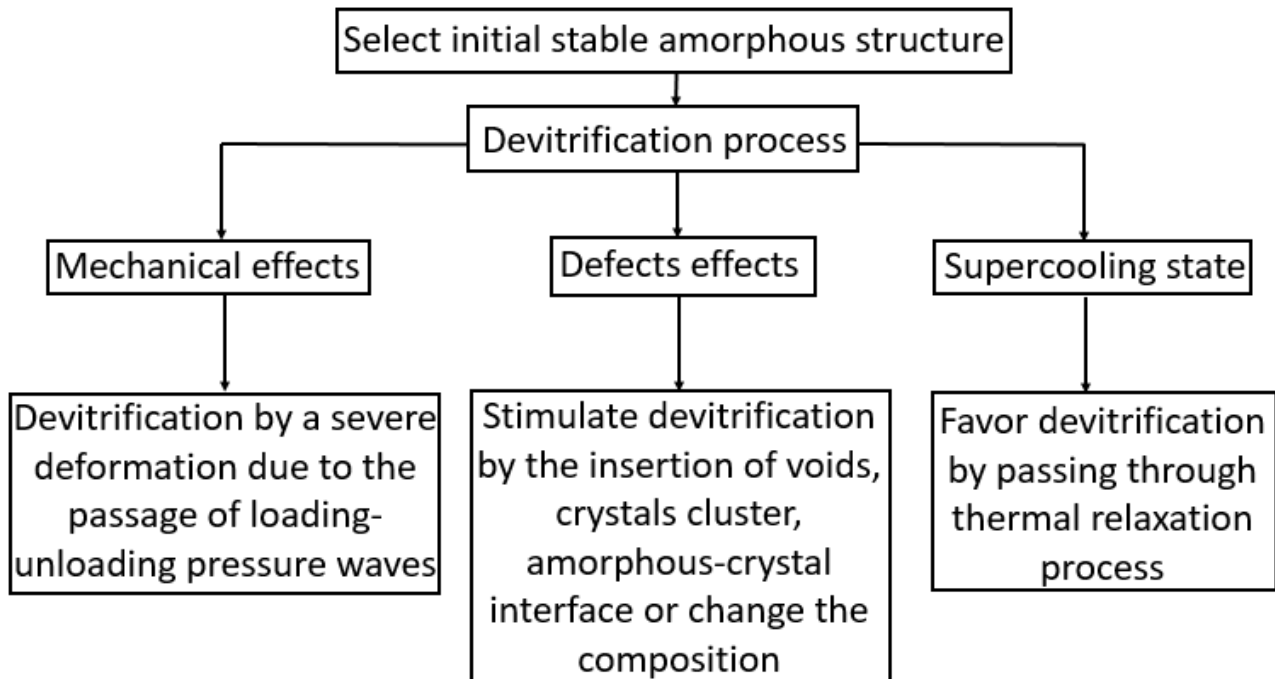


Figure 5.1: Representation of metallic glass devitrification investigation strategy flowchart.

This task was tackled using three main axes in order to clarify the devitrification mechanism. Firstly, devitrification is caused by pure non thermal effects, such as mechanical stress under high absorbing fluence, which leads to localized

STZ forming in the MG due to loading-unloading pressure waves [381]. Second, incorporate any defects (crystal inclusions, voids, glass-crystal interfaces) present in the amorphous structure and couple it to the laser process in order to stimulate devitrification. Lastly, this complex phase transformation is caused by laser annealing within the supercooled domain and mechanical stress during thermal relaxation of the system.

Once devitrification is captured, other legitimate questions follow. Among them, is this devitrification total or partial (composites), what is the location and the size of these crystallites within the amorphous matrix, and is there any segregation effects during this process. After setting and performing simulations, all these ambiguous questions will be answered.

### 5.3 Devitrification by including defects

As mentioned previously in the devitrification strategy Figure 5.1, the role of defects during the laser-matter interaction event was explored. The amorphous-crystalline phase change is a competition between the ordered and the disordered phase. So, in order to facilitate the crossing of the energy barrier and reach a more stable energy valley via a devitrification process, several kinds of defects were created as shown in Figure 5.2.

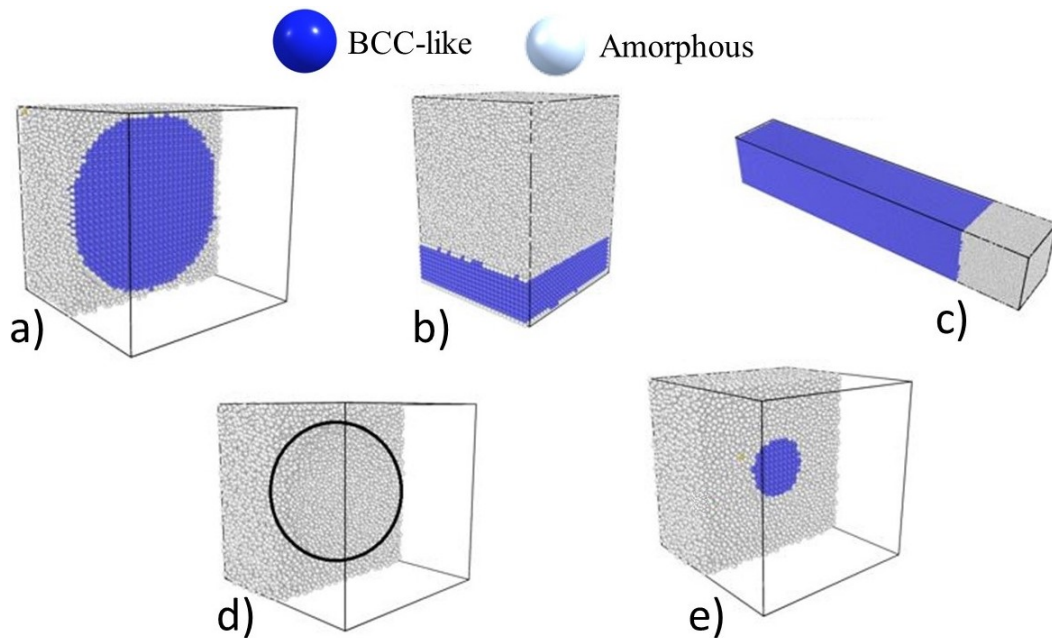


Figure 5.2: Defects designed to trigger devitrification in  $\alpha$ -Cu<sub>50</sub>Zr<sub>50</sub> structure, a-e) Represent a BCC-like crystalline sphere inclusion within amorphous structure with proportion of 46.1 and 2.3 % respectively. b-c) Show a crystalline BCC-like-amorphous interface with a BCC-like proportion of 20.5 and 82.3 % respectively. d) Represent void inclusion within the amorphous structure.

In Figure 5.2, we have successfully built a  $\alpha$ -Cu<sub>50</sub>Zr<sub>50</sub> amorphous structure with three different kinds of defects. In a) and e), we have BCC-like crystalline sphere seeds with different radius (4.94 and 1.94 Å for a) and e) respectively). In b) and c), we have an amorphous-crystal interface with the amorphous part as a dominant proportion in b) and minor in c). Finally, in d) we artificially created a spherical void with a radius of 4.94 Å within the amorphous structure. These initial structures were replicated ( $\sim 400$  nm) by following the propagation of laser deposition energy along the  $x$ -axis in order to perform a laser-matter interaction. A pulse duration of 100 fs and a large range of fluence conditions ranging from  $F_{\text{abs}} = 30\text{-}150$  mJ/cm<sup>2</sup> were used.

Analysis of the results after energy deposition revealed that no crystals had formed in the samples. Defects that lower the free energy barrier combined with the P-wave mechanical mechanism at a high fluence laser working regime would cause severe distortions to the amorphous system and facilitate devitrification. Apparently, applying this technique did not affect the local amorphous structure despite all the speculations. In the current work, it is impossible to give a final answer on whether the  $\alpha$ -Cu<sub>50</sub>Zr<sub>50</sub> persists in a metastable state rather than the ordered crystalline phase. The only hint to effectively resolve the devitrification issue for this composition is metadynamic computation.

Devitrification was not achievable using the previous defective approaches. This approach is not always flexible due to the difficulty of constructing and examining such complex structures in experimental laboratories. However, this failure was useful enough to give us an idea of the next study. In other words, find a suitable amorphous CuZr composition for further investigation.

## 5.4 CuZr initial specimen configurations

To perform a laser-matter interaction simulation, we prepared the initial amorphous systems with different composition stoichiometry. Regarding the superior glass forming ability of CuZr system in the composition range  $30 \leq \% \text{-Zr} \leq 50$  [382], the strategy was to produce an amorphous structure with a composition that is rich in Zr in order to increase the probability of capturing the amorphous-crystal transformation.

For this purpose, several initial BCC-like crystalline supercells with a random distribution of Cu and Zr atoms identified as suitable for this study with the following compositions were prepared: Cu<sub>19.4</sub>Zr<sub>80.6</sub>, Cu<sub>19.9</sub>Zr<sub>80.1</sub>, Cu<sub>21.9</sub>Zr<sub>78.1</sub>,

$\text{Cu}_{23.5}\text{Zr}_{76.5}$ ,  $\text{Cu}_{24.9}\text{Zr}_{75.1}$ , and  $\text{Cu}_{26}\text{Zr}_{74}$ . The simulation boxes were periodic and filled with 31250 atoms. It corresponds to the dimension of  $8.13 \times 8.13 \times 8.13$  nm<sup>3</sup> following  $x$ ,  $y$ , and  $z$  directions respectively. Then, they were subjected to an amorphization cycle achieved by employing EAM interatomic potential [316]. The process started by heating the systems to 2000 K using a rate of  $10^{13}$  K.s<sup>-1</sup> and then cooling down to 300 K with a quenching rate of  $10^{11}$  K.s<sup>-1</sup>. Ultimately, the amorphous structures were relaxed at a target temperature of 300 K and a pressure of 1 bar during a time period of 100 ps. All these stages were performed under the NPT ensemble with the Nose-Hoover thermostat. The final result is shown in Figure 5.3.

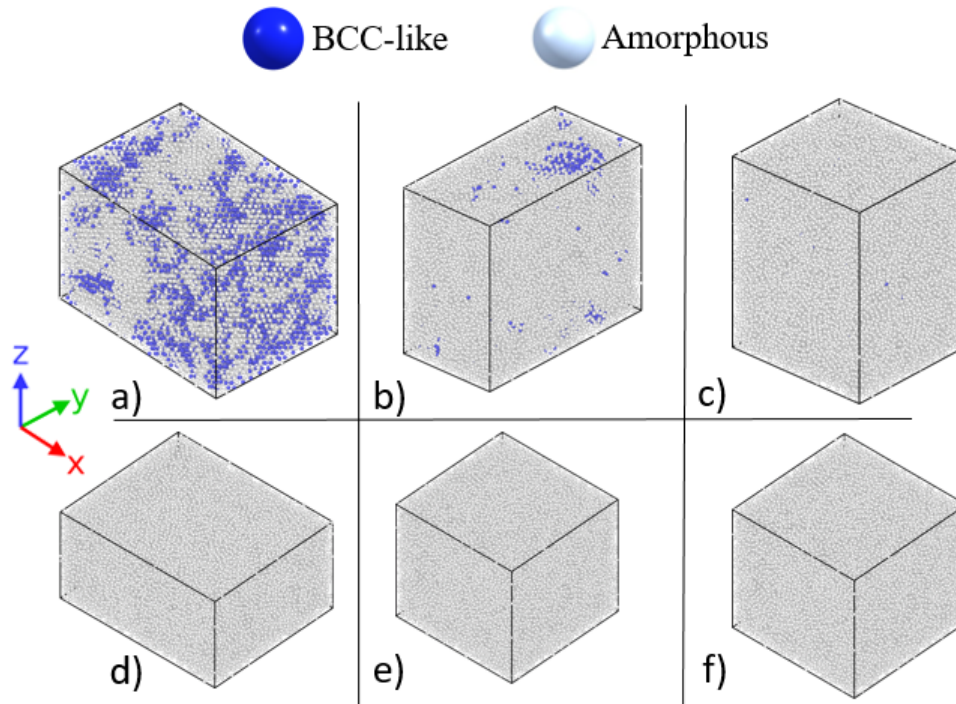


Figure 5.3: Representation of different  $\text{Cu}_{1-x}\text{Zr}_x$  metallic glasses samples produced after amorphization cycle, the compositions are: (a)  $\text{Cu}_{19.4}\text{Zr}_{80.6}$ , (b)  $\text{Cu}_{19.9}\text{Zr}_{80.1}$ , (c)  $\text{Cu}_{21.9}\text{Zr}_{78.1}$ , (d)  $\text{Cu}_{23.5}\text{Zr}_{76.5}$ , (e)  $\text{Cu}_{24.9}\text{Zr}_{75.1}$ , and (f)  $\text{Cu}_{26}\text{Zr}_{74}$ . The local atom's structure is colored according to the common neighbor analysis algorithm (CNA) [278].

Figure 5.3 presents a local crystallography analysis obtained throughout the amorphization process. The different compositions exhibit competition between amorphous and crystalline phases. We have three contrasted behaviors. The first category is represented in Figure 5.3 a). It corresponds to the  $\alpha\text{-Cu}_{19.4}\text{Zr}_{80.6}$  partially amorphized with an amount of  $\sim 40\%$  BCC-like structure. The second category is reported in Figure 5.3 b). The  $\alpha\text{-Cu}_{19.9}\text{Zr}_{80.1}$  is partially vitrified due to the presence of crystallized clusters with a concentration lower than 4%. The last category is composed by completely stabilized MGs structures as exposed in

Figure c), d), e), f) corresponding to compositions  $\alpha$ -Cu<sub>21.9</sub>Zr<sub>78.1</sub>,  $\alpha$ -Cu<sub>23.5</sub>Zr<sub>76.5</sub>,  $\alpha$ -Cu<sub>24.9</sub>Zr<sub>75.1</sub>, and  $\alpha$ -Cu<sub>26</sub>Zr<sub>74</sub> respectively.

Based on these MD calculations, the amorphous  $\alpha$ -Cu<sub>21.9</sub>Zr<sub>78.1</sub> was selected as the initial structure to investigate amorphous-crystalline phase change triggered by ultrafast laser. To obtain detailed information about the disorder-order local structure of the samples, a complementary analysis involving RDFs was performed as shown in Figure 5.4.

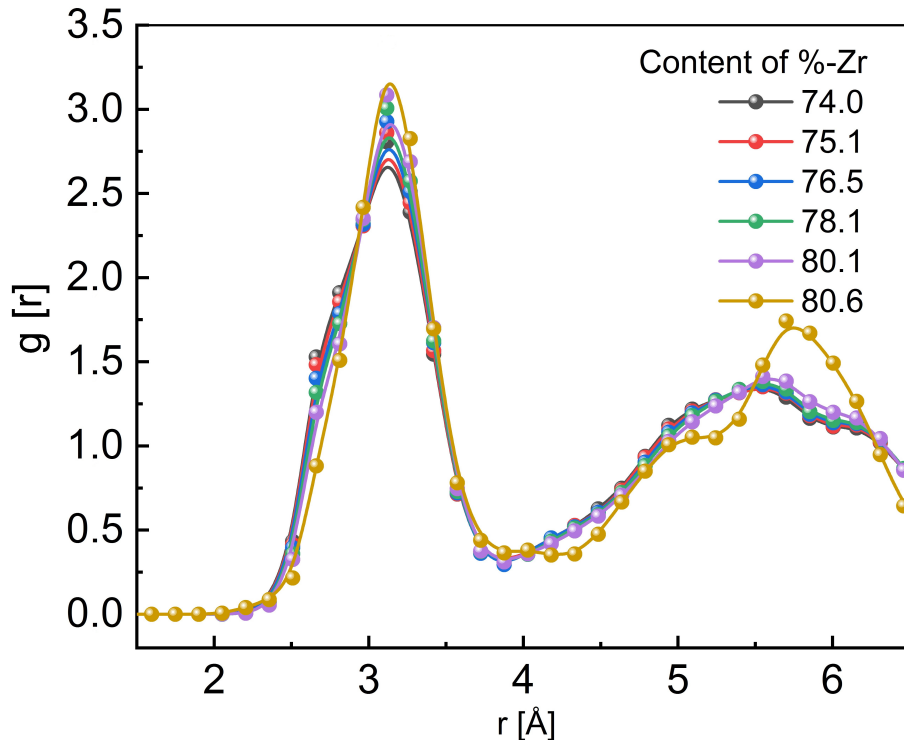


Figure 5.4: The total RDFs of the various CuZr MGs after the amorphization process. The complete amorphization of the sample is characterized by the double splitting of the second peak.

The results reveal that for the completely vitrified amorphous structures  $\alpha$ -Cu<sub>26</sub>Zr<sub>74</sub>,  $\alpha$ -Cu<sub>24.9</sub>Zr<sub>75.1</sub>,  $\alpha$ -Cu<sub>23.5</sub>Zr<sub>76.5</sub> and  $\alpha$ -Cu<sub>21.9</sub>Zr<sub>78.1</sub>, a double splitting of the RDF's second peak typical of amorphization is noticed whatever the stoichiometry. In the contrary, a single pronounced peak is observed for the  $\alpha$ -Cu<sub>19.4</sub>Zr<sub>80.6</sub> structure which is the footprint of an already existing crystal.

### 5.4.1 Spontaneous crystallization

An additional precaution must be taken into consideration when studying the vitrification-devitrification cycle study due to a phenomenon related to spontaneous crystallization. The purpose of this simulation is to check whether spon-

taneous crystallization appears within the amorphous  $\alpha$ -Cu<sub>21.9</sub>Zr<sub>78.1</sub> box during long annealing at a temperature of 300 K. This effect is undesirable, it creates confusion about the origin of devitrification. It could be a direct laser effect or may be caused by the instability of the amorphous structure. A complementary simulation was performed on  $\alpha$ -Cu<sub>21.9</sub>Zr<sub>78.1</sub> to investigate such behavior. The  $\alpha$ -Cu<sub>21.9</sub>Zr<sub>78.1</sub> amorphous configuration was annealed at room temperature (300 K) for 100 ns using the NPT ensemble. The result is shown in Figure 5.5.

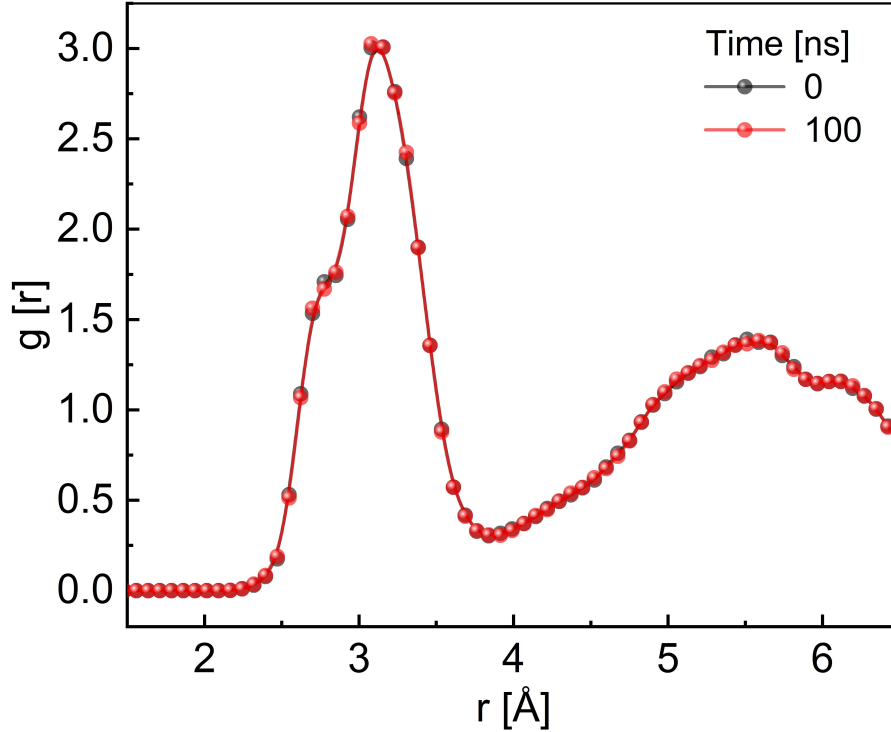


Figure 5.5: The total RDFs of  $\alpha$ -Cu<sub>21.9</sub>Zr<sub>78.1</sub> at different times  $t = 0$  ns and  $t = 100$  ns. The plots demonstrate that the double splitting of the second peak is preserved confirming the amorphous character of the structure.

To probe the local atomic structure modification, RDFs were computed as presented in Figure 5.5. By analyzing and comparing RDFs at  $t = 0$  and 100 ns the profile is exactly the same and the double splitting is well preserved. The results indicate that the initial amorphous structure is dominant, stable, and does not undergo spontaneous crystallization.

#### 5.4.2 Melting and glass transition temperatures

Initially, to clarify the thermodynamics behind the devitrification of  $\alpha$ -Cu<sub>21.9</sub>Zr<sub>78.1</sub>, two characteristic temperatures are needed  $T_m$  and  $T_g$ . Therefore, the evolution of the normalized volume with respect to the equilibrium volume ( $V_0$ ) versus the temperatures was collected during the heating process from 300 K to 2000 K at

a rate of  $10^{13}$  K/s as described in chapter 3. The obtained results are shown in Figure 5.6.

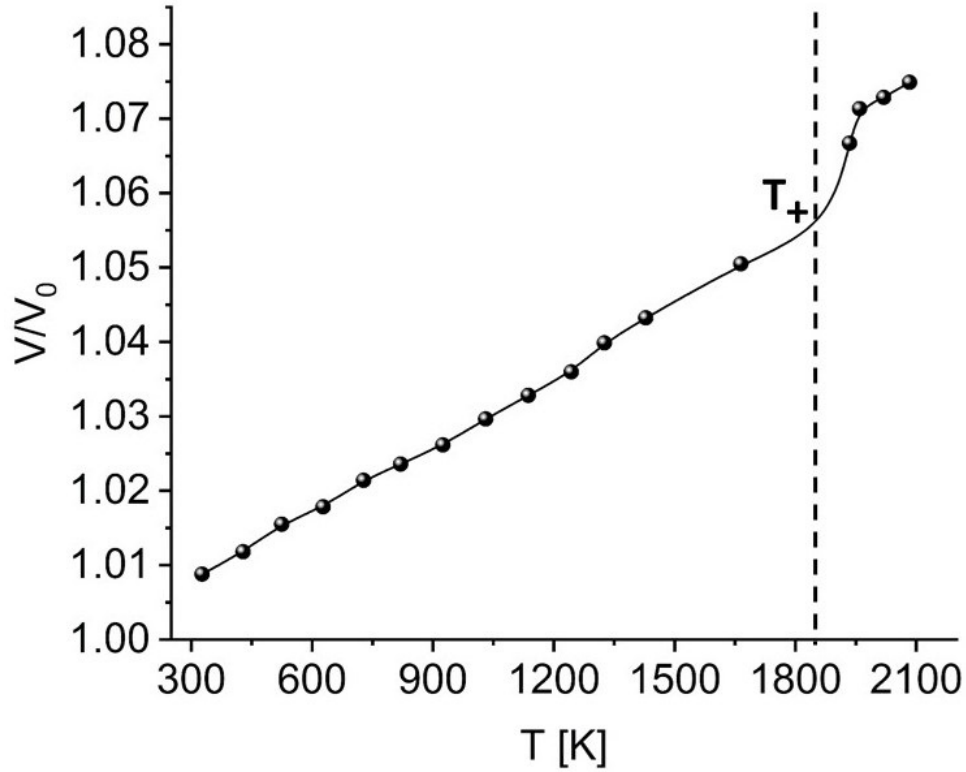


Figure 5.6: *in silico* computation of the normalized volume versus temperature in BCC-like- $\text{Cu}_{21.9}\text{Zr}_{78.1}$  alloy to determine the melting temperature  $T_+$  during the heating stage.

According to the above curve, a solid-liquid phase transition occurs at  $T_+ \sim 1850$  K, which coincides with the normalized volume jump.

The formula used in chapter 3 to estimate the melting point needs the knowledge of  $T_-$ . It is important to note that this value is determined during the cooling stage where the temperature drops from 2000 K to 300 K at a rate of  $10^{11}$  K/s. It is assumed here that the  $T_- = T_g$ . Figure 5.7 shows the evolution of the normalized volume versus temperature during the fast cooling stage.

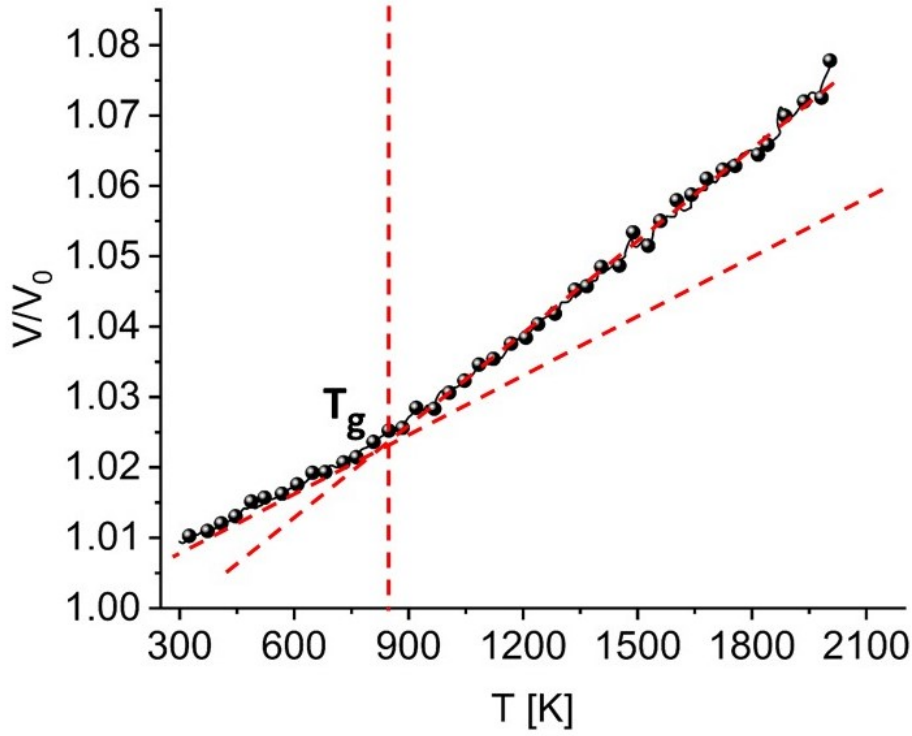


Figure 5.7: *in silico* computation of the normalized volume versus temperature in  $\alpha$ -Cu<sub>21.9</sub>Zr<sub>78.1</sub> amorphous alloy to determine the glass transition temperature  $T_g$  during the cooling stage.

The curve above gives a value of  $T_g \sim 830$  K where the change of the slope marks the liquid-glass transition. Furthermore, Based on the previously obtained temperatures  $T_+$  and  $T_-$  calculated value of  $T_m \sim 1440$  K. The sample has a relatively wide supercooled temperature region of  $|T_m - T_g| = 610$  K which means inferior stability against crystallization. This makes  $\alpha$ -Cu<sub>21.9</sub>Zr<sub>78.1</sub> a promising candidate for exploring devitrification.

### 5.4.3 Laser-matter computational details

The laser-material interaction process in amorphous ( $\alpha$ ) CuZr alloys is modelled using a TTM-MD hybrid method [264, 383, 265, 306, 306] as implemented in the LAMMPS software [384, 229]. Several initial random solid solutions with BCC-like crystalline structure and various stoichiometries including Cu<sub>19.4</sub>Zr<sub>80.6</sub>, Cu<sub>19.9</sub>Zr<sub>80.1</sub>, Cu<sub>21.9</sub>Zr<sub>78.1</sub>, Cu<sub>23.5</sub>Zr<sub>76.5</sub>, Cu<sub>24.9</sub>Zr<sub>75.1</sub>, and Cu<sub>26</sub>Zr<sub>74</sub> were first modeled using the embedded atom model parameterization of Mendelev *et al* [316]. Each  $8.13 \times 8.13 \times 8.13$  nm<sup>3</sup> simulation cell is made periodic and filled with 31250 atoms. All samples are subjected to a classical amorphization cycle using MD as described in [303]. First, the system is heated up to 2000 K in the liquid state at a rate of  $10^{13}$  K.s<sup>-1</sup> and then it is quenched at 300 K using a rate of  $10^{11}$  K.s<sup>-1</sup> where another equilibration run is performed during 100 ps in the NPT ensemble (isothermal-isobaric) using the Nosé-Hoover thermostat and barostat

[385]. Then, the obtained amorphous cell is replicated up to  $211.31 \times 7.61 \times 10.50 \text{ nm}^3$  size as described *e.g.*, in the work of Cao *et al.* [386]. An MD timestep of  $\delta t = 1 \text{ fs}$  is used for all simulations. Finally, the simulation box is extended twice (vacuum region) in the  $x$ -direction to create the surface of the material and is further equilibrated for another 100 ps.

The TTM-MD equations are solved on an electronic grid of  $702 \times 1 \times 1$  during 30 ps. The ultrafast laser operating conditions of  $\tau = 100 \text{ fs}$  pulse duration, and  $F_{\text{abs}} = 34 \text{ mJ/cm}^2$  absorbed fluence are employed to preclude the system from ablation. After the laser pulse, the system is tracked during 16 ns in the microcanonical ensemble (NVE). To prevent pressure wave reflection, a damping region defined as Non-Reflecting Boundary Condition (NRBC) characterized by  $\gamma_{\text{damp}} = 2.5 \cdot 10^{-3} \text{ eV ps \AA}^{-2}$  is used as described in [303]. Electronic properties are selected from Refs. [208, 340, 338] assuming they do not substantially change with composition in amorphous CuZr alloys [340]. All the structural analysis are performed using the Common Neighbor Analysis (CNA) [387] and Polyhedral Template Matching (PTM) [388] algorithms as implemented in the OVITO software [275] applied here to Cu and Zr sublattices.

## 5.5 CuZr alloy nanocomposite creation via ultrafast laser

To favor the devitrification process within the amorphous structure from a thermodynamic point of view, the simulation strategy was to choose ultrafast laser conditions close to supercooling conditions. This supercooling, combined with the mechanical effect of loading and unloading pressure waves, results in substantial atom mobility. This permits reorganization into a more stable and energetically less expensive position.

To understand this amorphous-crystal phase change different properties were provided and combined with structural observations via OVITO [275] to detect the presence of a newly formed crystalline phase. The temporal evolution of the RDFs during the thermal relaxation process was performed to track the emergence of a sharp peak that marks the presence of crystals. In addition, the Gibbs free energy was computed to provide a quantitative insight into the transition from a metastable amorphous state to a crystal. The results shown in Figure 5.8 demonstrate that a devitrification process is occurring.

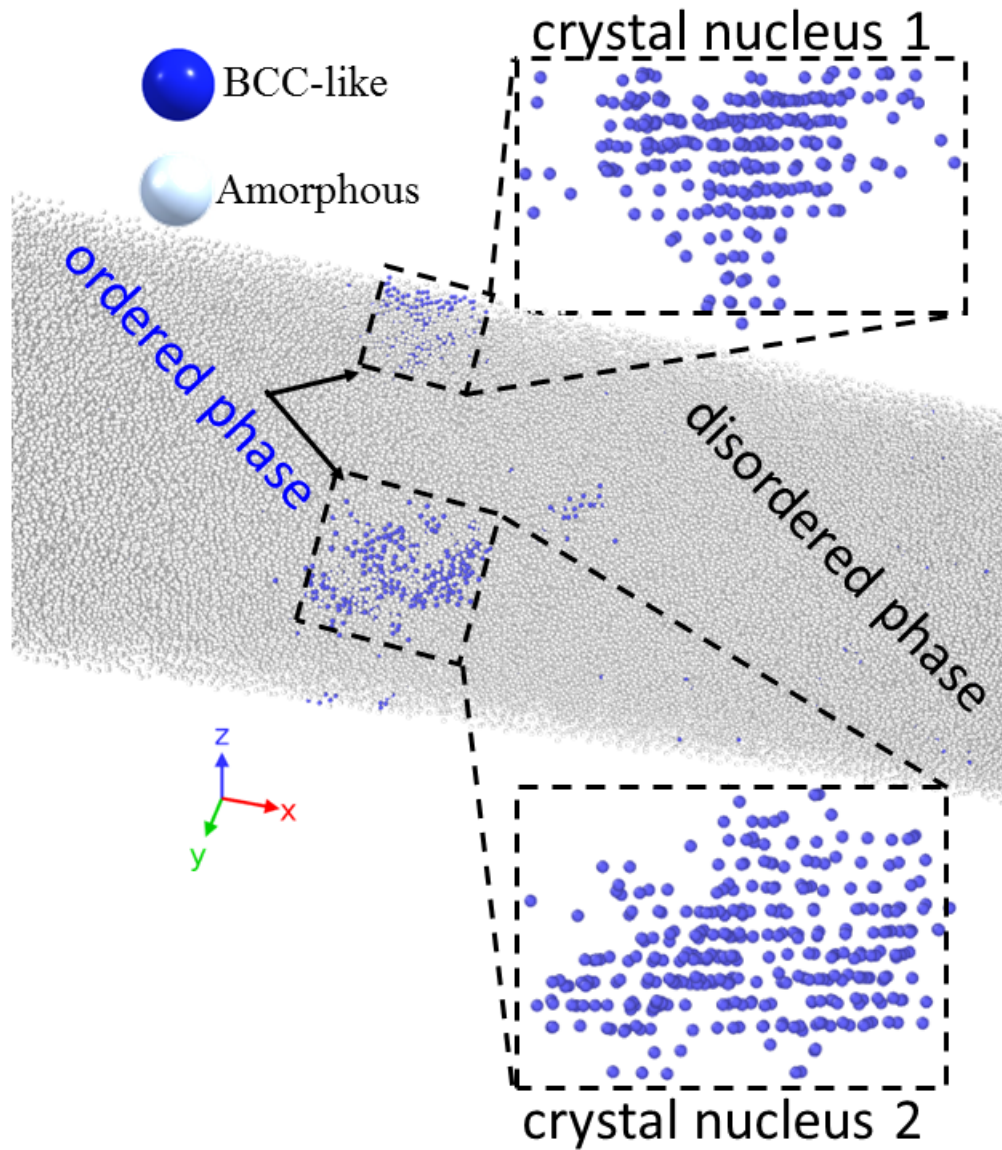


Figure 5.8: Nucleation of BCC-like nuclei ( $\sim 15$  atomic planes) within the amorphous  $\alpha$ - $\text{Cu}_{21.9}\text{Zr}_{78.1}$  at  $t \sim 8$  ns after the laser-energy deposition.

The conducted laser-matter interaction permits the emergence of the first crystalline germ of a few BCC-like atomic planes (roughly  $\sim 2 - 5 \text{ \AA}$ ) within the disordered amorphous phase. Additionally, the result reveals an induced transformation is taking place at  $t \sim 8.5$  ns. An extremely crucial question here is to identify the mechanism that led to this situation.

### 5.5.1 Local structure during the ultrafast laser devitrification

The CNA algorithm recognizes the emergence of BCC-like crystalline germs within the amorphous matrix. This structure matches the prediction of the CuZr phase diagram at high-temperature where a solid solution of Cu in the BCC  $\beta$ -Zr phase is expected for this specific composition [389]. The characteristic size of

the crystalline nanocrystals that nucleate in the subsurface region is about  $\sim 2 - 5 \text{ \AA}$ . The growth of the crystalline phase deeper inside the material is shown in Figure 5.9.

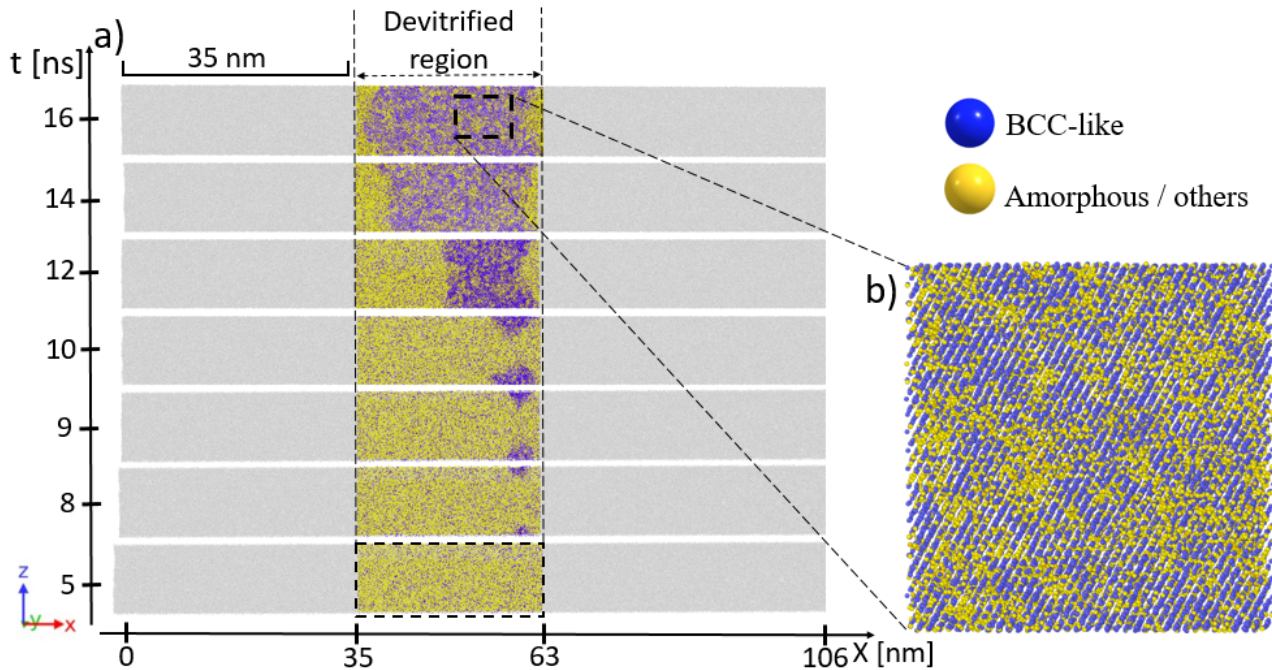


Figure 5.9:  $\alpha$ -Cu<sub>21.9</sub>Zr<sub>78.1</sub> atomic configurations after ultrafast laser irradiation as a function of time. Emphasize of the devitrified region. a) global view of the devitrified region located at  $35 \leq x \leq 63$  nm, b) magnification of a devitrified subdomain at  $t = 16$  ns. The atoms are colored according to their local atomic structure computed using the PTM algorithm. Atoms colored in grey rely to hidden amorphous and liquid domains.

Figure 5.9(a) indicates that the first crystal seeds within the Cu<sub>21.9</sub>Zr<sub>78.1</sub> amorphous structure do not form instantly but rather at  $t \sim 8$  ns in a devitrified region located at  $x \sim 63$  nm. As the seeds grow, they coalesce to form a crystallization front at  $t = 9$  ns and travel through the devitrified region that reaches a final thickness of  $\sim 30$  nm at the end of the process. The freshly nucleated crystal phase is not transient and survives until the end of the simulation at  $t = 16$  ns. Furthermore, Figure 5.9(b) shows a zoom of the devitrified region at  $t = 16$  ns where the PTM analysis clearly shows crystalline atomic planes. The CuZr nanocrystals have the global Cu (21.9 %) and Zr (78.1 %) concentrations without segregation/crystallization effects. A detailed quantitative study was performed to identify the number of BCC-like structure atoms and the propagation velocity of the crystal front. The results are shown in Figure 5.10.

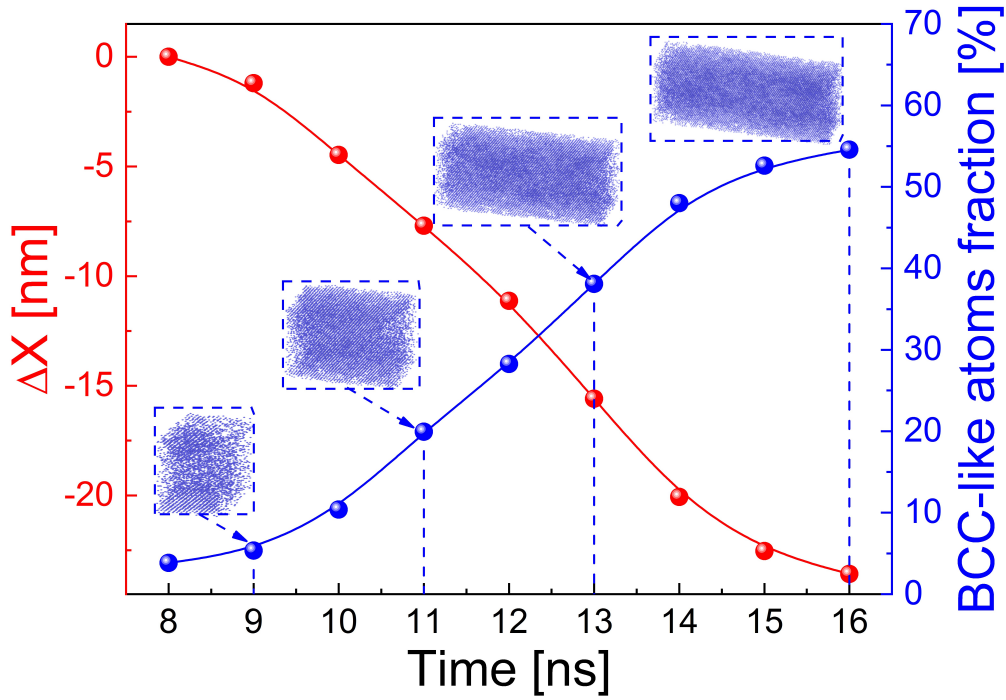


Figure 5.10: Mean position of the crystallization front propagation toward the surface versus time at  $t = 8-16$  ns during the devitrification process in the  $\alpha$ -Cu<sub>21.9</sub>Zr<sub>78.1</sub> MG sample. In blue, we can notice the formed crystalline BCC-like atoms at  $t = 9, 11, 13$  and  $16$  ns.

Figure 5.10 provides the variation of the crystallization front's relative position  $\Delta X = x(t) - x(0)$  with  $x(0) = 63$  nm as function of time. At  $t = 9$  ns, the fraction of crystalline phase is originally  $\sim 5$  %. Beyond  $t = 9$  ns, the crystallization front travels the sample which permits the crystalline phase fraction to increase up to  $55$  % at  $t = 16$  ns. The front propagates toward the melted surface ( $-x$  direction) with an average velocity of  $2.77 \text{ m}\cdot\text{s}^{-1}$  ( $\sim 100$  times slower than the sound velocity in air). This means that the crystallization is partial, localized ( $\sim 0-30$  nm) and relatively slow as compared *e.g.*, to the devitrification of CuTi amorphous alloys that occurs only under supercooling condition with a crystallization front velocity of  $\sim 40 \text{ m}\cdot\text{s}^{-1}$  [390].

To track the emergence of crystalline solid solution during devitrification, a complementary analysis involving RDFs at several key times is computed in the devitrified region ( $35 \leq x \leq 63$  nm). The shape of the RDFs is as illustrated in Figure 5.11.

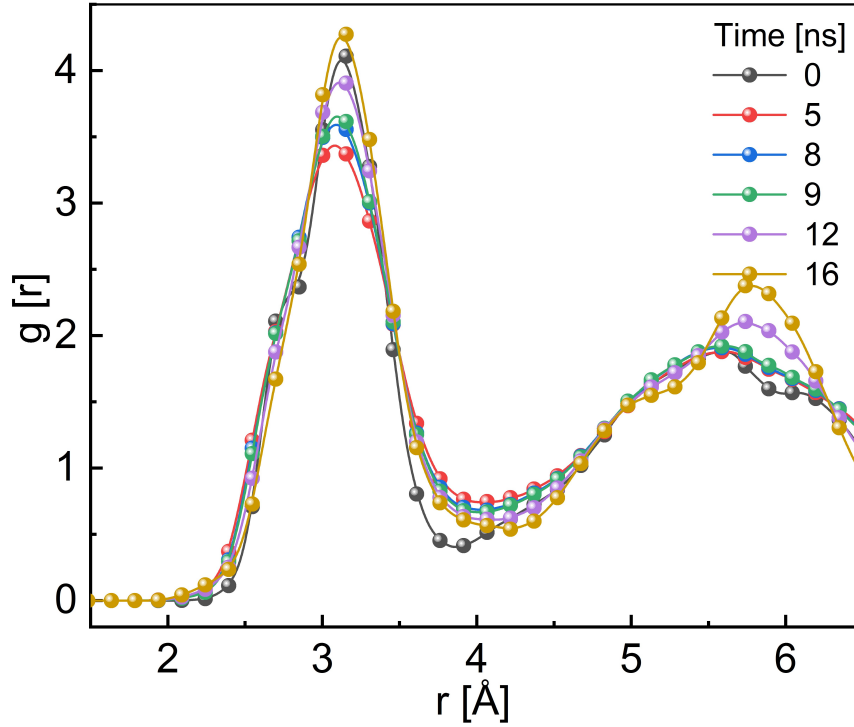


Figure 5.11: RDFs evolution in the  $\alpha$ -Cu<sub>21.9</sub>Zr<sub>78.1</sub> sample at different times during the devitrification process. The double splitting of the secondary peak typical of the amorphous state disappears proving the emergence of a crystalline structure.

At  $t = 0$  ns, we observe that the structure is amorphous, characterized by the presence of the second peak double splitting. At  $t = 5$  ns, the decrease of the first peak intensity together with the disappearance of the double splitting and the appearance of a broader second peak indicate that the system liquefies in this region. Beyond  $t = 5$  ns, the intensity of the first peak starts rising and the shape of RDFs becomes sharper confirming a local ordered atomic rearrangement. The first and second peaks reach their maximum at  $t = 16$  ns where no double peak is observed. Instead, a single narrowed peak that indicates the growth of a crystalline structure within the amorphous material is detected.

### 5.5.2 Confirmation of crystalline state by virtual XRD analysis

In order to probe the local structure and compare the obtained results with the experimental data, further examination of the structures was performed during the devitrification process using XRD pattern. To achieve this purpose, two configurations at  $t = 0, 16$  ns corresponding to amorphous and partially crystalline  $\alpha$ -Cu<sub>21.9</sub>Zr<sub>78.1</sub> with 114052 atoms each were selected.

A virtual XRD pattern was computed by employing MD simulation as implemented in LAMMPS by Coleman *et al* [391, 392]. This algorithm is based on

Bragg's law [393] where the diffraction intensities are calculated at each point on the Fourier space using the structure factor equation. In the present work, the Lorentz polarization factor is included to get the diffraction intensities. The XRD was computed for both amorphous and crystallized samples, with scanning angles in the range of  $20 \leq 2\theta \leq 120^\circ$ . The results are shown in Figure 5.12.

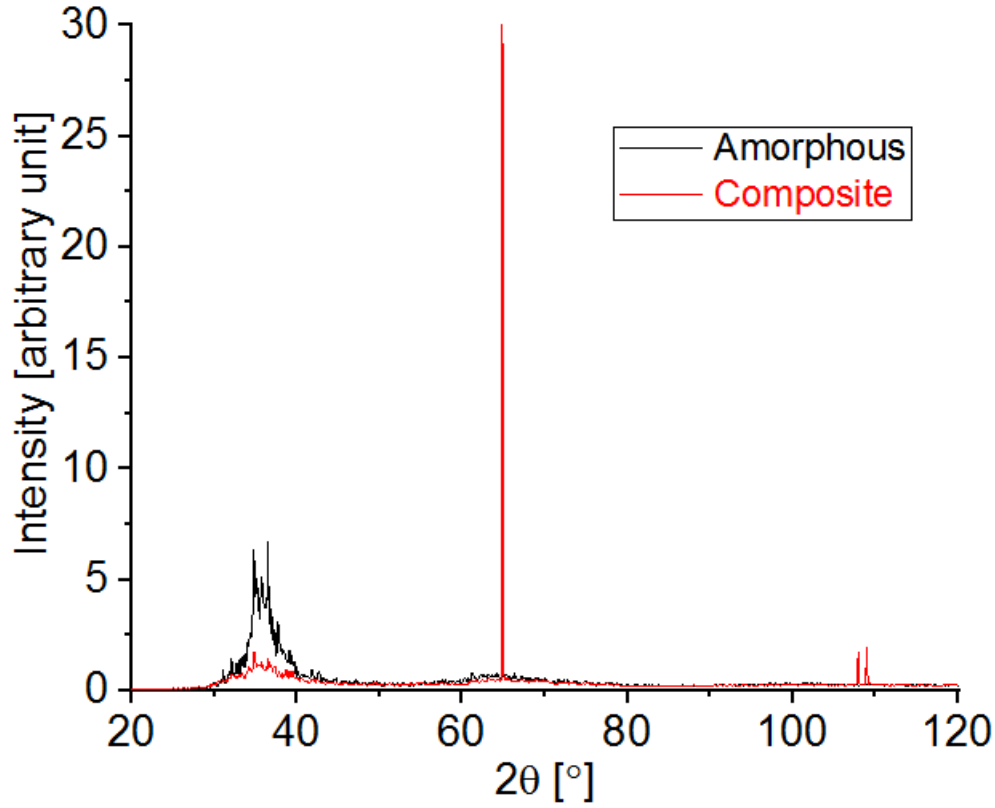


Figure 5.12: Evolution of the virtual XRD patterns in  $\alpha\text{-Cu}_{21.9}\text{Zr}_{78.1}$  within the range of  $20 \leq 2\theta \leq 120$  at times: 0 (amorphous) and 16 ns (crystalline) during the devitrification process via ultrafast laser irradiation.

The simulations reveal that the amorphous and crystalline structures exhibited a radically different XRD profile. The amorphous structure is characterized by a broad profile with a maximum at low-angle  $2\theta \sim 35^\circ$  for the intensity of  $\sim 8$ . Except for the range of angles  $60 \leq 2\theta \leq 70^\circ$  where the intensity had a slight hump, the rest of the curve is flat with a noisy value around 0 intensity. Furthermore, we observed an agreement on both the shape and position of the amorphous broad peak situated at low angles  $30 \leq 2\theta \leq 45^\circ$  [394]. On the other hand, as presented by the red plot the broad peak at angles  $30 \leq 2\theta \leq 45^\circ$  intensity drops from 8 to  $\sim 1$  without completely disappearing meaning that we obtained a composite system where crystal cohabit with an amorphous structure. The emerging crystalline structure is confirmed by the presence of the narrow peak with an intensity of  $\sim 30$  that we noticed around the angle  $2\theta \sim 65^\circ$ . In

addition, two other peaks with lower intensities of  $\sim 2$  were detected at angles  $2\theta \sim 106$  and  $109^\circ$ . This signature indicates that ordered phase is present in the amorphous sample.

Meanwhile, we compared the theoretical XRD patterns of the  $\alpha\text{-Cu}_{21.9}\text{Zr}_{78.1}$  devitrified sample to the available experimental sets of crystallines  $\text{CuZr}_2$  and  $\text{CuZr}_3$  in order to identify the most similar structure to the crystalline part of the composite and the atomic planes. The results are as shown in Figure 5.13.

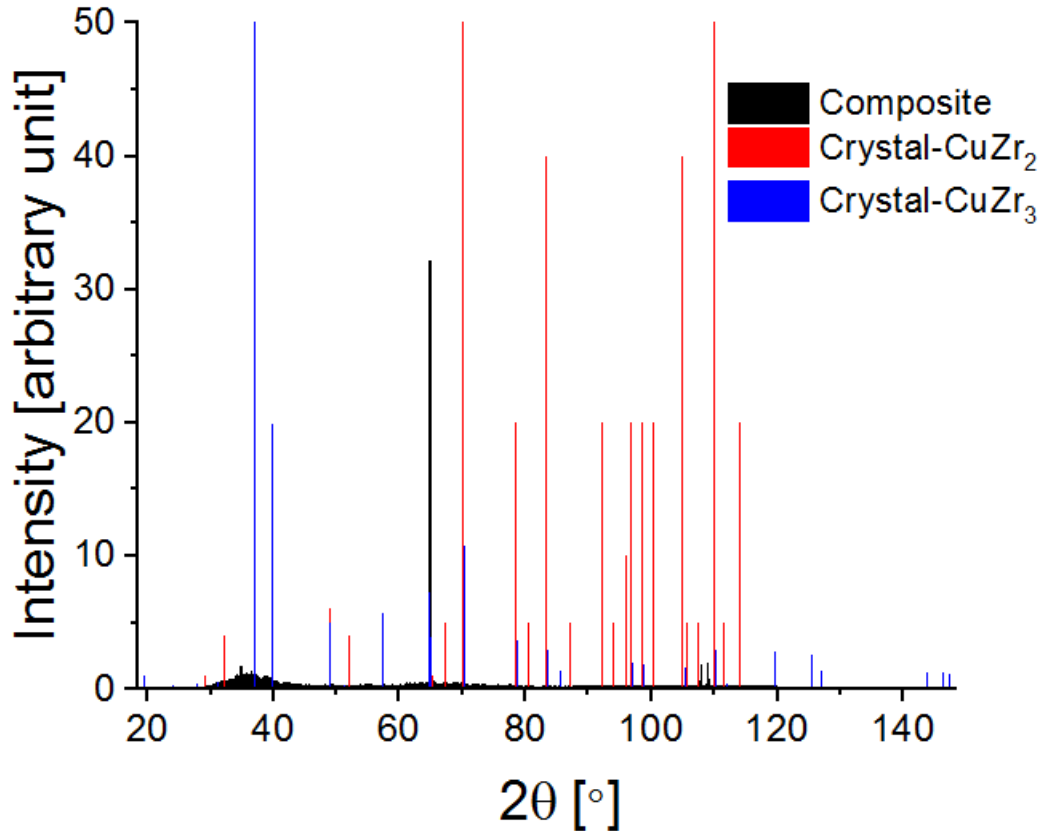


Figure 5.13: Virtual XRD patterns of  $\alpha\text{-Cu}_{21.9}\text{Zr}_{78.1}$  compared to the experimental patterns of the crystalline structures  $\text{CuZr}_2$  and  $\text{CuZr}_3$ .

We found a reasonable match between the main sharp peak at the angle position of  $2\theta \sim 65^\circ$  that characterizes the crystallinity of the  $\alpha\text{-Cu}_{21.9}\text{Zr}_{78.1}$  composite and an existing peak within the BCC crystalline  $\text{CuZr}_3$  corresponding to the atomic plane [202]. In a lesser extent, the two extremes peak at angle  $2\theta \sim 110^\circ$  has a lesser intensity. However, no satisfactory correspondence was found with the atomic planes of the experimental data structures.

## 5.6 Devitrification mechanism in $\alpha\text{-Cu}_{21.9}\text{Zr}_{78.1}$

The main purpose of this section is to provide a deeper understanding of the thermodynamic properties responsible for this devitrification. When the laser energy is delivered, the system is driven to a nonequilibrium state where electrons are hot and the lattice is still relatively cold. Therefore, a process of electron-phonon relaxation takes place to balance the energy. The two temperature dynamics defines an ionic temperature gradient inducing stress accumulation that manifests in the form of a compression pressure wave followed by a rarefaction pressure wave due to relaxation of the system. Pressure waves operate at times between  $t = 0\text{-}200$  ps. The computed spatial evolution of pressure is shown in Figure 5.14.

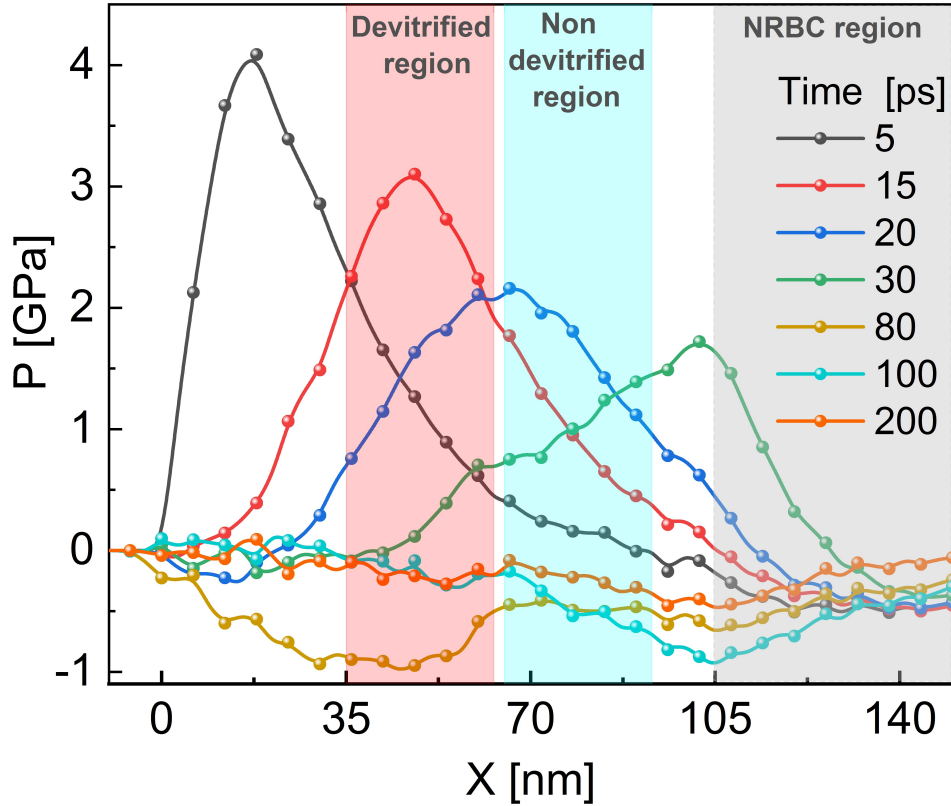


Figure 5.14: Spatial evolution of the local pressure profile in  $\alpha\text{-Cu}_{21.9}\text{Zr}_{78.1}$  at  $t=0\text{-}200$  ps. The laser processing conditions are  $\tau = 100$  fs,  $F_{\text{abs}} = 34$  mJ/cm<sup>2</sup> for the pulse duration and absorbed fluence respectively. A devitrified zone (in salmon), a non-devitrified zone (in aqua) are chosen to compare the impact of pressure on polyhedra, and NRBC region (in gray).

At  $t = 5$  ps, the pressure reaches its maximum value of  $\sim 4$  GPa and gradually dwindles to  $\sim 3.1, 2.2, 1.7, 0.2$  GPa associated to  $t = 15, 20, 30,$  and  $200$  ps respectively. Simultaneously, a negative pressure of  $\sim -1$  GPa corresponding to the rarefaction pressure wave propagation is detected at  $t = 80\text{-}100$  ps. As mentioned previously, the amorphous-crystal transformation starts at  $t \sim 8$  ns,

much later after the complete absorbance of the pressure waves. Therefore, the correlation between the pressure waves and the phase transformation is fairly indirect, and we will discuss this aspect later on. To interpret the devitrification phenomenon, in the following we further investigate the atomic local arrangement evolution of the sample during the process. All MG exhibit a unique fraction of polyhedra structure, which is considered as the footprint of the amorphous structure. In this context, it is generally argued that the formation/breakage of the polyhedra network has a major impact on the glass stability [395]. Here, we track the proportions of the two most prevalent polyhedra, namely  $\langle 0, 1, 10, 4 \rangle$  ( $Z15_{I1}$ ) and  $\langle 0, 2, 8, 5 \rangle$  ( $Z15_{I2}$ ), in devitrified region as well as in a non-devitrified domain. The polyhedra fraction evolution is shown in Figure 5.15.

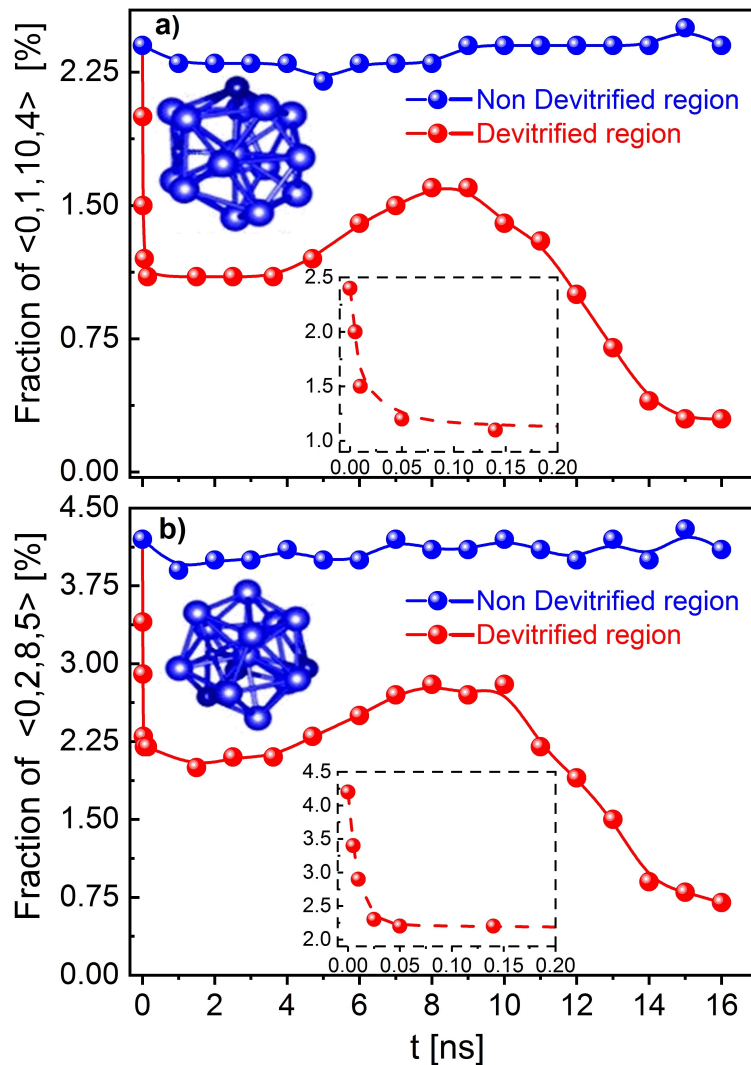


Figure 5.15: Time evolution of the polyhedra at  $t = 0-16$  ns within the  $\alpha$ -Cu<sub>21.9</sub>Zr<sub>78.1</sub> MG in the devitrified region located at  $35 \leq x \leq 63$  nm and in a non-devitrified domain located at  $65 \leq x \leq 93$  nm, a)  $\langle 0, 1, 10, 4 \rangle$ , b)  $\langle 0, 2, 8, 5 \rangle$ . A zoom in the time range of 0-0.2 ns is provided.

At  $t = 0$  ns, Figures 5.15(a) and (b) show a significant fraction of polyhedra in the initial structure *c.a.*, 2.4 and 4.2 % in both regions for Z15<sub>I1</sub> and Z15<sub>I2</sub>, respectively. However, these fractions quickly drop down to 1.1, 2.1 % at  $t = 0.05$  ns for Z15<sub>I1</sub> and Z15<sub>I2</sub> respectively in the region that will devitrify while both Z15<sub>I1</sub> and Z15<sub>I2</sub> % fluctuate without any substantial breaking in the non-devitrified region.

The zoomed region in both Figure 5.15(a) and (b) shows that most of the fraction polyhedra decrease happens during  $t = 0-0.05$  ns, a substantial drop of polyhedra in the devitrified zone and this coincide exactly to the times when the compression wave operates. Therefore, we can correlate the breaking of these polyhedra networks to compression effect. On contrary, as the rarefaction wave has the same maximum amplitude of  $\sim -1$  GPa in both the devitrified and non-devitrified investigated regions. It operates at  $t \sim 0.05-0.15$  ns, the polyhedra fraction fluctuates around a constant value of 1.1, 2.1 % for Z15<sub>I1</sub> and Z15<sub>I2</sub> respectively in the devitrified region. we can thus confirm that the pressure compression wave is the precursor of the amorphous structure embrittlement breaking the polyhedra network. Furthermore, it is worthy to notice that while the pressure quickly vanishes after  $t = 0.2$  ns, the polyhedra breaking process stops and a plateau is noticed with a proportion of 0.9 % Z15<sub>I1</sub> and 1.9 % of Z15<sub>I2</sub> until  $\sim 5$  ns in the devitrified region. An intermediate regime, associated with the frustration and recombination of polyhedra is recorded within the devitrified region at  $t \sim 5-8$  ns time range whereas the non-devitrified region is found to have a constant proportion of Z15<sub>I1</sub> and Z15<sub>I2</sub> polyhedra equivalent to those observed before the laser energy deposition. When the system devitrifies at  $t > 8$  ns, the fraction of both Z15<sub>I1</sub> and Z15<sub>I2</sub> decreases to 0.3 and 0.7 % in the devitrified region, respectively. In addition to the pressure profile, the space and time evolution of the temperature is shown in Figure 5.16.

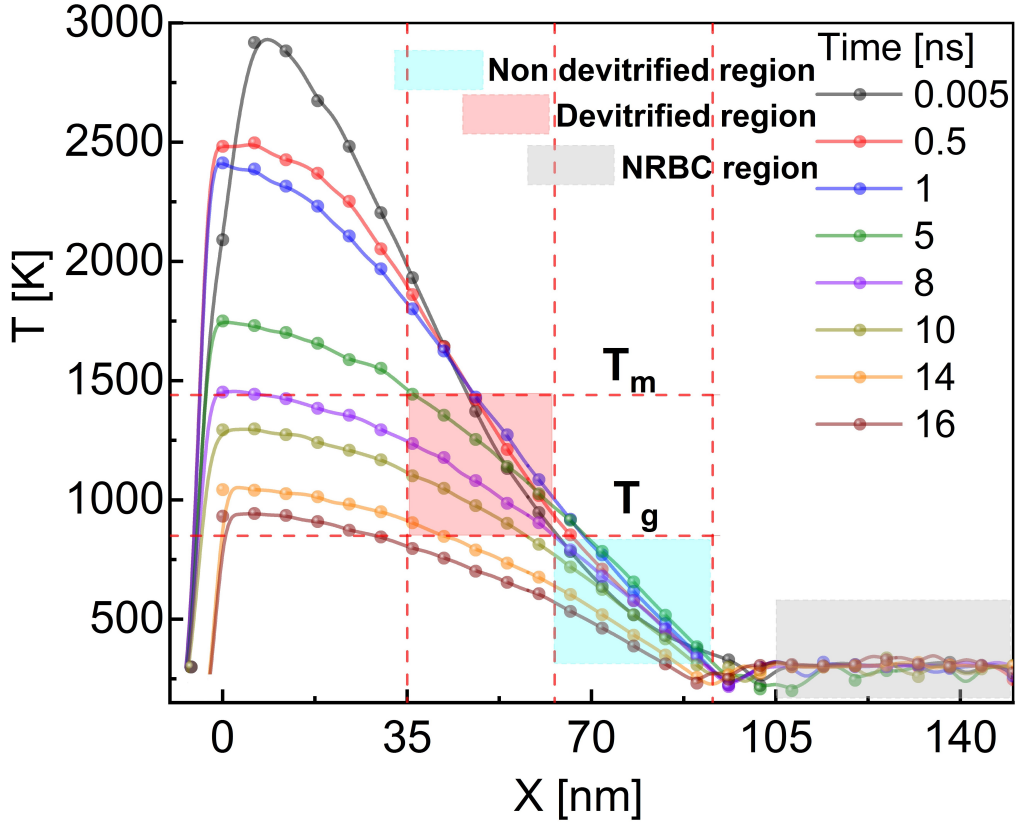


Figure 5.16: Spatial evolution profile of the local lattice temperature in  $\alpha\text{-Cu}_{21.9}\text{Zr}_{78.1}$  at several key times 0.005, 0.5, 1, 5, 8, 10, 14, and 16 ns of the devitrification process. A devitrified zone (in salmon) and a non-devitrified zone (in aqua) are chosen to investigate the impact of temperature on the devitrification process.

At  $t = 5$  ps, we observe the amorphous-liquid transition for  $X < 40$  nm with a maximum temperature  $T \sim 3000$  K ( $T_m \approx 1440$  K). Moreover, we noticed that in the devitrified region for  $1 \leq t \leq 8$  ns the temperature drop from  $\sim 1800$  to 1250 K marking a thermal relaxation of the amorphous sample. At  $t = 8$  ns,  $T \sim 0.87 T_m$  and this corresponds to the time where the first crystal seed is formed as shown in Figure 5.8. The temperature gradually decreases to  $T \sim 780$  K slightly below the theoretical temperature  $T_g \sim 830$  K. At  $t = 16$  ns, the amount of crystalline structure becomes relatively stable, and the crystallization wave ceases to propagate.

As a consequence, we conclude that the fast cooling stage from  $T_m$  to  $T_g$  is a determinant mechanism to promote the devitrification process in a region where the local atomic skeleton made of the  $Z15_{I1}$  and  $Z15_{I2}$  polyhedra has already been drastically weakened by the compressive pressure waves early process. In addition, it is noteworthy that the temperature in the non-devitrified zone is below  $T_g$ . This confirms that the optimal temperature range to favor crystal

nucleation is in the vicinity of  $T_g$ . This thermodynamics kinetic tendency is motivated by the sharp increase of the viscosity below  $T_g$  preventing any substantial atoms reorganization.

Accordingly, the devitrification is caused by a thermomechanical effect that consists in the propagation of a compression wave that fragilizes the glass by breaking the extended rigid polyhedra network during  $t \sim 0-0.05$  ns as precursor of devitrification followed by a temperature around  $T_g$  that promotes the phase transformation.

This observation confirms that the optimal temperature range to favor crystal nucleation is in the vicinity of  $T_g$ . This thermodynamical kinetic tendency ensured that above  $T_m$ , the nucleation rate is zero due to liquefaction. On the contrary, for temperatures approaching  $T_g$  the viscosity increases sharply preventing any substantial atoms reorganization. The extra results shown in Figure 5.17 reveal additional information about P-T during devitrification.

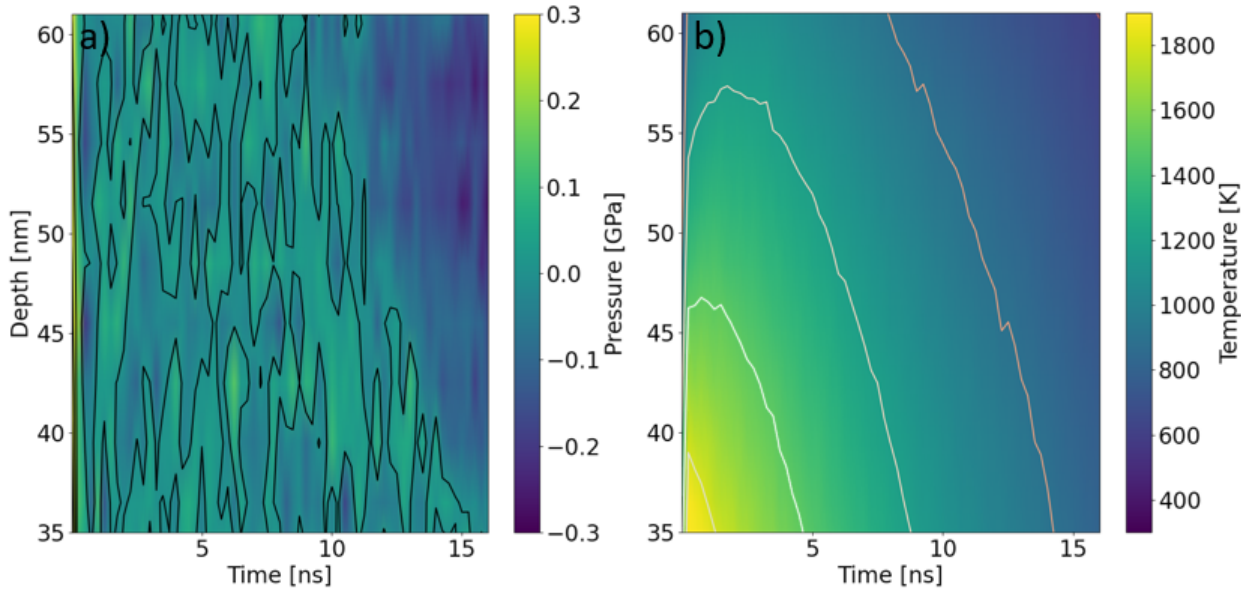


Figure 5.17: Spatiotemporal evolution of thermodynamic quantities within the  $\alpha$ -Cu<sub>21.9</sub>Zr<sub>78.1</sub> devitrified region: a) pressure (contour delimits the local region under contraction), and b) lattice temperature (contour delimits different temperature regimes below and above the melting temperature).

Based on the pressure evolution at  $t \sim 8-16$  ns shown in Figure 5.17(a),  $\alpha$ -Cu<sub>21.9</sub>Zr<sub>78.1</sub> undergoes a negative global pressure of  $\sim -0.3$  GPa. This tendency is explained by the fact that once the crystalline nucleus reaches its critical size to prevent its collapse a negative pressure is needed in order to survive within the glassy environment. Figure 5.17(b) shows that at  $t = 1$  ns,  $T$  is 1900 K, and

it starts to decrease to an average of  $\sim 800$  K at  $t = 16$  ns. This is a part of the devitrification process mechanism puzzle controlled by lowering the temperature in the amorphous matrix through thermal relaxation.

Accordingly, we conclude that devitrification is caused by thermomechanical effects. The first stage consists of the compression pressure wave that fragiles the glass by breaking the extended rigid polyhedra network for  $t \sim 0-0.2$  ns. Nevertheless, for  $t \sim 0.2-8$  ns, the system is no longer under mechanical stress, and a frustration-recombination of polyhedra crystals within the glassy matrix starts. As a result, the recombination dynamics is restrained at  $t \sim 8-16$  ns by the temperature effect around  $T_g$ , allowing the atoms to reconfigure themselves into a crystalline state by a thermal relaxation process.

### 5.6.1 Critical temperature of the crystals growth

In the following, a computation is performed to determine the critical temperature  $T_c$  below which the crystals are formed and compare it to the previous temperature determined at 8 ns ( $\sim 0.87 T_m$ ). An additional brick of comprehension is brought by invoking classical nucleation models [396, 397]. The standard Classical Nucleation Theory (CNT) assumes that devitrification occurs in two correlated distinct stages namely nucleation and growth. The devitrification that intervenes in  $\alpha\text{-Zr}_{78.1}\text{Cu}_{21.9}$  is homogeneous, in contrast to the heterogeneous process that may intervene due to impurities or crystalline seeds already present in the amorphous structure.

As shown in Figure 5.8, the nucleation starts with the emergence of a nucleus with a minimal critical size ( $\sim 2-5 \text{ \AA}$ ) that settles within the amorphous matrix [398]. Assuming that the formed nucleus has a spherical shape, the change of Gibbs free energy in an undercooled liquid is defined by Equation 5.1 as:

$$\Delta G^{crystal}(T) = -\frac{4\pi r^3}{3} \Delta G_V(T) + 4\pi r^2 \sigma_{C-G} \quad (5.1)$$

where  $\Delta G_V$  represents the free energy difference per volume between the glassy and the crystalline states,  $\sigma_{C-G}$  is the crystal-glass interfacial free energy, and  $r$  is the radius of the crystal nucleus.

During the devitrification  $\Delta G_V(T) \approx \Delta H_m \left(1 - \frac{T}{T_m}\right)$  where  $\Delta H_m$  is the melting enthalpy. The critical temperature  $T_c$  below which the nucleus survives within the liquid environment during the devitrification is provided by:

$$T_c = T_m \left( 1 - \frac{2\sigma_{C-G}}{\Delta H_m r} \right) \quad (5.2)$$

$\sigma_{C-G} = 0.11 \text{ J/m}^2$  is a reasonable approximation in the composition range of  $\sim 40\text{-}78.1 \%$ ,  $\sigma_{C-G}$  is assumed to not vary substantially [399].  $\Delta H_m = 8.20 \times 10^9 \text{ J/m}^3$  [400], and  $r \approx 5 \text{ \AA}$ . We end up with a final value of  $T_c \approx 0.94 T_m$ , whereas at  $t = 8 \text{ ns}$  when the devitrification starts  $T \approx 0.87 T_m$  which is below the predicted  $T_c$ . Therefore, we can conclude that the CNT is able to successfully predict a temperature range for CuZr MG devitrification confirmed by MD simulation.

### 5.6.2 Spatial cartography of temperature and pressure during devitrification

We have selected the final time  $t = 16 \text{ ns}$  to probe the local temperature and pressure within the transformed amorphous  $\alpha\text{-Cu}_{21.9}\text{Zr}_{78.1}$  as shown in Figure 5.18.

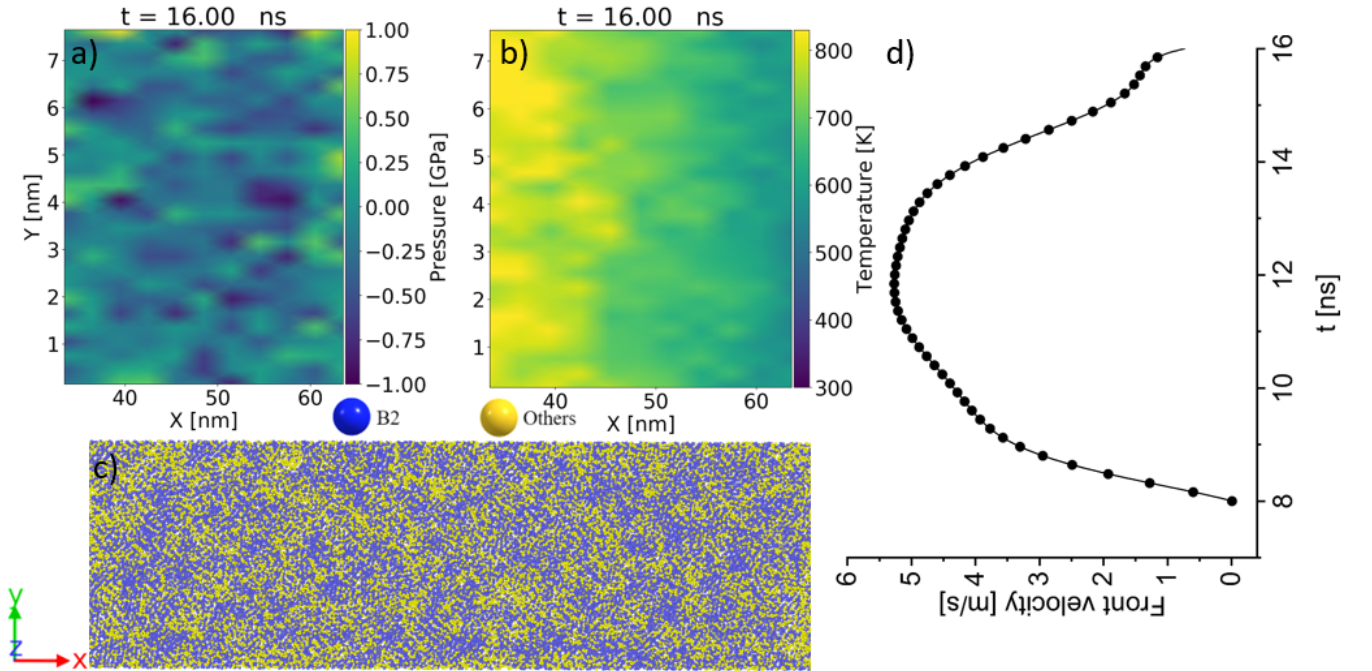


Figure 5.18: Spatial evolution of a) pressure, b) temperature saturated at  $T_g$ , c) the spatial atomic transformed region within  $\alpha\text{-Cu}_{21.9}\text{Zr}_{78.1}$  analyzed at  $t = 16 \text{ ns}$  after ultrafast laser energy deposition, and d) crystallization front velocity during the devitrification. An irradiation of  $\tau = 100 \text{ fs}$  pulse duration and  $F_{\text{abs}} = 34 \text{ mJ/cm}^2$  absorbed fluence are used.

The formed BCC-like heterogeneous phase shown in Figure 5.18 c) is slightly distorted. When we project this on the pressure cartography, a stain with a negative value of  $\sim -1 \text{ GPa}$  is detected. On the other hand, in zones with a major phase corresponding to a mix of amorphous/defects, the local pressure is

less contrasted and oscillates between  $\sim 0.2$  and 1 GPa. we explain this tendency of forming negative pressure zones as a driving force to prevent the collapse of the ordered BCC-like crystalline phase. Moreover, Figure 5.18 b) shows the temperature profile and indicates that the temperature in the devitrified region is between  $\sim 900$  K and 700 K. Based on these temperature conditions, it is not necessary to extend the simulation time beyond 16 ns. This assumption is confirmed by Figure 5.18 d) where the propagation of the crystallization front is computed in the range of  $t = 8-16$  ns.

We can recognize three distinct regimes for producing crystal front. The first stage from  $t \sim 8-11$  ns, we have a fast propagation of the crystallization wave with a maximum velocity of  $\sim 5.5 \text{ m.s}^{-1}$ , higher than the velocity of sound where both nucleation and growth occurs. However, in the range of  $t \sim 11-13.5$  ns this velocity is constant and oscillates around  $\sim 5 \text{ m.s}^{-1}$  meaning that the process of devitrification is still ongoing. During the third portion of the process in the time range of  $t \sim 13.5-16$  ns the velocity is dramatically decreasing to reach a value of  $\sim 0.75 \text{ m.s}^{-1}$  marking the end of the devitrification process. The last stage strongly supports the conclusion that a simulation after a time of 16 ns is useless. The crystallization wave has almost completely been extinguished.

### 5.6.3 Entropy computation during the devitrification

This partial devitrification of the  $\alpha\text{-Cu}_{21.9}\text{Zr}_{78.1}$  sample may be seen as a disorder-order flip. For a deeper analysis and complementary probe of the transition, we used a thermodynamic property based on order and disorder known as entropy. This property is computed using the entropy formula  $S_S^i = -2\pi\rho k_B \int_0^{r_m} [g(r)\ln(g(r)) - g(r) + 1] r^2 dr$  described in [283, 284]. The result shown in Figure 5.19 indicates the temporal behavior of entropy.

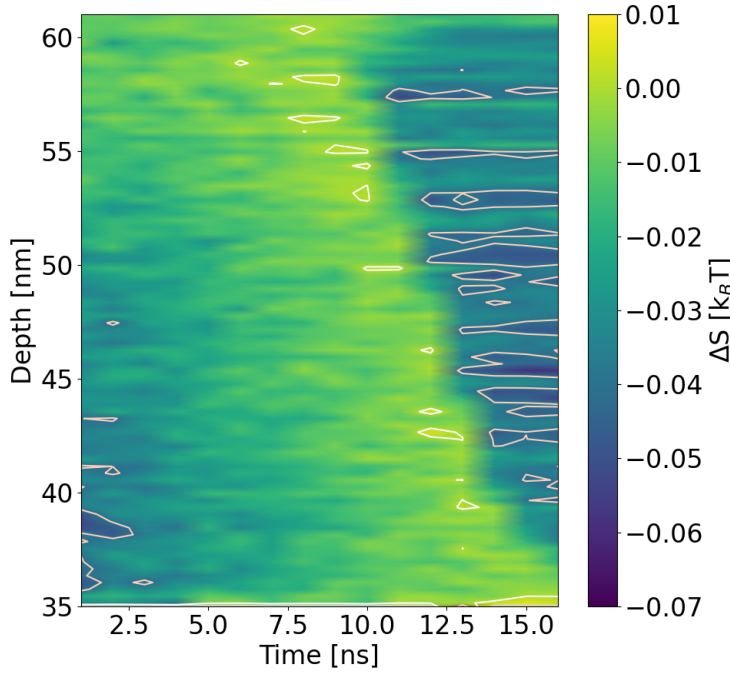


Figure 5.19: Space and time evolution of the entropy variation  $\Delta S = S(t = t_n) - S(t = 0)$  with respect to the initial amorphous phase (at  $t = 0$  ns) during the devitrification. The ordered-crystalline region is colored in dark blue whereas the amorphous region is emphasized by light green environments.

During the propagation of the heat generated by the laser, the entropy  $\Delta S$  rises to reach a value of  $\sim 0.01 k_B T$  at  $t \sim 8$  ns. At later times of  $t \sim 8-16$  ns, the nucleation and growth intervene making the entropy  $\Delta S$  decrease to  $\sim -0.07 k_B T$ . This indicates a rearrangement of atoms in an ordered state.

Four kinds of crystallization types can take place within the amorphous matrix during devitrification [401]. The primary is obtained when the product phase has a different composition when compared to the parent glassy phase. Then, eutectic phases are characterized by two or more phases nucleating and growing simultaneously. Also, spinodal/binodal decomposition involves phase separation (also called segregation) of the glassy phase prior to devitrification. All these three do not fit with our findings. Therefore, the devitrification process observed in the simulation consists in a polymorphous devitrification process since the obtained nanocrystal has a similar composition to the parent amorphous phase.

### 5.6.4 Amorphous CuZr-alloy devitrification free energy computation

Although the investigation on devitrification of amorphous  $\alpha$ -Cu<sub>21.9</sub>Zr<sub>78.1</sub> material reveals the presence of nanocrystals within the amorphous target. The transformation was approached and treated from multiple perspectives, including structural analysis, RDF, and entropy. Nevertheless, the transition from a metastable-to-stable structure is marked by a minimum Gibbs free energy. Therefore, to facilitate understanding, we have successfully computed this quantity as shown in Figure 5.20.

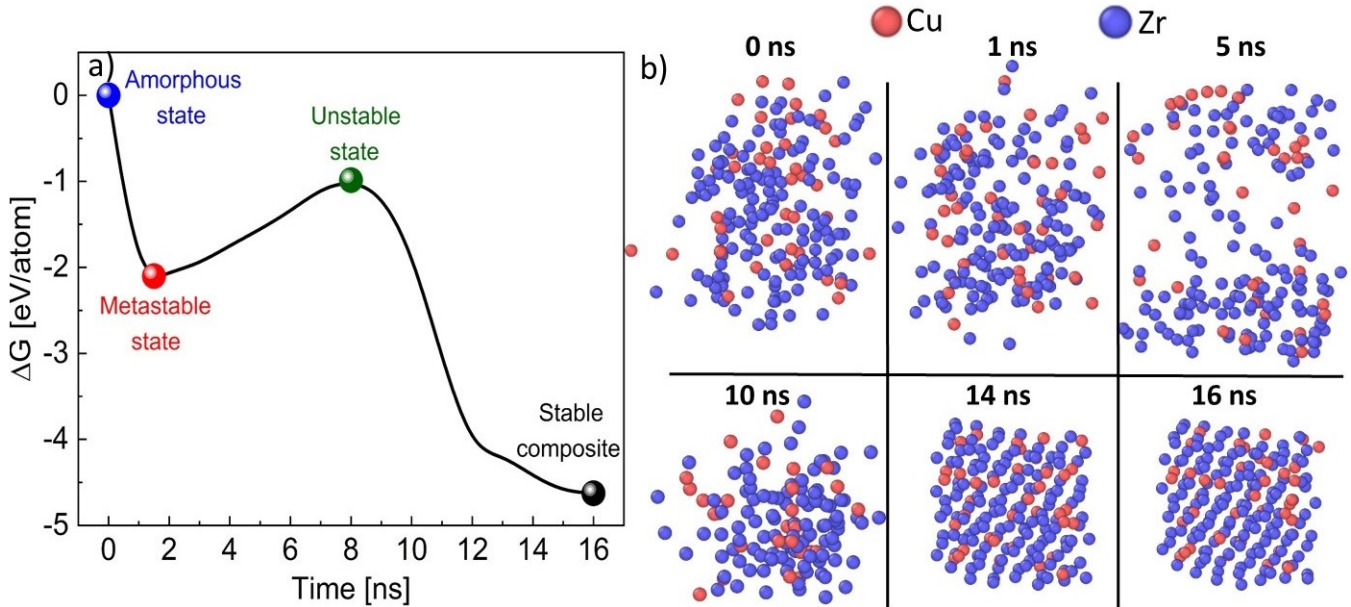


Figure 5.20: Gibbs free energy calculation using the PM7 semiempirical method, a) Normalized free-energy landscape obtained for multiple configurations ( $\Delta G = G(t = t_n) - G(t = 0)$ ) of 184 atoms at  $t = 0$ -16 ns. b) Different atomic configurations captured during the devitrification process used to compute the Gibbs free energy at  $t = 0, 1, 5, 10, 14,$  and  $16$  ns. The copper and zirconium atoms are colored in red and blue respectively.

In the following, we employ a semiempirical quantum mechanics approach known as the PM7 method [402] implemented in the Gaussian package [403] to compute the Gibbs free energy  $\Delta G$  as a signature of the devitrification process. The PM7 method is a parametric approach with good accuracy over CPU costs ratio that uses databases of *ab initio* and experimental data.

For the Gibbs free-energy simulation purpose, we select 184 atoms from the  $\alpha$ -Cu<sub>21.9</sub>Zr<sub>78.1</sub> in the devitrified region and tracked them from 0 to 16 ns. Figure 5.20(a) indicates that during the phase change four key times can be noticed. First, at  $t = 0$  ns the system is in an amorphous metastable state used as a reference value. Then, at  $t = 1$  ns after the laser energy deposition, the structure

is in a metastable state with  $\Delta G \approx -2.2$  eV/atom. The Gibbs free energy of the system significantly increases at  $t = 2-8$  ns where it becomes unstable mainly due to heat propagation.

In this regime, no crystal is formed and this tendency is quantitatively confirmed by the increase of  $\Delta G \approx -0.9$  eV/atom. Here again, we confirm the important role of the temperature upon devitrification as demonstrated at time  $t = 8-16$  ns where the Gibbs free energy drastically decreases to  $\Delta G \approx -4.8$  eV/atom which coincides with the thermal relaxation. This substantial energy drop is a marker of the phase change into a more stable nanocomposite with minimal energy as shown in Figure 5.20(b).

From the result, one can assume a straight link between the Gibbs free energy variations and the polyhedra evolution during the devitrification process *i.e.*, a drop in the Gibbs free energy is associated with the breaking of polyhedra in the  $t \sim 0-0.05$  ns range. This suggests that reducing the number of polyhedra increases the stability of the system. On the other hand, the free energy increases significantly while the pressure vanishes at  $t \sim 1-8$  ns, indicating that the polyhedron network is a powerful estimator of the devitrification process. At  $t > 8$  ns, the combination of the critical number of broken polyhedra and thermal relaxation leads to a reduction of the free energy that stabilizes the composite and allows the identification of the transition between amorphous and nanocrystalline states.

## 5.7 Application to phononic thermal conductivity

To start exploring the performances of the freshly-built nanocomposite, MD was employed to compute the phononic thermal conductivity ( $\kappa_a$ ). It has been demonstrated in recent studies that there is a possibility to improve  $\kappa_a$  of materials by using a femtosecond laser treatment on nanoparticles. This was mainly achieved in alumina and titanium dioxide as reported in the works of Ha *et al* [404, 405]. However, to our knowledge, no literature discussed  $\kappa_a$  improvement in the amorphous structure post treated with an ultrafast laser. Furthermore, since amorphous CuZr alloys exhibit low  $\kappa_a$  values, the objective of this research is to examine the possible influence of crystal growth on  $\kappa_a$ .

Practically,  $\kappa_a$  is calculated in both the amorphous and composite structures employing the Green–Kubo method as implemented in LAMMPS [406, 407, 408]. The phonon thermal conductivity is given by the following equation:

$$\kappa_a = \frac{V}{3k_B T^2} \int_0^\infty \langle J(0)J(t) \rangle dt \quad (5.3)$$

where  $V$ ,  $k_B$ ,  $T$ ,  $J$ , and  $t$  describe volume, Boltzmann constant, temperature, instantaneous heat flux (with contributions from all components  $J_x$ ,  $J_y$ , and  $J_z$ ), and time respectively.

We use a 3D-periodic simulation cell made of  $\sim 400,000$  atoms and probe the temperature sensitivity of the thermal conductivity for the both amorphous and nanocomposite systems. The thermal conductivity is computed in the 300-900 K temperature range. For this purpose, we first distribute the atom velocities and then equilibrate the system during 20 ps within the NVE ensemble using a MD timestep of 1 fs. Then, we used a statistical method to compute the averaged value of the spontaneous heat autocorrelation flux  $\langle J(0)J(t) \rangle$  during 400 ps in the NVE ensemble. The result is illustrated in Figure 5.21 (see appendix L).

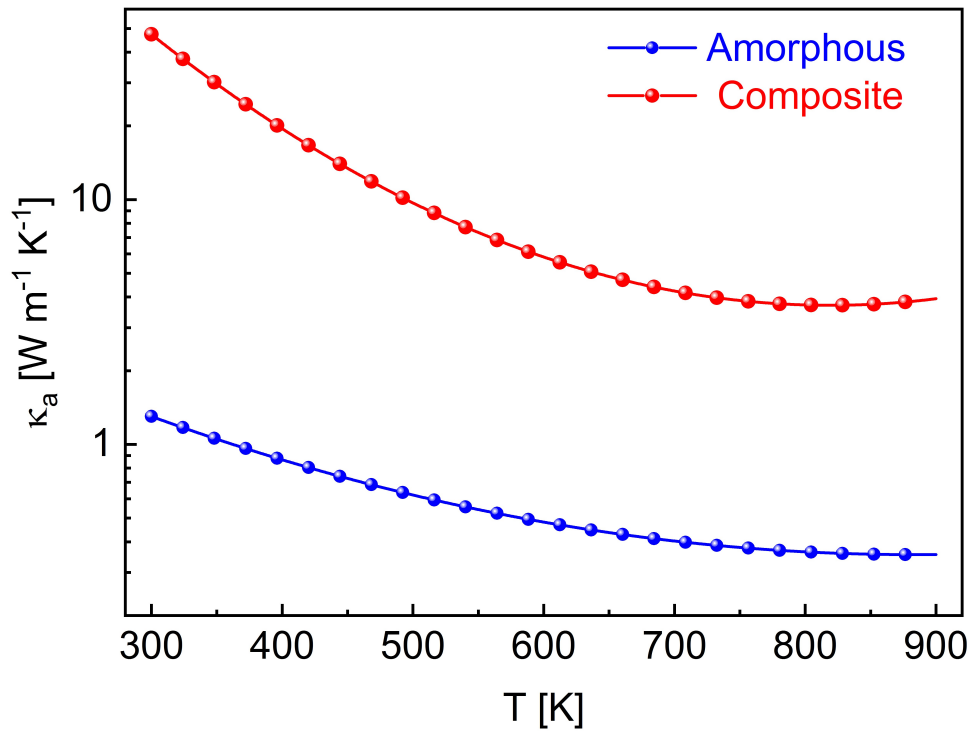


Figure 5.21: Phononic thermal conductivity of  $\alpha$ -Zr<sub>78.1</sub>Cu<sub>21.9</sub> in the amorphous phase and in the nanocomposite at various temperatures. Note the factor 36 between the two phases at  $T = 300$  K.

$\kappa_a$  of both the nanocomposite and amorphous structures decreases when the temperature increases due to the rise of the phonon–phonon scattering rate [409].  $\kappa_a$  of the amorphous structure also decreases significantly by 72 % (1.30 W

$\text{m}^{-1}\text{K}^{-1}$  at 300 K to  $0.36 \text{ W m}^{-1}\text{K}^{-1}$  at 900 K), whereas the composites one decreases by 92 % ( $47.33 \text{ W m}^{-1}\text{K}^{-1}$  at 300 K to  $3.74 \text{ W m}^{-1}\text{K}^{-1}$  at 900 K). These results show that  $\kappa_a$  of the nanocomposite is  $\sim 36$  and  $\sim 9$  times larger than the one of the amorphous phase at  $T = 300, 900 \text{ K}$ , respectively. Therefore, the presence of nanocrystals within the amorphous  $\alpha\text{-Zr}_{78.1}\text{Cu}_{21.9}$  structure leads to the sharp increase of  $\kappa_a$  confirming that the local devitrification of amorphous structures is a promising approach for the creation of high-performance materials with exceptional properties at room temperature.

## 5.8 Summary conclusion

In this study, the TTM-MD method is used to investigate and capture the devitrification process induced by an ultrafast laser irradiating an  $\alpha\text{-Cu}_{21.9}\text{Zr}_{78.1}$  sample. Our findings show that the composition of the sample plays a crucial role in predicting the laser-induced devitrification. Additionally, we did not observe any segregation effect but a locally-formed BCC solid solution nanoalloy retained the global initial chemical composition of the sample. At the investigated fluence and pulse duration laser conditions, the main mechanism behind this phase transition is found to be the local atomic rearrangements (breaking of polyhedra) due to the collaborative effect of the compressive pressure wave and thermal relaxation. The temperature plays a major role where the highest crystallization occurs at temperatures over  $T_g$ . Importantly, we observed that the BCC-like phase is not transient but rather stable over time within the amorphous matrix. These results demonstrate the devitrification feasibility by ultrafast laser pulse and suggest that this method could be further employed in materials processing to create a new generation of nanoarchitected systems with enhanced properties, reduced costs, optimized manufacturing processes, and improved materials efficiency for modern industrial technologies.

# Conclusion and perspectives

The theoretical work presented here is a fundamental modeling of the laser-matter interaction process with crystalline and amorphous CuZr alloy targets using a hybrid TTM-MD approach as implemented in LAMMPS software. We found that a variety of structural modifications occurred during the ultrashort laser energy deposition process, such as martensitic transition and devitrification. Moreover, defects such as twinning, point defects, and cavitation. It was demonstrated that the phase change depends on the initial atomic arrangement (amorphous or crystalline) and the composition. A meticulous investigation was conducted in order to accurately predict experimental results and beyond. The methodology we followed for performing the simulation was based on three standard stages, i.e., identify (define) the material, its electronic properties, and interatomic potential, develop a suitable system setup, and manage the post-processing of the obtained results with OVITO and Python. With all of these fruitful achievements, we can now refine the next generation of materials with outstanding properties for surgical precision applications.

However, because of a few limitations of the implemented model, there is still much work to be done in the future. First, find a way to compute the input electronic properties such  $C_e(T_e)$ ,  $\kappa_e(T_e)$  and  $g_e(T_e)$  using first principle computation especially for the  $\alpha$ -Cu<sub>50</sub>Zr<sub>50</sub> amorphous structures. Then, extend the computation of all these properties for all the possible amorphous compositions by invoking machine learning techniques. Moreover, the LAMMPS package needs some improvement, since in the concurrent version only a constant  $g_e$  is possible to use. Thus, for a realistic implementation, an electronic dependent  $g_p(T_e)$  is necessary to be employed. Referring back to the chapter 4, the experimental setup is generally a multipulse laser (train of pulses). The code should therefore be enhanced to model at least two pulses as well as a change in electronic properties on the fly. The reason is after the first laser shot we are no longer irradiating the same material.

Further, since we do not light the same material in multipulse modeling because the system is in a liquid state, it is very difficult to change its properties on the fly. As long as a reliable EAM potential can be found for the CuZr alloy, it is better to develop a proper potential that is optimized for the electronic temperature. In addition, one limitation of the concurrent version of potential is that rarely the effect of oxygen is included as seen in chapter 4. Developing a ReaxFF potential would provide a great opportunity to investigate and elucidate the mechanism behind the oxidation issues of our metallic glasses. The package is written in such a way that the heat is diffused following the  $x$  direction. An improvement is possible by passing from 1D to 3D heat diffusion. A machine learning method can be developed in chapter 5 to identify metallic glasses with low GFA and susceptible to crystalline transformations based on their stoichiometry. This method can be used to study them with the aid of atomistic methods. Laser-matter interactions are not well studied for other classes of materials, for instance high entropy alloys, which may exhibit interesting evolution, polycrystalline targets, or polymorphous targets for a specific application. A very interesting additional work could be undertaken by computing Gibbs free energy on the amorphous sample and providing an explanation of preferably forming  $\text{ZrO}_2$  instead of  $\text{CuO}$ . An alternative starting point in chapter 5 might be the study of mechanical (tensile, shear, compression, etc.), electrical, and transport properties of the glassy nanocomposite (devitrified) and determining whether any of these properties are enhanced.

Despite all the provided clarifications, one of the most pertinent questions remains unanswered. Using the same composition and laser operating conditions as those in chapters 3 and 5, it is possible to observe these phase transitions experimentally. Furthermore, a promising investigation of amorphous-crystal phase transition may be extended to interesting titanium-based metallic glasses alloys, such as NiTi and CuTi. The previous material (both crystalline and amorphous phases) was already thoroughly studied in the framework of TTM-MD. Based on this unique exploration, we are able to comprehend the crystallization process as shown in Figure C 5.22.

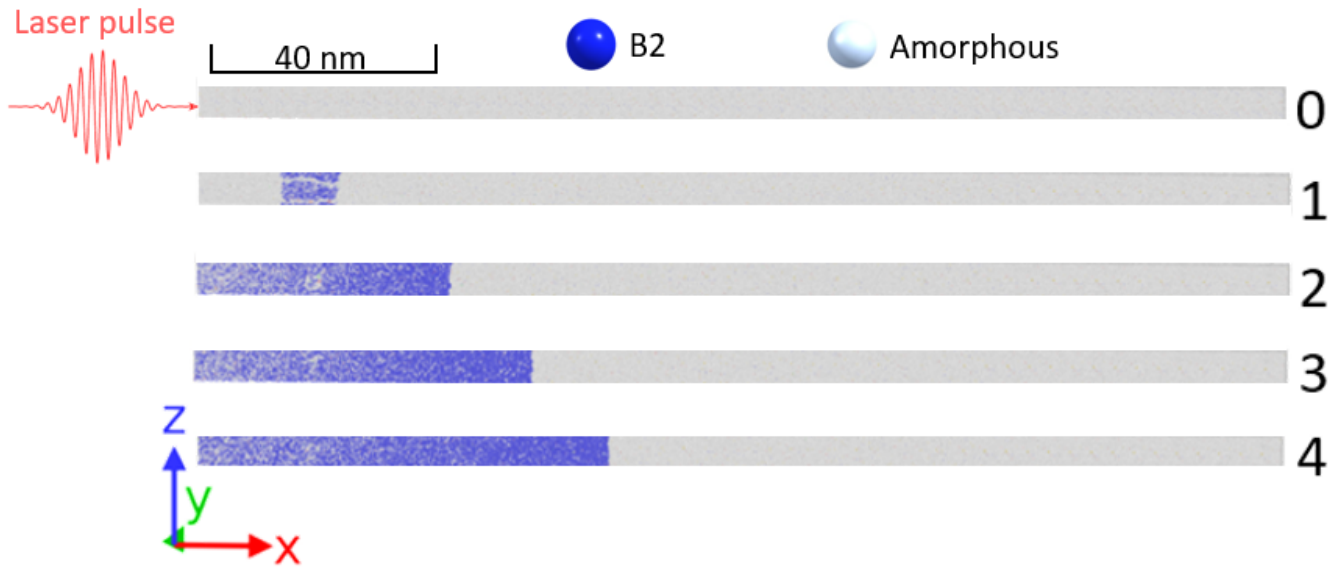


Figure C 5.22: Preliminary result of the  $\alpha$ -Cu<sub>50</sub>Ti<sub>50</sub> total devitrification during resolidification process via ultrafast irradiation of  $\tau = 100$  fs pulse duration and  $F_{\text{abs}} = 30$  mJ/cm<sup>2</sup> absorbed fluence at key times: 0 (amorphous), 1, 2, 3, and 4 ns (crystalline).

A modified version of the current TTM-MD sources code was developed to perform a more realistic laser-matter interaction. Our future work will focus on comparing crystallization kinetics using different laser-induced thermodynamics, and we see that the  $\alpha$ -Cu<sub>50</sub>Ti<sub>50</sub> response is radically different since the devitrification is occurring on all the material simultaneously. However, for the  $\alpha$ -Cu<sub>21.9</sub>Zr<sub>78.1</sub> the effects is local. A more in-depth study of novel phase transformations, the mechanisms associated with femtosecond irradiation, the pulse shape (and its duration) effect, and the evolution of shock waves will pave the way for physics-guided advanced laser pulse processing.

## Vita

2019–2022: Ph.D Physics Student at Hubert Curien laboratory, UMR CNRS 5516, University of Lyon, Saint-Etienne, France.

2017–2017: M.Sc Theoretical Physics and Applications, University of Cergy-Pontoise, Cergy-Pontoise, France.

2015–2017: M.Sc Laser-Matter Physics, University of Tizi Ouzou, Tizi Ouzou, Algeria.

2013–2015: B.Sc General Physics, University of Tizi Ouzou, Tizi Ouzou, Algeria.

2011–2013: National Institute of Electronics And Electrical Engineering, University of Boumerdes, Boumerdes, Algeria.

2010–2011: High School Certificate of Mathematics, Tizi-Ouzou, Algeria.

## Articles and Conferences

December–2022: Dynamics of Cu-Zr metallic glass devitrification under ultrafast laser excitation revealed by atomistic modeling. Authors: **Djafar Iabbaden**, Jonathan Amodeo, Claudio Fusco, Florence Garrelie and Jean-Philippe Colombier, in preparation.

November–2022: Molecular dynamics simulation of structural evolution in crystalline and amorphous CuZr alloys upon ultrafast laser irradiation. Authors: **Djafar Iabbaden**, Jonathan Amodeo, Claudio Fusco, Florence Garrelie and Jean-Philippe Colombier, Physical Review Materials 6(12), 126001.

June–2022: Invited Speaker to International Symposium Fundamentals of Laser Assisted Micro and Nanotechnologies FLAMN-2022, Topic: Molecular Dynamics Simulation of Structural Evolution in Crystal and Amorphous CuZr Alloys under Ultrafast Laser Irradiation. Authors: **Djafar Iabbaden**, Jonathan Amodeo, Claudio Fusco, Florence Garrelie and Jean-Philippe Colombier, Saint-Petersburg, Russia.

June–2022: 20th International Conference Laser Optics ICLO-2022, Topic: Molecular Dynamics Simulation of Structural Evolution in Crystal and Amorphous

CuZr Alloys under Ultrafast Laser Irradiation. Authors: **Djafar Iabbaden**, Jonathan Amodeo, Claudio Fusco, Florence Garrelie and Jean-Philippe Colombier, Saint-Petersburg, Russia.

October–2021: V International Conference on Ultrafast Optical Science, Topic: Molecular Dynamics Simulation of Structural Evolution in Crystal and Amorphous Alloys under Ultrafast Laser Irradiation. Authors: **Djafar Iabbaden**, Jonathan Amodeo, Claudio Fusco, Florence Garrelie and Jean-Philippe Colombier, Lebedev Physical Institute, Russia.

2022: High-Density Nanowells Formation in Ultrafast Laser-Irradiated Thin Film Metallic Glass. Authors: Mathilde Prudent, **Djafar Iabbaden**, Florent Bourquard, Stéphanie Reynaud, Yaya Lefkir, Alejandro Borroto, Jean-François Pierson, Florence Garrelie and Jean-Philippe Colombier, Nano-Micro Letters 14.1 (2022): 1-15.

# Appendix A

## Build LAMMPS with make in MPI

The objective of this section is to summarize the numerical procedure in order to perform MD simulation and also the LAMMPS installing procedure from scratch in MPI. As mentioned previously, LAMMPS is an open source software which is under heavy development with several packages giving access to different features.

The modeling process involves Three main key steps, namely, (1) initialization where the atomistic geometry is defined, (2) Computation of the of atomic forces by solving Newton's equation of motion using a specific integration scheme, and (3) post-process the concerned output properties. These steps are summarized in the flowchart shown in Figure [A.1](#).

In order to install LAMMPS, first step is to download it from the official website (in my case version 3Mar20) and unzip it. Then, go inside the **src** directory and start to build LAMMPS in parallel (check that gcc and gfortran are installed) by typing in the terminal the following command:

```
make  
mpi
```

Now, display all the possible packages that can install by tapping :

```
make ps
```

To install a given package, execute these commands in the terminal:

```
make yes-  
'name_of_the_package'
```

Once everything is installed without errors, recompile everything again.

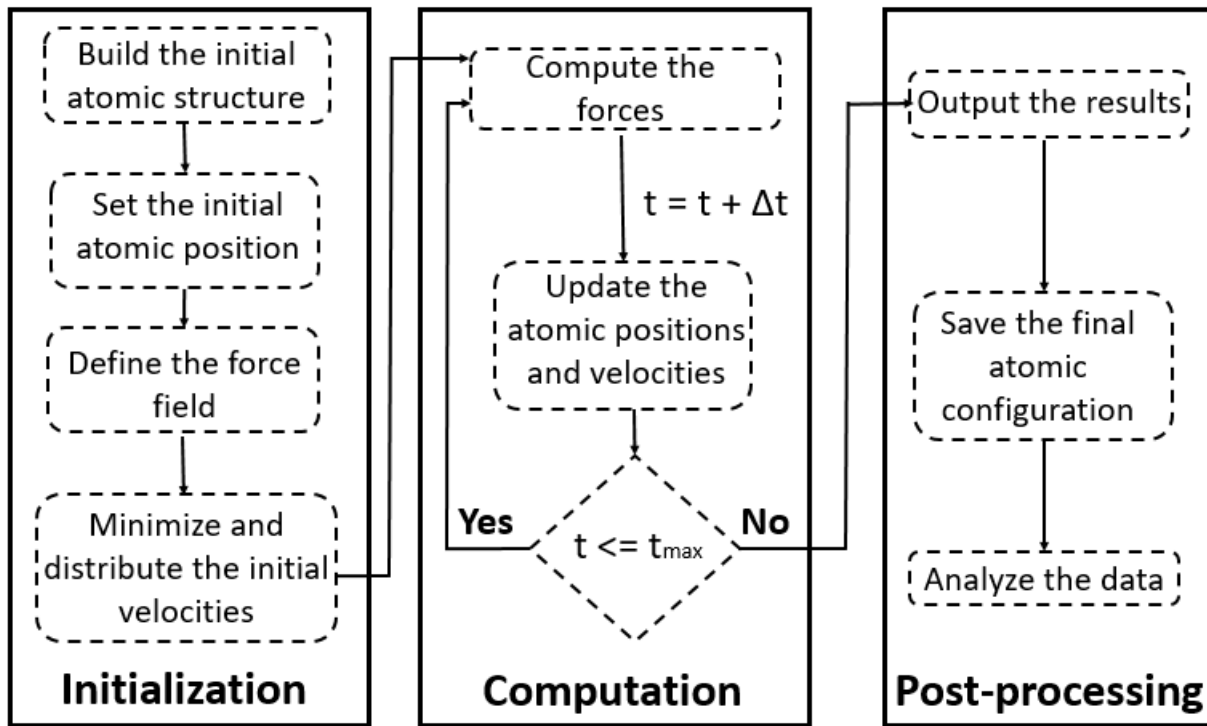


Figure A.1: Numerical workflow diagram representing the steps applied in MD simulation realized using LAMMPS.

```
make
mpi
```

An executable named **lmp\_mpi** will be used either by calling it via a path or simply by copying it into the working directories. You need to run the following command to execute your input script:

```
mpirun -np 96 /path/to/lammps/src/lmp_mpi -in
in.input
```

# Appendix B

## LAMMPS script to determine the melting temperatures

An executable named **lmp\_mpi** will be used either by calling it via a path or simply by copying it into the working directories. You need to run the following command to execute your input script. The following LAMMPS script sample permits the computation of the B<sub>2</sub>-Cu<sub>50</sub>Zr<sub>50</sub> crystal melting point:

```
##### Tm #####
units metal
atom_style atomic
dimension 3
boundary p p p
atom_style      atomic

read_data      CuZr_initial_54_000_B2_positions.lmp

timestep 0.001
pair_style eam/fs
pair_coeff * * Cu-Zr_4.eam.fs Cu Zr

thermo 100000
thermo_style custom step temp press pe

minimize 0 1.0e-8 1000000 10000000
fix      1 all box/relax iso 1.0 vmax 0.001
minimize 0 1.0e-8 1000000 10000000
unfix    1
minimize 0 1.0e-8 1000000 10000000
```

```
thermo_style custom step temp press pe vol
velocity all create 600.0 873847
fix 1 all nve
run 100000
unfix 1

fix 1 all npt temp 300 2000 0.1 iso 1.0 1.0 1.0
run 1700000
unfix 1
```

```
write_data liquid.lmp
##### END script #####
```

Here is a python script to plot the potential energy versus temperature in the B<sub>2</sub>-Cu<sub>50</sub>Zr<sub>50</sub> crystal alloys during the liquefaction (solid-liquid) phase change process.

```
import numpy as np
from matplotlib import pyplot as plt
from mpl_toolkits.axes_grid1 import make_axes_locatable

Fname="Tm.dat"
data = np.loadtxt(Fname)
x = data[:,1]
y = data[:,3]/54000

fig = plt.figure(figsize=(9,9))
ax = fig.gca()
plt.plot(x, y)

ax.set_xlabel("T (K)", fontsize=20)
ax.set_ylabel("Potential energy per atom (eV)", fontsize=20)
plt.xticks(fontsize = 20)
plt.yticks(fontsize = 20)
plt.autoscale()
fig.savefig("Tm_B2.png")
plt.show()
```

```
#####PRDF#####
```

```
units          metal
dimension       3
boundary        p p p
variable        t index 1000
atom_style      atomic
```

```
read_data       liquid.lmp
```

```
pair_style      eam/fs
pair_coeff       * * Cu-Zr_4.eam.fs Cu Zr
timestep        0.001
```

```
thermo          1000
thermo_style    custom step temp press vol
```

```
compute         RDF all rdf 100 1 1
fix             rdf all ave/time 1 1 $t c_RDF[*] file Cu-Cu.dat mode vector
run            $t
```

```
#####
```

Here is a python script that we have used for post-processing the sketch of the PRDF obtained for the liquid structure of both  $B_2\text{-Cu}_{50}\text{Zr}_{50}$  and  $C_{11b}\text{-Cu}_{33.3}\text{Zr}_{66.7}$ .

```
import numpy as np
from matplotlib import pyplot as plt
import matplotlib.pyplot as plt
from mpl_toolkits.axes_grid1 import make_axes_locatable
from scipy.interpolate import make_interp_spline
# loading weird data

for fname in ('Zr-Zr.dat', 'Cu-Zr.dat', 'Cu-Cu.dat'):
    data=np.loadtxt(fname)
    r=data[:,1]
    gr=data[:,2]
    r = np.array(r)
    gr = np.array(gr)
    rmin = 0
    rmax = 8
```

```
rnew = np.linspace(r.min(), r.max(), 300)
gfg = make_interp_spline(r, gr, k=3)
gr_new = gfg(rnew)
plt.xlim(rmin, rmax)
plt.xlabel('r ($\AA$)', fontsize=32)
plt.ylabel('g(r)', fontsize=32)
plt.xticks(fontsize = 36)
plt.yticks(fontsize = 36)
legend = fname.split('.')[0]
legend = legend.split('_')
legend = '.'.join(legend)
plt.plot(rnew, gr_new, label = legend , linewidth=5)
plt.legend(loc=(0.75, 0.75), fontsize=25)
plt.show()
```

# Appendix C

## LAMMPS script to prepare amorphous sample

A LAMMPS script to build from scratch a MG sample by mimicking the experimental approach at each stage of the calculation. The first stage describes the atomic configuration production minimized and thermalized at 300 K. It was followed by heating above the melting temperature and fast quenching. The obtained structure will be replicated and used for laser-matter interaction investigations.

```
##### MG elaboration #####
units metal
dimension 3
boundary p p p
atom_style atomic

lattice      bcc 3.229
region      whole block 0 20 0 20 0 20
create_box  2 whole
lattice      sc 3.229
create_atoms 1 region whole
lattice      sc 3.229 origin 0.5 0.5 0.5
create_atoms 2 region whole

timestep 0.001
pair_style eam/fs
pair_coeff * * Cu-Zr_4.eam.fs Cu Zr

thermo 100000
thermo_style custom step temp press fnorm vol pe density
```

```

dump          2 all custom 10 rlx.dump id type x y z
minimize     0 1.0e-8 100000 1000000
fix          1 all box/relax aniso 1.0 vmax 0.001
minimize     0 1.0e-8 100000 1000000
unfix        1
minimize     0 1.0e-8 100000 1000000
undump       2

thermo 100000
thermo_style custom step temp press vol density
velocity     all create 600.0 873847
fix          1 all nve
run          100000
unfix        1

dump         3 all custom 100000 heating.dump id type x y z
fix          1 all npt temp 300 2000 0.1 aniso 1.0 1.0 1.0
run          1700000
unfix        1
undump       3

dump         4 all custom 1000000 annealing.dump id type x y z
fix          1 all npt temp 2000 2000 0.1 aniso 1.0 1.0 1.0
run          10000000
unfix        1
undump       4

dump         5 all custom 1000000 quenching.dump id type x y z
fix          1 all npt temp 2000 300 0.1 aniso 1.0 1.0 1.0
run          170000000
unfix        1
undump       5

dump 6       all custom 1000000 relaxing.dump id type x y z
fix          1 all npt temp 300 300 0.1 aniso 1.0 1.0 1.0
run          10000000
unfix        1

```

undump           6

write\_data amorphous.lmp

##### END script #####

# Appendix D

## Simulation of laser-matter interactions using LAMMPS

This section shows an input example of LAMMPS to perform a laser-matter interaction simulation in  $B_2\text{-Cu}_{50}\text{Zr}_{50}$  crystalline structure.

```
#####Laser-matter interaction#####

units      metal
dimension  3
boundary   p p p
echo       both

variable   Nevery equal 100
variable   Nrepeat equal 10
variable   Nfreq equal 10000
variable   deltax equal 30
variable   deltay equal 3
variable   deltaz equal 3

atom_style atomic
neighbor   0.3 bin
neigh_modify every 20 delay 0 check no

read_data  int_B2.lmp
pair_style eam/fs
pair_coeff  * * Cu-Zr_4.eam.fs Cu Zr
timestep   0.001

thermo_style custom step lx ly lz xlo xhi ylo yhi zlo zhi temp press
```

thermo 1000

velocity all create 600 44543 dist gaussian  
fix 1 all nve  
run 5000  
unfix 1

variable t equal temp  
run 0

fix simnpt1 all npt temp  $\{t\}$  300 0.1 aniso 1.0 1.0 1.0  
run 5000  
unfix simnpt1

fix simnpt2 all npt temp 300 300 0.1 aniso 1.0 1.0 1.0  
run 5000  
unfix simnpt2

write\_data stage\_1.lmp

variable l\_map\_x equal xhi-xlo  
variable l\_map\_y equal yhi-ylo  
variable l\_map\_z equal zhi-zlo

change\_box all x final 0  $\{l\_map\_x\}$  remap  
change\_box all y final 0  $\{l\_map\_y\}$  remap  
change\_box all z final 0  $\{l\_map\_z\}$  remap

variable l\_xlo equal xlo  
variable l\_xhi equal xhi  
variable l\_ylo\_vac equal ylo  
variable l\_yli\_vac equal yhi  
variable l\_zlo\_vac equal zlo  
variable l\_zli\_vac equal zhi  
variable l\_nrbc equal xhi-1000  
variable l\_vac equal lx\*(0.5)

region del0 block  $\{l\_xlo\}$   $\{l\_vac\}$   $\{l\_ylo\_vac\}$   $\{l\_yli\_vac\}$

```

                                ${l_zlo_vac} ${l_zli_vac}
group del0 region del0
delete_atoms      group del0

region NRBC block ${l_nrbc} ${l_xhi} ${l_ylo_vac} ${l_yli_vac}
                                ${l_zlo_vac} ${l_zli_vac}
group NRBC region NRBC

write_data      stage_2.lmp

compute spa all stress/atom NULL
compute volvoronoi all voronoi/atom
compute KE all ke/atom

reset_timestep 0

thermo_style    custom step temp press
thermo          1000
restart         20000 file.restart

compute chunkX all chunk/atom bin/1d x lower ${deltax} units box
fix density_X all ave/chunk ${Nevery} ${Nrepeat}
                ${Nfreq} chunkX density/number file density_X.out

variable temp atom c_KE/(1.5*8.61e-5)
fix temp_profile all ave/chunk ${Nevery} ${Nrepeat} ${Nfreq}
                chunkX v_temp file temp.out

variable meanpress atom -(c_spa[1]+c_spa[2]+c_spa[3])/(3*10000)
fix press_profile all ave/chunk ${Nevery} ${Nrepeat} ${Nfreq}
                chunkX v_meanpress c_volvoronoi[1] file pressure.out

compute chunkYZ all chunk/atom bin/3d x lower ${deltax} y lower
                ${deltay} z lower ${deltaz} units box

fix chunkYZ all ave/chunk ${Nevery} ${Nrepeat} ${Nfreq} chunkYZ
                density/number v_temp v_meanpress c_volvoronoi[1] file local_py.out

```

```

fix                5 NRBC viscous 0.0025
dump               sn all custom 10000 TTM_MD.dump id type x y z
                  v_meanpress c_volvoronoi[1]

fix                1 all nve
fix  TTM all ttm/mod 13423 ttm_parameters 702 1 1 T_init 100 T_out.out
thermo             1000
thermo_style       custom step temp press f_TTM[1] f_TTM[2]
run                30000
unfix              TTM
unfix              1

fix                2 all nve
thermo_style       custom step temp press
thermo             5000
run                170000
undump             sn

write_data         final_strc.lmp
unfix              2
unfix              visc
##### END script #####

```

A python script is used for post-processing the pressure and temperature in order to produce the spatio-temporal color maps.

```

import numpy as np
import matplotlib.pyplot as plt
from numpy import *

#Spatial limits following x
xmin = 0
xmax = 200

#Saturation values of the property
vmin = -5
vmax = 20

# filename input

```

```

fname = "pressure.out"

#Frequency incrementation in the file
timeStepIncrement = 10000 ; # equal to Nfreq chosen in LAMMPS script

#Rescale time axis to ps equal to the timestep in the lammps script)
timeFactor = 0.001 ; # factor to convert time in (ps)

timeSteps={} # list of arrays for each timestep

# read data and skip the 3 first lines
data=np.loadtxt(fname,skiprows = 3,max_rows=1)
nrows = int(data[1]) # number of rows per time block
blockId = 0 # time block number

while True :
    try :
        data=np.loadtxt(fname, skiprows =3+ (nrows+1)*blockId, max_rows=1)
        time = timeStepIncrement * timeFactor * (blockId + 1)
        data=np.loadtxt(fname,skiprows=3(nrows+1)*blockId+1,max_rows=nrows)
        timeSteps[time] = data.copy()
        blockId += 1
        print(str(blockId))
    except :
        print("Finished loading data")
        break ;

# create matrices
X = [] # spatial coordinate
T = [] # time coordinates
V = [] # data values
S = [] # VORONOI

# read the property in the 1 corresponds to column which is for instance
#X or coord1, 3 is the property like density, Temp or pressure
for time in timeSteps.keys() :
    X.append(timeSteps[time][:,1])
    T.append([float(time)]*nrows)

```

```

    V.append(timeSteps[time][:,3])
    S.append(timeSteps[time][:,4])
#Ignore the zero division since the volume in the vacuum is 0
np.seterr(divide='ignore', invalid='ignore')

# convert angstroms to nm
X = np.array(X)
X = X * 0.1

#Shift the surface position to 0
X = X-201.03

V = np.array(V)
S = np.array(S)

#Define the pressure P= constraint/volume
V = V/S

where_are_NaNs = isnan(V)
V[where_are_NaNs] = 0

fig = plt.figure( figsize=(10,10) )
plt.rcParams.update({'font.size': 24})

#User define sturation values
plt.pcolormesh(T, X, V, shading = "gouraud", cmap='RdBu_r', vmax, vmin)

#Plots only the limits we want
plt.ylim(xmin, xmax)
#Invert the y axis
plt.gca().invert_yaxis()
plt.grid()

#Set legends and label
plt.colorbar().set_label('Pressure (GPa)')
plt.xlabel('Time (ns)')
plt.ylabel('Depth (nm)')
#Output the color maps in a png format

```

```
plt.savefig("Pressure_map.png")
```

A python script to plot the pressure evolution in a sample at specific times.

```
import numpy as np
from matplotlib import pyplot as plt
import matplotlib.pyplot as plt
from mpl_toolkits.axes_grid1 import make_axes_locatable
from scipy.interpolate import make_interp_spline

# loading data

blockIdx = 0
timeSteps={};
Fname="pressure.out"
data = np.loadtxt(Fname, skiprows=3, max_rows=1)
timeIdx = int(data[0])
nRows = int(data[1])
while True:
    try:
        data=np.loadtxt(Fname, skiprows=3+(nRows+1)*blockIdx, max_rows=1)
        timeIdx = int(data[0])
        data=np.loadtxt(Fname,skiprows=4(nRows+1)*blockIdx,max_rows=nRows)
        timeSteps[timeIdx] = data.copy();
        blockIdx += 1;
    except:
        print("Finished loading data")
        break;

fig = plt.figure(figsize=(11,11))
ax = fig.gca()

#Plot the blocks we want
times = [10000, 20000, 40000, 60000, 80000, 100000, 120000, 150000]

for timestep in times:
    print("plotting step", timestep)
    data = timeSteps[timestep];
```

```

X = data[:,1]*0.1 #convert to nm
X = X-201.03
P = data[:,3]/data[:,4] # Compute the pressure
X = np.array(X)
P = np.array(P)
Xmin = -100
Xmax = 200 #Define the saturation values
Pmin = -5
Pmax = 25
plt.xlim(Xmin, Xmax)
plt.ylim(Pmin,Pmax)
plt.xlabel('X ($nm$)', fontsize=24)
plt.ylabel('P (GPa)', fontsize=24)
plt.xticks(fontsize = 24)
plt.yticks(fontsize = 24)
plt.plot(X, P, label = str(timestep/1000) + 'ps', linewidth=3)
plt.legend(loc=(0.75, 0.4), fontsize=24)
plt.grid()
plt.show()
fig.savefig("P_plot.png") #produce the final plot in png format

```

In the python script below, we provide all the necessary ingredients to post process data in order to obtain the pure spatial profile (x-y) of pressure (or any other local property) behavior by cutting following the  $z$ -direction.

```

import numpy as np
from matplotlib import pyplot as plt
from mpl_toolkits.axes_grid1 import make_axes_locatable

# loading weird data

blockIdx = 0
timeSteps={};
Fname="local_py.out"
data = np.loadtxt(Fname, skiprows=3, max_rows=1)
timeIdx = int(data[0])
nRows = int(data[1])
while True:
    try:
        data=np.loadtxt(Fname, skiprows=3+(nRows+1)*blockIdx , max_rows=1)

```

```

    timeIdx = int(data[0])
    data=np.loadtxt(Fname,skiprows=4(nRows+1)*blockIdx,max_rows=nRows)
    timeSteps[timeIdx] = data.copy();
    #timeIdx += 5000;
    blockIdx += 100;
except:
    print("Finished loading data")
    break;
#iterate over the entirety of loaded data
for timestep in timeSteps.keys():
    print("plotting step", timestep)
    #load the data of the time step
    data = timeSteps[ timestep ];
    dataX = np.array(data[:, 1]) * 0.1
    dataY = np.array(data[:, 2]) * 0.1
    dataZ = np.array(data[:, 3]) * 0.1
    x_unique = np.unique(dataX)
    y_unique = np.unique(dataY)
    z_unique = np.unique(dataZ)

    x_unique = x_unique-205

    # Extract pressure
    c = data[:,3] / data[:,4]
    #temp = data[:,2]

    # Create a grid and reshape the value array
    # into a grid, this is only necessary if one uses pcolormesh as plot
    X , Y = np.meshgrid(x_unique, y_unique)
    values = np.reshape(c, (x_unique.shape[0], y_unique.shape[0],
    z_unique.shape[0]) );
    # cut the 3D cake for a slice to plot
    # We take 3 cells around the center of the domain in z-direction
    PlotDataSlice = values[:, :, z_unique.shape[0]//2-3:z_unique.shape[0]//2
    +5 ];
    # average to reduce variability
    PlotDataSliceAvg = np.average(PlotDataSlice, axis=2)

```

```

minXval = 35
maxXval = 65

minIdx = np.where(x_unique < minXval)[0][-1]
maxIdx = np.where(x_unique > maxXval)[0][0]
#generate a figure
fig = plt.figure( figsize=(9,9) )
ax = fig.gca()

print(X[:,minIdx:maxIdx].shape, Y[:,minIdx:maxIdx].shape)
im = ax.pcolormesh(X[:,minIdx:maxIdx],Y[:,minIdx:maxIdx],
PlotDataSliceAvg[minIdx:maxIdx,:].transpose(), vmin = -1, vmax = 1,
shading = "gouraud")#, aspect='equal')#, norm=norm )
#ax.set_xlim([minXval,maxXval], size='x-large')
ax.set_xlabel("X (nm)", fontsize=24)
ax.set_ylabel("Y (nm)", fontsize=24)
plt.rcParams.update({'font.size':24})
plt.xticks(fontsize=24)
plt.yticks(fontsize=24)

ax.set_title("t = " + str(timestep*0.000001) + " ns")

xtick_loc = [-20, 0, 50]
ytick_loc = [-15, 0, 50]
# set the colorbar to the right of the plot, make it as high as
#the vertical axis by introducing a colorbar axis we call cax
divider=make_axes_locatable(ax)

colorbarAxis = divider.append_axes("right", size="5%", pad=0.05)
#fig.colorbar(im, cax=colorbarAxis, orientation='vertical',
#ticks=[0, 1500, 3000]).set_label("£T£ [K]")
fig.colorbar(im, cax=colorbarAxis, orientation='vertical').set_label
("$P$ (GPa)")
fig.tight_layout()
#plt.show()
fig.savefig("P_Timestep_shape"+ str(timestep*0.000001)+".png",dpi=150)
plt.close()

```

# Appendix E

## ABINIT script to compute the internal energy

An example of ABINIT script sample content showing the internal energy computation of  $B_2\text{-Cu}_{50}\text{Zr}_{50}$  crystal using the first principle approach in order to obtain the electronic heat capacity  $C_e(T_e)$ .

```
ndtset 40
occopt 3
tsmear: 0.0000032
tsmear+ 0.0079
acell 6.164286175 6.164286175 6.164286175
rprim      1.0000000000  0.0000000000  0.0000000000
           0.0000000000  1.0000000000  0.0000000000
           0.0000000000  0.0000000000  1.0000000000
ecutsm 0.05
nband 400
ntypat 2
znucl 29 40

natom 2
typat 1 2
xred
0.0 0.0 0.0
0.5 0.5 0.5

ecut 30.0
pawcutdg 60
pawovlp -1
ixc 1
```

```
ngkpt 8 8 8
nshiftk 1
shiftk 0.5 0.5 0.5
nstep 200
tolddf 1.0d-7
```

# Appendix F

## Input parameter file of ttm/mod

Bellow, a typical example of ttm\_parameters input file. In this script, the odd lines are considered as a comment and ignored. The even ones are those considered and used in the execution of the input script.

```
a_0
2.10739e-06
a_1
1.09849e-06
a_2
-2.69409e-08
a_3
3.41032e-10
a_4
-1.52801e-12
C_0
0.0
A
1.61448e-06
rho_e
1
D_e
10065.36
gamma_p
11.76
gamma_s
0
#v0
0
#I
```

```
1000
#left_surface
352
#right_surface
702
#skin_layer
9
#width
0.1
#Press_factor
0
#free_path
0
#ionic_dens
0.0596
#moving of surface
1
#minimum of T_e
300
```

# Appendix G

## Gaussian script to compute Gibbs free energy

Bellow, a typical example of ttm\_parameters input file. In this script, we provide a typical Gaussian input file capable of computing Gibbs free energy at a given configuration and determined pressure-temperature. The odd lines are considered as a comment and ignored. The even ones are those considered and used in the execution of the input script.

```
%mem=3880MW
%chk=CuZr_16ns_20atoms_freq_740
%nprocshared=128
#p bp86/3-21G scf=(maxcycle=500,QC) freq=noraman Temperature=740
Gaussian Test Job 01 pressure=-2467
0 1
40 3.05981440 3.53511600 5.11921300
40 3.64990230 6.59701790 5.53664300
40 6.84985350 6.72763790 5.27235310
40 5.98999020 3.78187400 4.86024300
29 8.03002930 5.23095790 3.55377000
40 9.25000000 4.14526800 5.59569310
29 3.00000000 4.48716800 7.75344320
29 5.22998050 4.64718800 7.46925300
40 7.80981440 5.61540810 7.84236280
40 5.25000000 7.63385790 7.86614320
40 9.78002930 7.14687790 6.23818300
29 10.19995120 6.58002800 9.20072310
40 3.53002930 6.06980790 9.91630310
40 5.95996090 3.28479000 9.78634300
40 8.93994140 3.84310900 10.23951290
```

40 6.27001960 6.48098800 10.71247280  
40 4.48999020 4.23700800 12.51553340  
29 8.94995120 7.10164800 11.10393330  
40 7.36987300 5.09112800 13.16636270  
40 4.80004880 6.95203800 13.79336250  
29 5.66992180 5.78236810 15.70696360

# Appendix H

## Fortran90 code to produce the initial ttm/md electron temperature

The purpose of this Fortran code is to generate the input file where to specify the  $T_e$  for each grid point. Each line has four numeric columns ( $i_x, i_y, i_z, T_e$ ). The number of lines is equal to the number of specified grid points ( $N_x \times N_y \times N_z$ ) where  $i_x, i_y, i_z$  are grid point indices ranging from 0 to  $N_x - 1, N_y - 1, N_z - 1$  in each dimension respectively. This example is for samples cut in the middle of the simulation box  $L_x/2$ .

```
program Te
implicit none

real, dimension(1)  :: T !Temperature array
real :: T_0 !Initial temperature in Kelvin
integer :: i !Increment following x
integer :: j !Increment following y
integer :: k !Increment following z
integer :: N_x !Grid point node index following x
integer :: N_y !Grid point node index following y
integer :: N_z !Grid point node index following z

print*,"Enter the value of Nx:"
read(*,*) N_x
print*,"Enter the value of Ny:"
read(*,*) N_y
print*,"Enter the value of Nz:"
read(*,*) N_z
print*,"Enter the value of T0:"
```

```

read(*,*) T_0

open(1,file='T_init')
  do i=0, N_x-1
  do j=0, N_y-1
  do k=0, N_z-1
  IF (i < N_x/2) THEN !Half space for free boundaries
    T(:) = 0 !Vacuum temperature
  ELSE
    T(:) = T_0 !Atoms initial temperatures
  END IF
write(*,*) 'Nx=', i, ', Ny=', j, ', Nz=', k, ', T0=', T, 'K'
write(1,*) i, j, k, T
  enddo
  enddo
  enddo
close(1)
  end program Te

```

# Appendix I

## LAMMPS input script to compute the XRD pattern

A typical LAMMPS script is provided to perform virtual XRD simulations on amorphous and crystalline CuZr alloy targets.

```
##### XRD #####

units          metal
dimension      3
boundary       p p p
echo           both
processors     1 * *

read_data      slice_0ns_all

pair_style     eam/fs
pair_coeff     * * Cu-Zr_4.eam.fs Cu Zr
timestep      0.001

variable      V string CuZr

thermo_style  custom step temp press
thermo       100

compute       XRD all xrd 1.541838 Cu Zr 2Theta 20 120 c 5 5 5 LP 1 echo

fix          1 all ave/histo/weight 1 100 100 20 120 1000 c_XRD[1] c_XRD[2] &
            mode vector file $V.hist.xrd
```

```
fix          2 all nve
run 1000
```

```
fix  2 all nve
run 1000
unfix 2
```

```
##### END script #####
```

A python script is present to post-process the previous data and fit them with a Gaussian function. Considering my data, the Gaussian profile is a reasonable approximation. Nevertheless, these functions must be appropriate for the results.

```
import matplotlib.pyplot as plt
import numpy as np
# import math
from scipy.optimize import curve_fit

filename = "CuZr.hist.xrd"
data = np.loadtxt(filename, skiprows=4)
#Read data angles or 2Theta vs Intensity
angles = data[:, 1]
I = data[:, 2]

#Define a Gaussian fitting function
def gauss(x, C, x0, sigma, A):
    return C*np.exp(-(x-x0)**2/(2*sigma**2)) + A
mini = I.min()
maxi =I.max()
amp = maxi-mini
ttheta = angles[I.argmax()]

popt, pcov = curve_fit(gauss, angles, I, p0=[amp,ttheta,1, mini])
#Plot the results
plt.plot(angles, I, label='data')
angles_fin = [i/1000 for i in range(int(angles.min()*1000,
int(angles.max()*1000))]

plt.plot(angles_fin, gauss(angles_fin, *popt), label='fit')
```

# Appendix J

## Entropy calculation using LAMMPS

A simple script to compute the entropy within slices of the transformed zone within the CuZr alloy composite as a function of space ( $x$ -direction) is calculated using the MD formalism achieved during 5 ps in the NVE ensemble. The output data `c_entropy[*]` is printed to a file named `entropy_5ns.out`.

```
##### ENTROPY #####
units          metal
dimension      3
boundary       p p p
echo           both
processors     1 * *
atom_style     atomic

read_data      slice_0ns_all

variable       Nevery equal 100
variable       Nrepeat equal 10
variable       Nfreq equal 5000
variable       deltax equal 3

neighbor 0.3 bin
neigh_modify  every 20 delay 0 check no

pair_style     eam/fs
pair_coeff     * * Cu-Zr_4.eam.fs Cu Zr
timestep      0.001

thermo_style   custom step temp press
thermo        1000
```

```
compute          entropy all entropy/atom 0.25 2.5 avg yes 2.5
```

```
thermo_style    custom step temp press pe
```

```
thermo 1000
```

```
compute          chunkX all chunk/atom bin/1d x lower ${deltax} units box
```

```
fix density_X all ave/chunk ${Nevery} ${Nrepeat} ${Nfreq} chunkX
```

```
              c_entropy[*] file entropy_5ns.out
```

```
fix          2 all nve
```

```
run 5000
```

```
unfix 2
```

```
##### END script #####
```

# Appendix K

## LAMMPS script for calculating the total RDF

The script provided herein is a LAMMPS MD input used to compute the total RDF in a specific portion of the target. A python script is also presented to post-process the result and plot the curve.

```
##### RDF #####
units          metal
dimension      3
boundary       p p p
echo           both
processors      1 * *

atom_style     atomic
neighbor       0.3 bin
neigh_modify   every 20 delay 0 check no

read_data      slice_0ns.lmp

pair_style     eam/fs
pair_coeff      * * Cu-Zr_4.eam.fs Cu Zr
timestep       0.001

thermo_style   custom step temp press
thermo         100
compute        RDF all rdf 100
fix rdf all ave/time 1 1 1000 c_RDF[*] file rdf_all.dat mode vector

run            1000
```

```
##### END script#####
```

```
import numpy as np
from matplotlib import pyplot as plt
import matplotlib.pyplot as plt
from mpl_toolkits.axes_grid1 import make_axes_locatable
from scipy.interpolate import make_interp_spline

blockIdx = 0
timeSteps={};
Fname="rdf_merge.dat"
data = np.loadtxt(Fname, skiprows=3, max_rows=1)
timeIdx = int(data[0])
nRows = int(data[1])
while True:
    try:
        data=np.loadtxt(Fname,skiprows=3+(nRows+1)*blockIdx, max_rows=1)
        timeIdx = int(data[0])
        data=np.loadtxt(Fname,skiprows=4+(nRows+1)*blockIdx,max_rows=nRows)
        timeSteps[timeIdx] = data.copy();
        blockIdx += 1;
    except:
        print("Finished loading data")
        break;

fig = plt.figure(figsize=(11,11))
ax = fig.gca()

times = [ 0, 5000000, 9000000, 10000000, 12000000, 14000000, 17000000]
for timestep in times:
    print("plotting step", timestep)
    data = timeSteps[timestep];
    r = data[:,1]
    gr = data[:,2]
    r = np.array(r)
    gr = np.array(gr)
    rmin = 1.5
    rmax = 6.4
    grmin = 0.0
```

```
grmax = 5.0
rnew = np.linspace(r.min(), r.max(), 300)
gfg = make_interp_spline(r, gr, k=2)
gr_new = gfg(rnew)
plt.xlim(rmin, rmax)
plt.ylim(grmin, grmax)
plt.xlabel('r ( $\AA$ )', fontsize=32)
plt.ylabel('g(r)', fontsize=32)
plt.xticks(fontsize = 36)
plt.yticks(fontsize = 36)
plt.plot(rnew, gr_new ,label = str(timestep/1000000), linewidth=4)
plt.legend(loc=(0.01, 0.50), fontsize=25)

plt.show()
fig.savefig("final_RDF.png")
```

# Appendix L

## LAMMPS script for computing equilibrium phononic thermal conductivity

The script below is a typical LAMMPS MD input file in order to calculate the atomic thermal conductivity of the composite produced sample at temperature  $T = 300$  K.

```
##### Kappa #####

processors      1 * *
variable        T equal 300
variable        V equal vol
variable        dt equal 0.001

variable        kB equal 1.3806504e-23
variable        eV2J equal 1.602e-19
variable        A2m equal 1.0e-10
variable        ps2s equal 1.0e-12
variable        convert equal ${eV2J}*${eV2J}/${ps2s}/${A2m}

variable        p equal 10      # correlation length
variable        s equal 400     # sample interval
variable        d equal $p*$s   # dump interval

units           metal
boundary        p p p
atom_style      atomic
```

```

read_data amorphous_slice.lmp #first atomic configuration

pair_style      eam/fs
pair_coeff      * * Cu-Zr_4.eam.fs Cu Zr
neighbor        2.0 bin
neigh_modify    delay 10
timestep        ${dt}

thermo_style    custom step temp etotal press vol lx
thermo 1000

velocity        all create $T 49284 mom yes rot yes dist gaussian
fix             1 all nve
run             20000

compute         myKE all ke/atom
compute         myPE all pe/atom
compute         myStress all stress/atom NULL virial

compute         flux all heat/flux myKE myPE myStress
variable        Jx equal c_flux[1]/vol
variable        Jy equal c_flux[2]/vol
variable        Jz equal c_flux[4]/vol

fix             JJ all ave/correlate $s $p $d &
                c_flux[1] c_flux[3] c_flux[4] type auto &
                file JOJT.dat ave running
variable        scale equal ${convert}/${kB}/$T/$T/$V*$s*${dt}
variable        k11 equal trap(f_JJ[3])*${scale}
variable        k22 equal trap(f_JJ[4])*${scale}
variable        k33 equal trap(f_JJ[5])*${scale}

thermo          $d
thermo_style    custom step temp v_Jx v_Jy v_Jz v_k11 v_k22 v_k33

run            400000
unfix          1

```

```
variable      kappa equal (v_k11+v_k22+v_k33)/3.0
print         "average conductivity: ${kappa}[W/mK]"
```

```
##### END  script#####
```

# Appendix M

## Electronic properties of CuZr systems

This section aims to provide TTM-MD simulation with input parameters mentioned in table 3.5. Before, it was relevant to mention that the electronic properties of systems can be accessed in two ways. The first option is either to compute them via the ab initio method using DFT or directly collect and use the experimental data. Both approaches have a good and bad aspects, DFT is accurate but we need a hundred or even thousands of atoms to have representative reliable amorphous states properties for instance. Thus, the computation cost is incredibly expensive. The second way is by utilizing available experimental data. They are available but less accurate, especially at high  $T_e$ .

### Electronic specific heat

In the case of the crystal structures, we have computed the  $C_e(T_e)$  using ABINIT package [410, 411] and compared it to the experimental data mentioned in table 3.5. However, in the case of amorphous structures, we have abstained using only the experimental parameters. The main reason is the simulation time big expense. Below are the  $C_e(T_e)$  different parameters computed for the B<sub>2</sub>-Cu<sub>50</sub>Zr<sub>50</sub>, C11<sub>b</sub>-Cu<sub>33.3</sub>Zr<sub>66.7</sub>,  $\alpha$ -Cu<sub>50</sub>Zr<sub>50</sub>, and  $\alpha$ -Cu<sub>33.3</sub>Zr<sub>66.7</sub>.

To get this parameter regardless the material (crystals or amorphous), we can compare the Equations M.1, 2.44, and as proposed by [254], resulting on  $C_0 = 0$ ,  $a_0 = 0$ ,  $a_2 = 0$ ,  $a_4 = 0$  and  $A = 0$ . Thus, we end up with the following coefficients:

$$C_e(T_e) = \gamma T_e \tag{M.1}$$

$$C_e(T_e) = a_1 X = 10^{-3} a_1 T_e \tag{M.2}$$

Finally, using values from table 3.5 we deduce  $\gamma$  (and implicitly the coefficient  $a_1$ ):

$$\begin{cases} \gamma(B_2\text{-Cu}_{50}\text{Zr}_{50}) = 1.53 \cdot 10^{-9} \text{ eV } \text{Å}^{-3} \text{ K}^{-2} \\ \gamma(C11_b\text{-Cu}_{33.3}\text{Zr}_{66.7}) = 1.17 \cdot 10^{-9} \text{ eV } \text{Å}^{-3} \text{ K}^{-2} \\ \gamma(\alpha\text{-Cu}_{50}\text{Zr}_{50}) = 2.01 \cdot 10^{-9} \text{ eV } \text{Å}^{-3} \text{ K}^{-2} \\ \gamma(\alpha\text{-Cu}_{33.3}\text{Zr}_{66.7}) = 2.40 \cdot 10^{-9} \text{ eV } \text{Å}^{-3} \text{ K}^{-2} \end{cases}$$

For the ordered structures, a first principle computation was performed to determine the electronic specific heat and compare it to the experimental values. The electronic specific heat is computed through first-principle calculations, within density functional theory (DFT) implemented in ABINIT package [412]. General gradient approximation (GGA) functional was used for the exchange-correlation energy combined with Projector Augmented Wave (PAW) method [413]. The lattice parameters of CuZr alloys were calculated using an  $8 \times 8 \times 8$  Monkhorst–Pack grid for the Brillouin zone sampling and a 409 eV energy cut-off. The internal energy  $U$  is computed using the Fermi-Dirac smearing. The electronic specific heat of  $B_2\text{-Cu}_{50}\text{Zr}_{50}$  and  $C11_b\text{-Cu}_{33.3}\text{Zr}_{66.7}$  systems is obtained by Equation M.3 sweeping the electronic temperatures from 0 to 8 eV.

$$C_e(T_e) = \frac{\partial U}{\partial T_e} \quad (\text{M.3})$$

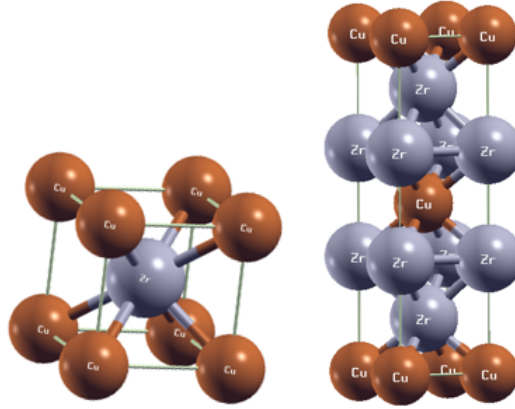


Figure M.1: Crystalline initial structures from the CIF file used in first principle computation visualized by XCrySDen [414]. Left:  $B_2\text{-Cu}_{50}\text{Zr}_{50}$ , and  $C11_b\text{-Cu}_{33.3}\text{Zr}_{66.7}$ . The gray, brown atoms correspond to Zr and Cu respectively.

The results of the electronic specific heat for the crystalline structure are shown in Figure M.2.

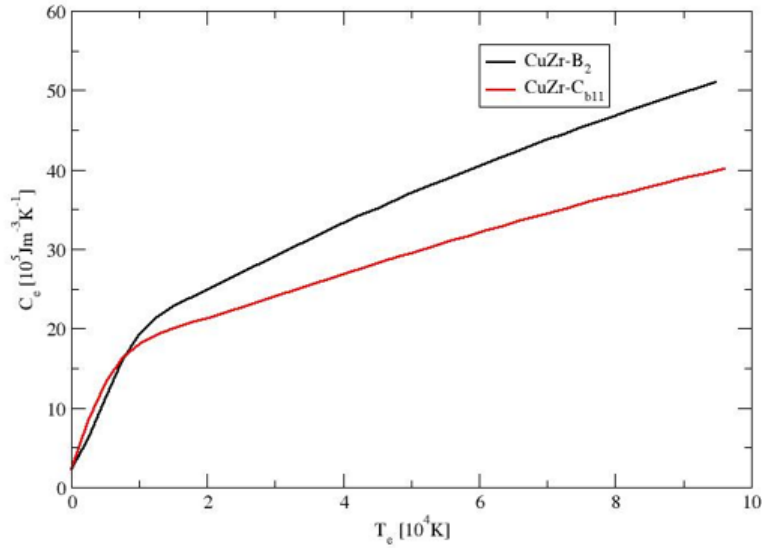


Figure M.2: DFT calculation of the electronic specific heat as a function of electronic temperature for the two crystalline phases of CuZr alloy.

The fitting procedure of the curves shown in Figure M.2 has been made according to Equation 2.44. The different parameters are summarized in the table M.1.

Table M.1: TTM-MD electronic specific heat fitting coefficients values obtained using DFT for crystalline CuZr binary systems.

Coefficients	B <sub>2</sub> -Cu <sub>50</sub> Zr <sub>50</sub>	C <sub>11b</sub> -Cu <sub>33.3</sub> Zr <sub>66.7</sub>
C <sub>0</sub>	0.00	0.00
a <sub>0</sub>	2.11e-06	3.31e-06
a <sub>1</sub>	1.10e-06	8.83e-07
a <sub>2</sub>	-2.69e-08	-2.40e-08
a <sub>3</sub>	3.41e-10	3.15e-10
a <sub>4</sub>	-1.53e-12	-1.44e-12
A	1.61e-06	5.00e-07

## Electronic thermal diffusion

The value of  $D_e(T_e)$  is computed at finite temperature (300 K) using the Equation 2.7 and the values mentioned in table 3.5.

$$\begin{cases} \kappa_e(\text{B}_2\text{-Cu}_{50}\text{Zr}_{50}) = 7.41 \text{ W m}^{-1} \text{ K}^{-1} \\ \kappa_e(\text{C11}_b\text{-Cu}_{33.3}\text{Zr}_{66.7}) = 20.58 \text{ W m}^{-1} \text{ K}^{-1} \\ \kappa_e(\alpha\text{-Cu}_{50}\text{Zr}_{50}) = 3.85 \text{ W m}^{-1} \text{ K}^{-1} \\ \kappa_e(\alpha\text{-Cu}_{33.3}\text{Zr}_{66.7}) = 3.68 \text{ W m}^{-1} \text{ K}^{-1} \end{cases}$$

$$\begin{cases} \kappa_e(\text{B}_2\text{-Cu}_{50}\text{Zr}_{50}) = 4.62 \cdot 10^{-3} \text{ eV ps } \text{\AA}^{-1} \text{ K}^{-1} \\ \kappa_e(\text{C11}_b\text{-Cu}_{33.3}\text{Zr}_{66.7}) = 12.8 \cdot 10^{-3} \text{ eV ps } \text{\AA}^{-1} \text{ K}^{-1} \\ \kappa_e(\alpha\text{-Cu}_{50}\text{Zr}_{50}) = 2.40 \cdot 10^{-3} \text{ eV ps } \text{\AA}^{-1} \text{ K}^{-1} \\ \kappa_e(\alpha\text{-Cu}_{33.3}\text{Zr}_{66.7}) = 2.30 \cdot 10^{-3} \text{ eV ps } \text{\AA}^{-1} \text{ K}^{-1} \end{cases}$$

$$\begin{cases} D_e(300\text{K}) = \frac{\kappa_e(300\text{K})}{C_e(300\text{K})} \\ D_e(300\text{K}) = \frac{\kappa_e(300\text{K})}{\gamma \times 300} \end{cases}$$

$$\begin{cases} D_e(\text{B}_2\text{-Cu}_{50}\text{Zr}_{50}) = 10005.36 \text{ \AA}^2 \text{ ps}^{-1} \\ D_e(\text{C11}_b\text{-Cu}_{33.3}\text{Zr}_{66.7}) = 36467.24 \text{ \AA}^2 \text{ ps}^{-1} \\ D_e(\alpha\text{-Cu}_{50}\text{Zr}_{50}) = 3980.10 \text{ \AA}^2 \text{ ps}^{-1} \\ D_e(\alpha\text{-Cu}_{33.3}\text{Zr}_{66.7}) = 3194.44 \text{ \AA}^2 \text{ ps}^{-1} \end{cases}$$

## Density of ions

Ion density represents the number of ions per unit volume. The density of the materials that we are dealing with was obtained using LAMMPS at 300 K (the molar mass used are  $77.39 \text{ g mol}^{-1}$ ,  $82.01 \text{ g mol}^{-1}$  for X-Cu<sub>50</sub>Zr<sub>50</sub> and X-Cu<sub>33.3</sub>Zr<sub>66.7</sub> compositions respectively) as summarized in table 3.5.

$$\begin{cases} n(\text{B}_2\text{-Cu}_{50}\text{Zr}_{50}) = \frac{7.66 \times 10^{+6} \times 6.02 \times 10^{+23}}{77.39} \\ n(\text{C11}_b\text{-Cu}_{33.3}\text{Zr}_{66.7}) = \frac{6.89 \times 10^{+6} \times 6.02 \times 10^{+23}}{82.01} \\ n(\alpha\text{-Cu}_{50}\text{Zr}_{50}) = \frac{7.18 \times 10^{+6} \times 6.02 \times 10^{+23}}{77.39} \\ n(\alpha\text{-Cu}_{33.3}\text{Zr}_{66.7}) = \frac{6.86 \times 10^{+6} \times 6.02 \times 10^{+23}}{82.01} \end{cases}$$

$$\begin{cases} n(\text{B}_2\text{-Cu}_{50}\text{Zr}_{50}) \approx 0.0596 \text{ atoms } \text{\AA}^{-3} \\ n(\text{C11}_b\text{-Cu}_{33.3}\text{Zr}_{66.7}) \approx 0.0517 \text{ atoms } \text{\AA}^{-3} \\ n(\alpha\text{-Cu}_{50}\text{Zr}_{50}) \approx 0.0559 \text{ atoms } \text{\AA}^{-3} \\ n(\alpha\text{-Cu}_{33.3}\text{Zr}_{66.7}) \approx 0.0505 \text{ atoms } \text{\AA}^{-3} \end{cases}$$

## Electron-phonon coupling factor

The electron-phonon coefficients mentioned in table 3.5 have to be converted to a  $\gamma_p$  as defined in Equation 2.37 such that the code can understand it. For each material with a given stoichiometry  $\text{Cu}_x\text{Zr}_{1-x}$ , the  $g_p(T_e)$  in both crystalline and amorphous states were computed at 300 K by a linear response approximation relation [208].

$$g_p(T_e) = xg_p^{\text{Cu}}(T_e) + (1 - x)g_p^{\text{Zr}}(T_e) \quad (\text{M.4})$$

$$\begin{cases} g_p(\text{B}_2\text{-Cu}_{50}\text{Zr}_{50}) \approx 3.75 \cdot 10^{17} \text{ W m}^{-3}\text{K}^{-1} \\ g_p(\text{C11}_b\text{-Cu}_{33.3}\text{Zr}_{66.7}) \approx 5.30 \cdot 10^{17} \text{ W m}^{-3}\text{K}^{-1} \\ g_p(\alpha\text{-Cu}_{50}\text{Zr}_{50}) \approx 3.50 \cdot 10^{17} \text{ W m}^{-3}\text{K}^{-1} \\ g_p(\alpha\text{-Cu}_{33.3}\text{Zr}_{66.7}) \approx 2.80 \cdot 10^{17} \text{ W m}^{-3}\text{K}^{-1} \end{cases}$$

$$\begin{cases} \gamma_p(\text{B}_2\text{-Cu}_{50}\text{Zr}_{50}) \approx \frac{3.75 \times 10^{+17} \frac{\text{W}}{\text{m}^3\text{K}} \times 77.39 \frac{\text{g}}{6.02 \times 10^{+23}}}{3 \times 0.596 \times 10^{+29} \frac{\text{atoms}}{\text{m}^3} 1.38 \times 10^{-23}} \times 0.602 \\ \gamma_p(\text{C11}_b\text{-Cu}_{33.3}\text{Zr}_{66.7}) \approx \frac{5.3 \times 10^{+17} \frac{\text{W}}{\text{m}^3\text{K}} \times 82.01 \frac{\text{g}}{6.02 \times 10^{+23}}}{3 \times 0.517 \times 10^{+29} \frac{\text{atoms}}{\text{m}^3} 1.38 \times 10^{-23}} \times 0.602 \\ \gamma_p(\alpha\text{-Cu}_{50}\text{Zr}_{50}) \approx \frac{3.5 \times 10^{+17} \frac{\text{W}}{\text{m}^3\text{K}} \times 77.39 \frac{\text{g}}{6.02 \times 10^{+23}}}{3 \times 0.559 \times 10^{+29} \frac{\text{atoms}}{\text{m}^3} 1.38 \times 10^{-23}} \times 0.602 \\ \gamma_p(\alpha\text{-Cu}_{33.3}\text{Zr}_{66.7}) \approx \frac{2.8 \times 10^{+17} \frac{\text{W}}{\text{m}^3\text{K}} \times 82.01 \frac{\text{g}}{6.02 \times 10^{+23}}}{3 \times 0.505 \times 10^{+29} \frac{\text{atoms}}{\text{m}^3} 1.38 \times 10^{-23}} \times 0.602 \end{cases}$$

$$\begin{cases} \gamma_p(\text{B}_2\text{-Cu}_{50}\text{Zr}_{50}) \approx 11.76 \text{ g mol}^{-1}\text{ps}^{-1} \\ \gamma_p(\text{C11}_b\text{-Cu}_{33.3}\text{Zr}_{66.7}) \approx 17.62 \text{ g mol}^{-1}\text{ps}^{-1} \\ \gamma_p(\alpha\text{-Cu}_{50}\text{Zr}_{50}) \approx 11.70 \text{ g mol}^{-1}\text{ps}^{-1} \\ \gamma_p(\alpha\text{-Cu}_{33.3}\text{Zr}_{66.7}) \approx 10.98 \text{ g mol}^{-1}\text{ps}^{-1} \end{cases}$$

## Skin penetration depth

Theoretically, the skin penetration depth is computed using the formula described in [208] as:

$$l_p = xl_p^{\text{Cu}} + (1 - x)l_p^{\text{Zr}} \quad (\text{M.5})$$

Where  $l_p^{\text{Cu}} = 12.2 \text{ nm}$ ,  $l_p^{\text{Zr}} = 16.4 \text{ nm}$ , are the penetration depth of Cu, Zr, and  $x$  is the percentage of Cu atoms present in each composition. The results for each material are listed in table 3.5.

We have to mention that the previous value cannot be injected directly into the script. For clarity, an extra computation should be performed to achieve a successful simulation. Since distances inside the code are defined in electronic mesh units, let's define a new value  $\Theta$  defined as  $\Theta = \frac{L_X}{N_X}$  where  $L_X$ ,  $N_X$  are respectively the box length and electronic meshing following  $x$ . Once  $\Theta$  is obtained in Å, we proceed to the computation of a new variable mentioned in the script `ttm_parameters` as `skin_layer =  $\frac{l_p}{\Theta}$` . This latter value has to be an integer otherwise LAMMPS simulation will crash. Thus, the formula we should keep in mind is:

$$l_p = \text{skin\_layer} \times \Theta \tag{M.6}$$

# Appendix N

## Calculation of NRBC dumping factors

As shown in Figure 3.14 the ultrafast laser temperature gradient leads to the generation of a pressure wave propagating from the surface to the bulk of the target. Thus, once these waves travel through the bulk and reach the back of the material it is reflected inducing a shearing with the rarefaction wave. In order to avoid a such nonphysical effect, we selected a part of the bottom region with a suitable viscosity to amortize the shock and prevent reflection. The computation approach consists of selecting a region at the rear of the material having a fixed length of 100 nm and after each simulation, we tune the stiffness (dumping factor) of the atomic layers till eliminating all the reflection. We have to keep in mind that the pressure wave traveling velocity at a laser fluence  $F_{\text{abs}} = 160 \text{ mJ/cm}^2$  is roughly  $\sim 58 \text{ \AA/ps}$  for  $\text{B}_2\text{-Cu}_{50}\text{Zr}_{50}$ , and  $\sim 45 \text{ \AA/ps}$  for both  $\alpha\text{-Cu}_{50}\text{Zr}_{50}$  and  $\alpha\text{-Cu}_{33.3}\text{Zr}_{66.7}$  [208]. A series of tests for each material were done to find the optimal damping factor  $\gamma_{\text{damp}}$  of the NRBC region. The difficulty is getting a quality absorbing boundary (stable and accurate) on the one hand, and on the other hand guaranteeing the stability of the discretized partial differential equations. To achieve this aim, for each material ( $\text{B}_2\text{-Cu}_{50}\text{Zr}_{50}$ ,  $\text{C11}_b\text{-Cu}_{33.3}\text{Zr}_{66.7}$ ,  $\alpha\text{-Cu}_{50}\text{Zr}_{50}$ , and  $\alpha\text{-Cu}_{33.3}\text{Zr}_{66.7}$ ) four distinct simulation simulations with  $\gamma_{\text{damp}} = 2.5 \cdot 10^{-4}$ ,  $2.5 \cdot 10^{-3}$ ,  $2.5 \cdot 10^{-2}$ , and  $2.5 \cdot 10^{-1} \text{ eV ps \AA}^{-2}$  were employed.

The initial generated structures have box dimensions ( $x$ ,  $y$ , and  $z$ ) of  $400.40 \times 16.15 \times 16.15$ ,  $400.62 \times 16.10 \times 16.77$ ,  $415.07 \times 14.61 \times 14.61$ ,  $403.33 \times 14.26 \times 12.34 \text{ nm}^3$  for  $\text{B}_2\text{-Cu}_{50}\text{Zr}_{50}$ ,  $\text{C11}_b\text{-Cu}_{33.3}\text{Zr}_{66.7}$ ,  $\alpha\text{-Cu}_{50}\text{Zr}_{50}$ , and  $\alpha\text{-Cu}_{33.3}\text{Zr}_{66.7}$  respectively. A periodic boundary was imposed following the  $y$  and  $z$  directions. As a result of laser heat propagation along the  $x$  direction, a free boundary was created by truncating the system in the middle, which means that the surface lies at  $L_x/2$  separating the vacuum and bulk regions.

The initial structure is minimized and heated for 15 ns to the room temperature (300 K) using NPT ensemble under 1 bar Nose-Hoover temperature and pressure controls. This procedure was followed by a TTM-MD stage of 30 ps. Furthermore, the systems are let to evaluate spontaneously during 120 ps in the NVE ensemble. In the computation domain, a region of 100 nm (from the rear of the simulation box) was selected and attributed a specific viscosity to mimic a bulk. Thus, since the deposition of the energy on the surface, the wave has to travel in all cases roughly 200 nm which means that at most (extreme case where the wave is the faster)  $t = 2000/58 \approx 34$  ps, so if there is any reflection in the simulation range 0-150 ps, we are able for sure to capture it. The obtained results are shown in figures [N.1](#), [N.2](#), [N.3](#), and [N.4](#).

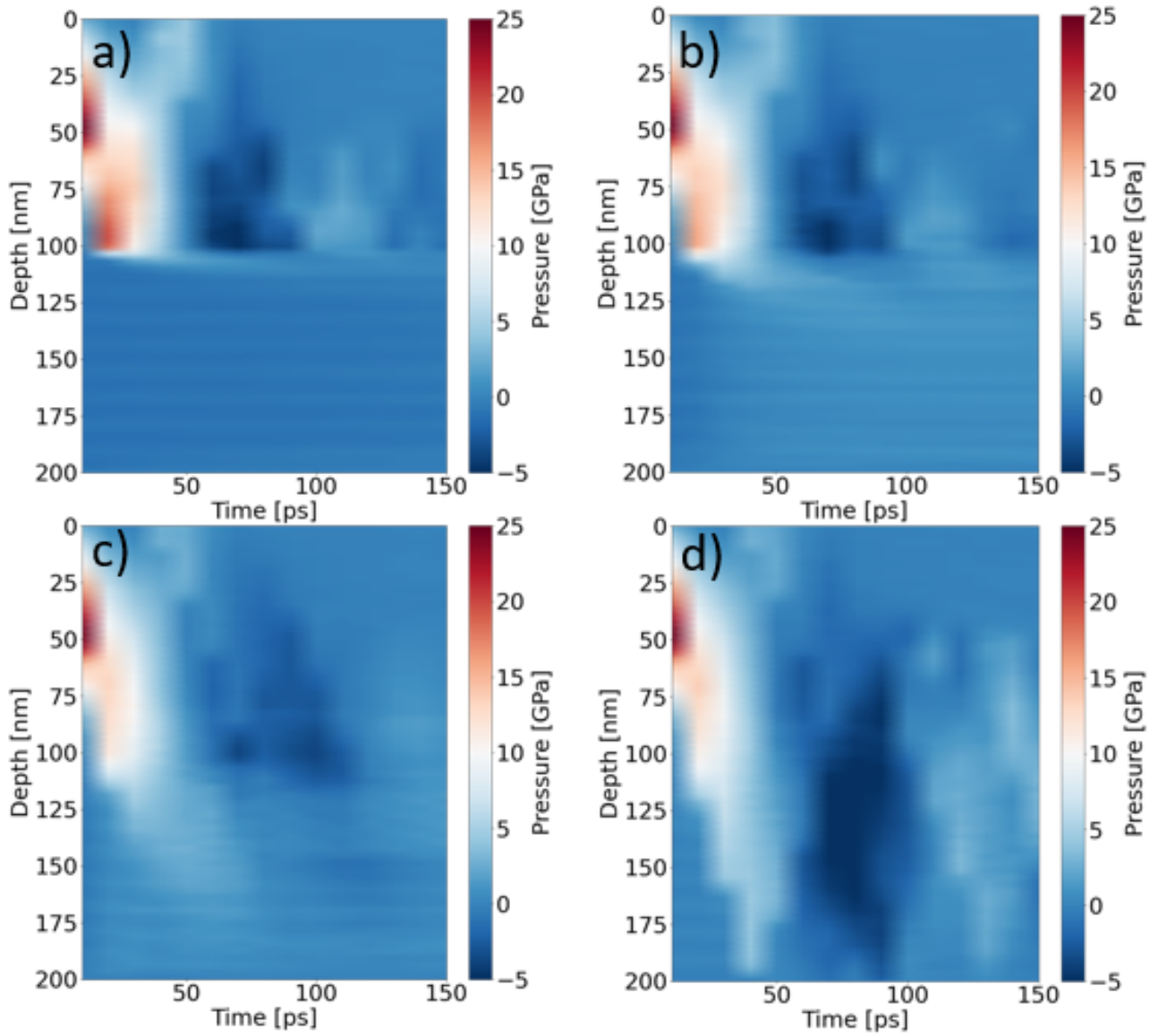


Figure N.1: Spatial-temporal pressure color maps profile in amorphous  $B_2-Cu_{50}Zr_{50}$  sample at instants  $t=0-150$  ps for several  $\gamma_{damp}$ . In a)  $\gamma_{damp} = 2.5 \cdot 10^{-1}$  eV ps  $\text{\AA}^{-2}$ , b)  $\gamma_{damp} = 2.5 \cdot 10^{-2}$  eV ps  $\text{\AA}^{-2}$ , c)  $\gamma_{damp} = 2.5 \cdot 10^{-3}$  eV ps  $\text{\AA}^{-2}$ , and d)  $\gamma_{damp} = 2.5 \cdot 10^{-4}$  eV ps  $\text{\AA}^{-2}$ . An ultrafast laser pulse of  $\tau = 100$  fs pulse duration and  $F_{abs} = 160$  mJ/cm<sup>2</sup> absorbed fluence is used in these simulations.

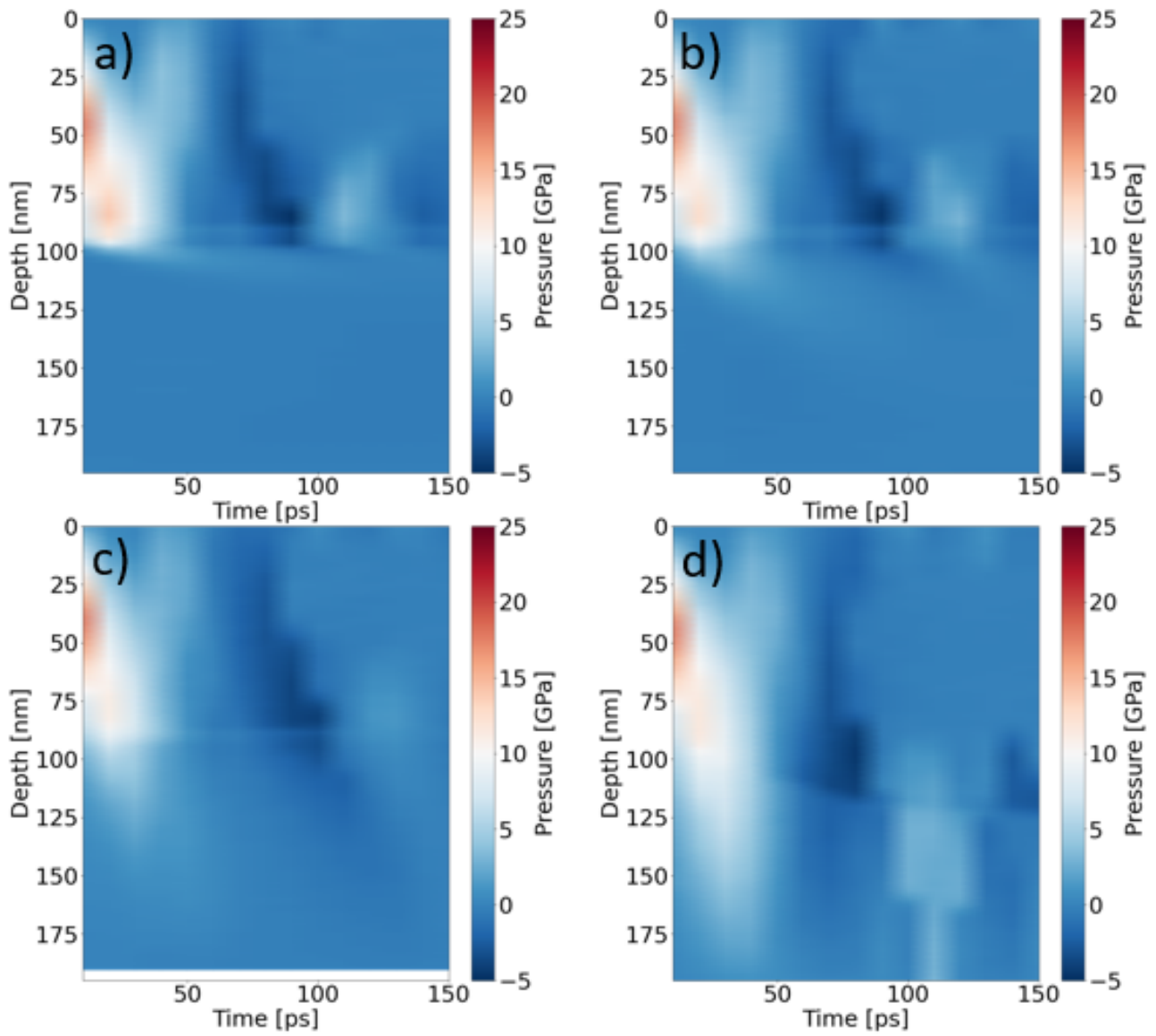


Figure N.2: Spatial-temporal pressure color maps profile in amorphous  $C_{11b}-Cu_{50}Zr_{50}$  sample at instants  $t=0-150$  ps for several  $\gamma_{damp}$ . In a)  $\gamma_{damp} = 2.5 \cdot 10^{-1}$  eV ps  $\text{\AA}^{-2}$ , b)  $\gamma_{damp} = 2.5 \cdot 10^{-2}$  eV ps  $\text{\AA}^{-2}$ , c)  $\gamma_{damp} = 2.5 \cdot 10^{-3}$  eV ps  $\text{\AA}^{-2}$ , and d)  $\gamma_{damp} = 2.5 \cdot 10^{-4}$  eV ps  $\text{\AA}^{-2}$ . An ultrafast laser pulse of  $\tau = 100$  fs pulse duration and  $F_{abs} = 160$  mJ/cm<sup>2</sup> absorbed fluence is used in these simulations.

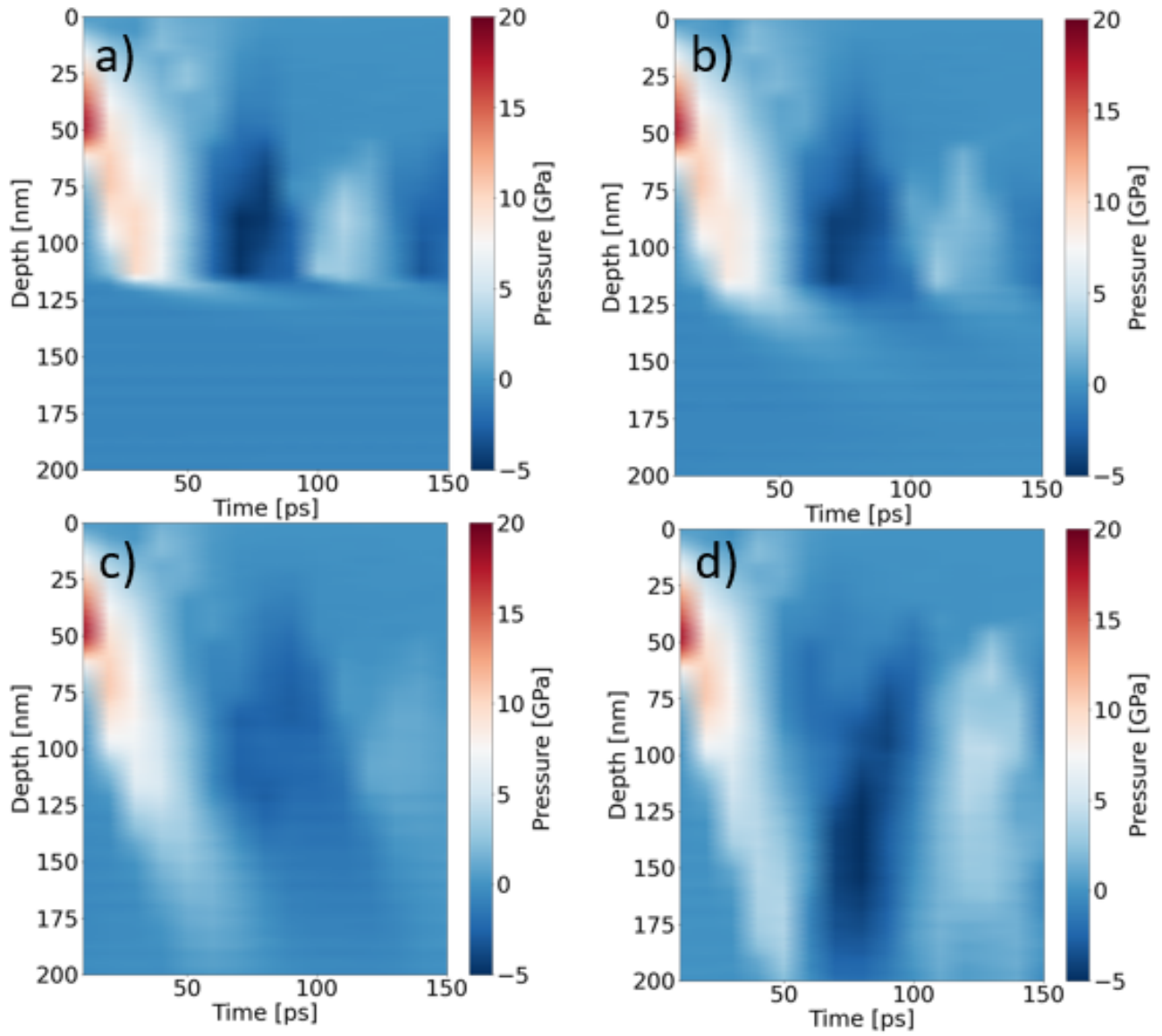


Figure N.3: Spatial-temporal pressure color maps profile in amorphous  $\alpha$ -Cu<sub>50</sub>Zr<sub>50</sub> sample at instants  $t=0$ -150 ps for several  $\gamma_{damp}$ . In a)  $\gamma_{damp} = 2.5 \cdot 10^{-1} \text{ eV ps } \text{\AA}^{-2}$ , b)  $\gamma_{damp} = 2.5 \cdot 10^{-2} \text{ eV ps } \text{\AA}^{-2}$ , c)  $\gamma_{damp} = 2.5 \cdot 10^{-3} \text{ eV ps } \text{\AA}^{-2}$ , and d)  $\gamma_{damp} = 2.5 \cdot 10^{-4} \text{ eV ps } \text{\AA}^{-2}$ . An ultrafast laser pulse of  $\tau = 100 \text{ fs}$  pulse duration and  $F_{abs} = 160 \text{ mJ/cm}^2$  absorbed fluence is used in these simulations.

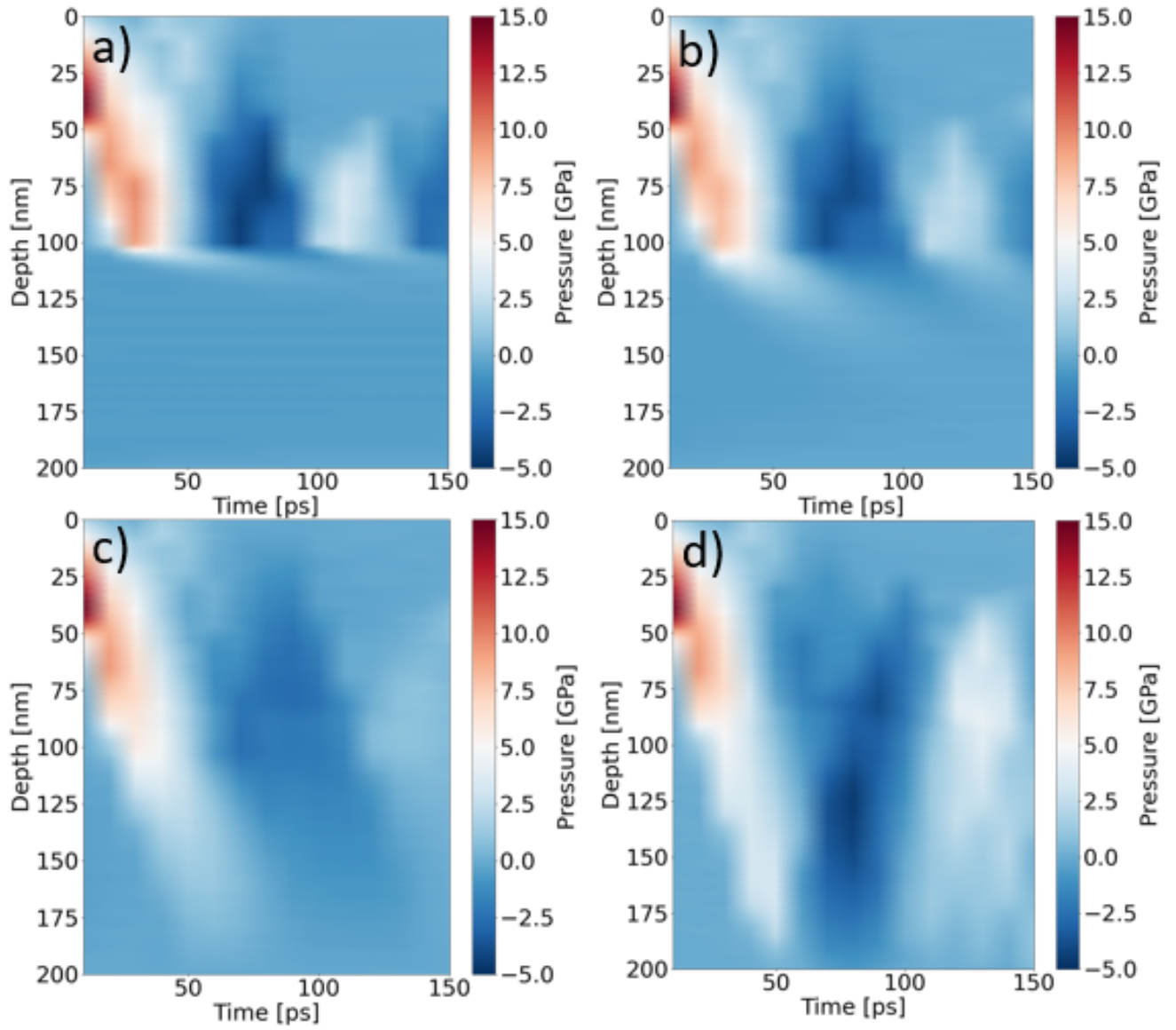


Figure N.4: Spatial-temporal pressure color maps profile in amorphous  $\alpha$ -Cu<sub>33.3</sub>Zr<sub>66.7</sub> sample at instants  $t = 0$ -150 ps for several  $\gamma_{damp}$ . In a)  $\gamma_{damp} = 2.5 \cdot 10^{-1} \text{ eV ps } \text{\AA}^{-2}$ , b)  $\gamma_{damp} = 2.5 \cdot 10^{-2} \text{ eV ps } \text{\AA}^{-2}$ , c)  $\gamma_{damp} = 2.5 \cdot 10^{-3} \text{ eV ps } \text{\AA}^{-2}$ , and d)  $\gamma_{damp} = 2.5 \cdot 10^{-4} \text{ eV ps } \text{\AA}^{-2}$ . An ultrafast laser pulse of  $\tau = 100 \text{ fs}$  pulse duration and  $F_{abs} = 160 \text{ mJ/cm}^2$  absorbed fluence is used in these simulations.

The pressure is computed according to the following formula:

$$P = \frac{1}{3V}(\sigma_{xx} + \sigma_{yy} + \sigma_{zz}) \quad (\text{N.1})$$

Where  $\sigma_{xx}$ ,  $\sigma_{yy}$ ,  $\sigma_{zz}$  are atomic constraints following  $x$ ,  $y$  and  $z$  respectively.  $V$  is the Voronoi volume obtained through the Voro++ package implemented in LAMMPS [415].

For the purpose of this study, Equation (N.1) is employed to discuss the spatial evolution of  $P$ -wave profiles in  $B_2\text{-Cu}_{50}\text{Zr}_{50}$  target material. Depending on the value of  $\gamma_{damp}$  the evolution shows distinct behaviors. In Figure N.1(a), we can clearly see that the value of  $2.5 \cdot 10^{-1} \text{ eV ps } \text{\AA}^{-2}$  is too large and not appropriate. The  $P$ -wave has a maximum value of  $\sim 25 \text{ GPa}$  and does not even penetrate into the NRBC region. Furthermore, a reflection was observed at  $t = 50 \text{ ps}$  mainly due to the abrupt change in viscosity at the Solid-NRBC interface domains.

Figure N.1(b) shows the evolution with a designed region of  $2.5 \cdot 10^{-2} \text{ eV ps } \text{\AA}^{-2}$  where the  $P$ -wave penetrates deeper inside the NRBC zone. It is accompanied by reflection. This result is quite similar to the one obtained in Figure N.1(a). From Figure N.1(c), the value of  $\gamma_{damp} = 2.5 \cdot 10^{-3} \text{ eV ps } \text{\AA}^{-2}$  is selected and seems to be appropriate as a choice. The reason is that the  $P$ -wave is thoroughly and gradually extinguished in the NRBC region without any detection of reflection indicating that the pressure-absorbing boundary condition is working properly.

In contrary, Figure N.1(d) corroborated that for  $\gamma_{damp} = 2.5 \cdot 10^{-4} \text{ eV ps } \text{\AA}^{-2}$ , a critical fraction of the pressure is reflected when the  $P$ -wave reaches the box limit inducing a significant non desired shear effect. A similar tests were conducted on the other targets as shown in Figures N.2, N.3, and N.4 corresponding to  $C11_b\text{-Cu}_{33.3}\text{Zr}_{66.7}$ ,  $\alpha\text{-Cu}_{50}\text{Zr}_{50}$ , and  $\alpha\text{-Cu}_{33.3}\text{Zr}_{66.7}$  respectively. It was found that the  $P$ -wave has exactly the same shape whereas the maximum value of pressure is  $\sim 5 \text{ GPa}$  less in amorphous targets compared to crystals.

Finally, such a NRBC region design has a double advantage. The first is reducing simulation time by handling a small system and getting reliable results at the same time. Second, reducing drastically the simulation time that is necessary for performing a longer simulation. Therefore, phenomena occurring at the scale of nanoseconds, for example can be captured.

# Bibliography

- [1] Gernot Krabbes, Günter Fuchs, Wolf-Rüdiger Canders, Hardo May, and Ryszard Palka. High temperature superconductor bulk materials. fundamentals-processing-properties control-application aspects. 2006.
- [2] C Suryanarayana and H Jones. Formation and characteristics of quasicrystalline phases-a review. *Indian Journal of Radio and Space Physics*, 3(4):253–293, 1988.
- [3] Dan Shechtman, Ilan Blech, Denis Gratias, and John W Cahn. Metallic phase with long-range orientational order and no translational symmetry. *Physical review letters*, 53(20):1951, 1984.
- [4] Herbert Gleiter. Nanocrystalline materials. In *Advanced Structural and Functional Materials*, pages 1–37. Springer, 1991.
- [5] C Suryanarayana. Nanocrystalline materials. *International materials reviews*, 40(2):41–64, 1995.
- [6] Herbert Gleiter. Nanostructured materials: basic concepts and microstructure. *Acta materialia*, 48(1):1–29, 2000.
- [7] C Suryanarayana. Recent developments in nanostructured materials. *Advanced Engineering Materials*, 7(11):983–992, 2005.
- [8] Herbert Gleiter. Our thoughts are ours, their ends none of our own: are there ways to synthesize materials beyond the limitations of today? *Acta Materialia*, 56(19):5875–5893, 2008.
- [9] Howard H Liebermann. Rapidly solidified materials. *Marcel Dekker*, 1993.
- [10] Tanjore R Anantharaman. Metallic glasses: production, properties and applications. *Trans Tech Publications SA, Trans Tech House, CH-4711 Aedermannsdorf, Switzerland, 1984. 302*, 1984.
- [11] Pol Duwez. Structure and properties of alloys rapidly quenched from the liquid state. *ASM Trans Quart*, 60(4):605–633, 1967.

- [12] C Suryanarayana. *Non-equilibrium processing of materials*. Elsevier, 1999.
- [13] TR Anantharaman and C Suryanarayana. A decade of quenching from the melt. *Journal of Materials Science*, 6(8):1111–1135, 1971.
- [14] H Jones. Rapid solidification of metals and alloys, institution of metallurgists. *London, UK*, 1982.
- [15] C Suryanarayana. *Rapidly Quenched Metals, A Bibliography, 1973-1979*. Springer, 1980.
- [16] Carl C Koch. Processing of metals and alloys. *Materials Science and Technology-A Comprehensive Treatment*, 15:193–245, 1991.
- [17] C Suryanarayana. *Bibliography on mechanical alloying and milling*. Cambridge International Science Publishing, Limited, 1996.
- [18] Cury Suryanarayana. Mechanical alloying and milling. *Progress in materials science*, 46(1-2):1–184, 2001.
- [19] Michael A Lieberman and Alan J Lichtenberg. *Principles of plasma discharges and materials processing*. John Wiley & Sons, 2005.
- [20] KS Sree. Principle of physical vapor deposition of thin films, 2006.
- [21] Enrique J Lavernia and Yue Wu. *Spray atomization and deposition*. Wiley-Blackwell, 1996.
- [22] G Martin and P Bellon. Driven alloys, vol. 50 of. *Solid State Physics*, pages 189–331, 1997.
- [23] H Jones and C Suryanarayana. Rapid quenching from the melt: An annotated bibliography 1958–72. *Journal of Materials Science*, 8(5):705–753, 1973.
- [24] Willens Klement, RH Willens, and POL Duwez. Non-crystalline structure in solidified gold–silicon alloys. *Nature*, 187(4740):869–870, 1960.
- [25] P Duwez. Metallic glasses-historical background. *Glassy Metals I*, pages 19–23, 1981.
- [26] BX Liu and O Jin. Formation and theoretical modeling of non-equilibrium alloy phases by ion mixing. *physica status solidi (a)*, 161(1):3–33, 1997.

- [27] Tao Zhang, Akihisa Inoue, and Tsuyoshi Masumoto. Amorphous zrn-dash;alndash;tm (tm=co, ni, cu) alloys with significant supercooled liquid region of over 100 k. *Materials Transactions, JIM*, 32(11):1005–1010, 1991.
- [28] Akihisa Inoue, Tao Zhang, and Tsuyoshi Masumoto. Al–la–ni amorphous alloys with a wide supercooled liquid region. *Materials transactions, JIM*, 30(12):965–972, 1989.
- [29] A. Inoue, T. Zhang, N. Nishiyama, K. Ohba, and T. Masumoto. Preparation of 16 mm diameter rod of amorphous  $zr_{65}al_{7.5}ni_{10}cu_{17.5}$ . *Materials Transactions, JIM*, 34(12) : 1234 – 1237, 1993.
- [30] Atakan Peker and William L Johnson. A highly processable metallic glass: Zr41. 2ti13. 8cu12. 5ni10. 0be22. 5. *Applied Physics Letters*, 63(17):2342–2344, 1993.
- [31] Nobuyuki Nishiyama, Maki Horino, and Akihisa Inoue. Thermal expansion and specific volume of  $pd_{40}cu_{30}ni_{10}p_{20}$ . *Materials Transactions, JIM*, 41(11) : 1432 – 1434, 2000.
- [32] Jean BIGOT. *Alliages Métalliques Amorphes*. Technique de L’ingénieur, M50. 1996.
- [33] Ranjan Ray. *Ultra-rapide Solidification Process*. Metals Hand Book, Vol7, P794. 1984.
- [34] Arthur L Schawlow and Charles H Townes. Infrared and optical masers. *Physical Review*, 112(6):1940, 1958.
- [35] AJ DeMaria, DA Stetser, and H Heynau. Self mode-locking of lasers with saturable absorbers. *Applied Physics Letters*, 8(7):174–176, 1966.
- [36] David E Spence, P Np Kean, and Wilson Sibbett. 60-fsec pulse generation from a self-mode-locked ti: sapphire laser. *Optics letters*, 16(1):42–44, 1991.
- [37] Stefan Nolte, Cl Momma, H Jacobs, A Tünnermann, Boris N Chichkov, Bernd Wellegehausen, and Herbert Welling. Ablation of metals by ultrashort laser pulses. *JOSA B*, 14(10):2716–2722, 1997.
- [38] Chris B Schaffer, André Brodeur, José F García, and Eric Mazur. Micromachining bulk glass by use of femtosecond laser pulses with nanojoule energy. *Optics letters*, 26(2):93–95, 2001.
- [39] Rafael R Gattass and Eric Mazur. Femtosecond laser micromachining in transparent materials. *Nature photonics*, 2(4):219–225, 2008.

- [40] Lawrence Shah, Jesse Tawney, Martin Richardson, and Kathleen Richardson. Femtosecond laser deep hole drilling of silicate glasses in air. *Applied surface science*, 183(3-4):151–164, 2001.
- [41] H Varel, D Ashkenasi, A Rosenfeld, M Wähmer, and EEB Campbell. Micromachining of quartz with ultrashort laser pulses. *Applied Physics A: Materials Science & Processing*, 65, 1997.
- [42] Jerzy Antonowicz, Peter Zalden, K Sokolowski-Tinten, K Georgharakis, R Minikayev, Anna Pietnoczka, F Bertram, M Chaika, M Chojnacki, P Dłużewski, et al. Devitrification of thin film cu–zr metallic glass via ultrashort pulsed laser annealing. *Journal of Alloys and Compounds*, 887:161437, 2021.
- [43] Jing Cao, Matthieu Lancry, Francois Brisset, Leo Mazerolles, Romuald Saint-Martin, and Bertrand Poumellec. Femtosecond laser-induced crystallization in glasses: growth dynamics for orientable nanostructure and nanocrystallization. *Crystal Growth & Design*, 19(4):2189–2205, 2019.
- [44] Sean D McAnany, Keith J Veenhuizen, Andrew M Kiss, Juergen Thieme, Daniel A Nolan, Bruce G Aitken, Volkmar Dierolf, and Himanshu Jain. Evolution of glass structure during femtosecond laser assisted crystallization of labgeo5 in glass. *Journal of Non-Crystalline Solids*, 551:120396, 2021.
- [45] Y Zhang, L Liu, G Zou, N Chen, A Wu, H Bai, and Y Zhou. Femtosecond laser-induced phase transformations in amorphous cu<sub>77</sub>ni<sub>6</sub>sn<sub>10</sub>p<sub>7</sub> alloy. *Journal of Applied Physics*, 117(2):023109, 2015.
- [46] Yu Teng, Jiajia Zhou, Kaniyarakkal Sharafudeen, Shifeng Zhou, Kiyotaka Miura, and Jianrong Qiu. Space-selective crystallization of glass induced by femtosecond laser irradiation. *Journal of non-crystalline solids*, 383:91–96, 2014.
- [47] Jing Cao, Bertrand Poumellec, Léo Mazerolles, François Brisset, Anne-Laure Helbert, Suzy Surble, Xuan He, and Matthieu Lancry. Nanoscale phase separation in lithium niobium silicate glass by femtosecond laser irradiation. *Journal of the American Ceramic Society*, 100(1):115–124, 2017.
- [48] Nan Shen. Nonlinear spectroscopy study of fuel layer uniformity in inertial confinement fusion targets.
- [49] Victor Malka, S Fritzler, E Lefebvre, M-M Aleonard, F Burgy, J-P Chambaret, J-F Chemin, K Krushelnick, G Malka, SPD Mangles, et al. Electron acceleration by

- a wake field forced by an intense ultrashort laser pulse. *Science*, 298(5598):1596–1600, 2002.
- [50] Winifried Denk, James H Strickler, and Watt W Webb. Two-photon laser scanning fluorescence microscopy. *Science*, 248(4951):73–76, 1990.
- [51] Jérôme Kasparian, Miguel Rodríguez, Guillaume Méjean, Jin Yu, Estelle Salmon, H Wille, R Bourayou, S Frey, Y-B André, André Mysyrowicz, et al. White-light filaments for atmospheric analysis. *Science*, 301(5629):61–64, 2003.
- [52] Peter R Smith, David H Auston, and Martin C Nuss. Subpicosecond photoconducting dipole antennas. *IEEE Journal of Quantum Electronics*, 24(2):255–260, 1988.
- [53] Tatsuhiko Aizawa and Tadahiko Inohara. Pico-and femtosecond laser micromachining for surface texturing. *Micromachining*, 1:1–24, 2019.
- [54] Andreas Ehn, Joakim Bood, Zheming Li, Edouard Berrocal, Marcus Aldén, and Elias Kristensson. Frame: femtosecond videography for atomic and molecular dynamics. *Light: Science & Applications*, 6(9):e17045–e17045, 2017.
- [55] Tibor Juhasz, Frieder H Loesel, Ron M Kurtz, Christopher Horvath, Josef F Bille, and Gerard Mourou. Corneal refractive surgery with femtosecond lasers. *IEEE Journal of Selected Topics in Quantum Electronics*, 5(4):902–910, 1999.
- [56] Nick Mamalis. Femtosecond laser: the future of cataract surgery? *Journal of Cataract & Refractive Surgery*, 37(7):1177–1178, 2011.
- [57] Samuel H Chung and Eric Mazur. Surgical applications of femtosecond lasers. *Journal of biophotonics*, 2(10):557–572, 2009.
- [58] H Kaz Soong and João Baptista Malta. Femtosecond lasers in ophthalmology. *American journal of ophthalmology*, 147(2):189–197, 2009.
- [59] Ginny Kullman and Roberto Pineda. Alternative applications of the femtosecond laser in ophthalmology. In *Seminars in ophthalmology*, volume 25, pages 256–264. Taylor & Francis, 2010.
- [60] Timothy V Roberts, Michael Lawless, Colin CK Chan, Mark Jacobs, David Ng, Shveta J Bali, Chris Hodge, and Gerard Sutton. Femtosecond laser cataract surgery: technology and clinical practice. *Clinical & experimental ophthalmology*, 41(2):180–186, 2013.

- [61] Catharina Latz, Thomas Asshauer, Christian Rathjen, and Alireza Mirshahi. Femtosecond-laser assisted surgery of the eye: Overview and impact of the low-energy concept. *Micromachines*, 12(2), 2021.
- [62] Ali Sami Alnaser, Sharjeel Ahmed Khan, Rashid Ashirovich Ganeev, and Emmanuel Stratakis. Recent advances in femtosecond laser-induced surface structuring for oil–water separation. *Applied Sciences*, 9(8):1554, 2019.
- [63] M Kamata and M Obara. Control of the refractive index change in fused silica glasses induced by a loosely focused femtosecond laser. *Applied Physics A*, 78(1):85–88, 2004.
- [64] Vedula R Bhardwaj, E Simova, PB Corkum, DM Rayner, C Hnatovsky, RS Taylor, B Schreder, M Kluge, and J Zimmer. Femtosecond laser-induced refractive index modification in multicomponent glasses. *Journal of applied physics*, 97(8):083102, 2005.
- [65] Tadamasa Toma, Yoshio Furuya, Wataru Watanabe, Kazuyoshi Itoh, Junji Nishii, and Kenichi Hayashi. Estimation of the refractive index change in glass induced by femtosecond laser pulses. *Optical review*, 7(1):14–17, 2000.
- [66] Kazuhiro Yamada, Wataru Watanabe, Tadamasa Toma, Kazuyoshi Itoh, and Junji Nishii. In situ observation of photoinduced refractive-index changes in filaments formed in glasses by femtosecond laser pulses. *Optics letters*, 26(1):19–21, 2001.
- [67] Roberto Osellame, Stefano Taccheo, Marco Marangoni, Roberta Ramponi, Paolo Laporta, Dario Polli, Sandro De Silvestri, and Giulio Cerullo. Femtosecond writing of active optical waveguides with astigmatically shaped beams. *JOSA B*, 20(7):1559–1567, 2003.
- [68] K Miura, Jianrong Qiu, H Inouye, T Mitsuyu, and K Hirao. Photowritten optical waveguides in various glasses with ultrashort pulse laser. *Applied Physics Letters*, 71(23):3329–3331, 1997.
- [69] Hong-Bo Sun, Shigeki Matsuo, and Hiroaki Misawa. Three-dimensional photonic crystal structures achieved with two-photon-absorption photopolymerization of resin. *Applied physics letters*, 74(6):786–788, 1999.
- [70] Andrius Marcinkevičius, Saulius Juodkazis, Mitsuru Watanabe, Masafumi Miwa, Shigeki Matsuo, Hiroaki Misawa, and Junji Nishii. Femtosecond laser-assisted three-dimensional microfabrication in silica. *Optics Letters*, 26(5):277–279, 2001.

- [71] Valeria Maselli, Jason R Grenier, Stephen Ho, and Peter R Herman. Femtosecond laser written optofluidic sensor: Bragg grating waveguide evanescent probing of microfluidic channel. *Optics Express*, 17(14):11719–11729, 2009.
- [72] B. Rethfeld, K. Sokolowski-Tinten, D. von der Linde, and S. I. Anisimov. Timescales in the response of materials to femtosecond laser excitation. *Applied Physics A*, 79(4):767–769, Sep 2004.
- [73] Bernd Huettnner. Short-pulse laser heating of metals: a new approach. In *Nonresonant Laser-Matter Interaction (NLMI-9)*, volume 3093, pages 366–373. SPIE, 1997.
- [74] HE Elsayed-Ali, TB Norris, MA Pessot, and GA Mourou. Time-resolved observation of electron-phonon relaxation in copper. *Physical Review Letters*, 58(12):1212, 1987.
- [75] Ričardas Buividas, Mindaugas Mikutis, Tadas Kudrius, Artūras Greičius, Gintas Šlekys, and Saulius Juodkazis. Femtosecond laser processing—a new enabling technology. *Lithuanian Journal of Physics*, 52(4), 2012.
- [76] Brian J Demaske, Vasily V Zhakhovsky, Nail A Inogamov, and Ivan I Oleynik. Ablation and spallation of gold films irradiated by ultrashort laser pulses. *Physical Review B*, 82(6):064113, 2010.
- [77] Laurent J Lewis and Danny Perez. Laser ablation with short and ultrashort laser pulses: Basic mechanisms from molecular-dynamics simulations. *Applied Surface Science*, 255(10):5101–5106, 2009.
- [78] Wenqian Hu, Yung C Shin, and Galen King. Energy transport analysis in ultrashort pulse laser ablation through combined molecular dynamics and monte carlo simulation. *Physical Review B*, 82(9):094111, 2010.
- [79] Sheng Tan, Jianjun Wu, Yu Zhang, Moge Wang, and Yang Ou. A model of ultra-short pulsed laser ablation of metal with considering plasma shielding and non-fourier effect. *Energies*, 11(11):3163, 2018.
- [80] Boris N Chichkov, C Momma, Stefan Nolte, F Von Alvensleben, and A Tünnermann. Femtosecond, picosecond and nanosecond laser ablation of solids. *Applied physics A*, 63(2):109–115, 1996.
- [81] Danny Perez and Laurent J Lewis. Ablation of solids under femtosecond laser pulses. *Physical Review Letters*, 89(25):255504, 2002.

- [82] Nadezhda M Bulgakova and Igor M Bourakov. Phase explosion under ultrashort pulsed laser ablation: modeling with analysis of metastable state of melt. *Applied surface science*, 197:41–44, 2002.
- [83] Jian Cheng, Chang-sheng Liu, Shuo Shang, Dun Liu, Walter Perrie, Geoff Dear-den, and Ken Watkins. A review of ultrafast laser materials micromachining. *Optics & Laser Technology*, 46:88–102, 2013.
- [84] MI Kaganov, EM Lifshitz, and LV Tanatarov. Relaxation between electrons and the crystalline lattice. *Soviet Physics-JETP*, 4:173–178, 1957.
- [85] SI Anisimov, BL Kapeliovich, TL Perelman, et al. Electron emission from metal surfaces exposed to ultrashort laser pulses. *Zh. Eksp. Teor. Fiz*, 66(2):375–377, 1974.
- [86] K Kiran Kumar, GL Samuel, and MS Shunmugam. Theoretical and experimental investigations of ultra-short pulse laser interaction on ti6al4v alloy. *Journal of Materials Processing Technology*, 263:266–275, 2019.
- [87] Dmitriy S Ivanov and Leonid V Zhigilei. Combined atomistic-continuum modeling of short-pulse laser melting and disintegration of metal films. *Physical Review B*, 68(6):064114, 2003.
- [88] S Laville, F Vidal, TW Johnston, O Barthélemy, M Chaker, B Le Drogoff, J Margot, and M Sabsabi. Fluid modeling of the laser ablation depth as a function of the pulse duration for conductors. *Physical review E*, 66(6):066415, 2002.
- [89] K Eidmann, J Meyer-ter Vehn, Th Schlegel, and S Hüller. Hydrodynamic simulation of subpicosecond laser interaction with solid-density matter. *Physical Review E*, 62(1):1202, 2000.
- [90] Jean-Philippe Colombier, Patrick Combis, Arkadi Rosenfeld, Ingolf V Hertel, Eric Audouard, and Razvan Stoian. Optimized energy coupling at ultrafast laser-irradiated metal surfaces by tailoring intensity envelopes: Consequences for material removal from al samples. *Physical Review B*, 74(22):224106, 2006.
- [91] Xxx Sedao, Anthony Abou Saleh, Anton Rudenko, Thierry Douillard, Claude Esnouf, Stephanie Reynaud, Claire Maurice, Florent Pigeon, Florence Garrelie, and Jean-Philippe Colombier. Self-arranged periodic nanovoids by ultrafast laser-induced near-field enhancement. *ACS photonics*, 5(4):1418–1426, 2018.
- [92] Alexey N Volkov and Gerard M O’Connor. Parallel direct simulation monte carlo of two-phase gas-droplet laser plume expansion from the bottom of a cylindrical

- cavity into an ambient gas. In *Computational Fluid Dynamics 2010*, pages 105–112. Springer, 2011.
- [93] Anton Rudenko, Jean-Philippe Colombier, and Tatiana Itina. Femtosecond laser irradiation of fused silica with a nanometric inhomogeneity. In *PIERS Proceedings*, pages 1870–1876, 2015.
- [94] Enrique Moreno, Huu Dat Nguyen, Razvan Stoian, and Jean-Philippe Colombier. Full explicit numerical modeling in time-domain for nonlinear electromagnetics simulations in ultrafast laser nanostructuring. *Applied Sciences*, 11(16):7429, 2021.
- [95] Thibault J-Y Derrien, Nicolas Tancogne-Dejean, Vladimir P Zhukov, Heiko Appel, Angel Rubio, and Nadezhda M Bulgakova. Photoionization and transient wannier-stark ladder in silicon: First-principles simulations versus keldysh theory. *Physical Review B*, 104(24):L241201, 2021.
- [96] EP Silaeva, Emile Bévillon, R Stoian, and Jean-Philippe Colombier. Ultrafast electron dynamics and orbital-dependent thermalization in photoexcited metals. *Physical Review B*, 98(9):094306, 2018.
- [97] Jean-Philippe Colombier, Anton Rudenko, Elena Silaeva, Hao Zhang, Xxx Sedao, Emile Bévillon, Stéphanie Reynaud, Claire Maurice, Florent Pigeon, Florence Garrelie, et al. Mixing periodic topographies and structural patterns on silicon surfaces mediated by ultrafast photoexcited charge carriers. *Physical Review Research*, 2(4):043080, 2020.
- [98] Hengyu Zhang, Shen Zhang, Dongdong Kang, Jiayu Dai, and M Bonitz. Finite-temperature density-functional-theory investigation on the nonequilibrium transient warm-dense-matter state created by laser excitation. *Physical Review E*, 103(1):013210, 2021.
- [99] SA Sato, K Yabana, Y Shinohara, T Otobe, K-M Lee, and GF Bertsch. Time-dependent density functional theory of high-intensity short-pulse laser irradiation on insulators. *Physical Review B*, 92(20):205413, 2015.
- [100] Marta. Castillejo, Paolo M. Ossi, and Leonid. Zhigilei. *5th Venice International School on Lasers in Materials Science, Lasers in Materials Science*.
- [101] Zhibin Lin, Robert A Johnson, and Leonid V Zhigilei. Computational study of the generation of crystal defects in a bcc metal target irradiated by short laser pulses. *Physical review B*, 77(21):214108, 2008.

- [102] Dmitriy S Ivanov, Zhibin Lin, Baerbel Rethfeld, Gerard M O'Connor, Thomas J Glynn, and Leonid V Zhigilei. Nanocrystalline structure of nanobump generated by localized photoexcitation of metal film. *Journal of Applied Physics*, 107(1):013519, 2010.
- [103] Chengping Wu, Derek A Thomas, Zhibin Lin, and Leonid V Zhigilei. Runaway lattice-mismatched interface in an atomistic simulation of femtosecond laser irradiation of ag film–cu substrate system. *Applied Physics A*, 104(3):781–792, 2011.
- [104] Dmitriy S Ivanov and Leonid V Zhigilei. Effect of pressure relaxation on the mechanisms of short-pulse laser melting. *Physical review letters*, 91(10):105701, 2003.
- [105] Derek A Thomas, Zhibin Lin, Leonid V Zhigilei, Evgeny L Gurevich, Silke Kittel, and Roland Hergenröder. Atomistic modeling of femtosecond laser-induced melting and atomic mixing in au film–cu substrate system. *Applied surface science*, 255(24):9605–9612, 2009.
- [106] Zhibin Lin, Elodie Leveugle, Eduardo M Bringa, and Leonid V Zhigilei. Molecular dynamics simulation of laser melting of nanocrystalline au. *The Journal of Physical Chemistry C*, 114(12):5686–5699, 2010.
- [107] Eaman T Karim, Zhibin Lin, and Leonid V Zhigilei. Molecular dynamics study of femtosecond laser interactions with cr targets. In *AIP Conference Proceedings*, volume 1464, pages 280–293. American Institute of Physics, 2012.
- [108] Leonid V Zhigilei, Zhibin Lin, and Dmitriy S Ivanov. Atomistic modeling of short pulse laser ablation of metals: connections between melting, spallation, and phase explosion. *The Journal of Physical Chemistry C*, 113(27):11892–11906, 2009.
- [109] E Leveugle, Dmitriy S Ivanov, and Leonid V Zhigilei. Photomechanical spallation of molecular and metal targets: molecular dynamics study. *Applied Physics A*, 79(7):1643–1655, 2004.
- [110] Chengping Wu and Leonid V Zhigilei. Microscopic mechanisms of laser spallation and ablation of metal targets from large-scale molecular dynamics simulations. *Applied Physics A*, 114(1):11–32, 2014.
- [111] Maxime Gill-Comeau and Laurent J Lewis. Ultrashort-pulse laser ablation of nanocrystalline aluminum. *Physical Review B*, 84(22):224110, 2011.

- [112] Xxx Sedao, Maxim V Shugaev, Chengping Wu, Thierry Douillard, Claude Esnouf, Claire Maurice, Stéphanie Reynaud, Florent Pigeon, Florence Garrelie, Leonid V Zhigilei, et al. Growth twinning and generation of high-frequency surface nanostructures in ultrafast laser-induced transient melting and resolidification. *ACS nano*, 10(7):6995–7007, 2016.
- [113] Chengping Wu and Leonid V Zhigilei. Nanocrystalline and polyicosahedral structure of a nanospike generated on metal surface irradiated by a single femtosecond laser pulse. *The Journal of Physical Chemistry C*, 120(8):4438–4447, 2016.
- [114] Miao He, Chengping Wu, Maxim V Shugaev, German D Samolyuk, and Leonid V Zhigilei. Computational study of short-pulse laser-induced generation of crystal defects in ni-based single-phase binary solid–solution alloys. *The Journal of Physical Chemistry C*, 123(4):2202–2215, 2019.
- [115] Maxim V Shugaev, Iaroslav Gnilitzkyi, Nadezhda M Bulgakova, and Leonid V Zhigilei. Mechanism of single-pulse ablative generation of laser-induced periodic surface structures. *Physical Review B*, 96(20):205429, 2017.
- [116] Zhengwang Zhu, Haifeng Zhang, Dagang Pan, Wensheng Sun, and Zhuangqi Hu. Fabrication of binary ni-nb bulk metallic glass with high strength and compressive plasticity. *Advanced Engineering Materials*, 8(10):953–957, 2006.
- [117] Fu-Fa Wu, Kang Cheung Chan, Song-Shan Jiang, Shun-Hua Chen, and Gang Wang. Bulk metallic glass composite with good tensile ductility, high strength and large elastic strain limit. *Scientific reports*, 4(1):1–6, 2014.
- [118] C. Zhang, L. Liu, K.C. Chan, Q. Chen, and C.Y. Tang. Wear behavior of hvof-sprayed fe-based amorphous coatings. *Intermetallics*, 29:80–85, 2012.
- [119] W.H. Wang, C. Dong, and C.H. Shek. Bulk metallic glasses. *Materials Science and Engineering: R: Reports*, 44(2):45–89, 2004.
- [120] J Fornell, N Van Steenberge, A Varea, E Rossinyol, E Pellicer, S Suriñach, MD Baró, and J Sort. Enhanced mechanical properties and in vitro corrosion behavior of amorphous and devitrified ti40zr10cu38pd12 metallic glass. *Journal of the Mechanical Behavior of Biomedical Materials*, 4(8):1709–1717, 2011.
- [121] JJ Si, XH Chen, YH Cai, YD Wu, T Wang, and XH Hui. Corrosion behavior of cr-based bulk metallic glasses in hydrochloric acid solutions. *Corrosion Science*, 107:123–132, 2016.

- [122] Marcel Miglierini and Ivan Škorvánek. Magnetic study of neutron irradiated fccsib metallic glass. *Materials Science and Engineering: A*, 147(1):101–106, 1991.
- [123] WH Wang. Bulk metallic glasses with functional physical properties. *Advanced Materials*, 21(45):4524–4544, 2009.
- [124] William L Johnson and John Plummer. Is metallic glass poised to come of age? *Nature materials*, 14(6):553–555, 2015.
- [125] Mark Telford. The case for bulk metallic glass. *Materials Today*, 7(3):36–43, 2004.
- [126] <http://www.liquidmetal.com>.
- [127] Li Zhong, Jiangwei Wang, Hongwei Sheng, Ze Zhang, and Scott X Mao. Formation of monatomic metallic glasses through ultrafast liquid quenching. *Nature*, 512(7513):177–180, 2014.
- [128] P Luo, CR Cao, F Zhu, YM Lv, YH Liu, P Wen, HY Bai, G Vaughan, M Di Michiel, Béatrice Ruta, et al. Ultrastable metallic glasses formed on cold substrates. *Nature communications*, 9(1):1389, 2018.
- [129] Rainer Behrisch and Wolfgang Eckstein. *Sputtering by particle bombardment: experiments and computer calculations from threshold to MeV energies*, volume 110. Springer Science & Business Media, 2007.
- [130] Sheng-Bao Qiu and Ke-Fu Yao. Novel application of the electrodeposition on bulk metallic glasses. *Applied Surface Science*, 255(5):3454–3458, 2008.
- [131] Morel H. and Turnbull D. Metastability of amorphous structures. *Nature*, 203(4948):964–964, Aug 1964.
- [132] C. A. Angell. Formation of glasses from liquids and biopolymers. *Science*, 267(5206):1924–1935, 1995.
- [133] René Fulchiron, Imane Belyamani, Joshua U. Otaigbe, and Véronique Bounor-Legaré. A simple method for tuning the glass transition process in inorganic phosphate glasses. *Scientific Reports*, 5(1):8369, Feb 2015.
- [134] Ali Bagheri Behboud. Development of nanostructured metallic glasses with high toughness. Master’s thesis, Middle East Technical University, 2021.

- [135] L.E Tanner and R Ray. Metallic glass formation and properties in zr and ti alloyed with be—i the binary zr-be and ti-be systems. *Acta Metallurgica*, 27(11):1727–1747, 1979.
- [136] Theodore A Waniuk, Jan Schroers, and William L Johnson. Critical cooling rate and thermal stability of zrticunibe alloys. *Applied Physics Letters*, 78(9):1213–1215, 2001.
- [137] Akihisa Inoue. Stabilization of metallic supercooled liquid and bulk amorphous alloys. *Acta materialia*, 48(1):279–306, 2000.
- [138] Walter. Kauzmann. The nature of the glassy state and the behavior of liquids at low temperatures. *Chemical Reviews*, 43(2):219–256, Oct 1948.
- [139] A. Lindsay Greer. Confusion by design. , 366(6453):303–304, December 1993.
- [140] T Egami and Y Waseda. Atomic size effect on the formability of metallic glasses. *Journal of Non-Crystalline Solids*, 64(1):113–134, 1984.
- [141] O.N. Senkov and D.B. Miracle. Effect of the atomic size distribution on glass forming ability of amorphous metallic alloys. *Materials Research Bulletin*, 36(12):2183–2198, 2001.
- [142] Tim Cullinan, Ilkay Kalay, Y Eren Kalay, Matt Kramer, and Ralph Napolitano. Kinetics and mechanisms of isothermal devitrification in amorphous cu<sub>50</sub>zr<sub>50</sub>. *Metallurgical and Materials Transactions A*, 46(2):600–613, 2015.
- [143] S.H. Zhou and R.E. Napolitano. Phase stability for the cu–zr system: First-principles, experiments and solution-based modeling. *Acta Materialia*, 58(6):2186–2196, 2010.
- [144] Eckart Kneller, Yunus Khan, and Ursula Gorres. The alloy system copper-zirconium. *Z. Metallkd.*, 77(1):43–48, 1986.
- [145] D Arias and JP Abriata. Cu-zr (copper-zirconium). *Journal of Phase Equilibria*, 11(5):452–459, 1990.
- [146] Aldo R Boccaccini, Delia S Brauer, and Leena Hupa, editors. *Bioactive Glasses*. Smart Materials Series. The Royal Society of Chemistry, 2017.
- [147] David A Porter and Kenneth E Easterling. *Phase transformations in metals and alloys (revised reprint)*. CRC press, 2009.
- [148] XY Liu. Heterogeneous nucleation or homogeneous nucleation? *The Journal of Chemical Physics*, 112(22):9949–9955, 2000.

- [149] Deniz Erdemir, Alfred Y Lee, and Allan S Myerson. Nucleation of crystals from solution: classical and two-step models. *Accounts of chemical research*, 42(5):621–629, 2009.
- [150] LQ Shen, P Luo, YC Hu, HY Bai, YH Sun, BA Sun, YH Liu, and WH Wang. Shear-band affected zone revealed by magnetic domains in a ferromagnetic metallic glass. *Nature communications*, 9(1):1–9, 2018.
- [151] Haichuan Zhang, Yingjie Li, Tianhao Xu, Jiabao Wang, Ziyang Huo, Pengbo Wan, and Xiaoming Sun. Amorphous co-doped mos 2 nanosheet coated metallic cos 2 nanocubes as an excellent electrocatalyst for hydrogen evolution. *Journal of Materials Chemistry A*, 3(29):15020–15023, 2015.
- [152] Matjaz Valant, Uroš Luin, Mattia Fanetti, Andraž Mavrič, Kateryna Vyshniakova, Zdravko Siketić, and Mitjan Kalin. Fully transparent nanocomposite coating with an amorphous alumina matrix and exceptional wear and scratch resistance. *Advanced Functional Materials*, 26(24):4362–4369, 2016.
- [153] H Guo, PF Yan, YB Wang, J Tan, ZF Zhang, ML Sui, and E Ma. Tensile ductility and necking of metallic glass. *Nature materials*, 6(10):735–739, 2007.
- [154] Zi-Jian Wang, Ming-Xing Li, Ji-Hao Yu, Xing-Bo Ge, Yan-Hui Liu, and Wei-Hua Wang. Low-iridium-content irnita metallic glass films as intrinsically active catalysts for hydrogen evolution reaction. *Advanced Materials*, 32(4):1906384, 2020.
- [155] A Schlegel, P Wachter, KP Ackermann, M Liard, and H-J Güntherodt. Optical properties of metallic glasses. *Solid State Communications*, 31(5):373–376, 1979.
- [156] Michail Papanikolaou, Konstantinos Salonitis, Mark Jolly, and Michael Frank. Large-scale molecular dynamics simulations of homogeneous nucleation of pure aluminium. *Metals*, 9(11), 2019.
- [157] John J. Chu and Craig A. Steeves. Thermal expansion and recrystallization of amorphous al and ti: A molecular dynamics study. *Journal of Non-Crystalline Solids*, 357(22):3765–3773, 2011.
- [158] Alexander E. Mayer and Vasiliy S. Krasnikov. Atomistic and continuum modeling of non-equilibrium melting of aluminum, 2015.
- [159] Avik Mahata, Mohsen Asle Zaeem, and Michael I Baskes. Understanding homogeneous nucleation in solidification of aluminum by molecular dynamics simulations. *Modelling and Simulation in Materials Science and Engineering*, 26(2):025007, jan 2018.

- [160] Dmitri V. Louzguine-Luzgin and Andrey I. Bazlov. Crystallization of fcc and bcc liquid metals studied by molecular dynamics simulation. *Metals*, 10(11), 2020.
- [161] Yanqiu Zhang and Shuyong Jiang. Atomistic mechanisms for temperature-induced crystallization of amorphous copper based on molecular dynamics simulation. *Computational Materials Science*, 151:25–33, 2018.
- [162] Yan Zhao, Xunli Wei, Yan Zhang, Jiachun Wang, and Dehong Huo. Crystallization of amorphous materials and deformation mechanism of nanocrystalline materials under cutting loads: A molecular dynamics simulation approach. *Journal of Non-Crystalline Solids*, 439:21–29, 2016.
- [163] Qi Zhang, Jincheng Wang, Sai Tang, Yujian Wang, Junjie Li, Wenquan Zhou, and Zhijun Wang. Molecular dynamics investigation of the local structure in iron melts and its role in crystal nucleation during rapid solidification. *Phys. Chem. Chem. Phys.*, 21:4122–4135, 2019.
- [164] Yun fei Mo, Ze an Tian, Rang su Liu, Zhao yang Hou, Li li Zhou, Ping Peng, Hai tao Zhang, and Yong chao Liang. Molecular dynamics study on microstructural evolution during crystallization of rapidly supercooled zirconium melts. *Journal of Alloys and Compounds*, 688:654–665, 2016.
- [165] D. V. Louzguine-Luzgin, M. Miyama, K. Nishio, A. A. Tsarkov, and A. L. Greer. Vitrification and nanocrystallization of pure liquid ni studied using molecular-dynamics simulation. *The Journal of Chemical Physics*, 151(12):124502, 2019.
- [166] Dmitri V. Louzguine-Luzgin, Rodion Belosludov, Masatoshi Saito, Yoshiyuki Kawazoe, and Akihisa Inoue. Glass-transition behavior of ni: Calculation, prediction, and experiment. *Journal of Applied Physics*, 104(12):123529, 2008.
- [167] Andrey I. Dmitriev, Anton Yu. Nikonov, and Werner Österle. Molecular dynamics sliding simulations of amorphous ni, ni-p and nanocrystalline ni films. *Computational Materials Science*, 129:231–238, 2017.
- [168] Khachatur V. Manukyan, Christopher E. Shuck, Mathew J. Cherukara, Sergei Rouvimov, Dmitry Y. Kovalev, Alejandro Strachan, and Alexander S. Mukasyan. Exothermic self-sustained waves with amorphous nickel. *The Journal of Physical Chemistry C*, 120(10):5827–5838, Mar 2016.
- [169] Zachary D McClure, Samuel Temple Reeve, and Alejandro Strachan. Role of electronic thermal transport in amorphous metal recrystallization: A molecular dynamics study. *The Journal of Chemical Physics*, 149(6):064502, 2018.

- [170] M. H. Bhat, V. Molinero, E. Soignard, V. C. Solomon, S. Sastry, J. L. Yarger, and C. A. Angell. Vitrification of a monatomic metallic liquid. *Nature*, 448(7155):787–790, Aug 2007.
- [171] Li Zhong, Jiangwei Wang, Hongwei Sheng, Ze Zhang, and Scott X. Mao. Formation of monatomic metallic glasses through ultrafast liquid quenching. *Nature*, 512(7513):177–180, Aug 2014.
- [172] Yang Li, JiaHao Li, and BaiXin Liu. The atomic-scale nucleation mechanism of niti metallic glasses upon isothermal annealing studied via molecular dynamics simulations. *Phys. Chem. Chem. Phys.*, 17:27127–27135, 2015.
- [173] M. Guerdane, F. Wendler, D. Danilov, H. Teichler, and B. Nestler. Crystal growth and melting in nizr alloy: Linking phase-field modeling to molecular dynamics simulations. *Phys. Rev. B*, 81:224108, Jun 2010.
- [174] S.Y. Liu, Q.P. Cao, X. Mu, T.D. Xu, D. Wang, K. Ståhl, X.D. Wang, D.X. Zhang, C. Kübel, and J.Z. Jiang. Tracing intermediate phases during crystallization in a ni-zr metallic glass. *Acta Materialia*, 186:396–404, 2020.
- [175] Quanwen Yang, Shujie Pang, and Tao Zhang. Crystallization of amorphous ni-zr alloys during heating with molecular dynamics simulations. *Journal of University of Science and Technology Beijing, Mineral, Metallurgy, Material*, 14:73–76, 2007.
- [176] S.A. Rogachev, O. Politano, F. Baras, and A.S. Rogachev. Explosive crystallization in amorphous cuti thin films: a molecular dynamics study. *Journal of Non-Crystalline Solids*, 505:202–210, 2019.
- [177] A. S. Rogachev, S. G. Vadchenko, A. S. Aronin, S. Rouvimov, A. A. Nepapushev, I. D. Kovalev, F. Baras, O. Politano, S. A. Rogachev, and A. S. Mukasyan. Self-propagating waves of crystallization in metallic glasses. *Applied Physics Letters*, 111(9):093105, 2017.
- [178] Muhammad Faruq, Antoine Villesuzanne, and Guosheng Shao. Molecular-dynamics simulations of binary pd-si metal alloys: Glass formation, crystallisation and cluster properties. *Journal of Non-Crystalline Solids*, 487:72–86, 2018.
- [179] Dung Nguyen-Trong, Kien Pham-Huu, and Phuong Nguyen-Tri. Simulation on the factors affecting the crystallization process of feni alloy by molecular dynamics. *ACS Omega*, 4(11):14605–14612, Sep 2019.

- [180] Bang yi Yu, Yong chao Liang, Ze an Tian, Rang su Liu, Ting hong Gao, Quan Xie, and Yun fei Mo. Md simulation on crystallization mechanisms of rapidly supercooled fe-ni alloys. *Journal of Crystal Growth*, 535:125533, 2020.
- [181] Yang Sun, Zhuo Ye, Feng Zhang, Ze Jun Ding, Cai-Zhuang Wang, Matthew J Kramer, and Kai-Ming Ho. Investigation of partitionless growth of al60sm11phase in al-10 at% sm liquid. *Modelling and Simulation in Materials Science and Engineering*, 26(1):015006, dec 2017.
- [182] L. Zhao, G.B. Bokas, J.H. Perepezko, and I. Szlufarska. Nucleation kinetics in al-sm metallic glasses. *Acta Materialia*, 142:1–7, 2018.
- [183] S Starikov, I Gordeev, Y Lysogorskiy, L Kolotova, and S Makarov. Optimized interatomic potential for study of structure and phase transitions in si-au and si-al systems. *Computational Materials Science*, 184:109891, 2020.
- [184] Dung Nguyen Trong, Van Cao Long, and Ștefan Țălu. The structure and crystallizing process of niau alloy: A molecular dynamics simulation method. *Journal of Composites Science*, 5(1), 2021.
- [185] Simin An, Jiahao Li, Yang Li, Shunning Li, Qi Wang, and Baixin Liu. Two-step crystal growth mechanism during crystallization of an undercooled ni50al50 alloy. *Scientific reports*, 6(1):1–10, 2016.
- [186] Mauricio A. P. Silva, José Pedro Rino, André Monteil, Sidney J. L. Ribeiro, and Younès Messaddeq. Molecular dynamics simulation on devitrification: Isothermal devitrification and thermodynamics of pbf2 glasses. *The Journal of Chemical Physics*, 121(15):7413–7420, 2004.
- [187] Géraldine Dantelle, Michel Mortier, André Monteil, Stéphane Chaussedent, and Mauricio A. P. Silva. Molecular dynamics simulation study of erbium induced devitrification in vitreous pbf2. *The Journal of Chemical Physics*, 127(9):094509, 2007.
- [188] S. Kazanc. Molecular dynamics study of pressure effect on crystallization behaviour of amorphous cuni alloy during isothermal annealing. *Physics Letters A*, 365(5):473–477, 2007.
- [189] Po Huang, De-Hui Zou, Gu-Qing Guo, and Liang Yang. Structural origin of the different devitrification behaviors between ZrCu and ZrPd metallic glasses. *EPL (Europhysics Letters)*, 107(6):66002, sep 2014.

- [190] S. Lesz and G. Dercz. Study on crystallization phenomenon and thermal stability of binary ni–nb amorphous alloy. *Journal of Thermal Analysis and Calorimetry*, 126(1):19–26, Oct 2016.
- [191] M.H. ENAYATI. Crystallization behavior of ni-nb amorphous alloys. *Scientia iranica*, 9(2):157–161, 2002.
- [192] Bulat N. Galimzyanov, Maria A. Doronina, and Anatolii V. Mokshin. Excellent glass former ni<sub>62</sub>nb<sub>38</sub> crystallizing under combined shear and ultra-high pressure. *Journal of Non-Crystalline Solids*, 572:121102, 2021.
- [193] Murat Celtek. The effect of atomic concentration on the structural evolution of zr<sub>100-x</sub>co<sub>x</sub> alloys during rapid solidification process. *Journal of Non-Crystalline Solids*, 513:84–96, 2019.
- [194] Q X Pei, C Lu, and H P Lee. Crystallization of amorphous alloy during isothermal annealing: a molecular dynamics study. *Journal of Physics: Condensed Matter*, 17(10):1493–1504, feb 2005.
- [195] M. Ohnuma, T. Abei, and H. Onodera. Crystallization of sputter deposited ti-al amorphous alloy. *MRS Proceedings*, 400:209, 1995.
- [196] Yuan-Chao Hu and Hajime Tanaka. Physical origin of glass formation from multicomponent systems. *Science advances*, 6(50):eabd2928, 2020.
- [197] JR Morris, Min Xu, YY Ye, DJ Sordelet, and MJ Kramer. Theoretical and experimental studies of devitrification pathways in the zr<sub>2</sub>cu<sub>1-x</sub>pd<sub>x</sub> metallic glass system. *Acta materialia*, 55(17):5901–5909, 2007.
- [198] Achraf Atila, Meryem Kbirou, Said Ouaskit, and Abdellatif Hasnaoui. On the presence of nanoscale heterogeneity in al<sub>70</sub>ni<sub>15</sub>co<sub>15</sub> metallic glass under pressure. *Journal of Non-Crystalline Solids*, 550:120381, 2020.
- [199] RE Ryltsev, BA Klumov, NM Chtchelkatchev, and K Yu Shunyaev. Computational crystallization of cu-zr-al glass-forming alloys. In *The Tenth International Conference on Materials Technologies and Modeling MMT-2018*, pages 1122–1129, 2018.
- [200] Si Lan, Zhenduo Wu, Xiaoya Wei, Jie Zhou, Zhaoping Lu, Jörg Neuefeind, and Xun-Li Wang. Structure origin of a transition of classic-to-avalanche nucleation in zr-cu-al bulk metallic glasses. *Acta Materialia*, 149:108–118, 2018.

- [201] KL Sahoo and Rina Sahu. Glass transition and crystallization of al–ni–la based metallic glasses studied by temperature modulated dsc. *Journal of non-crystalline solids*, 365:33–36, 2013.
- [202] J Tan, Fu Sheng Pan, CJ Li, JF Wang, and J Eckert. Effect of fe on crystallization process of zr-co-al-(fe) bulk metallic glasses. In *Materials Science Forum*, volume 745, pages 734–739. Trans Tech Publ, 2013.
- [203] Xiunan Yang, Chao Zhou, Qijing Sun, Lina Hu, John C Mauro, Chunzhen Wang, and Yuanzheng Yue. Anomalous crystallization as a signature of the fragile-to-strong transition in metallic glass-forming liquids. *The Journal of Physical Chemistry B*, 118(34):10258–10265, 2014.
- [204] S Mechler, N Wanderka, and M-P Macht. Crystallization behavior of low temperature pre-annealed zr<sub>46</sub>. 8ti<sub>8</sub>. 2ni<sub>10</sub>cu<sub>7</sub>. 5be<sub>27</sub>. 5—bulk glass. *Materials Science and Engineering: A*, 375:355–358, 2004.
- [205] M Wollgarten, S Mechler, E Davidov, N Wanderka, and M-P Macht. Decomposition and crystallization of pd<sub>40</sub>cu<sub>30</sub>ni<sub>10</sub>p<sub>20</sub> and zr<sub>46</sub>. 8ti<sub>8</sub>. 2cu<sub>7</sub>. 5ni<sub>10</sub>be<sub>27</sub>. 5 metallic glasses. *Intermetallics*, 12(10-11):1251–1255, 2004.
- [206] U Kühn, K Eymann, N Mattern, J Eckert, A Gebert, B Bartusch, and L Schultz. Limited quasicrystal formation in zr–ti–cu–ni–al bulk metallic glasses. *Acta materialia*, 54(18):4685–4692, 2006.
- [207] Andrea Sauter, Felix Roosen-Runge, Fajun Zhang, Gudrun Lotze, Artem Feoktystov, Robert MJ Jacobs, and Frank Schreiber. On the question of two-step nucleation in protein crystallization. *Faraday discussions*, 179:41–58, 2015.
- [208] Sébastien Marinier and Laurent J Lewis. Femtosecond laser ablation of cu x zr 1- x bulk metallic glasses: a molecular dynamics study. *Physical Review B*, 92(18):184108, 2015.
- [209] Chunguang Tang and Peter Harrowell. Anomalously slow crystal growth of the glass-forming alloy cuzr. *Nature materials*, 12(6):507–511, 2013.
- [210] Yunrui Duan, Jie Li, Xingfan Zhang, Tao Li, Hamidreza Arandiyani, Yanyan Jiang, and Hui Li. Crystallization behavior of a confined cuzr metallic liquid film with a sandwich-like structure. *Physical Chemistry Chemical Physics*, 21(25):13738–13745, 2019.
- [211] Chubing Peng, Lu Cheng, and Masad Mansuripur. Experimental and theoretical investigations of laser-induced crystallization and amorphization in phase-change optical recording media. *Journal of Applied Physics*, 82(9):4183–4191, 1997.

- [212] Xuan He, Chaxing Fan, Bertrand Poumellec, Qiming Liu, Huidan Zeng, François Brisset, Guorong Chen, Xiujian Zhao, and Matthieu Lancry. Size-controlled oriented crystallization in  $\text{SiO}_2$ -based glasses by femtosecond laser irradiation. *JOSA B*, 31(2):376–381, 2014.
- [213] Jia-Min Shieh, Zun-Hao Chen, Bau-Tong Dai, Yi-Chao Wang, Alexei Zaitsev, and Ci-Ling Pan. Near-infrared femtosecond laser-induced crystallization of amorphous silicon. *Applied physics letters*, 85(7):1232–1234, 2004.
- [214] WP Zhou, FR Liu, N Bai, YH Wan, X Lin, and JM Chen. Crystallization of amorphous  $\text{Ge}_2\text{Sb}_2\text{Te}_5$  films induced by an ultraviolet laser. *Applied surface science*, 285:97–101, 2013.
- [215] Guangjun Zhang, Donghong Gu, Xiongwei Jiang, Qingxi Chen, and Fuxi Gan. Crystallization of amorphous  $\text{Ge}_2\text{Sb}_2\text{Te}_5$  films induced by a single femtosecond laser pulse. *Solid state communications*, 133(4):209–212, 2005.
- [216] Ilkay Kalay, Matthew J Kramer, and Ralph E Napolitano. Crystallization kinetics and phase transformation mechanisms in  $\text{Cu}_{56}\text{Zr}_{44}$  glassy alloy. *Metallurgical and Materials Transactions A*, 46(8):3356–3364, 2015.
- [217] JM Wheeler, R Raghavan, and J Michler. Temperature invariant flow stress during microcompression of a  $\text{Zr}$ -based bulk metallic glass. *Scripta Materialia*, 67(2):125–128, 2012.
- [218] Y Yang, JC Ye, J Lu, FX Liu, and PK Liaw. Effects of specimen geometry and base material on the mechanical behavior of focused-ion-beam-fabricated metallic-glass micropillars. *Acta materialia*, 57(5):1613–1623, 2009.
- [219] JC Ye, J Lu, Y Yang, and PK Liaw. Extraction of bulk metallic-glass yield strengths using tapered micropillars in micro-compression experiments. *Intermetallics*, 18(3):385–393, 2010.
- [220] I Kalay, MJ Kramer, and Ralph E Napolitano. High-accuracy x-ray diffraction analysis of phase evolution sequence during devitrification of  $\text{Cu}_{50}\text{Zr}_{50}$  metallic glass. *Metallurgical and Materials Transactions A*, 42(5):1144–1153, 2011.
- [221] June Gunn Lee. *Computational Materials Science An Introduction, Second Edition*. Published November 28, 2016 by CRC Press, 2017.
- [222] B. J. Alder and T. E. Wainwright. Phase transition for a hard sphere system. *The Journal of Chemical Physics*, 27(5):1208–1209, 1957.
- [223] <http://lammps.sandia.gov/>.

- [224] <http://ambermd.org/>.
- [225] <http://www.ks.uiuc.edu/Research/namd/>.
- [226] A Smolyanitsky and VK Tewary. Numerical simulation of nanoscale systems and materials. In *Modeling, Characterization, and Production of Nanomaterials*, pages 87–111. Elsevier, 2015.
- [227] Jonathan Richard Shewchuk et al. An introduction to the conjugate gradient method without the agonizing pain, 1994.
- [228] Loup Verlet. Computer” experiments” on classical fluids. i. thermodynamical properties of lennard-jones molecules. *Physical review*, 159(1):98, 1967.
- [229] Steve Plimpton. Fast parallel algorithms for short-range molecular dynamics. *Journal of computational physics*, 117(1):1–19, 1995.
- [230] <https://www.ctcms.nist.gov/potentials/>.
- [231] J E Lennard-Jones. Cohesion. *Proceedings of the Physical Society*, 43(5):461–482, sep 1931.
- [232] Murray S. Daw, Stephen M. Foiles, and Michael I. Baskes. The embedded-atom method: a review of theory and applications. *Materials Science Reports*, 9(7):251 – 310, 1993.
- [233] Murray S. Daw and M. I. Baskes. Semiempirical, quantum mechanical calculation of hydrogen embrittlement in metals. *Phys. Rev. Lett.*, 50:1285–1288, Apr 1983.
- [234] Murray S. Daw and M. I. Baskes. Embedded-atom method: Derivation and application to impurities, surfaces, and other defects in metals. *Phys. Rev. B*, 29:6443–6453, Jun 1984.
- [235] S. M. Foiles, M. I. Baskes, and M. S. Daw. Embedded-atom-method functions for the fcc metals cu, ag, au, ni, pd, pt, and their alloys. *Phys. Rev. B*, 33:7983–7991, Jun 1986.
- [236] [https://lammps.sandia.gov/doc/pair\\_eam.html](https://lammps.sandia.gov/doc/pair_eam.html).
- [237] M. I. Baskes. Modified embedded-atom potentials for cubic materials and impurities. *Phys. Rev. B*, 46:2727–2742, Aug 1992.
- [238] M. I. Baskes. Application of the embedded-atom method to covalent materials: A semiempirical potential for silicon. *Phys. Rev. Lett.*, 59:2666–2669, Dec 1987.

- [239] Jerry Tersoff. Empirical interatomic potential for silicon with improved elastic properties. *Physical Review B*, 38(14):9902, 1988.
- [240] Jerry Tersoff. New empirical approach for the structure and energy of covalent systems. *Physical review B*, 37(12):6991, 1988.
- [241] Adri CT Van Duin, Siddharth Dasgupta, Francois Lorant, and William A Goddard. Reaxff: a reactive force field for hydrocarbons. *The Journal of Physical Chemistry A*, 105(41):9396–9409, 2001.
- [242] Kimberly Chenoweth, Adri CT Van Duin, and William A Goddard. Reaxff reactive force field for molecular dynamics simulations of hydrocarbon oxidation. *The Journal of Physical Chemistry A*, 112(5):1040–1053, 2008.
- [243] Hasan Metin Aktulga, Joseph C Fogarty, Sagar A Pandit, and Ananth Y Grama. Parallel reactive molecular dynamics: Numerical methods and algorithmic techniques. *Parallel Computing*, 38(4-5):245–259, 2012.
- [244] Lianchi Liu, Yi Liu, Sergey V Zybin, Huai Sun, and William A Goddard III. Reaxff-1g: Correction of the reaxff reactive force field for london dispersion, with applications to the equations of state for energetic materials. *The Journal of Physical Chemistry A*, 115(40):11016–11022, 2011.
- [245] Pierre Hirel. AtomsK: A tool for manipulating and converting atomic data files. *Computer Physics Communications*, 197:212 – 219, 2015.
- [246] <https://www.atomic-scale-physics.de/lattice/>.
- [247] <http://rruff.geo.arizona.edu/AMS/amcsd.php>.
- [248] <http://www.crystallography.net/cod/>.
- [249] Erik Bitzek, Pekka Koskinen, Franz Gähler, Michael Moseler, and Peter Gumbusch. Structural relaxation made simple. *Physical review letters*, 97(17):170201, 2006.
- [250] Dieter Bäuerle. *Laser processing and chemistry*. Springer Science & Business Media, 2013.
- [251] J Hohlfeld, S-S Wellershoff, J GÜdde, U Conrad, V Jähnke, and E Matthias. Electron and lattice dynamics following optical excitation of metals. *Chemical Physics*, 251(1-3):237–258, 2000.

- [252] Mischa Bonn, Daniel N Denzler, Stephan Funk, Martin Wolf, S-Svante Wellerhoff, and Julius Hohlfeld. Ultrafast electron dynamics at metal surfaces: Competition between electron-phonon coupling and hot-electron transport. *Physical Review B*, 61(2):1101, 2000.
- [253] Xavier Gonze. A brief introduction to the abinit software package. *Zeitschrift für Kristallographie-Crystalline Materials*, 220(5-6):558–562, 2005.
- [254] C. Kittel. *Introduction to Solid State Physics*. Wiley, 2004.
- [255] Bastian Holst, Martin French, and Ronald Redmer. Electronic transport coefficients from ab initio simulations and application to dense liquid hydrogen. *Physical Review B*, 83(23):235120, 2011.
- [256] Aakash Yadav, PC Deshmukh, Ken Roberts, NM Jisrawi, and SR Valluri. An analytic study of the wiedemann–franz law and the thermoelectric figure of merit. *Journal of Physics Communications*, 3(10):105001, oct 2019.
- [257] NA Inogamov and Yu V Petrov. Thermal conductivity of metals with hot electrons. *Journal of Experimental and Theoretical Physics*, 110(3):446–468, 2010.
- [258] Carsten Schaefer, Herbert M Urbassek, and Leonid V Zhigilei. Metal ablation by picosecond laser pulses: A hybrid simulation. *Physical review B*, 66(11):115404, 2002.
- [259] H. Hakkinen and Uzi Landman. Superheating, melting, and annealing of copper surfaces. *Phys. Rev. Lett.*, 71:1023–1026, Aug 1993.
- [260] M. W. Finnis, P. Agnew, and A. J. E. Foreman. Thermal excitation of electrons in energetic displacement cascades. *Phys. Rev. B*, 44:567–574, Jul 1991.
- [261] Weirong Yuan and Tatyana Sizyuk. Ablation study in gold irradiated by single femtosecond laser pulse with electron temperature dependent interatomic potential and electron–phonon coupling factor. *Laser Physics*, 31(3):036002, 2021.
- [262] Mohammad W Ullah and Mauricio Ponga. A local two-temperature model for electronic heat conduction in molecular dynamics simulations. *arXiv preprint arXiv:1810.12357*, 2018.
- [263] A M Rutherford and D M Duffy. The effect of electron–ion interactions on radiation damage simulations. *Journal of Physics: Condensed Matter*, 19(49):496201, nov 2007.
- [264] [https://lammps.sandia.gov/doc/fix\\_ttm.html](https://lammps.sandia.gov/doc/fix_ttm.html).

- [265] DM Duffy and AM Rutherford. Including the effects of electronic stopping and electron-ion interactions in radiation damage simulations. *Journal of Physics: Condensed Matter*, 19(1):016207, 2006.
- [266] VV Pisarev and SV Starikov. Atomistic simulation of ion track formation in uo2. *Journal of Physics: Condensed Matter*, 26(47):475401, 2014.
- [267] Ahmed E. Ismail, Stephen Martin Foiles, Jeffery A. Greathouse, and Paul Stewart Crozier. The effect of electron-ion coupling on radiation damage simulations of a pyrochlore waste form. Technical report, United States, Nov 2009. SAND-2009-6892.
- [268] Carolyn L Phillips and Paul S Crozier. An energy-conserving two-temperature model of radiation damage in single-component and binary lennard-jones crystals. *The Journal of chemical physics*, 131(7):074701, 2009.
- [269] E. Bonderup and P. Hvelplund. Stopping power and energy straggling for swift protons. *Phys. Rev. A*, 4:562–569, Aug 1971.
- [270] Carolyn L Phillips, Rudolph J Magyar, and Paul S Crozier. A two-temperature model of radiation damage in  $\alpha$ -quartz. *The Journal of chemical physics*, 133(14):144711, 2010.
- [271] D. F. Swinehart. The beer-lambert law. *Journal of Chemical Education*, 39(7):333, Jul 1962.
- [272] <https://www.ovito.org/>.
- [273] <https://www.paraview.org/>.
- [274] <https://www.ks.uiuc.edu/Research/vmd/>.
- [275] Alexander Stukowski. Visualization and analysis of atomistic simulation data with ovito—the open visualization tool. *Modelling and simulation in materials science and engineering*, 18(1):015012, 2009.
- [276] J. Dana. Honeycutt and Hans C. Andersen. Molecular dynamics study of melting and freezing of small lennard-jones clusters. *The Journal of Physical Chemistry*, 91(19):4950–4963, Sep 1987.
- [277] Daniel Faken and Hannes Jónsson. Systematic analysis of local atomic structure combined with 3d computer graphics. *Computational Materials Science*, 2(2):279–286, 1994.

- [278] Alexander Stukowski. Structure identification methods for atomistic simulations of crystalline materials. *Modelling and Simulation in Materials Science and Engineering*, 20(4):045021, may 2012.
- [279] Peter Mahler Larsen, Søren Schmidt, and Jakob Schiøtz. Robust structural identification via polyhedral template matching. *Modelling and Simulation in Materials Science and Engineering*, 24(5):055007, may 2016.
- [280] Alexander Stukowski. Computational analysis methods in atomistic modeling of crystals. *Jom*, 66(3):399–407, 2014.
- [281] [https://www.ovito.org/docs/current/reference/pipelines/modifiers/construct\\_surface\\_mesh.html](https://www.ovito.org/docs/current/reference/pipelines/modifiers/construct_surface_mesh.html).
- [282] [https://www.ovito.org/docs/current/reference/pipelines/modifiers/wigner\\_seitz\\_analysis.html](https://www.ovito.org/docs/current/reference/pipelines/modifiers/wigner_seitz_analysis.html).
- [283] Pablo M Piaggi and Michele Parrinello. Entropy based fingerprint for local crystalline order. *The Journal of chemical physics*, 147(11):114112, 2017.
- [284] RE Nettleton and MS Green. Expression in terms of molecular distribution functions for the entropy density in an infinite system. *The Journal of Chemical Physics*, 29(6):1365–1370, 1958.
- [285] Eugene G Gamaly. The physics of ultra-short laser interaction with solids at non-relativistic intensities. *Physics Reports*, 508(4-5):91–243, 2011.
- [286] Razvan Stoian and Jean-Philippe Colombier. Advances in ultrafast laser structuring of materials at the nanoscale. *Nanophotonics*, 9(16):4665–4688, 2020.
- [287] Thomas Danz, Till Domröse, and Claus Ropers. Ultrafast nanoimaging of the order parameter in a structural phase transition. *Science*, 371(6527):371–374, 2021.
- [288] Jun Takeda, Wataru Oba, Yasuo Minami, Toshiharu Saiki, and Ikufumi Katayama. Ultrafast crystalline-to-amorphous phase transition in ge<sub>2</sub>sb<sub>2</sub>te<sub>5</sub> chalcogenide alloy thin film using single-shot imaging spectroscopy. *Applied Physics Letters*, 104(26):261903, 2014.
- [289] Ričardas Buividas, Gediminas Gervinskas, Anton Tadich, Bruce CC Cowie, Vyngantas Mizeikis, Arturas Vailionis, Dominique de Ligny, Eugene G Gamaly, Andrei V Rode, and Saulius Juodkazis. Phase transformation in laser-induced micro-explosion in olivine (fe, mg) <sub>2</sub>si<sub>4</sub>. *Advanced Engineering Materials*, 16(6):767–773, 2014.

- [290] Lena Bressel, Dominique de Ligny, Camille Sonnevile, Valérie Martinez, Vyngantas Mizeikis, Buividas, and Saulius Juodkazis. Femtosecond laser induced density changes in  $\text{geo}_2$  and  $\text{sio}_2$  glasses: fictive temperature effect. *Optical materials express*, 1(4):605–613, 2011.
- [291] K Sokolowski-Tinten, J Bialkowski, M Boing, A Cavalleri, and D Von Der Linde. Thermal and nonthermal melting of gallium arsenide after femtosecond laser excitation. *physical review B*, 58(18):R11805, 1998.
- [292] SK Sundaram and Eric Mazur. Inducing and probing non-thermal transitions in semiconductors using femtosecond laser pulses. *Nature materials*, 1(4):217–224, 2002.
- [293] Andrea Cavalleri, Cs Tóth, Craig W Siders, JA Squier, F Ráksi, P Forget, and JC Kieffer. Femtosecond structural dynamics in  $\text{vo}_2$  during an ultrafast solid-solid phase transition. *Physical review letters*, 87(23):237401, 2001.
- [294] Simon Wall, Daniel Wegkamp, Laura Foglia, K Appavoo, J Nag, RF Haglund, Julia Stähler, and Martin Wolf. Ultrafast changes in lattice symmetry probed by coherent phonons. *Nature communications*, 3(1):1–6, 2012.
- [295] HM Urbassek and L Sandoval. Molecular dynamics modeling of martensitic transformations in steels. *Phase transformations in steels*, pages 433–463, 2012.
- [296] C-H Lu, EN Hahn, BA Remington, BR Maddox, EM Bringa, and MA Meyers. Phase transformation in tantalum under extreme laser deformation. *Scientific reports*, 5(1):1–8, 2015.
- [297] W Petry, A Heiming, J Trampenau, M Alba, Chr Herzig, HR Schober, and G Vogl. Phonon dispersion of the bcc phase of group-iv metals. i. bcc titanium. *Physical Review B*, 43(13):10933, 1991.
- [298] J H. Li and B X. Liu. Structural phase transformation in ni–hf and ni–ti systems studied by molecular dynamics simulation. *Journal of the Physical Society of Japan*, 74(10):2699–2702, 2005.
- [299] Yu R Kolobov, EV Golosov, TN Vershinina, MV Zhidkov, AA Ionin, SI Kudryashov, SV Makarov, LV Seleznev, DV Sinitsyn, and AE Ligachev. Structural transformation and residual stresses in surface layers of  $\alpha + \beta$  titanium alloys nanotextured by femtosecond laser pulses. *Applied Physics A*, 119(1):241–247, 2015.

- [300] Samuel T Murphy, Szymon L Daraszewicz, Yvelin Giret, Matthew Watkins, Alexander L Shluger, Katsumi Tanimura, and Dorothy M Duffy. Dynamical simulations of an electronically induced solid-solid phase transformation in tungsten. *Physical Review B*, 92(13):134110, 2015.
- [301] L Ben-Mahfoud, EP Silaeva, R Stoian, and Jean-Philippe Colombier. Structural instability of transition metals upon ultrafast laser irradiation. *Physical Review B*, 104(10):104104, 2021.
- [302] Golden Kumar, Hong X Tang, and Jan Schroers. Nanomoulding with amorphous metals. *Nature*, 457(7231):868–872, 2009.
- [303] Djafar Iabbaden, Jonathan Amodeo, Claudio Fusco, Florence Garrelie, and Jean-Philippe Colombier. Molecular dynamics simulation of structural evolution in crystalline and amorphous cuzr alloys upon ultrafast laser irradiation. *Physical Review Materials*, 6(12):126001, 2022.
- [304] S I Anisimov. Electron emission from metal surfaces exposed to ultrashort laser pulses. *Sov. Phys. JETP*, 39(375):3, 1975.
- [305] Mohammad Rezaul Karim, Micheal Kattoura, Seetha R. Mannava, Vijay K. Vasudevan, Arif S. Malik, and Dong Qian. A computational study on the microstructural evolution in near-surface copper grain boundary structures due to femtosecond laser processing. *Computational Mechanics*, 61(1):105–117, Feb 2018.
- [306] Vladimir Stegailov, Sergey Starikov, and Genri Norman. Atomistic simulation of laser ablation of gold: The effect of electronic pressure. In *AIP Conference Proceedings*, volume 1426, pages 905–908. American Institute of Physics, 2012.
- [307] Byoung Seo Lee and Seungho Park. Applying tersoff-potential and bond-softening models in a molecular dynamics study of femtosecond laser processing. *Journal of Applied Physics*, 126(4):045109, 2019.
- [308] Harald O. Jeschke, Martin E. Garcia, and K. H. Bennemann. Theory for the ultrafast ablation of graphite films. *Phys. Rev. Lett.*, 87:015003, Jun 2001.
- [309] Hsien-Wei Chen, Kai-Chieh Hsu, Yu-Chen Chan, Jenq-Gong Duh, Jyh-Wei Lee, Jason Shian-Ching Jang, and Guo-Ju Chen. Antimicrobial properties of zr–cu–al–ag thin film metallic glass. *Thin Solid Films*, 561:98–101, 2014.
- [310] Liusi Yu, Junlei Tang, Hu Wang, Yingying Wang, Jichao Qiao, Mihai Apreutesei, and Bernard Normand. Corrosion behavior of bulk (zr58nb3cu16ni13al10) 100-

- xyx (x= 0, 0.5, 2.5 at.%) metallic glasses in sulfuric acid. *Corrosion Science*, 150:42–53, 2019.
- [311] Chen Li, Hao Zhang, Guanghua Cheng, Nicolas Faure, Damien Jamon, Jean-Philippe Colombier, and Razvan Stoian. Initial cumulative effects in femtosecond pulsed laser-induced periodic surface structures on bulk metallic glasses. *Journal of Laser Micro/Nanoengineering*, 11(3), 2016.
- [312] Mathilde Prudent, Florent Bourquard, Alejandro Borroto, Jean-François Pierson, Florence Garrelie, and Jean-Philippe Colombier. Initial morphology and feedback effects on laser-induced periodic nanostructuring of thin-film metallic glasses. *Nanomaterials*, 11(5):1076, 2021.
- [313] Michael S Titus, McLean P Echlin, Peter Gumbsch, and Tresa M Pollock. Dislocation injection in strontium titanate by femtosecond laser pulses. *Journal of Applied Physics*, 118(7):075901, 2015.
- [314] McLean P. Echlin, Michael S. Titus, Marcus Straw, Peter Gumbsch, and Tresa M. Pollock. Materials response to glancing incidence femtosecond laser ablation. *Acta Materialia*, 124:37–46, 2017.
- [315] Chengping Wu, Martin S Christensen, Juha-Matti Savolainen, Peter Balling, and Leonid V Zhigilei. Generation of subsurface voids and a nanocrystalline surface layer in femtosecond laser irradiation of a single-crystal ag target. *Physical Review B*, 91(3):035413, 2015.
- [316] MI Mendeleev, Yang Sun, Feng Zhang, Cai-Zhuang Wang, and Kai-Ming Ho. Development of a semi-empirical potential suitable for molecular dynamics simulation of vitrification in cu-zr alloys. *The Journal of Chemical Physics*, 151(21):214502, 2019.
- [317] Daan Frenkel and Berend Smit. *Understanding molecular simulation: from algorithms to applications*, volume 1. Elsevier, 2001.
- [318] Wenjin Zhang, Yufeng Peng, and Zhongli Liu. Molecular dynamics simulations of the melting curve of nial alloy under pressure. *AIP Advances*, 4(5):057110, 2014.
- [319] E Gowdini, AA Ahmad, A Mabudi, NL Hadipour, and B Kharazian. A molecular dynamics study on the thermal properties of carbon-based gold nanoparticles. *Journal of Molecular Modeling*, 26(11):1–9, 2020.

- [320] Mohammad Atif Faiz Afzal, Andrea R Browning, Alexander Goldberg, Mathew D Halls, Jacob L Gavartin, Tsuguo Morisato, Thomas F Hughes, David J Giesen, and Joseph E Goose. High-throughput molecular dynamics simulations and validation of thermophysical properties of polymers for various applications. *ACS Applied Polymer Materials*, 3(2):620–630, 2020.
- [321] Gonglin Yuan, Zengxin Wei, and Qiumei Zhao. A modified polak–ribière–polyak conjugate gradient algorithm for large-scale optimization problems. *IIE Transactions*, 46(4):397–413, 2014.
- [322] MA Turchanin, PG Agraval, and AR Abdulov. Thermodynamic assessment of the cu-ti-zr system. ii. cu-zr and ti-zr systems. *Powder Metallurgy and Metal Ceramics*, 47(7):428–446, 2008.
- [323] N Mattern, A Schöps, U Kühn, J Acker, O Khvostikova, and J Eckert. Structural behavior of  $\text{Cu}_x\text{Zr}_{100-x}$  metallic glass ( $x= 35- 70$ ). *Journal of Non-Crystalline Solids*, 354(10-11):1054–1060, 2008.
- [324] KK Song, S Pauly, Y Zhang, P Gargarella, R Li, NS Barekar, U Kühn, M Stoica, and J Eckert. Strategy for pinpointing the formation of b2 cuzr in metastable cuzr-based shape memory alloys. *Acta Materialia*, 59(17):6620–6630, 2011.
- [325] Mahendra Madhukar Khandpekar, Anik Shrivastava, DS Gowtam, M Mohape, and VP Deshmukh. Prediction of glass forming ability in cu xzr 1-x alloys using molecular dynamics. : , , , 6(5):650–660, 2015.
- [326] Fatih Sikan, Bengisu Yasar, and Ilkay Kalay. Nanocrystallization in cu-zr-al-sm bulk metallic glasses. *Metallurgical and Materials Transactions A*, 49(4):1328–1335, Apr 2018.
- [327] MI Mendeleev, MJ Kramer, RT Ott, DJ Sordelet, D Yagodin, and P Popel. Development of suitable interatomic potentials for simulation of liquid and amorphous cu–zr alloys. *Philosophical Magazine*, 89(11):967–987, 2009.
- [328] Ilkay Kalay. *Devitrification kinetics and phase selection mechanisms in copper-zirconium metallic glasses*. Iowa State University, 2010.
- [329] A Păduraru, Abder Kenoufi, Nicholas P Bailey, and Jacob Schiøtz. An interatomic potential for studying cuzr bulk metallic glasses. *Advanced Engineering Materials*, 9(6):505–508, 2007.
- [330] Yu A. Babanov, V. R. Schvetsov, and A. F. Sidorenko. Atomic structure of binary amorphous alloys by combined exafs and x-ray scattering. *Physica B: Condensed Matter*, 208-209:375–376, 1995.

- [331] M Bionducci, F Buffa, G Licheri, G Navarra, B Bouchet-Fabre, and JM Tonnerre. Determination of the partial structure factors of amorphous cu<sub>zr</sub> by anomalous x-ray scattering and reverse monte carlo. *Zeitschrift für Naturforschung A*, 51(1-2):71–82, 1996.
- [332] Gang Duan, Donghua Xu, Qing Zhang, Guoyun Zhang, Tahir Cagin, William L Johnson, and William A Goddard III. Molecular dynamics study of the binary cu<sub>46</sub>zr<sub>54</sub> metallic glass motivated by experiments: Glass formation and atomic-level structure. *Physical Review B*, 71(22):224208, 2005.
- [333] HS Chen and Yo Waseda. Structure of glassy zrcu and nbni alloys. *physica status solidi (a)*, 51(2):593–599, 1979.
- [334] Yong Gan and JK Chen. Integrated continuum-atomistic modeling of nonthermal ablation of gold nanofilms by femtosecond lasers. *Applied Physics Letters*, 94(20):201116, 2009.
- [335] Maxim V. Shugaev and Leonid V. Zhigilei. Thermoelastic modeling of laser-induced generation of strong surface acoustic waves. *Journal of Applied Physics*, 130(18):185108, 2021.
- [336] Maxim V. Shugaev, Miao He, Yoann Levy, Alberto Mazzi, Antonio Miotello, Nadezhda M. Bulgakova, and Leonid V. Zhigilei. *Laser-Induced Thermal Processes: Heat Transfer, Generation of Stresses, Melting and Solidification, Vaporization, and Phase Explosion*, pages 1–81. Springer International Publishing, Cham, 2020.
- [337] [https://docs.lammps.org/fix\\_viscous.html](https://docs.lammps.org/fix_viscous.html).
- [338] P Garoche and J Bigot. Comparison between amorphous and crystalline phases of copper-zirconium alloys by specific-heat measurements. *Physical review B*, 28(12):6886, 1983.
- [339] S. Uporov, V. Bykov, and S. Estemirova. Electrical and thermal conductivities of rapidly crystallized cu-zr alloys: The effect of anharmonicity. *Physica B: Condensed Matter*, 499:97–106, 2016.
- [340] CL Choy, KW Tong, HK Wong, and WP Leung. Thermal conductivity of amorphous alloys above room temperature. *Journal of applied physics*, 70(9):4919–4925, 1991.
- [341] Hv Löhneysen, M Platte, W Sander, HJ Schink, GV Minnigerode, and K Samwer. Low temperature thermal properties of amorphous superconducting zrcu. *Le Journal de Physique Colloques*, 41(C8):C8–745, 1980.

- [342] Xiangyang Zhang and Huseyin Sehitoglu. Crystallography of the  $b2 \rightarrow r \rightarrow b19$  phase transformations in niti. *Materials Science and Engineering: A*, 374(1-2):292–302, 2004.
- [343] Won-Seok Ko, Blazej Grabowski, and Jörg Neugebauer. Development and application of a ni-ti interatomic potential with high predictive accuracy of the martensitic phase transition. *Physical Review B*, 92(13):134107, 2015.
- [344] JS Bowles and JK Mackenzie. The crystallography of martensite transformations. *Acta metallurgica*, 2(1):129–137, 1954.
- [345] <https://www.atomic-scale-physics.de/lattice/struk/b19.html>.
- [346] Vijay Kumar Sutrar and D. Roy Mahapatra. Single and multi-step phase transformation in cuzr nanowire under compressive/tensile loading. *Intermetallics*, 18(4):679–687, 2010.
- [347] [https://www.ovito.org/docs/current/reference/pipelines/modifiers/displacement\\_vectors.html](https://www.ovito.org/docs/current/reference/pipelines/modifiers/displacement_vectors.html).
- [348] Miao He, Eaman T Karim, Maxim V Shugaev, and Leonid V Zhigilei. Atomistic simulation of the generation of vacancies in rapid crystallization of metals. *Acta Materialia*, 203:116465, 2021.
- [349] Eaman T Karim, Chengping Wu, and Leonid V Zhigilei. Molecular dynamics simulations of laser-materials interactions: General and material-specific mechanisms of material removal and generation of crystal defects. In *Fundamentals of laser-assisted micro-and nanotechnologies*, pages 27–49. Springer, 2014.
- [350] Jordi Sort, Luiz Fernando Bonavina, Aïda Varea, Carlos Souza, Walter J Botta, Claudio S Kiminami, Claudemiro Bolfarini, Santiago Surinach, Maria Dolors Baró, and Josep Nogués. Out-of-plane magnetic patterning based on indentation-induced nanocrystallization of a metallic glass. *small*, 6(14):1543–1549, 2010.
- [351] J Fornell, E Rossinyol, S Surinach, MD Baró, WH Li, and J Sort. Enhanced mechanical properties in a zr-based metallic glass caused by deformation-induced nanocrystallization. *Scripta Materialia*, 62(1):13–16, 2010.
- [352] Zhichao Ma, Fangzhou Lu, Xiaoxi Ma, Hongwei Zhao, Kaiyang Zeng, and Luquan Ren. Cyclic stress induced surface nanocrystallization adjacent to indentation edge of zr-based bulk metallic glass at room temperature. *Applied Surface Science*, 506:145044, 2020.

- [353] Zijiao Zhang, Hongwei Sheng, Zhangjie Wang, Bernd Gludovatz, Ze Zhang, Easo P George, Qian Yu, Scott X Mao, and Robert O Ritchie. Dislocation mechanisms and 3d twin architectures generate exceptional strength-ductility-toughness combination in crconi medium-entropy alloy. *Nature communications*, 8(1):1–8, 2017.
- [354] Yongjun Tian, Bo Xu, Dongli Yu, Yanming Ma, Yanbin Wang, Yingbing Jiang, Wentao Hu, Chengchun Tang, Yufei Gao, Kun Luo, et al. Ultrahard nanotwinned cubic boron nitride. *Nature*, 493(7432):385–388, 2013.
- [355] Prateek Uttam, Vanish Kumar, Ki-Hun Kim, and Akash Deep. Nanotwinning: Generation, properties, and application. *Materials & Design*, 192:108752, 2020.
- [356] Y Pan, YQ Li, QH Zheng, and Y Xu. Point defect of titanium sesquioxide  $\text{Ti}_2\text{O}_3$  as the application of next generation li-ion batteries. *Journal of Alloys and Compounds*, 786:621–626, 2019.
- [357] Lipeng Hu, Tiejun Zhu, Xiaohua Liu, and Xinbing Zhao. Point defect engineering of high-performance bismuth-telluride-based thermoelectric materials. *Advanced Functional Materials*, 24(33):5211–5218, 2014.
- [358] CT Liu, JH Zhu, MP Brady, CG McKamey, and LM Pike. Physical metallurgy and mechanical properties of transition-metal laves phase alloys. *Intermetallics*, 8(9-11):1119–1129, 2000.
- [359] Juan A Hofer, Carlos J Ruestes, Eduardo M Bringa, and Herbert M Urbassek. Effect of subsurface voids on the nanoindentation of fe crystals. *Modelling and Simulation in Materials Science and Engineering*, 28(2):025010, 2020.
- [360] Anh-Son Tran, Te-Hua Fang, and Jhih-Wei Hsiao. Incipient plasticity and voids nucleation of nanocrystalline gold nanofilms using molecular dynamics simulation. *Current Applied Physics*, 19(3):332–340, 2019.
- [361] AL Bowman, S Mun, S Nouranian, BD Huddleston, SR Gwaltney, MI Baskes, and MF Horstemeyer. Free volume and internal structural evolution during creep in model amorphous polyethylene by molecular dynamics simulations. *Polymer*, 170:85–100, 2019.
- [362] Peng Wen, Brian Demaske, Simon R Phillpot, Douglas E Spearot, Gang Tao, and Shuqiang Yuan. Void collapse and subsequent spallation in  $\text{Cu}_{50}\text{Zr}_{50}$  metallic glass under shock loading by molecular dynamics simulations. *Journal of Applied Physics*, 125(21):215903, 2019.

- [363] Binbin Xin, Arnaud Le Febvrier, Rui Shu, Anna Elsukova, Venkat Venkataramani, Yunfeng Shi, Ganpati Ramanath, Biplab Paul, and Per Eklund. Engineering faceted nanoporosity by reactions in thin-film oxide multilayers in crystallographically layered calcium cobaltate for thermoelectrics. *ACS Applied Nano Materials*, 4(9):9904–9911, 2021.
- [364] Anupam Neogi and Nilanjan Mitra. On shock response of nano-void closed/open cell copper material: Non-equilibrium molecular dynamic simulations. *Journal of Applied Physics*, 115(1):013504, 2014.
- [365] Chenyu Zou, Yun Kyung Shin, Adri CT Van Duin, Huazhi Fang, and Zi-Kui Liu. Molecular dynamics simulations of the effects of vacancies on nickel self-diffusion, oxygen diffusion and oxidation initiation in nickel, using the reaxff reactive force field. *Acta Materialia*, 83:102–112, 2015.
- [366] H Liu, XM Wang, H Liang, ZN Zhao, L Li, ZF Yue, and CH Deng. The effect of void defect on the evolution mechanisms of dislocations and mechanical properties in nickel-based superalloys by molecular dynamics simulation of real  $\gamma/\gamma'$  structures. *International Journal of Solids and Structures*, 191:464–472, 2020.
- [367] Cheng-Yu Shih, Maxim V Shugaev, Chengping Wu, and Leonid V Zhigilei. Generation of subsurface voids, incubation effect, and formation of nanoparticles in short pulse laser interactions with bulk metal targets in liquid: molecular dynamics study. *The Journal of Physical Chemistry C*, 121(30):16549–16567, 2017.
- [368] Maxim V Shugaev and Leonid V Zhigilei. Thermodynamic analysis and atomistic modeling of subsurface cavitation in photomechanical spallation. *Computational Materials Science*, 166:311–317, 2019.
- [369] Eaman T Karim, Maxim V Shugaev, Chengping Wu, Zhibin Lin, Hisashi Matsumoto, Maria Conneran, Jan Kleinert, Robert F Hainsey, and Leonid V Zhigilei. Experimental characterization and atomistic modeling of interfacial void formation and detachment in short pulse laser processing of metal surfaces covered by solid transparent overlayers. *Applied Physics A*, 122(4):1–11, 2016.
- [370] Chongchun Jiang, Yunjie Mo, Hong Wang, Ruihao Li, Min Huang, and Shaoji Jiang. Molecular dynamics simulation of the production of hollow silver nanoparticles under ultrafast laser irradiation. *Computational Materials Science*, 196:110545, 2021.
- [371] Mathilde Prudent, Djafar Iabbaden, Florent Bourquard, Stéphanie Reynaud, Yaya Lefkir, Alejandro Borroto, Jean-François Pierson, Florence Garrelie, and

- Jean-Philippe Colombier. High-density nanowells formation in ultrafast laser-irradiated thin film metallic glass. *Nano-Micro Letters*, 14(1):1–15, 2022.
- [372] Eaman T Karim, Maxim Shugaev, Chengping Wu, Zhibin Lin, Robert F Hainsey, and Leonid V Zhigilei. Atomistic simulation study of short pulse laser interactions with a metal target under conditions of spatial confinement by a transparent overlayer. *Journal of Applied Physics*, 115(18):183501, 2014.
- [373] DH Trevena. Cavitation and the generation of tension in liquids. *Journal of Physics D: Applied Physics*, 17(11):2139, 1984.
- [374] Leonid V Zhigilei. Dynamics of the plume formation and parameters of the ejected clusters in short-pulse laser ablation. *Applied Physics A*, 76(3):339–350, 2003.
- [375] J Cui, JS Li, J Wang, HC Kou, JC Qiao, S Gravier, and JJ Blandin. Rheological behavior of cu–zr-based metallic glass in the supercooled liquid region. *Journal of alloys and compounds*, 592:189–195, 2014.
- [376] M Apreutesei, Alain Billard, and Philippe Steyer. Crystallization and hardening of zr-40 at.% cu thin film metallic glass: Effects of isothermal annealing. *Materials & Design*, 86:555–563, 2015.
- [377] J Zemp, Massimo Celino, Bernd Schönfeld, and Jörg F Löffler. Crystal-like rearrangements of icosahedra in simulated copper-zirconium metallic glasses and their effect on mechanical properties. *Physical review letters*, 115(16):165501, 2015.
- [378] RE Ryltsev and NM Chtchelkatchev. Polytetrahedral short-range order and crystallization stability in supercooled cu<sub>64</sub>.<sub>5</sub>zr<sub>35</sub>.<sub>5</sub> metallic liquid. *Journal of Crystal Growth*, 531:125374, 2020.
- [379] Tobias Brink and Karsten Albe. From metallic glasses to nanocrystals: Molecular dynamics simulations on the crossover from glass-like to grain-boundary-mediated deformation behaviour. *Acta Materialia*, 156:205–214, 2018.
- [380] Lu Xie, Pascal Brault, Jean-Marc Bauchire, Anne-Lise Thomann, and Larbi Bedra. Molecular dynamics simulations of clusters and thin film growth in the context of plasma sputtering deposition. *Journal of Physics D: Applied Physics*, 47(22):224004, 2014.
- [381] JS Langer. Shear-transformation-zone theory of deformation in metallic glasses. *Scripta materialia*, 54(3):375–379, 2006.

- [382] SG Hao, CZ Wang, MJ Kramer, and KM Ho. Microscopic origin of slow dynamics at the good glass forming composition range in zr 1- x cu x metallic liquids. *Journal of Applied Physics*, 107(5):053511, 2010.
- [383] G. E. Norman, S. V. Starikov, V. V. Stegailov, I. M. Saitov, and P. A. Zhilyaev. Atomistic Modeling of Warm Dense Matter in the Two-Temperature State. *Contrib. Plasm. Phys.*, 53(2):129–139, 2013.
- [384] Aidan P Thompson, H Metin Aktulga, Richard Berger, Dan S Bolintineanu, W Michael Brown, Paul S Crozier, Pieter J in't Veld, Axel Kohlmeyer, Stan G Moore, Trung Dac Nguyen, et al. Lammmps-a flexible simulation tool for particle-based materials modeling at the atomic, meso, and continuum scales. *Computer Physics Communications*, 271:108171, 2022.
- [385] Denis J Evans and Brad Lee Holian. The nose–hoover thermostat. *The Journal of chemical physics*, 83(8):4069–4074, 1985.
- [386] AJ Cao, YQ Cheng, and E Ma. Structural processes that initiate shear localization in metallic glass. *Acta Materialia*, 57(17):5146–5155, 2009.
- [387] Alexander Stukowski. Structure identification methods for atomistic simulations of crystalline materials. *Modelling and Simulation in Materials Science and Engineering*, 20(4):045021, 2012.
- [388] Peter Mahler Larsen, Søren Schmidt, and Jakob Schiøtz. Robust structural identification via polyhedral template matching. *Modelling and Simulation in Materials Science and Engineering*, 24(5):055007, 2016.
- [389] SH Zhou and RE Napolitano. Phase stability for the cu–zr system: first-principles, experiments and solution-based modeling. *Acta Materialia*, 58(6):2186–2196, 2010.
- [390] AS Rogachev, SG Vadchenko, AS Aronin, S Rouvimov, AA Nepapushev, ID Kovalev, Florence Baras, O Politano, SA Rogachev, and AS Mukasyan. Self-propagating waves of crystallization in metallic glasses. *Applied Physics Letters*, 111(9):093105, 2017.
- [391] SP Coleman, DE Spearot, and L Capolungo. Virtual diffraction analysis of ni [0 1 0] symmetric tilt grain boundaries. *Modelling and Simulation in Materials Science and Engineering*, 21(5):055020, 2013.
- [392] Shawn P Coleman, Mehrdad M Sichani, and Douglas E Spearot. A computational algorithm to produce virtual x-ray and electron diffraction patterns from atomistic simulations. *Jom*, 66(3):408–416, 2014.

- [393] J Epp. X-ray diffraction (xrd) techniques for materials characterization. In *Materials characterization using nondestructive evaluation (NDE) methods*, pages 81–124. Elsevier, 2016.
- [394] Lu Xie, Pascal Brault, Anne-Lise Thomann, and Larbi Bedra. Molecular dynamic simulation of binary zrxcu100- x metallic glass thin film growth. *Applied surface science*, 274:164–170, 2013.
- [395] Mathieu Leocmach and Hajime Tanaka. Roles of icosahedral and crystal-like order in the hard spheres glass transition. *Nature communications*, 3(1):974, 2012.
- [396] M Fanfoni and M Tomellini. The johnson-mehl-avrami-kohnogorov model: a brief review. *Il Nuovo Cimento D*, 20(7):1171–1182, 1998.
- [397] Vladimir M Fokin, Edgar D Zanotto, Nikolay S Yuritsyn, and Jörn WP Schmelzer. Homogeneous crystal nucleation in silicate glasses: A 40 years perspective. *Journal of Non-Crystalline Solids*, 352(26-27):2681–2714, 2006.
- [398] Laurent Cormier. Nucleation in glasses—new experimental findings and recent theories. *Procedia Materials Science*, 7:60–71, 2014.
- [399] Dong-Hee Kang, Hao Zhang, Hanbyeol Yoo, Hyun Hwi Lee, Soohyong Lee, Geun Woo Lee, Hongbo Lou, Xiaodong Wang, Qingping Cao, Dongxian Zhang, et al. Interfacial free energy controlling glass-forming ability of cu-zr alloys. *Scientific reports*, 4(1):1–5, 2014.
- [400] Katsunori Yamaguchi, Young-Cheol Song, Toshiaki Yoshida, and Kimio Itagaki. Thermodynamic investigation of the cu-zr system. *Journal of alloys and compounds*, 452(1):73–79, 2008.
- [401] Dmitri V Louzguine-Luzgin and Akihisa Inoue. Nano-devitrification of glassy alloys. *Journal of Nanoscience and Nanotechnology*, 5(7):999–1014, 2005.
- [402] James JP Stewart. Optimization of parameters for semiempirical methods via more modifications to the nndo approximations and re-optimization of parameters. *Journal of molecular modeling*, 19(1):1–32, 2013.
- [403] M. J. Frisch, G. W. Trucks, H. B. Schlegel, G. E. Scuseria, M. A. Robb, J. R. Cheeseman, G. Scalmani, V. Barone, G. A. Petersson, H. Nakatsuji, X. Li, M. Caricato, A. V. Marenich, J. Bloino, B. G. Janesko, R. Gomperts, B. Mennucci, H. P. Hratchian, J. V. Ortiz, A. F. Izmaylov, J. L. Sonnenberg, D. Williams-Young, F. Ding, F. Lipparini, F. Egidi, J. Goings, B. Peng,

- A. Petrone, T. Henderson, D. Ranasinghe, V. G. Zakrzewski, J. Gao, N. Rega, G. Zheng, W. Liang, M. Hada, M. Ehara, K. Toyota, R. Fukuda, J. Hasegawa, M. Ishida, T. Nakajima, Y. Honda, O. Kitao, H. Nakai, T. Vreven, K. Throssell, J. A. Montgomery, Jr., J. E. Peralta, F. Ogliaro, M. J. Bearpark, J. J. Heyd, E. N. Brothers, K. N. Kudin, V. N. Staroverov, T. A. Keith, R. Kobayashi, J. Normand, K. Raghavachari, A. P. Rendell, J. C. Burant, S. S. Iyengar, J. Tomasi, M. Cossi, J. M. Millam, M. Klene, C. Adamo, R. Cammi, J. W. Ochterski, R. L. Martin, K. Morokuma, O. Farkas, J. B. Foresman, and D. J. Fox. Gaussian~16 Revision C.01, 2016. Gaussian Inc. Wallingford CT.
- [404] J Ha, Y Seo, T-Y Choi, and D Kim. Enhanced thermal conductivity of alumina nanoparticle suspensions by femtosecond laser irradiation. *International Journal of Heat and Mass Transfer*, 107:755–760, 2017.
- [405] Jeonghong Ha, Hyeonjin Jeon, Tae-Youl Choi, and Dongsik Kim. Enhancement of thermal conductivity of titanium dioxide nanoparticle suspensions by femtosecond laser irradiation. *International Journal of Heat and Mass Transfer*, 133:662–668, 2019.
- [406] Donatas Surblys, Hiroki Matsubara, Gota Kikugawa, and Taku Ohara. Application of atomic stress to compute heat flux via molecular dynamics for systems with many-body interactions. *Physical Review E*, 99(5):051301, 2019.
- [407] Paul Boone, Hasan Babaei, and Christopher E Wilmer. Heat flux for many-body interactions: corrections to lammmps. *Journal of chemical theory and computation*, 15(10):5579–5587, 2019.
- [408] Donatas Surblys, Hiroki Matsubara, Gota Kikugawa, and Taku Ohara. Methodology and meaning of computing heat flux via atomic stress in systems with constraint dynamics. *Journal of Applied Physics*, 130(21):215104, 2021.
- [409] John M Ziman. *Electrons and phonons: the theory of transport phenomena in solids*. Oxford university press, 2001.
- [410] Xavier Gonze, J-M Beuken, Razvan Caracas, F Detraux, M Fuchs, G-M Rignanese, Luc Sindic, Matthieu Verstraete, G Zerah, F Jollet, et al. First-principles computation of material properties: the abinit software project. *Computational Materials Science*, 25(3):478–492, 2002.
- [411] Xavier Gonze, Bernard Amadon, Gabriel Antonius, Frédéric Arnardi, Lucas Baguet, Jean-Michel Beuken, Jordan Bieder, François Bottin, Johann Bouchet, Eric Bousquet, Nils Brouwer, Fabien Bruneval, Guillaume Brunin, Théo Cavignac, Jean-Baptiste Charraud, Wei Chen, Michel Côté, Stefaan Cottenier, Jules

- Denier, Grégory Geneste, Philippe Ghosez, Matteo Giantomassi, Yannick Gillet, Olivier Gingras, Donald R. Hamann, Geoffroy Hautier, Xu He, Nicole Helbig, Natalie Holzwarth, Yongchao Jia, François Jollet, William Lafargue-Dit-Hauret, Kurt Lejaeghere, Miguel A.L. Marques, Alexandre Martin, Cyril Martins, Henrique P.C. Miranda, Francesco Naccarato, Kristin Persson, Guido Petretto, Valentin Planes, Yann Pouillon, Sergei Prokhorenko, Fabio Ricci, Gian-Marco Rignanese, Aldo H. Romero, Michael Marcus Schmitt, Marc Torrent, Michiel J. van Setten, Benoit Van Troeye, Matthieu J. Verstraete, Gilles Zérah, and Josef W. Zwanziger. The abinitproject: Impact, environment and recent developments. *Computer Physics Communications*, 248:107042, 2020.
- [412] Xavier Gonze, Bernard Amadon, Gabriel Antonius, Frédéric Arnardi, Lucas Baguet, Jean-Michel Beuken, Jordan Bieder, François Bottin, Johann Bouchet, Eric Bousquet, et al. The abinit project: Impact, environment and recent developments. *Computer Physics Communications*, 248:107042, 2020.
- [413] Marc Torrent, François Jollet, François Bottin, Gilles Zérah, and Xavier Gonze. Implementation of the projector augmented-wave method in the abinit code: Application to the study of iron under pressure. *Computational Materials Science*, 42(2):337–351, 2008.
- [414] Anton Kokalj. Xcrysden—a new program for displaying crystalline structures and electron densities. *Journal of Molecular Graphics and Modelling*, 17(3-4):176–179, 1999.
- [415] Chris Rycroft. Voro++: A three-dimensional voronoi cell library in c++. Technical report, Lawrence Berkeley National Lab.(LBNL), Berkeley, CA (United States), 2009.